Seismic Performance and Building Height Limits of Ductile Reinforced Concrete Masonry Shear Walls with Boundary Elements

Nader Essam Aly

A Thesis
In The Department of
Building, Civil, and Environmental Engineering

Presented in Partial Fulfillment of the Requirements
For the Degree of
Doctor of Philosophy (Civil Engineering) at
Concordia University
Montréal, Québec, Canada

October 2019

CONCORDIA UNIVERSITY

School of Graduate Studies

This is to certify that the thesis prepared

By: Nader Essam Aly

Entitled: Seismic Performance and Building Height Limits of Ductile Reinforced Concrete Masonry Shear Walls with Boundary Elements

and submitted in partial fulfillment of the requirements for the degree of

Doctor of Philosophy (Civil Engineering)

complies with the regulations of the University and meets the accepted standards with respect to originality and quality.

Signed by the final examining committee:

_____ Chair
Dr. Akshay Kumar Rathore

_____ External Examiner
Dr. Nigel Shrive

_____ External to Program
Dr. Ramin Sedaghati

_____ Examiner
Dr. Ashutosh Bagchi

_____ Examiner
Dr. Anjan Bhowmick

_____ Thesis supervisor
Dr. Khaled Galal

Approved by _____
Dr. Michelle Nokken, Graduate Program Director

_____
Dr. Amir Asif, Dean
Gina Cody School of Engineering and Computer Science

Date of Defense: 2019-11-26

ABSTRACT

Seismic Performance and Building Height Limits of Ductile Reinforced Concrete Masonry Shear Walls with Boundary Elements

Nader Essam Aly, Ph.D.
Concordia University, 2019

The National Building Code of Canada, NBCC-15, has recently added a new Seismic Force Resisting System (SFRS) category, ductile shear walls, for Reinforced Concrete Masonry (RCM) buildings. Although it is given a higher ductility-related force modification factor, R_d=3.0, compared to that of moderately ductile walls R_d=2.0, NBCC-15 assigned the same building height limits for the ductile and moderately ductile RCM walls. The research work outlined herein contributes to the understanding of the seismic performance and collapse capacity of ductile RCM shear wall buildings with boundary elements. The main objective is to develop *component* and *system* levels, solutions and design recommendations to enhance the overall seismic performance of RCM buildings.

At the *component* (structural element) level, it is proposed to utilize RCM shear walls with boundary elements built using C-shaped masonry blocks. To quantify the component's seismic performance, six half-scale high-rise RCM shear walls were constructed and tested under high constant axial compressive load, along with in-plane fully reversed cyclic loading synchronized with top moment. The tested walls represented the plastic hinge region of prototype 6- and 12-storey RCM structural walls. The studied parameters are the boundary element's length, the boundary element's vertical reinforcement ratio, the wall's shear span-to-depth ratio, the type of masonry blocks used in constructing the boundary elements (stretcher or C-shaped), and the lap splicing of vertical rebars in the plastic hinge region.

At the *system* (building) level, a hybrid structural system composed of ductile and gravity walls is proposed. The ductile walls are RCM shear walls with boundary elements, whereas the gravity walls are conventional rectangular RCM walls with no special seismic detailing. Several archetype buildings were designed according to NBCC-15 and the Canadian masonry design standard CSA

S304-14 with varying heights, location's seismicity, ductile shear wall ratios and cross-sectional configurations. Validated macro-modelling approaches were utilized to simulate the nonlinear response of the buildings. A series of linear and nonlinear, pseudo-static and dynamic time-history analyses were performed to quantify the influence of the studied parameters on the seismic response and collapse capacity. Besides, the possibility of increasing the height limits of ductile RCM shear walls was evaluated. Finally, the potential for reducing and terminating the specially detailed boundary elements over the building's height was investigated.

The results of the experimental testing confirmed that the presence of the well-detailed and confined boundary elements is capable of mitigating the impacts of the high axial compression load. Using the C-shaped masonry blocks instead of the regular stretcher blocks in constructing the boundary elements enhanced the construction and performance of the walls. Lap splicing of vertical rebars increased the initial lateral stiffness, the rate of stiffness and strength degradation, and slightly limited the displacement ductility. However, with proper detailing of the splice and confinement of the end zones, the premature tensile bond failure was prevented.

Based on the findings of the numerical simulations, it was suggested to increase the height limits of RCM buildings with ductile shear walls with boundary elements. In addition, the results emphasized that utilizing the ductile walls with boundary elements, instead of the traditional rectangular walls, in the proposed hybrid structural system enhanced the structural response and optimized the design. Furthermore, the results demonstrated the possibility of vertically reducing and terminating the specially detailed boundary elements. Therefore, the experimental and numerical results of this research form a step forward in presenting RCM shear walls with boundary elements as a practical and competitive SFRS.

Dedications

To my beloved parents; Amal and Essam,

To my lovely wife; Shorouk Khalaf,

To my beautiful daughter; Jamila,

To my brothers; Mohamed and Omar.

Acknowledgements

All praise and gratitude be to Allah the Most Gracious, the Most Compassionate, and the Most Merciful with the blessings of whom the good deeds are fulfilled

I would like to express my sincere thanks and appreciation to my supervisor, Professor Khaled Galal. This research would have never been possible without his continuous motivation, support, guidance, and encouragement. He was always there to provide the technical advice and the positive attitude needed to stay motivated and move forward with my research. It was an honour being one of his graduate students. I would also like to thank the examination committee, Dr. Nigel Shrive, Dr. Ramin Sedaghati, Dr. Ashutosh Bagchi, and Dr. Anjan Bhowmick, for their thorough review of the thesis, valuable suggestions and remarks.

My sincere thanks and gratitude are due to my friend, partner, and brother Mohammed Albutainy, without his help and motivation, I would not have completed this research. I would also like to thank my special friend and brother Mohamed Yosry. Profound thanks are due to my friend and the postdoctoral fellow Dr. Ahmed Ashour, for his suggestions and guidance. Also, I would like to thank my colleagues and friends Dr. Ashraf Osman, Dr. Ala' Obaidat, Dr. Khalid Al-Otaibi, Dr. Hamid Arabzadeh, Omer Yagob, Shadman Hosseinzadeh, Layane Hamzeh, Belal Abdelrahman, and Omar Gouda for their support, discussions, hints, and motivation. Special thanks are due to the staff of the Structures Laboratory at Concordia University (Jaime Yeargans, Roberto Avila, Nicolas Silva-Castellon, Andy Shin-Pong, and Riccardo Gioia) for their support and assistance during the experimental work. I also express my sincere appreciation to Martine Leclerc and Patrice Bélanger from École Polytechnique de Montréal for their technical support during the experimental work. I am thankful for the undergraduate students, Natalio Ghannoum, Akalu Nega, Alexandre Wakim, Zixuan Wang, Hazem Akil, Sanoshan Veerasingam, Mohab Othman, and Rebecca Mossa for their help during the experimental work. Many thanks are due to my master's supervisor at the American University of Sharjah, Dr. Mohammed AlHamaydeh, who prepared me very well for the Ph.D.

The support from the Natural Science and Engineering Research Council of Canada (NSERC), l'Association des Entrepreneurs en Maçonnerie du Québec (AEMQ), the Canadian Concrete Masonry Producers Association (CCMPA), and the Canadian Masonry Design Centre (CMDC) is much appreciated. Also, I would like to acknowledge the financial support from Concordia University.

I am very thankful to my parents, Amal and Essam, who are the real cause behind any success I can achieve in this life. No words can sufficiently express my appreciation for their efforts, support, motivation, and advice. It is also a blessing to have a supportive and understanding wife and partner in life. I express my sincerest thanks to my wife, Shorouk Khalaf, for her endless support. I am also thankful to my beautiful daughter, Jamila, for her innocent smiles, which eased the long hours of work.

Co-Authorship

This thesis has been prepared in accordance with the regulations for a sandwich (manuscript-based) thesis format. The research presented herein includes experimental, numerical, and analytical work carried out solely by Nader Aly. Advice and guidance were provided for the whole thesis by the academic supervisor Professor Khaled Galal. This thesis consists of the following chapters, which are based on published and submitted papers in peer-reviewed journals:

Chapter 3

Aly, N., and Galal, K. (2019). Experimental investigation of axial load and detailing effects on the inelastic response of reinforced concrete masonry structural walls with boundary elements, *ASCE Journal of Structural Engineering*, submitted for publication in July 2019.

Chapter 4

Aly, N., and Galal, K. (2019). In-plane cyclic response of high-rise reinforced concrete masonry structural walls with boundary elements, *Engineering Structures Journal*, submitted for publication in August 2019.

Chapter 5

Aly, N., and Galal, K. (2019). Seismic performance and height limits of ductile reinforced masonry shear wall buildings with boundary elements. *Engineering Structures Journal*, 190, 171–188.

Chapter 6

Aly, N., and Galal, K. (2019). Effect of ductile shear wall ratio and cross-section configuration on the seismic behavior of reinforced concrete masonry shear wall buildings. *ASCE Journal of Structural Engineering,* accepted-in press.

Table of Contents

List of Figures

List of Tables

Chapter 1

Introduction

1.1 Background

Masonry is one of the most ancient construction materials. As an alternative building material, it offers relatively rapid construction, due to its modular nature, and built-in soundproofing and fire insulation characteristics. Unreinforced Masonry (URM) has been extensively used in low-rise buildings located in low seismic hazard regions. With the evolution of building codes and design standards, the use of URM became limited, and more demand was shifted towards Reinforced Concrete Masonry (RCM) structural systems. RCM was used in mid- and high-rise buildings, but also in regions with low seismicity (Drysdale and Hamid, 2005). Multi-storey masonry buildings have been effectively utilized in regions with low seismic hazard, such as the 24-storey apartment building (Place Louis Riel) in Winnipeg (Drysdale and Hamid, 2005) and the 20-storey building in Brazil (Correa, 2016). However, the application in regions with moderate and high seismicity is still limited due to the challenges involved with conventional types of masonry Seismic Force Resisting Systems (SFRS) and the typical wall load-bearing structural system. The most common SFRS in masonry buildings is RCM structural walls.

Masonry buildings have been perceived incapable of achieving a ductile seismic response. This perception stems from the observed damage and response of URM buildings during previous earthquake events (Zhao and Wang, 2015). Bruneau and Yoshimura (1996) presented an assessment of the damage to masonry buildings after the Hyogo-ken Nanbu (Kobe) earthquake in 1995. The authors concluded that most of the URM buildings found in the earthquake site were severely damaged. However, it was reported that the few reinforced masonry buildings that existed in the Kobe area showed a satisfactory seismic response. The capacity design philosophy introduced by Park and Paulay (1975) requires selecting, designing, and detailing a region or a component in the structure to develop a stable energy dissipation mechanism (i.e., without a sudden loss in load-carrying capacity). In addition, non-ductile (brittle) failure modes, such as shear failure, must be suppressed. Therefore, for the RCM shear walls to be ductile in a seismic event, it shall be capable of sustaining large reversible cycles of inelastic deformations without significant degradation in strength. This can be achieved by integrating confined boundary elements at the ends of the rectangular RCM shear walls as shown in Figure 1.1.

Incorporating confined boundary elements to the RCM shear wall's ends is one way of achieving the ductile response. RCM shear walls constructed with boundary elements demonstrate significant enhancement in the wall's curvature ductility compared with that of rectangular walls (Shedid et al., 2010a, 2010b; Banting and El-Dakhakhni, 2012, 2014; Ezzeldin et al., 2016; and Ezzeldin et al., 2017). This is because the presence of the boundary elements allows the placement of several layers of vertical reinforcement with confining hoops. Hence, it has a primary purpose of increasing the ultimate compression strain by confining the grout core and delaying the crushing of the compression toes. Besides, the closely spaced hoops are capable of delaying the buckling of vertical reinforcement. The increased thickness of the added boundary element also stabilizes and reduces the depth of the compression zone. Consequently, RCM shear walls with boundary elements present a potential competitive SFRS for mid- and high-rise masonry buildings located in moderate and high seismic hazard regions.

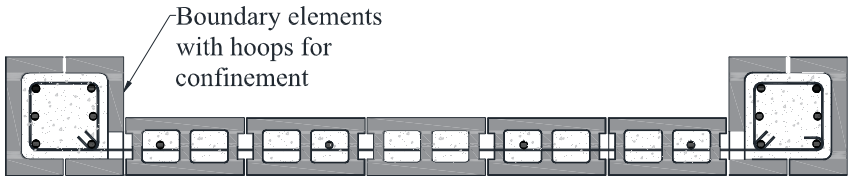

Figure 1.1 RCM shear wall with confined boundary elements

1.2 Motivation and Research Significance

Reinforced masonry shear wall buildings are a potential competitive building system. El-Sokkary and Galal (2018) compared the construction material quantities of RCM and Reinforced Concrete (RC) shear wall buildings. That study considered six multi-storey buildings with different number of floors and located in high and low seismicity regions in Canada. It was demonstrated that the average total construction materials' cost of RCM buildings compared with that of RC buildings was 0.97. Therefore, it was concluded that RCM buildings could be an economical alternative to RC buildings. A new ductile type of RCM shear walls was added in the 2015 edition of the National Building Code of Canada (NBCC-15). The Canadian masonry design standard (i.e. CSA S304-14) assigned special design and detailing requirements to the ductile RCM walls to ensure a stable ductile response and to qualify for the higher ductility-related response modification factor (R_d) of 3.0. The higher ductility-related response modification factor (R_d) would result in reduced seismic design forces and more competitive designs. However, the ductile

type of RCM shear walls is assigned the same building height limits of moderately ductile RCM shear walls, which has a ductility-related response modification factor (R_d) of 2.0. On the contrary, ductile RC shear walls in NBCC-15 are assigned No Limit (NL) for the building heights regardless of the location's seismic hazard, whereas the moderately ductile RC walls are assigned a 60 m height limit when $I_E F_a S_a(0.2)$ is higher than 0.75. This could be attributed to the limited research concerned with the seismic performance and collapse capacity of ductile RCM shear walls.

As previously discussed, the ductile response could be achieved in RCM shear walls by utilizing confined masonry boundary elements at the walls' ends. Previous confinement techniques focused on enhancing the response of rectangular RCM shear walls by increasing the compressive strain capacity of the compression zones. The placement of confinement plates (Priestley and Elder, 1982) or confinement combs (Shing et al., 1993) in the compression toes, or the addition of fibre polymers in the grout mix (Snook et al., 2005) or fine/welded wire mesh in the grouted cells of the blocks (Dhanasekar and Shrive, 2002) increases the maximum usable compressive strain. Thus, it would potentially improve the section's curvature ductility. Nonetheless, the integration of confined masonry boundary elements not only improves the strain capacity of the compression zones but also offers a solution to the lateral instability of rectangular RCM shear walls. Rectangular RCM walls typically have a single layer of vertical reinforcement. Consequently, the vertical rebars at the wall's ends are loaded with large reversible cycles of inelastic strains due to lateral loads from seismic actions. Hence, the rebars are susceptible to buckling which would result in face-shell spalling and loss of the wall's lateral stability.

There are currently no experimental research studies that investigated the response of high-rise ductile RCM masonry shear walls with boundary elements under simulated earthquake actions. The majority of available experimental tests on RCM shear walls with boundary elements focused on low-rise walls subjected to relatively low axial compressive loads. Furthermore, the masonry boundary elements of most tested walls were proposed to be built using the standard concrete stretcher blocks shown in Figure 1.2(a). This type of boundary elements limits the spacing of the transverse reinforcement to the height of the blocks, due to the modular nature of masonry construction and the standardized shapes of masonry units. Besides, the concrete grout core will be divided by the blocks' webs. With the currently established construction techniques, most masonry buildings utilize a load-bearing walls structural system. Thus, RCM shear walls are

typically subjected to high axial compressive forces, which would adversely affect its ductility and energy dissipation capacity. Therefore, there is a need for more detailed experimental studies that investigate and quantify the inelastic response of high-rise RCM shear walls subjected to high axial compressive loads.

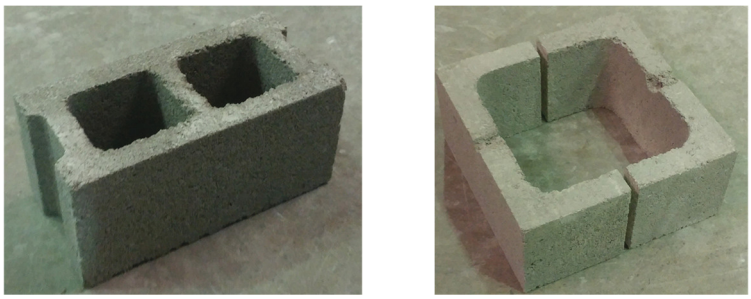

(a) (b)

Figure 1.2 Types of concrete masonry units used in forming the boundary elements: (a) half-scale standard stretcher blocks; (b) half-scale C-Shaped blocks

Additionally, numerical studies are necessary to propose alternative structural layouts for masonry buildings and demonstrate the enhanced structural performance of buildings utilizing ductile RCM shear walls with boundary elements. Moreover, nonlinear numerical analyses are required to evaluate the possibility of relaxing the assigned height limits in NBCC-15 to ductile RCM shear walls. No previous studies were performed to validate the NBCC-15 specified building height limits for ductile RCM shear wall buildings based on seismic collapse performance. As such, the experimental and numerical research program reported in this thesis was designed to address and overcome the previous limitations. The ductile RCM shear walls considered in this research are proposed to have masonry boundary elements constructed using the C-shaped masonry blocks shown in Figure 1.2(b). Boundary elements built using the C-shaped blocks were proved to have an enhanced overall structural response (Obaidat, 2017). This is because it provides more flexibility in the vertical reinforcement arrangement, tolerates having a uniform grout core, and allows the use of closely spaced hoops for confinement and buckling prevention of vertical rebars. Obaidat et al. (2018) demonstrated that reducing the spacing of hoops, increasing the vertical reinforcement ratio, and increasing the compressive strength of grout improved the stress-strain response of masonry boundary elements built using C-shaped blocks.

1.3 Objectives and Scope of Work

This research aims at evaluating and quantifying the seismic performance and collapse capacity of masonry buildings with ductile RCM shear walls with boundary elements. Experimental and numerical investigations are performed to quantify the component and system seismic performance. The primary objective is to propose component and system levels, design and detailing recommendations to ensure satisfactory seismic response and low seismic collapse risk.

At the component-level, it is proposed to utilize RCM shear walls with boundary elements to reduce the depth of the compression zone and enhance the compression strain capacity. The shear walls' boundary elements are proposed to be built using the C-shaped concrete masonry blocks. At the system-level, a hybrid structural system composed of ductile and gravity walls is proposed. This hybrid structural system allows using various ductile shear walls' arrangements and ratios (i.e. ratios of ductile shear walls' area in one direction to the total floor area). Thus, it would be possible to recommend building height limits for ductile RCM shear walls with boundary elements based on standard acceptance criteria.

To achieve the main objective, the research scope of work includes the following:

- Constructing and testing six half-scale fully grouted high-rise RCM shear walls with boundary elements, built using C-shaped blocks, under a constant axial compressive load and quasi-static reversed cyclic loading synchronized with top moment. The studied parameters are the boundary element's size, the boundary element's vertical reinforcement ratio, the wall's shear span-to-depth ratio, the type of boundary elements' masonry blocks, and the lap splicing of vertical rebars in the plastic hinge region.
- Developing a reliable numerical modelling approach for RCM shear walls with boundary elements.
- Calibrating and validating the developed numerical models based on available experimental tests of RCM shear walls with boundary elements.
- Proposing a structural layout for masonry buildings with ductile shear wall configurations and ratios that optimize the design, cost, and structural performance.
- Performing linear dynamic, nonlinear pseudo-static, and nonlinear dynamic time-history analyses on archetype masonry buildings with varying heights and location's seismicity.

The prototype buildings utilize the proposed structural layout of ductile and gravity walls, and the analyses are conducted based on the standard performance assessment methodology of the Federal Emergency Management Agency (FEMA P695, 2009).

- Quantifying the enhancements in the inelastic structural performance and seismic collapse capacity.
- Proposing building height limits for ductile RCM shear walls with boundary elements.

1.4 Thesis Layout

This thesis is comprised of seven chapters and two appendices. The chapters present and discuss all the details of the performed experimental, numerical, and analytical research work. The contents of the chapters and the appendices are as follows:

- Chapter 1 consists of background; motivation and research significance; objectives and scope of work; and a description of the thesis layout.
- Chapter 2 provides a detailed literature review of RCM shear walls with boundary elements. It presents a summary of the previous experimental and numerical research studies that investigated the component and system levels performance of ductile RCM shear walls. It also contains a review of existing numerical modelling techniques for RCM shear walls.
- Chapter 3 investigates the effects of axial load and detailing on the inelastic response of RCM shear walls with boundary elements. This is achieved by constructing and testing three half-scale RCM shear walls with boundary elements. The tested walls varied in the boundary elements' sizes and vertical reinforcement ratios. This chapter also includes a description of the test setup, design and construction of the test walls, and the construction materials' properties. It proposes practical component-level seismic detailing recommendations to enhance the overall structural performance of RCM shear walls with boundary elements subjected to high axial compressive loads.
- Chapter 4 quantifies the in-plane cyclic response of high-rise RCM structural walls with boundary elements. It describes the experimental testing setup, design and construction of specimens, and the test walls constituent materials' properties. It analyzes the testing results of four half-scale slender RCM shear walls with boundary elements. The studied parameters were the wall's shear span-to-depth ratio, the type of boundary elements' masonry blocks

(stretcher or C-shaped), and the lap splicing of vertical reinforcement in the plastic hinge region.

- Chapter 5 presents a validated nonlinear numerical macro-modelling approach that is most suitable for flexural dominant RCM shear walls with boundary elements. Additionally, it utilizes the developed model to evaluate and quantify the seismic performance and collapse capacity of high-rise prototype RCM shear wall buildings. It employs nonlinear pseudo-static and dynamic time-history analyses based on the standardized methodology of FEMA P695. Building height limits are proposed for the ductile type of RCM shear walls based on the standard criteria of FEMA P695 for satisfactory structural performance.
- Chapter 6 evaluates the effect of ductile shear wall ratio (i.e. ratio of ductile shear walls' area in one direction to the total floor area) and cross-section configuration (i.e. rectangular or with boundary elements) on the seismic behaviour of RCM shear wall buildings. It focuses on proposing a hybrid structural layout, ductile shear wall configurations and ratios for masonry buildings to enhance the overall structural performance. It also develops and validates an alternative numerical macro-modelling approach for RCM shear walls with boundary elements considering the nonlinear shear-flexure interaction. Besides, it utilizes a series of linear and nonlinear, pseudo-static and dynamic response history analyses performed using the validated model.
- Chapter 7 provides a summary of the performed research work, the main findings and conclusions, and the recommendations for future work.
- Two appendices are provided at the end of the thesis to present supplemental information to the previous chapters and more details about the research assumptions and limitations. The chapters included a clear and concise presentation of the research background, methodology, and findings.

It is noteworthy that, for the completeness of each chapter, some overlap in the content exists. This is mainly in the introduction and background of each chapter, the experimental test setup description, the specimens' instrumentation, the testing procedure, and the loading protocol. In addition, the testing results of wall W7 are repeated in chapters 3 and 4 as it was the reference specimen.

Chapter 2

Literature Review

2.1 Introduction

This chapter presents a detailed literature review of the previous research performed on RCM shear walls. The emphasis is on flexural dominant walls, walls with end-confinement, and walls with boundary elements. Section 2.2 summarizes the previous experimental work on RCM shear walls failing in flexure, whereas section 2.3 focuses on the experimental tests of RCM walls with end-confinement. Section 2.4 discusses the numerical studies investigating the performance of RCM shear walls at the component and system levels. The different modelling approaches available for simulating the nonlinear response of RCM shear walls are discussed in section 2.5. Finally, a summary of the presented literature and concluding remarks are given in section 2.6.

2.2 In-Plane Cyclic Response of Flexural Dominant RCM Shear Walls

Several experimental studies investigated the influence of axial load on the seismic performance of RCM shear walls. For instance, Shedid et al. (2008) tested six full-scale fully grouted rectangular RCM shear walls, with an aspect ratio of 2, under quasi-static cyclic loading to evaluate the impact of vertical reinforcement and axial load on the structural response. The walls were tested up to 50% strength degradation to capture the post-peak response. It was observed that flexural dominant RCM shear walls were capable of achieving a ductile response. This was seen in the capability of the walls to sustain large inelastic deformations with small strength degradation and high energy dissipation capacity. The authors highlighted that the inelastic rotations were concentrated in the lower portion, up to a height approximately equal to half of the wall's length, whereas the upper part deformed as a rigid body. Besides, the yielding of the outermost reinforcement bars extended to the bottom footing a length less than 150mm. Interestingly, the authors noted that the axial load had a minor impact on the top of wall displacement at the onset of the yield of outermost reinforcement. On the other hand, yield displacement was significantly affected by the increase in the amount of vertical reinforcement. Based on their experimental results, increasing the axial load from 0% to 10% of the masonry compressive strength (f'_m) resulted in only a 13% increase in yield displacement and no evident impact on the displacement at 20% strength degradation. Conversely, an increase in the vertical reinforcement ratio from 0.29% to 1.31% increased the displacement at the onset of yield by approximately 114% and

reduced the drift at 20% strength degradation from 2.2% to 1.6%. The authors also observed that the displacements at ultimate loads were only marginally influenced by vertical reinforcement ratio and axial compressive stress. Therefore, they concluded that the displacement ductility is mostly affected by the amount of vertical reinforcement and less influenced by the axial load level.

In a thorough analysis of the experimental study by Shedid et al. (2008), Shedid et al. (2009) concluded that the ductility-related response modification (R_d) as defined in the Canadian standards was significantly affected by the amount of vertical reinforcement and less impacted by the axial load level. The increase in vertical reinforcement ratio from 0.29% to 1.31% decreased the calculated value of the ductility-related response modification (R_d) from 3.5 to 1.9. On the other hand, an increase in the axial compressive stress from 0 to 1.5 MPa ($10\%f'_m$) only reduced R_d from 1.9 to 1.7. It was also observed, based on their analysis results, that the increase in axial load level increased the initial stiffness. However, the increase in the initial stiffness was accompanied by more rapid stiffness degradation. In another experimental study by Kikuchi et al. (2004), it was also observed that the level of axial compressive stress substantially increased the initial stiffness of the tested walls. Kikuchi et al. (2004) tested 19 fully grouted RCM shear walls under constant axial load and cyclic lateral loading to quantify their inelastic capacity. The walls were of a two-third scale and varied in aspect ratio, vertical axial stress, wall reinforcement, and techniques for strengthening the sliding failure. The authors observed that there was a great scatter in the experimentally measured initial stiffness, defined as secant stiffness at first flexure crack, of the tested walls regardless of the aspect ratio. Therefore, they concluded that the axial load should be an important consideration when estimating the initial stiffness of RCM shear walls. They highlighted that existing equations overestimate the initial stiffness of structural walls. It can be seen from the previous studies that the influence of axial load on RCM shear walls is complex, and more experimental testing is required to better understand and quantify the inelastic response.

Ten full-scale fully grouted RCM shear walls were tested by Zhao and Wang (2015) to investigate the influence of horizontal reinforcement, vertical reinforcement, and axial stress on the inelastic response. The walls were constructed using a new type of concrete masonry blocks (i.e. cleaning-hole block units and collar-beam block units). Four walls were designed to fail in shear, and the remaining six were designed to be flexural dominant walls. The ten walls had an aspect ratio of 1.57. Furthermore, they were tested under constant axial stress and fully reversed

cyclic loading. The authors reported the failure modes, hysteretic response, stiffness degradation, displacement ductility, energy dissipation, and equivalent viscous damping. It was noted that the flexural dominant walls failed due to the rupture of vertical reinforcement and toe-crushing without yielding of horizontal reinforcement bars. Conversely, the walls designed to fail in shear failed due to widely open diagonal cracks. In addition, the walls failing in flexure had a much higher stiffness degradation compared to the shear-dominated walls. Thus, flexural dominant walls would develop a much lower base shear at higher lateral displacements. Furthermore, the displacement ductility ranged between 2.04-2.55 for shear-dominated walls and 2.34-4.21 for flexural dominant walls. This confirmed that the ductility of shear walls is highly affected by the amount and distribution of horizontal reinforcement. Nevertheless, the authors highlighted that the axial stress did not significantly influence the ductility but increased the lateral capacity. The energy dissipation capacity of flexure walls was around 1.5 times that of shear-dominated walls. The equivalent viscous damping was shown to be ranging between 7% to 12% at the onset of yield and 9% to 14% at three times the yield displacement. Based on that, the authors suggested assigning equivalent damping ratios based on the design limit states.

2.3 In-Plane Cyclic Response of End-Confined RCM Shear Walls

Priestley and Elder (1982) highlighted three reasons that make slender concrete masonry shear walls more critical regarding available displacement ductility compared to squat walls. Firstly, the wall displacement ductility is inversely proportional to its effective aspect ratio. Thus, for the same wall cross-section, reinforcement arrangement, and level of axial load, the section displacement ductility will decrease with the increase in the effective height of the wall. Secondly, the higher potential for lateral instability in the compression zones of the plastic hinge regions due to the longer unsupported height also adversely affects the section displacement ductility. Thirdly, the need for lap splices in the plastic hinge regions in tall masonry structural walls because of the impracticality of inserting the blocks on long starter bars (Kelln and Feldman, 2015). The bond conditions are typically undesirable in the plastic hinge zones due to the cyclic reversals of yield stress. This issue is more distinct in slender walls since the lap splice region is subjected to almost a constant moment. Conversely, the squat walls are subjected to a high moment gradient. To evaluate the impact of these factors on the response of slender concrete masonry structural walls, Priestley and Elder (1982) tested three slender concrete masonry shear walls. Their objective was to investigate the influence of axial load level, confinement plates, and lap splicing in potential

plastic hinge zones on the walls' overall response to seismic loading. The tested walls were three stories high with an aspect ratio of 2.5. The dimensions and reinforcement of the walls are shown in Figure 2.1. The walls were tested under reversed cyclic loading until failure with at least three full cycles at each displacement amplitude, which was a multiple of yield displacement. The termination condition of the test was when the wall is incapable of sustaining the applied vertical load. Walls 1 and 2 had high axial stress of 1.9 MPa, whereas wall 3 was tested under low axial stress of 0.744 MPa. Wall 2 was the only wall with 600mm long stainless-steel confinement plates placed at each end of the wall in the second to eighth mortar bed joints. In addition to the low axial load on wall 3, the lap splice was 1.3 times longer than the lap splice length in walls 1 and 2.

The experimental results showed that there was no base slip recorded in neither wall 1 nor wall 2. This was also confirmed in the absence of softening response in the load-displacement hysteresis loops. For wall 3, which had a lower axial load, the base slip was present and contributed to about 5% of the total deformation. The utilization of the confinement plates resulted in a considerable enhancement in the wall's seismic response.

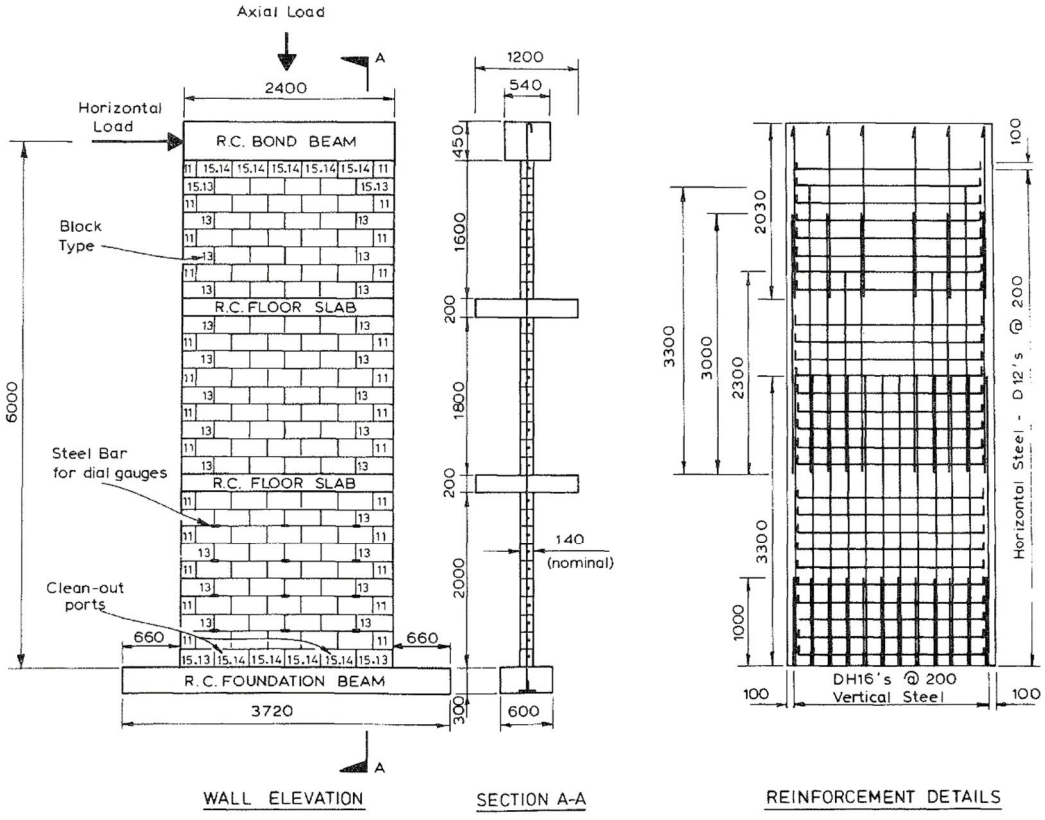

Figure 2.1 Walls' dimensions and reinforcement details (Priestley and Elder, 1982)

The presence of the confining plates in wall 2 effectively restrained the vertical splitting. Hence, it resulted in a much lower extent of damage in the compression zone of wall 2 compared to that of wall 1. Besides, the plates confined the grout core and reduced the possibility of vertical bars buckling in the compression zone. Thus, tensile bond failures in in the lap spliced extreme tension vertical bars were delayed in wall 2 compared to wall 1. Wall 1 failed at the ductility level of 3.9 with bond failure in tensile reinforcement and significant crushing in grout core, as present in Figure 2.2(a). Wall 2 failed after two cycles at the ductility factor of 5.68 due to face-shell spalling and bond failure of tension reinforcement at one end. However, as seen in Figure 2.2(b), there was no significant damage to the grout core. Therefore, unlike wall 1, the authors mentioned that wall 2 could have been repaired with the available techniques at that time. The final damage state of wall 3 is shown in Figure 2.2(c). Wall 3 failed, due to a complete failure of the compression zone, after two cycles at the displacement factor of 6.2. Furthermore, at the same levels of strength degradations, wall 2 was capable of attaining three times the cumulative ductility of wall 1.

The presence of the lap splice in the potential plastic hinge region in the three tested walls resulted in smaller crack widths along the centre portion of the lab and greatly reduced vertical compression strains compared to regions below and above the lap splice. There were mainly two adverse effects due to the lapping of flexural reinforcement in the plastic hinge region. First, it reduced the extent of plasticity due to the increase in stiffness and strength from doubling the reinforcement along the lap splice. Thus, it concentrated the plasticity in a smaller length (less than $0.2l_w$) which resulted in a remarkable increase in the compressive strain at relatively low ductility. This, in turn, caused early vertical splitting in the compression zones of the walls. The other adverse effect of splicing was the tensile bond failure of outermost vertical bars. This occurred in the loading cycles succeeding the vertical splitting of compression zones. In wall 3, which had the lowest axial load, vertical splitting occurred earlier but did not extend along the lap length. This was attributed to the long lap length and the smaller compression zone due to the lower axial load. The authors concluded that in general the presence of lap splices in plastic hinge regions is problematic and should be avoided as much as possible. Preventing lap splicing in the plastic hinge region would allow a greater spread of plasticity and consequently a reduction in peak compressive strains and prevention of tensile bond failures. It was also concluded that the use of confinement plates in the critical regions of the wall (i.e. compression zone in potential plastic hinge) significantly enhanced the response of slender concrete masonry walls to seismic loading. It

allowed substantially higher peak compression strains and higher ductility capacity compared to unconfined walls.

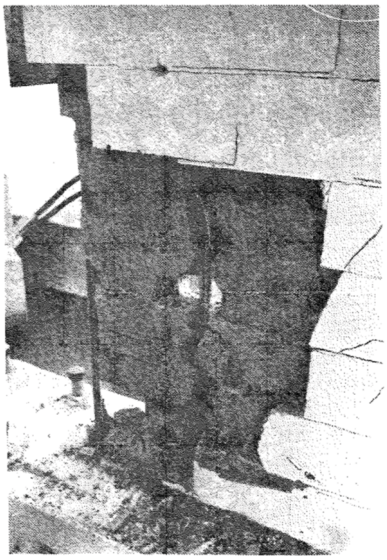

(a) Wall 1 after two cycles at $\mu = 3.9$

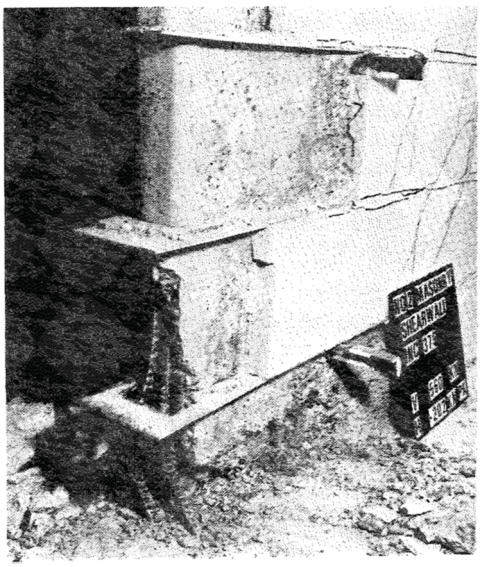

(b) Wall 2 after two cycles at $\mu = 5.68$

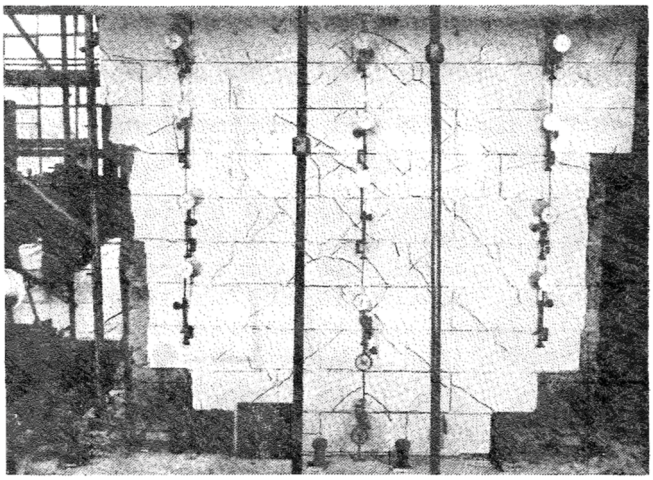

(c) Wall 3 after two cycles at $\mu = 6.4$

Figure 2.2 Final damage states of walls (Priestley and Elder, 1982)

The enhancements in RCM shear walls' ductility and displacement capacity due to the presence of confined boundary elements have been observed in the experimental study by Shedid et al. (2010a). The authors tested seven RCM shear walls designed to have the same lateral resistance, but with three different cross-sectional configurations, as illustrated in Figure 2.3. The tested walls were rectangular, flanged, and end-confined half-scale walls representing 2- and 3-

storey high RCM structural walls. The studied parameters were the aspect ratio and cross-sectional configuration. The walls were subjected to displacement-controlled reversed cyclic loading to investigate its' in-plane seismic response. It was concluded that the addition of end confinement (i.e., boundary elements) resulted in at least a 106% increase in the ductility capacity compared to the rectangular RCM wall with similar lateral resistance. Furthermore, the end-confined wall had a drift capacity, measured at 20% degradation of strength, more than twice that of the comparable rectangular RCM wall. In addition to the enhanced performance of end-confined walls, a saving of 40% was observed in the required vertical reinforcement.

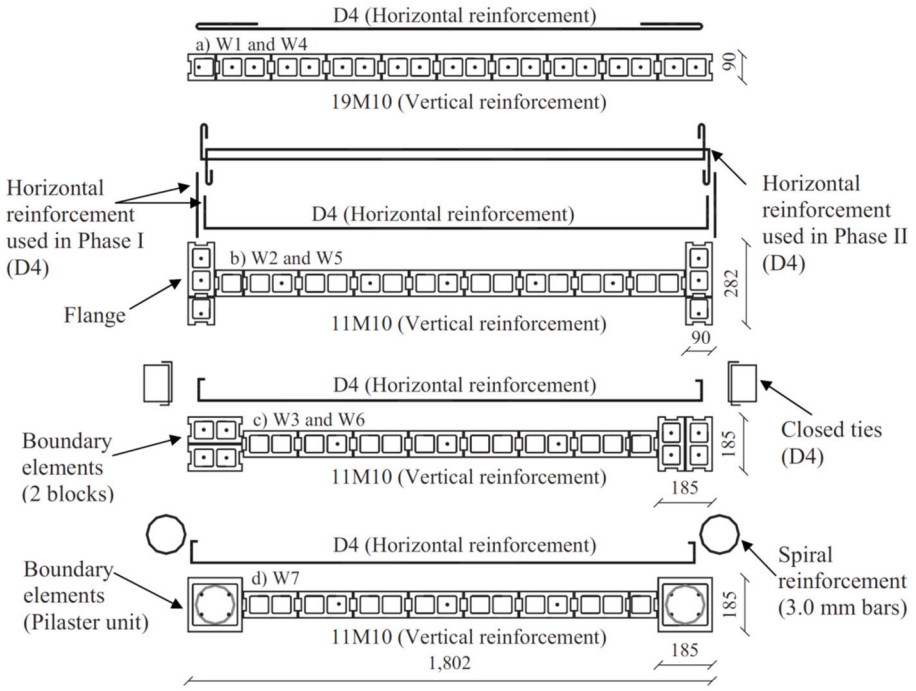

Figure 2.3 Cross-sectional dimensions and reinforcement details of tested walls, dimensions are in mm (Shedid et al., 2010a)

It was also demonstrated that the impact of cross-sectional configuration was independent of the wall height. Thus, the wall height does not significantly influence the response, whereas the cross-section shape has a noteworthy contribution to the overall behaviour. For that reason, the plastic hinge length is typically a function of the wall's length with a minor contribution from the wall's height. That study also highlighted that the proposed end configurations significantly enhanced the overall seismic performance of RCM walls with limited changes in masonry conventional construction methods. It was concluded that RCM shear walls having end confinement are capable of attaining high ductility and energy dissipation capacities. This would

result in reduced seismic design forces making RCM a competitive alternative construction material.

Banting and El-Dakhakhni (2012) presented an experimental investigation of RCM shear walls with confined boundary elements. The authors' study was motivated by the results of the previous experimental investigation by Shedid et al. (2010a). Banting and El-Dakhakhni (2012) tested RCM walls with boundary elements considering a broader range of design parameters to establish the characteristics and design methodology of this newly proposed SFRS. The authors highlighted that previous confinement techniques, such as the addition of the stainless-steel confinement plates in mortar bed joints by Priestley and Elder (1982), resulted in increasing the ultimate compressive strain. However, it did not solve the instability issues arising from the single row of vertical reinforcement in conventional RCM walls, as shown in Figure 2.4(a). The vertical reinforcement, at the wall's ends, in traditional rectangular RCM walls is subjected to significant inelastic strains that are reversed in tension and compression. Thus, the vertical bars are susceptible to buckling, which will cause premature face-shell spalling and loss of stability. On the other hand, the use of ties in the boundary elements, as shown in Figure 2.4(c) would delay the onset of vertical bars buckling. Therefore, it will mitigate the impact of face-shell spalling on the overall strength degradation and stability.

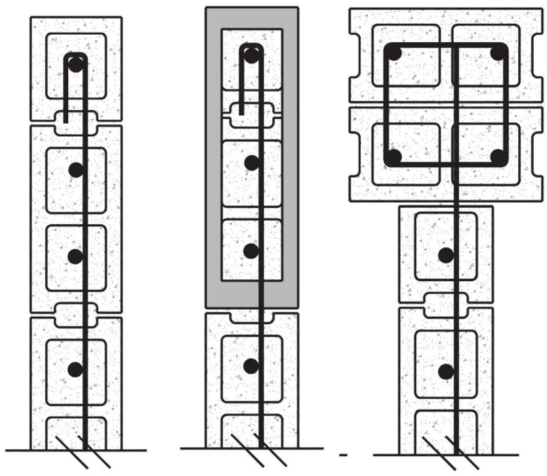

Figure 2.4 RCM walls configurations (Banting and El-Dakhakhni, 2012): (a) conventional rectangular RCM wall; (b) rectangular RCM wall with confinement plates; and (c) RCM wall with confined boundary element

The authors' objective was to quantify the in-plane seismic performance of RCM shear walls with boundary elements and highlight its potential as a new competitive SFRS for masonry buildings. The testing program included four walls that are 4.0 m high and 1.8 m in length, which makes their aspect ratio equal to 2.21. The studied parameters were the presence of inter-storey slabs, the continuation of boundary elements above the first-floor and the level of axial loads. The authors chose three levels of axial loads that are representative of midrise RCM buildings. The intent was to have axial load levels that would result in neutral axis depths within the confined boundary element and away from the boundary element (i.e., in the web, which is the unconfined part of the wall). Investigating the curtailment of the boundary elements above the plastic hinge region aimed to assess the possibility of optimizing the design to reduce the material and construction expenses. The authors studied the effect of the presence of inter-storey slabs to quantify the observation of Shedid et al. (2010a). Shedid et al. (2010a) highlighted that the presence of inter-storey slabs resulted in changing the cracks spread and propagation. The four walls in the experimental investigation of Banting and El-Dakhakhni (2012) were tested under quasi-static reversed cyclic loading protocol. The utilized test setup is presented in Figure 2.5. A displacement-controlled hydraulic actuator applied the lateral load, whereas the axial pressure was applied using two force-controlled actuators. Out-of-plane movements were restrained at each slab level using two braces connected to the strong wall using hinged boundary conditions.

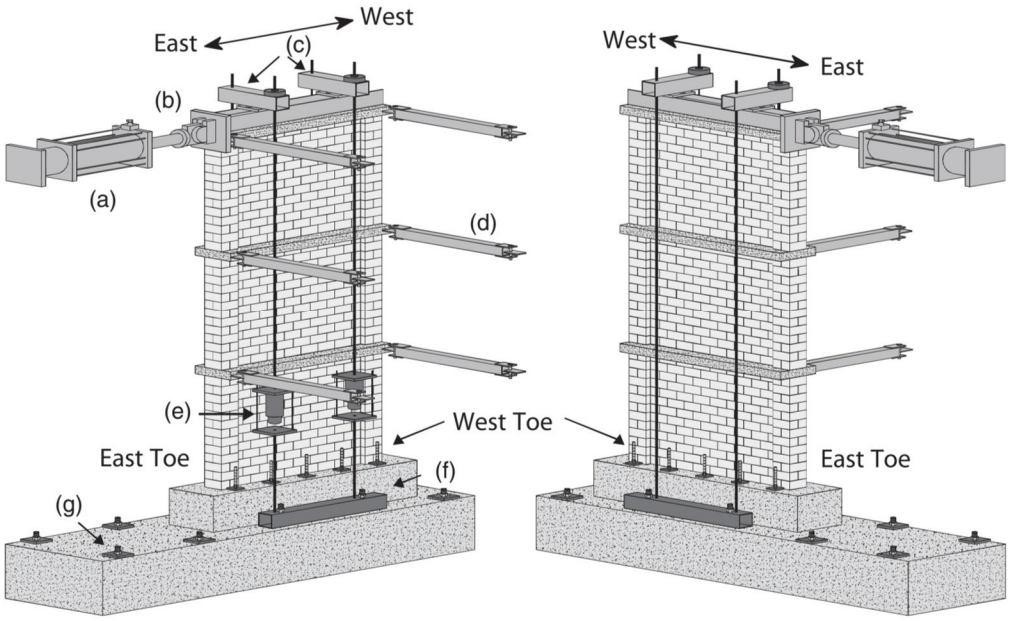

Figure 2.5 Test setup (Banting and El-Dakhakhni, 2012)

The results of that experimental study were used to establish the force- and displacement-based seismic performance parameters of RCM shear walls with boundary elements. The results confirmed that boundary elements with two layers of vertical reinforcement and transverse reinforcement (i.e., ties) for confinement, significantly improved the post-peak response. This is due to its ability in delaying the buckling of vertical rebars and providing confinement to the grout core. Thus, the face-shell spalling and vertical cracking did not result in a significant drop in strength. Failure of tested walls occurred mostly due to the crushing of compression toes and fracture of vertical reinforcing bars. This happened at high drift ratios ranging between 2.4% and 3.7% for the different walls, as shown in the load-displacement envelops of the tested walls given in Figure 2.6.

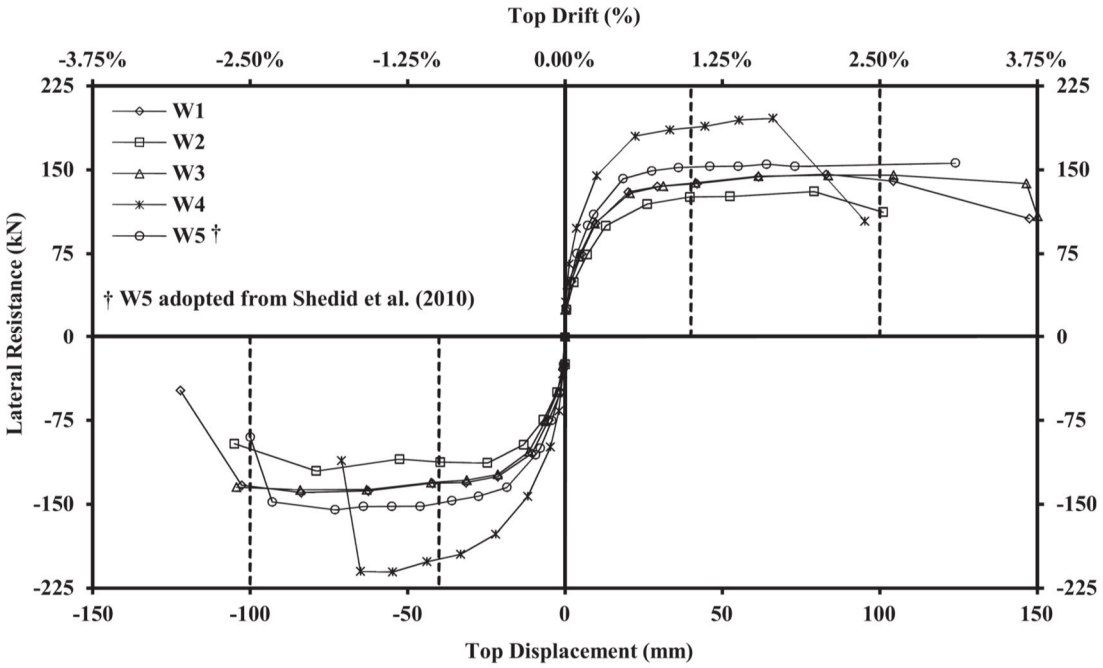

Figure 2.6 Load-displacement envelops of the tested walls (Banting and El-Dakhakhni, 2012)

The wall with discontinued boundary elements above the first story (W2) had two clear plastic hinges above and below the first-floor slab. The inelasticity was simultaneously spreading upward from the first-floor and downward from the second floor. The authors concluded that reducing the boundary elements to flanges above the first-floor slab decreased the elastic stiffness by 26% and resulted in two plastic hinges. Besides, as the flanged ends offered no confinement to the vertical bars, the bars buckled and caused face-shell spalling which resulted in reducing the wall's effective length and its ultimate load capacity.

The presence and detailing of inter-storey slabs affected the propagation of cracking and restrained the extent of inelastic curvature. The diagonal cracks were concentrated below the first-floor slab for the wall with inter-storey slabs (W1) and were spread over first and second floors in the wall without inter-storey slabs (W3). Thus, the extent of cracking (both horizontal and diagonal) was less when inter-storey slabs were present. The high axial load on the wall resulted in increasing its lateral resistance, but limited it is ductility and drift capacities. Furthermore, it was highlighted that the presence of inter-storey slabs in the wall with high axial load was less effective in resisting the spread and propagation of cracking as a result of the high shear forces. The stiffness degradation was not significantly affected by neither the presence of inter-storey slabs nor the curtailment of the confined boundary elements above the first-floor. It was mainly impacted by the increase in axial load. The wall with high axial load had the smallest ratio between the stiffness at ultimate load or ultimate top displacement and the yield stiffness. The authors calculated the equivalent viscous damping from the three deformation types (flexure, shear, and base sliding). It was observed that most of the equivalent viscous damping was due to flexure deformation at all ductility levels. The contribution from flexure and shear was increasing with the increase in ductility levels and was constant from base sliding. It was concluded that the overall seismic performance of the tested walls demonstrates the capability of this new construction approach (addition of confined boundary elements to the rectangular wall's ends) in significantly enhancing the ductility and thus reducing the seismic design forces. The displacement ductility of the tested walls ranged between 6.6 and 15.2 at corresponding ultimate top displacements ranging from 1.8% to 3.7%, respectively, as shown in Figure 2.6.

Another experimental program was designed by Banting and El-Dakhakhni (2014) to establish prescriptive design requirements for the confinement of RCM shear walls with boundary elements. The test matrix consisted of five half-scale RCM walls with boundary elements having varying heights, lengths, and vertical reinforcement ratios. The aim was to prove that; with confinement, the compressive strain of masonry is increased. Therefore, the associated increase in inelastic tension and compression strains in the vertical bars would not result in loss of stability. This is because the closed ties provided in the boundary elements are expected to postpone the buckling of vertical reinforcement bars in the plastic hinge region. The authors emphasized that the utilization of boundary elements in RCM shear walls will not require the use of any special materials or construction technologies. Consequently, it will be a practical and feasible SFRS for

RCM buildings in regions with moderate and high seismicity. The experimental results demonstrated that the force-based response of the walls was highly dependent on the horizontal extent of the boundary elements. In addition, the increase in the walls' aspect ratios resulted in increasing the experimentally measured plastic hinge length, curvature ductility, and displacement ductility. The results also suggested that an increase in vertical reinforcement ratio would adversely affect the displacement ductility of the wall. Furthermore, it was recommended to account for shear deformations in design, as it had a major contribution to the walls' structural response. Based on their findings, it was concluded that the presence of boundary elements inhibited the buckling of vertical rebars and delayed the crushing of grout core in compression toes. Additionally, it prevented the sudden drop in lateral strength at the onset of cracking and face-shell spalling. Therefore, the lateral confinement in the boundary elements resulted in a substantial improvement in the overall response of RCM shear walls.

The effect of different types of confinement reinforcement on the ductility and energy dissipation capacity of RCM shear walls was also assessed by Snook et al. (2005). The authors tested nine cantilever masonry shear walls with two different aspect ratios under reversed cyclic loading and constant axial load representing seismic excitations. The walls had three types of confinement: steel confinement plates, seismic reinforcement combs, and polymer fibres mixed with the grout. The test results indicated that the use of these confinement techniques only modestly enhanced the displacement and energy dissipation capacities of the walls. Compared to the placement of confinement plates or seismic reinforcement combs in mortar joints, the addition of polymer fibres in the grout mix resulted in the highest increase in energy dissipation and drift capacities. Furthermore, mixing the fibres with the grout increased the shear resistance which reduced the observed shear damage (i.e. the diagonal cracks and shear deformations) in the tested walls.

The enhancement in the system-level seismic performance of RCM buildings having shear walls with boundary elements was quantified by Ezzeldin et al. (2017). That study presented the results of experimental testing of a two-storey one-third scale RCM building with boundary elements. The building had four shear walls with boundary elements in the direction of loading and was tested under reversed cyclic loading until failure. It focused on assessing the influence of the system-level characteristics on the overall seismic performance. Additionally, it quantified the

impact of utilizing shear walls with boundary elements instead of the conventional rectangular walls. The authors compared their experimental results with the results of a previously tested building, by Ashour et al. (2016), having the same configuration, layout and, lateral resistance, but with rectangular shear walls. The results focused on the hysteretic behaviour, damage sequence, failure modes, and torsional response. It was reported that the tested building with boundary elements had ultimate strength that was 55% higher than the sum of individual walls' strengths. This was due to the influence of the slabs in restraining the walls' in-plane rotations at the floors' levels. As a result, the walls did not respond as perfect cantilevers, and the overall lateral resistance of the building was higher than the sum of the lateral capacity of the individual walls. The reported load-displacement response showed similar response between the two buildings until 0.9% drift ratio. After that, the building with boundary element walls showed less strength degradation and higher energy dissipation capacity. The walls orthogonal to the loading direction had cracks at initial loading stages, demonstrating the possibility that they acted as tension members and contributed to the overall response.

The building with confined boundary elements reached the failure criterion (i.e. 20% degradation in strength) at a higher drift ratio (2.2%) compared to the building with rectangular walls which failed at 1.9% drift. Besides, Ezzeldin et al. (2017) highlighted that the presence of confined boundary elements in the walls delayed the fracture of vertical reinforcement and the crushing of grout core. Furthermore, the confined boundary elements resulted in improving the displacement capacity by postponing the strength degradation to higher drifts. The displacement ductility of the building with confined boundary elements was 20% and 40% higher than the building with rectangular walls at 20% and 50% strength degradation, respectively. The two buildings had similar energy dissipation capacities until 1.5% drift ratio. However, the presence of confined boundary elements resulted in 17% and 25% increase in the energy dissipation capacity at 2.2% and 3.5% drifts, respectively. Additionally, there was a 15% increase, on average, in the equivalent viscous damping for the building with shear walls having confined ends. Therefore, this would result in reduced seismic demands for the building with boundary elements as a result of the increased damping and energy dissipation capacity. Finally, the building with boundary elements had a 60% reduction in the twist angle as a result of the increase in its torsional resistance and the associated reduction in the eccentricity between the centre of mass and centre of rigidity.

2.4 Numerical Analysis of RCM Shear Walls

Shedid et al. (2011) quantified the seismic response modification factors for RCM shear walls as defined by 2008 edition of the American Society of Civil Engineers (ASCE7-08) and the 2010 edition of National Building Code of Canada (NBCC-10). The study covered rectangular, flanged, and end-confined (with boundary elements) RCM shear walls with aspect ratios of 1.5 and 2.2. Nonlinear dynamic analysis was used to calculate the seismic force reduction factor (R) and displacement modification factor (C_d) of ASCE7-08. For the ductility-related response modification factor (R_d) and the overstrength-related response modification factor (R_o) of NBCC-10, the equal-displacement approach was adopted for the calculation. The nonlinear dynamic analysis was performed using ten ground motions with varying frequencies and acceleration to velocity ratios.

The results of walls with the aspect ratio of 2.2 showed an average R value close to the value specified in ASCE7-08 for rectangular walls. However, the calculated R values for flanged and end-confined walls were 36% and 90% higher than the value of the rectangular wall, respectively. According to NBCC-10, R_d and R_o were calculated following the equal-displacement approach by idealizing the nonlinear load-displacement response into a bilinear relationship. The R_d was calculated as the ratio between the elastic lateral load and the idealized wall lateral capacity, and the value of R_o was estimated as the ratio of the maximum capacity to the design capacity. The calculated R_d values for rectangular walls were significantly higher compared to the value that was assigned in S304.1-04 (CSA, 2004). For the flanged and end-confined walls, R_d values were 50% and 100% higher than the rectangular wall, respectively. The calculated overall response modification factor (i.e. R_d x R_o) was 30% higher for flanged walls and 70% higher for end-confined walls when compared to the values of the rectangular walls. Moreover, the flanged and end-confined walls only required 58% of the rectangular walls' vertical reinforcement to have the same lateral capacity. The authors calculated the inelastic rotational demands for flanged and end-confined walls and compared them against the inelastic rotational capacities estimated according to the concrete design standard A23.3-04 (CSA, 2004). It was found that flanged and end-confined RCM walls could achieve a high level of inelastic displacement capacity and thus could be assigned a higher R_d or at least the 3.5 value specified in A23.3-04 for ductile RC shear walls. The study concluded that rectangular RCM shear walls are capable of achieving high ductility. However, the use of flanged or end-confined walls resulted in a significant enhancement in the

seismic response modification factors, which would increase the competitiveness of RCM buildings.

More recently, Ezzeldin et al. (2016) investigated the impact of adding boundary elements on the seismic collapse risk of RCM shear walls. The authors designed 20 RCM shear walls with different configurations and gravity loads using the seismic response modification factor (R) of ASCE7-10 given to rectangular RCM walls. FEMA P695 (2009) methodology was used to quantify the seismic performance and collapse safety of the selected archetype walls. Nonlinear static and dynamic analyses were used to investigate the collapse capacity and seismic response. The results demonstrated that the addition of boundary elements increased the walls' period-based ductility and collapse capacity. It was found that RCM walls with boundary elements fully satisfies the acceptance criteria of FEMA P695 (2009). The walls had collapse probabilities much lower than 20% at the Maximum Considered Earthquake (MCE). Therefore, it was concluded that higher seismic response modification factor (R) could be assigned to RCM shear walls with boundary elements.

2.5 Numerical Modelling Techniques

The nonlinear response of RCM shear walls can be simulated numerically using either micro-modelling or macro-modelling. Micro-modelling utilizes continuum-elements to represent the shear walls. This usually includes solid elements, shell elements, or fibre shell elements. On the other hand, macro-modelling employs line-elements, such as lumped-plasticity plastic hinge elements, fibre-section concentrated plasticity elements, and distributed inelasticity beam-column elements. Micro-modelling of shear walls produces accurate response simulation which captures nonlinear shear response and shear-flexure and torsion interaction. However, it requires a fine level of meshing and detailing and thus, it is computationally expensive. Furthermore, micro-modelling typically employs an implicit solution algorithm which usually results in convergence issues when degradation in strength starts (Pugh et al., 2015). Alternatively, utilizing line-element models to simulate the nonlinear response of shear walls features reasonable accuracy and relatively high computational efficiency (Pugh et al., 2015). This makes it a preferred choice in engineering practice (Pugh et al., 2015).

The simplest and most common formulation in the category of line-element models is the lumped-plasticity plastic hinge element model. Despite its simplicity, it requires a pre-definition

of the moment-rotation for the plastic hinge zones of the member. This makes it unable to account for the variation in axial and shear loads. Furthermore, its accuracy is dependent on the plastic hinge calibration parameters. A more innovative version of this element model is the fibre section type. In this element model, a fibre section is assigned instead of defining the plastic hinge moment-rotation. This enables the model to capture the impact of axial load on the flexural response. However, this element model is based on a linear strain assumption which is typically not valid in the cases of long planar, boundary element or flanged walls.

A more meticulous category of the line-element models is the distributed plasticity element model. The distributed plasticity element models typically use either Displacement-Based (DB) or Forced-Based (FB) beam-column elements. DB finite element formulations are based on the assumption of linear curvature and constant average axial strain, while FB formulations assume linear moment and constant axial force. As a result, DB elements are sensitive to members' meshing, whereas FB elements sometimes encounter convergence issues with strength degradation (Pugh et al., 2015). However, the distributed plasticity models (DB or FB) are competent tools for nonlinear response simulations due to their reasonable accuracy and numerical stability (Pugh et al., 2015; and Calabrese et al., 2010).

Several fibre element formulations were proposed to account for the nonlinear shear response and coupling of shear-flexure interaction such as Alemdar and White, (2005), and Jiang and Kurama, (2010). Although these element models resolve a major drawback associated with fibre elements, they are computationally expensive and numerically unstable. The use of continuum models could guarantee accurate response predictions that account for the nonlinear shear and torsion-flexure interaction. However, the high computational demand of these element models limits their applications in the field of seismic design and performance assessment of structural systems. Additionally, convergence problems are common with continuum elements utilizing an implicit solution algorithm (Pugh et al., 2015). In most cases, using distributed plasticity models with proper calibration and regularization techniques, it is possible to provide a reasonable simulation of the nonlinear response for earthquake engineering applications. Regularization techniques are necessary for both DB and FB beam-column elements to ensure an objective simulation of the response when softening sectional behaviour is expected (Calabrese et al., 2010).

Several researchers used distributed-plasticity beam-column elements to simulate the inelastic response of RCM shear walls (e.g. Bedeir et al., 2017; Ezzeldin et al., 2016; Siyam et al., 2016; and Abdel-Latif et al., 2015). Bedeir et al. (2017) used FB beam-column elements to model RCM shear walls in *OpenSees* (McKenna et al., 2000). The authors added a bilinear shear force-shear strain relation to all the integration points of the FB element to account for the shear deformations. Ezzeldin et al. (2016) and Siyam et al. (2016) simulated the nonlinear response of RCM shear walls using DB beam-column elements in *OpenSees* platform. They aggregated *OpenSees* pinching4 hysteretic load-deformation relation to the DB element to account for the shear response. Moreover, in their model, the authors accounted for the strain penetration by incorporating a zero-length element section at the base of the wall. In the zero-length element section, the reinforcing bars were assigned the hysteretic bar stress versus bar slip model introduced by Zhao and Sritharan (2007). The use of beam-column (i.e. line-element model along the centreline of the wall) element models to simulate shear walls' response produces reasonably accurate simulations. However, it does not capture the shear deformations and the shift in the neutral axis along the wall's cross-section during the loading history. Thus, the rocking response and the interaction of the wall with interconnected members in- and out-of-plane is not accounted for (Orakcal et al., 2004). The simulation of shear response using empirical models defined independently from the flexural modelling parameters results in an uncoupled response between nonlinear shear and flexure. The analytical predictions based on uncoupled response might underestimate the vertical compressive strains for slender walls and overestimate the lateral load capacity for walls with low and moderate aspect ratios (Kolozvari et al., 2015a).

Kolozvari et al. (2015a) proposed an analytical modelling approach for simulating the nonlinear response of RC shear walls. The proposed model captures the nonlinear shear response and the coupled Shear-Flexure Interaction (SFI). The authors highlighted that experimental studies confirmed the SFI and that shear and flexural yielding occur almost simultaneously. Additionally, in most cases, shear deformations contribute to at least 20% of the total top lateral displacement, depending on the wall's aspect ratio. Existing methodologies for modelling the nonlinear interaction between shear and flexure responses are either empirical (i.e., without behaviour or mechanics-based formulation) or incapable of capturing the cyclic response. Furthermore, the sensitivity of existing modelling approaches is not fully assessed for the different material and modelling parameters. Current modelling approaches also lack comprehensive validation of

predicted response at global and local levels. Kolozvari et al. (2015a) aimed to develop a "novel" modelling approach for RC structural walls that is capable of capturing the SFI under cyclic loading conditions. Their proposed model is an improved version, to include SFI, of the Multiple Vertical Line Element Model (SFI-MVLEM) which was introduced by Vulcano et al. (1988) and modified by Orakcal et al. (2004). In their model, SFI-MVLEM, the uniaxial macro-fibre elements of the original MVLEM model were replaced with RC panel elements subjected to membrane actions. This allowed coupling of the axial and shear responses at the macro-fibre (panel) level and coupling of the shear and flexure responses at the model element level. Figure 2.7 shows the element models of the original MVLEM and the proposed SFI-MVLEM. The RC panel element response is simulated using a 2-dimensional constitutive panel model based on the Fixed-Strut-Angle-Model (FSAM) which was extended by Orakcal et al. (2012). In the proposed SFI-MVLEM, the walls are modelled as (n) number of MVLEM elements vertically over the wall's height and (m) number of macro-fibre panel elements along the wall's length. The macro-fibre panels in each element are connected at the top and bottom using two rigid beams. The number of degrees of freedom in the SFI-MVLEM is increased to 6+m, compared to 6 only in the original formulation, to define the horizontal normal strain (ε_x) on each panel using the additional (m) degrees of freedom in the horizontal direction.

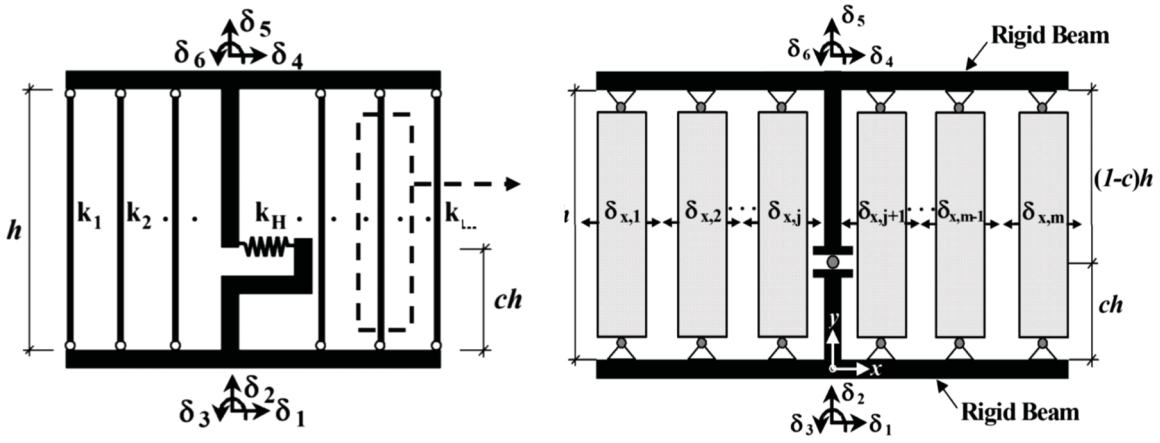

(a) Original MVLEM (b) Proposed SFI- MVLEM

Figure 2.7 Element models (Kolozvari et al., 2015a)

The original FSAM formulation was based on the concept of smeared stresses and the assumption that there is a perfect bond between the concrete and reinforcing steel. Therefore, the

model did not account for the impact of bond-slip deformations and bond stresses on the simulated response. It also assumed zero contribution from the reinforcement dowel action to the shear resistance and assumed that the concrete compression strut matches the direction of the concrete crack. The FSAM formulation incorporated in the proposed model (i.e., the SFI-MVLEM) was modified to include a shear resistance mechanism along cracks. The original FSAM formulation assumed that the principal stresses in concrete are along the crack direction, which reflects that shear stresses along cracks due to shear strains are ignored. This assumption leads to the overestimation of sliding shear strains in panels with unequal reinforcement in horizontal and vertical directions. Thus, the shear deformations might be overestimated, and the wall's lateral load capacity might be underestimated. The authors added a shear resistance mechanism along cracks to simulate the shear aggregate interlock effect and the reinforcement dowel action. The shear aggregate interlock effect was modelled using a simple friction-based cyclic model, and the reinforcement dowel action was represented using a linear elastic constitutive model as shown in Figure 2.8. The predicted stiffness and load-deformation properties for the wall at any level of applied deformation will depend on the RC panel constitutive model, the assigned tributary areas of concrete and reinforcement, and their constitutive material models. In the SFI-MVLEM, the uniaxial stress-strain relationship of reinforcing steel is represented using the nonlinear hysteretic model of Menegotto and Pinto (1973), and the concrete uniaxial response along the fixed struts' direction is modelled using Chang and Mander (1994) stress-strain constitutive relationship.

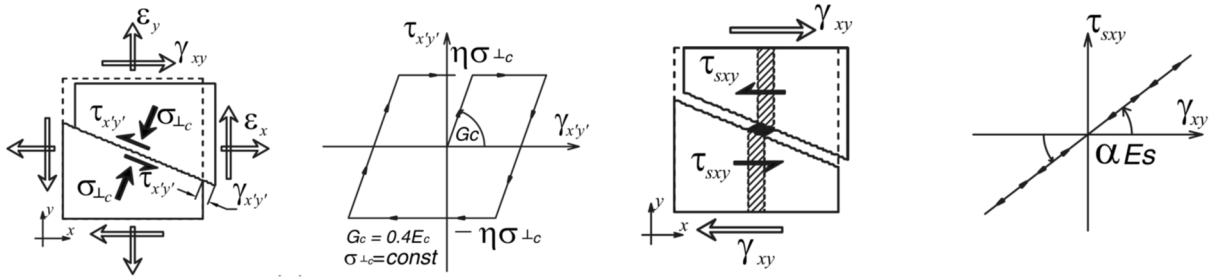

(a) Shear aggregate interlock model (b) Dowel action model

Figure 2.8 Shear resistance mechanism (Kolozvari et al., 2015a)

The implemented constitutive relationship for concrete in the RC panel element was extended to account for critical behavioural features under biaxial loading, such as compression softening, biaxial hysteretic damage, and tension stiffening. The proposed model (SFI-MVLEM) with the

modified FSAM formulation was shown to be capable of capturing the overall cyclic behaviour of RC structural walls, including the load-deformation response, and nonlinear shear and flexure deformation contribution to total top displacement over the entire loading history.

The sensitivity of model response to the wall configuration and modelling parameters was investigated. The model was proven capable of capturing behavioural response changes (e.g., the shape of load-deformation response, the contribution of nonlinear shear deformation, and changes in lateral load capacity) due to variations in walls' aspect ratio and web reinforcement ratio. It was also shown that the overall load-displacement behaviour was not very sensitive to the modelling parameters of the shear resistance mechanism. However, the pinching response and contribution of shear deformation were reduced when the contribution of dowel action was increased in the shear resistance mechanism. The model predictions were not substantially impacted by the model discretization (i.e., number of vertical elements over wall height or number of panel elements along walls length). The authors highlighted that this proposed model is not suitable for walls with aspect ratios less than 1 (substantial SFI is expected). This is due to the assumption that the resultant (from concrete and steel contributions) horizontal normal stress within each RC panel is equal to zero. This assumption was needed to complete the strain field and matches with the boundary condition of no lateral load applied over the wall height except at the top. Additionally, more representative models for the shear resistance mechanism along cracks can be incorporated to enhance the model predictions and limit its sensitivity to the modelling parameters.

2.6 Summary and Concluding Remarks

It is clear that there is a remarkable amount of effort done previously in coming up with a confinement technique or a cross-section configuration to enhance the overall performance of RCM shear walls. However, it is important to note that among the several confinement approaches proposed in the literature, only the integration of confined boundary elements was capable of enhancing the lateral stability of RCM shear walls. Utilizing confinement plates (Priestley and Elder, 1982) or confinement combs (Shing et al., 1993) in the compression toes, or even adding fibre polymers in the grout mix (Snook et al., 2005) or fine/welded wire mesh in the grouted cells of the blocks (Dhanasekar and Shrive, 2002) enhances the maximum usable compressive strain. Therefore, these techniques are capable of increasing the section's curvature ductility and thus enhancing the overall displacement ductility and energy dissipation capacity. Nevertheless, they

do not offer any enhancement to the lateral stability issue encountered in RCM shear walls with a single layer of vertical reinforcement when subjected to large reversible cycles of inelastic strains in the plastic hinge region. The addition of confined boundary elements to the ends of rectangular walls with at least two layers of vertical reinforcement and transverse reinforcement provides an enhancement to the wall's lateral stability by delaying the onset of vertical reinforcement buckling. It also improves the ductility and energy dissipation capacity through confinement of the compression zones.

It is evident that ductile RCM shear walls with boundary elements are a potential alternative SFRS for masonry buildings in moderate and high seismicity regions. As seen in the literature review, several experimental studies concluded that the integration of the confined boundary elements at the wall's ends significantly enhanced the overall seismic performance of the wall. Additionally, the numerical studies showed a high seismic collapse capacity for RCM shear walls with boundary elements. However, the utilized type of masonry blocks (i.e. the standard stretcher blocks) in forming the boundary elements in previous studies has some limitations. For instance, it does not give flexibility in the vertical reinforcement arrangements and the spacing of hoops. Moreover, it does not allow having a uniform concrete grout core. Therefore, more studies are still needed to investigate the impact of other design parameters (including the type of boundary elements' blocks) on the response of RCM shear walls with confined boundary elements. Furthermore, it can be seen from the previous studies that the impact of axial load on RCM shear walls is complex and more experimental testing is required to better understand and quantify the inelastic response. More tests are also required to investigate the influence of the presence of lap splices in the vertical reinforcement of high-rise walls on the overall response when end-confinement is utilized.

Chapter 3

Experimental Investigation of Axial Load and Detailing Effects on the Inelastic Response of Reinforced Concrete Masonry Structural Walls with Boundary Elements

3.1 Abstract

In typical wall load-bearing Reinforced Masonry (RM) buildings, the lateral and vertical forces are resisted by rectangular shear walls. Thus, the walls will be subjected to high vertical forces from gravity loads, which are expected to limit its displacement and energy dissipation capacities. Besides, the rectangular RM shear walls have limited lateral stability because of the single layer of vertical reinforcement. The intent of this study is to investigate the inelastic cyclic response of RM structural walls subjected to an axial compressive stress that results in pre-compression ratios, $P/A_g f'_m$, higher than 10%. The main objective is to propose practical component-level seismic detailing recommendations to enhance the overall structural performance. In this respect, three half-scale fully grouted RM shear walls were tested under constant axial load, in-plane fully reversed cyclic loading, and top moment. The tested specimens are flexural dominant to simulate the response of mid- and high-rise RM shear walls under strong seismic actions. The walls were designed to have enlarged boundary elements built using C-shaped blocks to evaluate the ability of end zone detailing and confinement to alleviate the impact of the high axial load. The test results demonstrated an overall enhanced structural performance for the three walls. The three specimens attained high ductility levels, high energy dissipation capacity, and failed in a ductile flexural mode. The presence of the well-detailed and confined boundary elements was effective in mitigating the impact of the high axial compression load. Thus, utilizing this type of masonry shear walls increases the competitiveness of masonry buildings as an alternative construction method.

3.2 Introduction

Axial load affects the response of structural walls. It was demonstrated by previous research studies and post-earthquakes reconnaissance reports that the increase in axial load adversely impacts the ductility and energy dissipation capacity of structural walls. The high axial load also enhances the structural behaviour by increasing the shear and flexural resistance. The results of the numerical parametric study by Shing et al. (1993) demonstrated that axial compressive strength increases the lateral shear resistance. Nevertheless, the adverse impacts outweigh the enhancements in structural response (Yuen and Kuang, 2014). The influence of axial load on Reinforced Concrete (RC) walls with confined boundary elements was experimentally investigated by (Su and Wong, 2007; Zhang and Wang, 2000; and Shegay et al., 2018). It was concluded that the high axial load increases the lateral capacity and initial stiffness. However, it substantially reduces the wall's ductility and energy dissipation capacity. The increase in axial load also increases the rate of stiffness degradation. Besides, the failure mechanism was heavily influenced by the level of axial load. The walls subjected to the high axial loads failed due to out-of-plane buckling, whereas the walls subjected to lower axial loads failed in a flexural mode due to crushing of compression toes. Extensive research efforts were undertaken to quantify the impact of axial load on the response of RC shear walls. Nevertheless, Yuen and Kuang (2014) highlighted that more experimental tests are still required to investigate the potential for rebar buckling and fracture due to low-cycle fatigue during seismic events when the axial load level is high. Additionally, Shegay et al. (2018) noted that there is a need for more testing of RC shear walls subjected to axial load ratios (i.e. $P/A_g f'_m$) higher than 10% with low shear demands (i.e. slender walls).

In RC shear wall buildings, the walls' axial forces resulting from gravity loads can be reduced by using a building frame structural system. It was highlighted by Su and Wong (2007) that RC shear walls in medium and high seismicity regions are typically favoured to be designed with a low axial load ratio to ensure the ductile response. However, in the case of Reinforced Masonry (RM) buildings, high axial load ratios are unavoidable since the building system is typically wall load-bearing. In a wall load-bearing structural system, the walls are responsible for resisting both the gravity loads and the lateral loads, which result in high axial compressive stresses. Therefore, the walls' inelastic rotational capacity might be limited, and the overall displacement ductility and energy dissipation capacity of the system will be reduced.

Similar to RC, several experimental studies investigated the influence of axial load on the seismic performance of RM shear walls. For instance, Shedid et al. (2008) tested six full-scale fully grouted rectangular RM shear walls, with an aspect ratio of 2, under quasi-static cyclic loading to evaluate the impact of vertical reinforcement and axial load on the structural response. Interestingly, they noted that the axial load had a minor impact on the top of wall displacement at the onset of yield in outermost reinforcement. On the other hand, yield displacement was significantly affected by the increase in the amount of vertical reinforcement. Based on their experimental results, increasing the axial load ratio, $P/A_g f'_m$, from 0% to 10% resulted in only a 13% increase in yield displacement and no impact on the displacement at 20% strength degradation. Conversely, an increase in the vertical reinforcement ratio from 0.29% to 1.31% increased the displacement at the onset of yield by approximately 114% and reduced the drift at 20% strength degradation from 2.2% to 1.6%. The researchers also observed that displacements at ultimate loads were only marginally influenced by vertical reinforcement ratio and axial compressive stress. Therefore, they concluded that displacement ductility is mostly impacted by the amount of vertical reinforcement and less influenced by the axial load level.

In a thorough analysis of the experimental study by Shedid et al. (2008), Shedid et al. (2009) concluded that the ductility-related response modification (R_d) as defined in the Canadian standards was significantly affected by the amount of vertical reinforcement and less impacted by the axial load level. The increase in vertical reinforcement ratio from 0.29% to 1.31% decreased the calculated value of the ductility-related response modification (R_d) from 3.5 to 1.9. On the other hand, an increase in axial compressive ratio (i.e. $P/A_g f'_m$) from 0 to 10% only reduced R_d from 1.9 to 1.7. It was also observed in their analysis results that the increase in axial load level increased initial stiffness. However, this increase in initial stiffness was accompanied by more rapid stiffness degradation. In another experimental study by Kikuchi et al. (2004), it was also observed that the level of axial compressive stress substantially increased the initial stiffness of the tested walls. They tested 19 fully grouted RM shear walls under constant axial load and cyclic lateral loading to quantify their inelastic capacity. The walls were of two-third scale and varied in aspect ratio, vertical axial stress, wall reinforcement, and techniques for strengthening sliding failure. The researchers observed that there was a great scatter in the experimentally measured initial stiffness, defined as secant stiffness at first flexure crack, of the tested walls regardless of the aspect ratio. Therefore, they concluded that axial load should be an important consideration

when estimating the initial stiffness of RM shear walls. They also highlighted that existing equations overestimates the initial stiffness of the walls.

A more recent experimental study was performed by Banting and El-Dakhakhni (2012) to investigate the impact of axial load and other parameters on the response of RM shear walls with confined boundary elements. The results of that study, in line with previous studies, demonstrated that high axial compressive loads increase the lateral capacity and initial stiffness, but limit the displacement and energy dissipation capacities. The wall's displacement ductility measured at ultimate displacement corresponding to 20% degradation in strength dropped by 34% when the axial pre-compression ratio, $P/A_g f'_m$, was increased from 5.4% to 9.8%. Additionally, it was highlighted that the stiffness degradation, between cycles, was significantly influenced by the increase in the axial load.

It is evident from the previous experimental studies that the axial compressive load on either RC or RM shear walls affects the cracking pattern, failure mode, and the ductile response. It has an adverse influence on the curvature ductility, displacement ductility, stiffness degradation, strength deterioration, and the energy dissipation capacity. In RM shear wall buildings, the high axial compressive loads are inevitable as a result of the wall load-bearing structural system. Recent research efforts by Aly and Galal (2019a, 2019b, 2019c) investigated the potential of using a hybrid structural system for masonry buildings composed of ductile and gravity walls in an attempt to reduce the axial compressive loads on the main walls that are resisting the lateral forces. However, the impact of the high axial compressive loads on the stiffness and strength degradation is more evident and perhaps more critical in RM shear walls. This is because it results in rapid face-shell spalling and strength degradation, as noted in the experimental testing by Shing et al. (1988) and Shedid et al. (2008). Thus, there is a need to quantify and enhance the inelastic response of the RM walls under the combined high axial loads and strong seismic excitations. Therefore, the primary objective of this study is to experimentally investigate and quantify the inelastic response of RM structural walls subjected to an axial compression stress that results in pre-compression ratios higher than 10% to propose mitigation techniques that would alleviate the adverse effects.

The experimental testing in this research evaluates the ability of detailing and confining the compression zones to control the axial compressive load effects on the ductile response of RM

shear walls. The tested walls are flexural dominant with a high aspect ratio of 10.55 to simulate the response of mid- and high-rise RM shear walls under severe seismic actions. Table 3.1 summarizes the characteristics of all RM shear walls with confined boundary elements that were tested under constant axial load and in-plane pseudo-static cyclic loading from (Banting and El-Dakhakhni, 2012, 2014; and Shedid et al., 2010).

Table 3.1 Database of RM shear walls with confined boundary elements

No.	Wall No. in Literature	Reference	l_w (mm)	h_w (mm)	AR	# of Stories	ρ_v (%)	ρ_h (%)	Axial Stress (MPa)	P/f'_mA_g (%)	Q_u/A_g (MPa)
1	W3	Shedid et al., 2010	1802	3990	2.21	3	0.56	0.3	0.89	5.4	0.76
2	W6	Shedid et al., 2010	1802	2660	1.48	2	0.55	0.6	0.88	5.4	1.23
3	W7	Shedid et al., 2010	1802	2660	1.48	2	0.55	0.6	0.88	5.4	1.20
4	W1	Banting and El-Dakhakhni, 2012	1803	3990	2.21	3	0.56	0.3	0.45	3.3	0.72
5	W2	Banting and El-Dakhakhni, 2012	1803	3990	2.21	3	0.56	0.3	0.45	3.3	0.64
6	W3	Banting and El-Dakhakhni, 2012	1803	3990	2.21	3	0.56	0.3	0.45	3.3	0.72
7	W4	Banting and El-Dakhakhni, 2012	1803	3990	2.21	3	0.56	0.3	1.34	9.8	1.03
8	Wall 1	Banting and El-Dakhakhni, 2014	2655	3990	1.50	3	0.51	0.3	0.89	6.0	1.12
9	Wall 2	Banting and El-Dakhakhni, 2014	1235	3990	3.23	3	0.69	0.3	0.89	6.0	0.63
10	Wall 3	Banting and El-Dakhakhni, 2014	1235	2660	2.15	2	0.69	0.6	0.89	6.0	0.89
11	Wall 4	Banting and El-Dakhakhni, 2014	1235	2660	2.15	2	1.17	0.6	0.89	6.0	1.21
12	Wall 5	Banting and El-Dakhakhni, 2014	1235	1900	1.54	1	0.69	0.6	0.89	6.0	1.22

In general, there is a limited number of tested RM shear walls with boundary elements. The results of these experimental studies reported a promising enhancement in the overall structural performance of RM shear walls with boundary elements. Nevertheless, a wider range of design parameters still needs to be considered to evaluate and quantify the performance at the component-level. It can be seen in Table 3.1 that the highest aspect ratio of tested RM shear wall with boundary elements was 3.23 for wall 2 tested by Banting and El-Dakhakhni (2014) to represent 3-storey buildings. In addition, all the tested RM shear walls with boundary elements, summarized in Table 3.1, had pre-compression ratios that are less than 10% of the masonry gross compressive strength. The walls were also subjected to moderate shear stresses ranging from 0.63 MPa to 1.23 MPa. Furthermore, only the study by Banting and El-Dakhakhni (2012) investigated the impact of axial load on the structural response. Thus, it is essential to verify the performance of RM walls with higher aspect ratios and subjected to higher axial compressive loads representing the expectations in mid- and high-rise masonry buildings.

Additionally, in most of the tested RM shear walls with boundary elements, the ratio between the spacing of transverse reinforcement and vertical rebars' diameter (s/d_b) in the boundary

element was 9.5. This ratio violates the buckling prevention requirements of TMS 402/602-16 and CSA S304-14. This was due to the use of the stretcher blocks in constructing the boundary elements, Figure 3.1(a), which limited the vertical spacing between transverse reinforcement to the standard height of the blocks. Only wall W7 tested by Shedid et al. (2010a) had pilaster blocks in the boundary elements with spiral reinforcement having a pitch of 30 mm. In this study, to achieve sufficient confinement in the tested walls, C-shaped concrete masonry blocks were used in the boundary elements (end zones) of the walls. As shown in Figure 3.1, the use of C-shaped blocks compared to conventional stretcher blocks allows flexibility in the boundary element's size, the spacing of transverse reinforcement, the arrangement of vertical reinforcement, and the compressive strength of grout. This made it possible to meet most design standards', including TMS 402/602-16 and CSA S304-14, seismic provisions for the spacing of buckling prevention hoops in the compression zone.

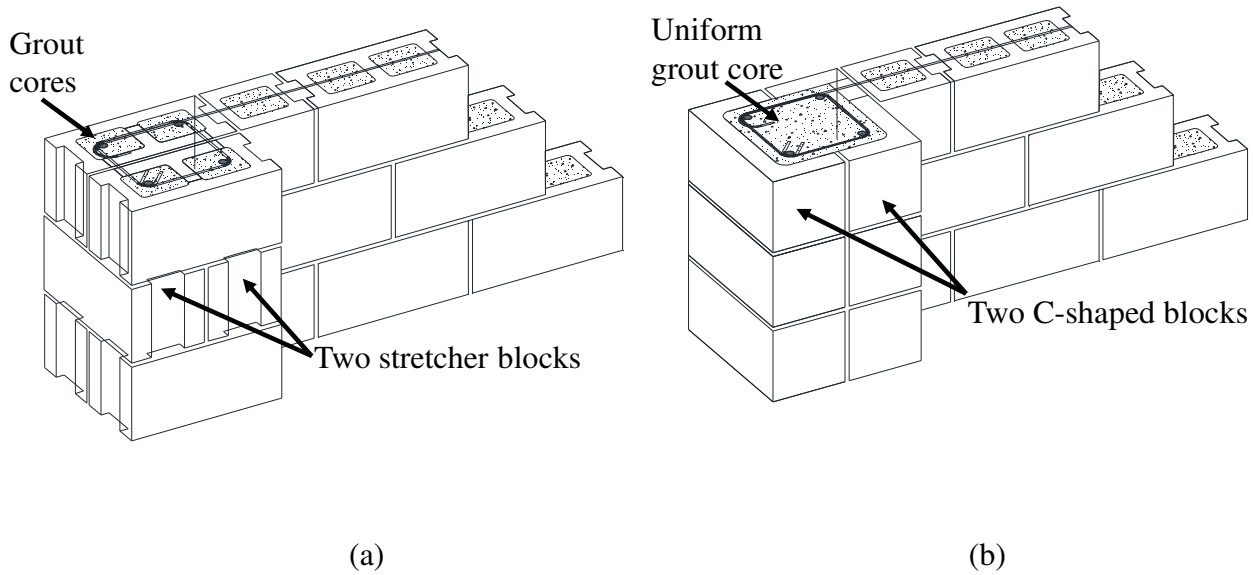

Figure 3.1 RM boundary element built using: (a) standard concrete stretcher blocks; and (b) C-shaped concrete masonry blocks

3.3 Experimental Program

The specimens of this study are part of an experimental program aiming at enhancing and quantifying the seismic performance of RM shear walls with boundary elements. The reported specimens in this study focus on investigating the influence of boundary elements' detailing: vertical reinforcement ratio (ρ_v), size, confinement, and compressive strength (f'_m), on the inelastic

structural performance of RM structural walls tested under an axial compressive stress that results in pre-compression ratios, $P/A_g f'_m$, higher than 10%. The objective is to assess the ability of boundary elements' detailing in mitigating the adverse effects of the high axial load on the strength degradation, curvature ductility, displacement ductility, energy dissipation capacity, and stiffness degradation. In this regard, three half-scale fully grouted RM shear walls with boundary elements were constructed and tested under high constant axial load, in-plane displacement-controlled fully reversed cyclic loading, and top moment to simulate the expected response under seismic actions. The dimensions and reinforcement details of the tested walls are summarized in Table 3.2. Additionally, the specimens' cross-sectional configuration and reinforcement detailing are presented in Figure 3.2.

As shown, the walls' webs were shifted to the edges of the boundary elements. This asymmetry in the cross-section would allow placing the insulation in the created space between the boundary elements. Also, this layout avoids creating a small recess in interior rooms, which might not be appealing to architects. It should be noted that in the actual building, the asymmetric walls will be placed symmetrically as pairs such that the center of rigidity of the two of these walls would be at their geometrical center. The walls were designated by a unified ID based on the sequence of tested walls in the experimental program at Concordia University. They were also given a unique parameter ID in this paper, which represents the varied parameters. For instance, W7 has the parameter of C_4^{190} which indicates that the boundary elements were made of **C**-shaped blocks with a length equal to 190 mm and had four (4) No. 3 vertical rebars. Due to the limitations in handling and testing such large-scale specimens, the tested walls were half-scale, and only the plastic hinge region was tested. The tested specimens represent half-scale shear walls from a 12-storey prototype RM building. This building utilizes the hybrid structural system proposed by Aly and Galal (2019a) for multi-story masonry buildings, which is composed of two types of walls; ductile and gravity walls. Furthermore, it is assumed to be an apartment building located in a region with moderate seismicity, such as Montréal, Canada. The prototype building has first-floor height of 3.2 m and a typical floor height of 3.0 m, which makes the total building height equal to 36.2 m. The half-scale height of the prototype building is 18.1 m, and the tested specimens' height (h_{tested}) is 2.38 m. The tested height simulates a conservative estimate of the plastic hinge region of a typical wall in the 12-storey prototype RM building. The plastic hinge height was estimated as

recommended by CSA S304-14 clause 16 for the extent of special detailing. The test walls have an effective height-to-length ratio (h_{eff}/l_w) of 7 and were designed to be flexure dominated.

All the specimens had an end confined cross-sectional configuration with rectangular or square boundary elements. The reference wall, W7-C_4^{190}, had a square 190mmx190mm boundary element made-up of C-shaped pilaster concrete masonry blocks and four No. 3 (diameter = 9.525 mm and area = 71 mm^2) vertical rebars. Wall W8-C_8^{190} had the same size of boundary element but with eight No. 3 vertical rebars. Conversely, wall W9-C_8^{290} had a rectangular 290mmx190mm boundary element with eight No. 3 vertical rebars. All vertical rebars were continuous over the height of the specimens with no lap splicing. The three tested walls had the same level of confinement achieved using hoops made of D4 (diameter = 5.73 mm and area = 25.8 mm^2) deformed wires and spaced at 60 mm, centre-to-centre, to satisfy the buckling prevention requirements of CSA S304-14 and TMS 402/602-16 (s/d_b = 6). Moreover, the walls were tested under the same level of axial compressive stress of 2.25 MPa. This axial stress value was selected to result in pre-compression ratios (i.e. $P/A_g f'_m$) higher than 10% to represent the expected axial loads in mid- and high-rise walls. The tested walls had pre-compression ratios ranging from 13.6% to 14.9%, as shown in Table 3.2, and neutral axis depths extending beyond the small boundary elements (i.e. the 190mmx190mm boundary elements). The axial pre-compression ratios were calculated using the gross compressive strengths of the web and the boundary elements based on their corresponding material properties. The walls were subjected to relatively low shear stresses ranging between 0.32 MPa and 0.43 MPa, shown in Table 2, compared to previous studies.

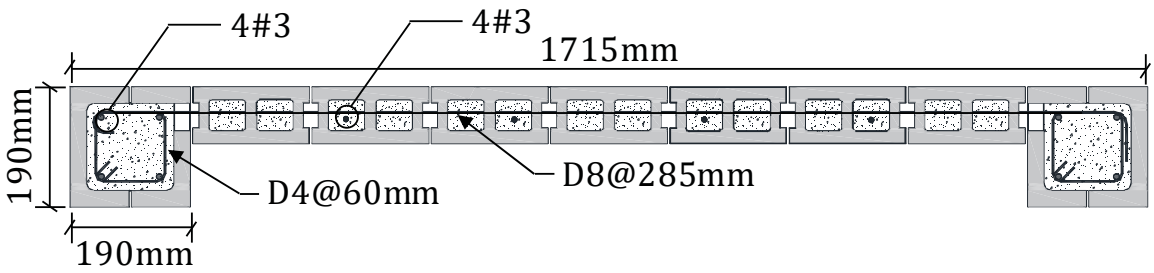

(a)

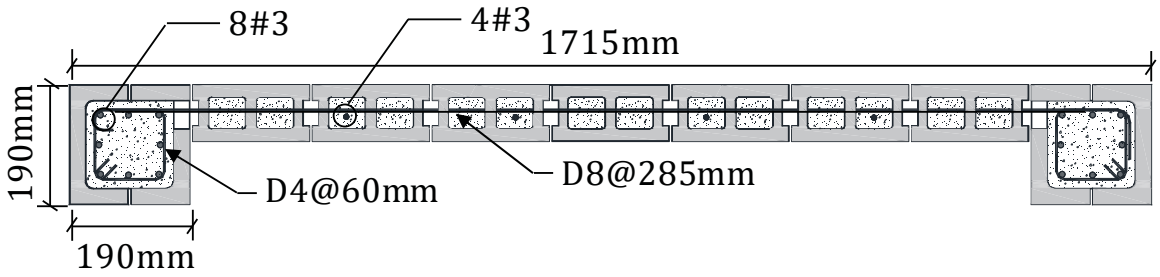

(b)

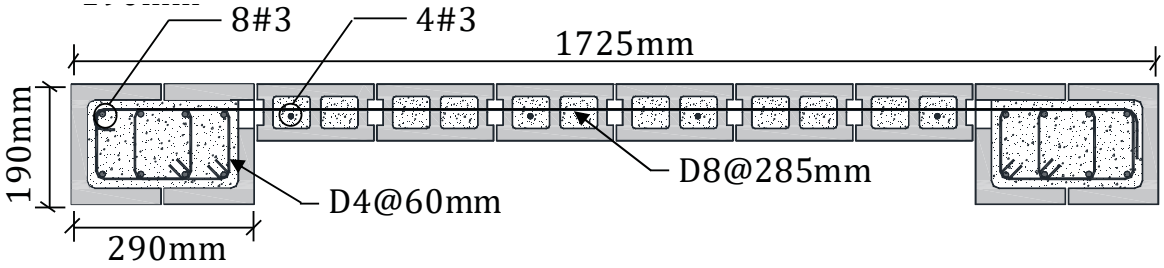

(c)

Figure 3.2 Cross-sectional configuration and detailing of test specimens: (a) wall W7-C_4^{190}; (b) wall W8-C_8^{190}; and (c) W9-C_8^{290}

Table 3.2 Details of tested walls

Unified ID*	Wall Length (mm)	Common Parameters										Studied Parameters			
		Web			Boundary Element			M/Vd	Axial Stress (MPa)	P/f'_mA_g (%)	Q_u/A_g (MPa)	Studied Parameter ID**	Boundary Element		
		Thickness (mm)	Vertical bars	Horizontal bars	Confinement	s/d_b	Width (mm)						Length (mm)	Vertical bars	ρ_v (%)
W7	1715	90	4#3	D8@285 mm	D4@60mm	6	190	8.8	2.25	14.9	0.32	C_4^{190}	190	4#3	0.79
W8	1715	90	4#3	D8@285 mm	D4@60mm	6	190	8.8	2.25	14.9	0.43	C_8^{190}	190	8#3	1.58
W9	1725	90	4#3	D8@285 mm	D4@60mm	6	190	8.8	2.25	13.6	0.35	C_8^{290}	290	8#3	1.03

* Based on the wall ID tested at Concordia University
** $d = 0.8l_w$
*** Based on the parameters studied in this paper

3.3.1 Design and construction of specimens

The walls were designed and detailed to meet the requirements of CSA S304-14, the design of masonry structures standard, for ductile RM shear walls. They also satisfy TMS 402/602-16, building code requirements and specifications for masonry structures, provisions for special RM shear walls. The walls were designed to fail in flexure by ensuring that the walls' shear capacity exceeds the shear demand corresponding to the formation of plastic hinge mechanism at the walls' base (i.e. following capacity design concept). Horizontal reinforcement was provided in every third masonry course using D8 (diameter = 8.11 mm and area = 51.61 mm^2) deformed wires with one end having 180^o standard hook and the other end at 90^o to allow placing it around the vertical bars at the walls' ends. Additional 180^o D8 deformed wires hooks that are well-developed in the wall web were provided in the masonry courses, which had no horizontal rebars. The additional horizontal hooks were intended to increase the shear flow resistance at the interface between the walls' web and the enlarged boundary elements and to avoid any slip deformation. Furthermore, sufficient amount and spacing of transverse reinforcement, D4 deformed wires spaced at 60 mm, were provided to delay the onset of buckling of vertical reinforcement in the walls' compression zone. Besides, the design ensured that the walls have sufficient inelastic rotational capacity meeting the requirements of CSA S304-14 for the inelastic rotational demand of ductile walls. Moreover, boundary elements were needed and were provided according to TMS 402/602-16 displacement-based check to ensure that the walls qualify as special walls.

The walls presented in this study were constructed by the same professional mason using half-scale concrete masonry blocks with the same compressive strength. Besides, the specimens were grouted in the same phase using the same grout mix design. The intent was to make the walls as similar as possible and to reduce the variation in response due to materials' variability. The concrete masonry stretcher blocks used for the walls' web were half-scale replicas of the standard depressed hollow 190mm blocks commonly used in North America, as shown in Figure 3.3(a). All web stretcher blocks were depressed standard concrete masonry units to accommodate the horizontal rebars and to allow the grout to flow smoothly and fill the cells. The walls' boundary elements were constructed using half-scale C-shaped concrete masonry blocks cut to form the required square or rectangular dimensions, as illustrated in Figure 3.3(b). The web blocks were laid in a running bond pattern with a 5 mm joint of pre-bagged Type-S mortar, whereas a stack pattern was used in constructing the boundary elements. The boundary elements were built in a

stack pattern to make the construction more practical and to make it possible to have rectangular boundary elements. The 5 mm mortar joints represent a half-scale replica of the standard 10 mm joints used in practice. The three walls were fully grouted using a fine concrete grout mixed in the laboratory according to CSA A179-14 requirements. The grouting was performed at three stages to ensure the continuity of grout in all blocks' cells and to avoid having any voids or cavities in the walls. Each stage was performed in a separate day, and one-third of the wall height was grouted. Two types of grout mix designs were used, a high strength fine grout in the walls' boundary elements and an ordinary strength fine grout in the walls' web. The boundary elements were grouted using the high strength grout to enhance the axial compressive resistance of the walls and reduce the depth of the compression zone. This is not a typical practice, as this is a newly proposed system to enhance the inelastic response and overcome previous limitations.

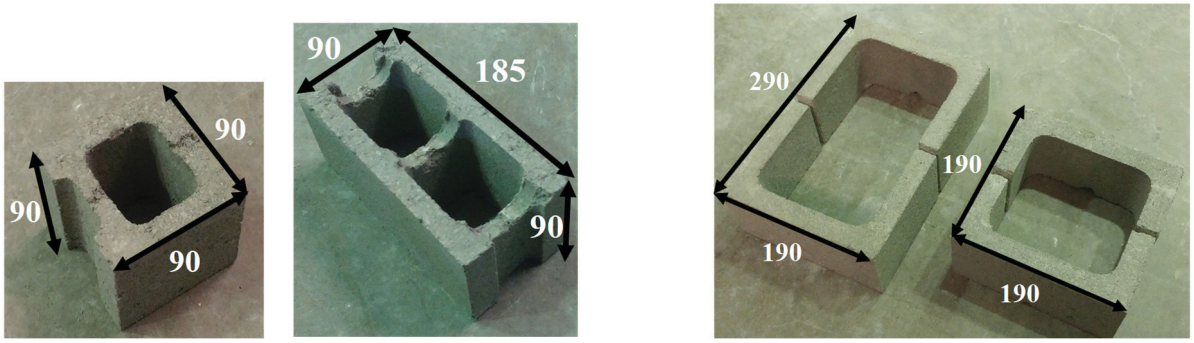

(a) (b)

Figure 3.3 Concrete masonry units: (a) half-scale half and full stretcher blocks; and (b) half-scale C-shaped blocks (all dimensions are in millimetres)

3.3.2 Properties of materials

The web half-scale stretcher blocks were tested in accordance with CSA A165-14 and ASTM C140-15. The average compressive strength ($f'_{b\text{-}web}$) was 34.7 MPa, based on testing three specimens, with a Coefficient of Variation (c.o.v) equal to 7.6%. For the boundary element C-shaped blocks, a coupon with a height-to-thickness ratio of 2 and a length-to-thickness ratio of 4, as recommended by ASTM C140-15, was cut from the block and tested. The average recorded compressive strength ($f'_{b\text{-}BE}$) for the tested specimens was 22.8 MPa (c.o.v = 4.8%). 50 mm mortar cube specimens, sampled during the construction of the walls, were tested according to CSA A179-14 and ASTM C109M-13. The average mortar compressive strength (f'_{mo}) was 15.1 MPa with a c.o.v equal to 14.3%. The walls' web area was filled with an ordinary strength fine grout designed

and mixed in the structures laboratory according to CSA A179-14. The specimens' average cylinder compressive strength ($f'_{gr\text{-}web}$), tested according to CSA A179-14, was 29.9 MPa (c.o.v = 4.8%). Conversely, the boundary elements were grouted with a high strength fine grout that was also designed and mixed in the structures laboratory in accordance with CSA A179-14. The average cylinder compressive strength of the boundary elements' grout ($f'_{gr\text{-}BE}$) was 43.2 MPa, with a c.o.v of 15.5%.

Masonry prisms were constructed from the stretcher blocks and the C-shaped blocks to represent the walls' webs and boundary elements, respectively. The web prisms were one-block long by four-blocks high, whereas the boundary element prims were made of four-courses high C-shaped pilaster blocks forming the dimensions of the square boundary elements (i.e. 190mm x 190mm). The web prims were grouted using the ordinary strength fine grout, while the boundary element prisms were grouted using the high strength fine grout. Five boundary element prisms and eight web prisms were tested according to CSA S304-14 to evaluate the average compressive strength (f_{av}) and the specified compressive strength (f'_m). The number of tested prisms is in agreement with the design standard, CSA S304-14 clause D3.2.3, which requires testing at least five prisms to find the compressive strength or ten if the c.o.v exceeds 15%. The average recorded compressive strength (f_{av}) was 11.3 MPa (c.o.v = 12%) and 25.5 MPa (c.o.v = 8%) for the web and boundary element prisms, respectively. The average values were corrected to account for the specimens' aspect ratio and standard deviation to calculate the specified compressive strength (f'_m) values according to CSA S304-14. The web prisms had a specified compressive strength (f'_m) of 8.7 MPa, and the boundary elements' specified compressive strength (f'_m) was 19.0 MPa. The walls were reinforced vertically using No. 3 bars having an average yield strength (f_y) of 460 MPa, average tensile strength (f_u) of 680 MPa, and average ultimate strain (at fracture) of 14%. The No. 3 rebars represented the half-scaled version of 20M bars. The horizontal web reinforcement and the additional hooks were of D8 deformed wires, to simulate the half-scaling of 15M rebars, with an average yield strength (f_y) of 535 MPa, average tensile strength (f_u) of 580 MPa, and average ultimate strain (at fracture) of 5.5%. The confining hoops provided in the boundary elements consisted of D4 deformed wires representing the 10M bars. The average yield strength (f_y) was 590 MPa, the average tensile strength (f_u) was 630 MPa, and the average ultimate strain (at fracture) was 4.5%. The yield strengths of D8 and D4 deformed wires were determined based on a 0.2% strain value, as specified by ASTM A1064M-15 when there is no clear yield point.

3.3.3 Instrumentation

The tested walls were instrumented internally with 5-mm strain gauges, and externally with Linear Variable Displacement Transducers (LVDTs) and linear potentiometers. A total of twenty 5-mm strain gauges were used in each of the tested walls over the height of the two outer most reinforcement bars, as shown in Figure 3.4(a). The strain gauges were given a designation that reflects the level (i.e. height above the base) and the bar number. For instance, S11 is the strain gauge at the first level and is attached to the reinforcing bar number 1. The strain gauges were used to measure the local strains in the reinforcement bars in order to evaluate the extent of yielding over the walls' height. In addition, the strain gauges attached to the reinforcing bars at the wall-foundation interface were used to capture the yield displacement (Δ_y) which is used in calculating the target displacements of the loading protocol. Nineteen LVDTs were attached to the tested walls as shown in Figure 3.4(b). LVDTs L1 to L12 were used to measure the vertical displacements on both sides of the walls to calculate the walls' curvature profiles over the height. LVDT L13 was attached between the top footing and the wall to measure any sliding deformations. To measure the sliding shear deformations at the walls' base, LVDT L15 was attached between the bottom footing and the wall. Additionally, to measure any uplift at the wall-foundation interfaces, LVDTs L14, L16, and L17 were attached between the footings and the wall. LVDTs L18 and L19 were used to monitor slip deformations between the walls' boundary elements and the web. For measuring the lateral displacements, the linear potentiometers P1-P4 were used and were attached to a rigid truss to ensure that the measured displacements are not influenced by any deformations in the testing frame. The linear potentiometer P5 was used to measure any slip between the wall's footing and the testing frame's transfer footing and was used to correct the top lateral displacements if needed. To measure the uplift between footing of the wall and the testing frame's transfer footing, if any, linear potentiometers P6 and P7 were used. Finally, the diagonal (shear) deformations were measured using potentiometers P8 and P9. All measured displacements and strains were recorded using a digital data acquisition system.

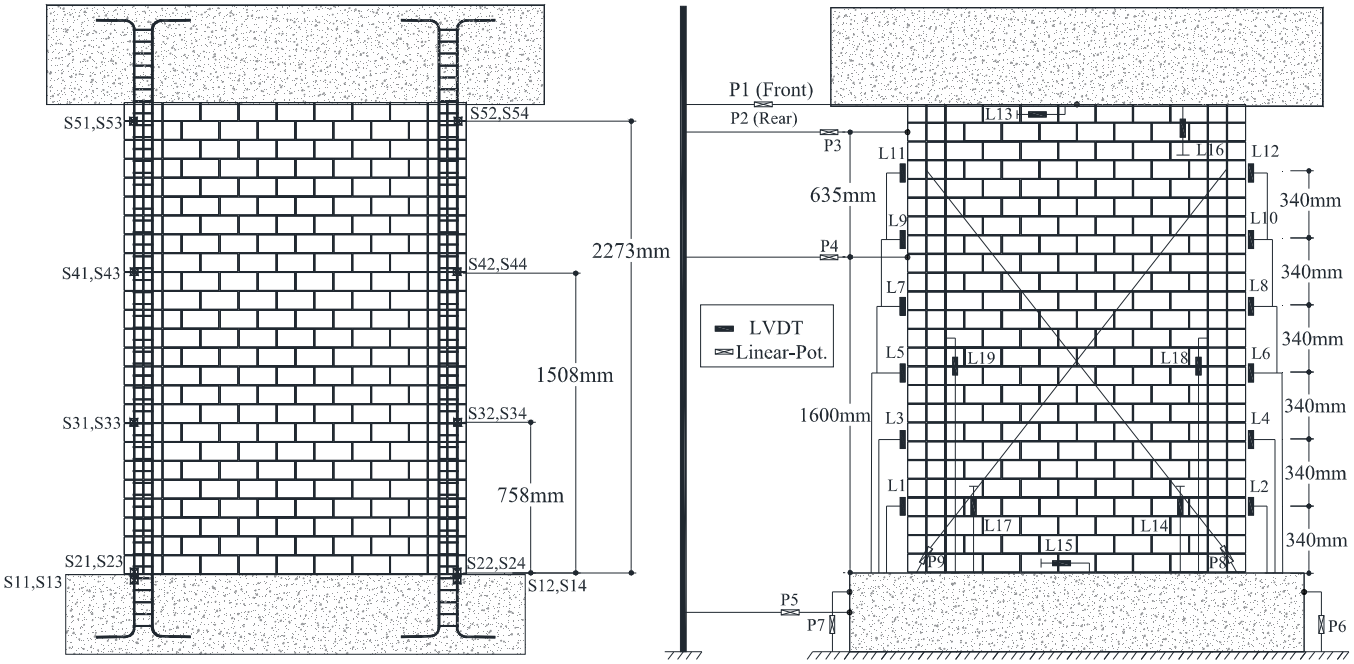

Figure 3.4 Instrumentation: (a) internal (strain gauges); and (b) external (LVDTs and Potentiometers)

3.3.4 Test setup and loading protocol

The tested walls are half-scale panels representing the plastic hinge region of 12-storey RM shear walls. Thus, they were tested by applying lateral displacements at the top of the physical specimens in addition to top overturning moments. The testing setup is shown in Figure 3.5. The lateral displacements were applied at the RC loading beam level using a double-acting horizontal hydraulic actuator with +/-734 kN and +/- 200 mm capacity in a displacement-controlled mode. The top moment and axial compression load were applied to the specimens by two vertical hydraulic actuators with +/-734 kN and +/- 200 mm capacity in a force-controlled mode. As shown in Figure 3.5(a), the three actuators were attached to a rigid steel reaction frame designed to remain elastic with negligible deformations at the capacity of the three actuators. The bottom RC footing of the wall was attached using 18-1in high strength prestressing rods to a larger transfer RC footing providing a fixed boundary condition to the wall's base. The transfer RC footing was fixed to the laboratory's strong floor by 12-2in high strength prestressing bolts. During the testing, the wall's out-of-plane displacements were restrained at the level of load application (i.e. the RC loading beam) and a level 1600 mm above the wall foundation. This level was selected to represent the

first-floor slab and to limit the unsupported height-to-thickness ratio of the wall to 16, as suggested by CSA S304-14 clause 16.9.3. The out-of-plane support system was designed to tolerate in-plane translational and rotational displacements since the tested specimens were subjected to lateral displacements as well as applied top moments. This was achieved by utilizing Polytetrafluoroethylene (PTFE) sheets and Delrin bars to minimize the contact friction, as shown in Figure 3.5(b). The horizontal and the two vertical actuators were synchronized to apply the lateral displacement and the corresponding top moment.

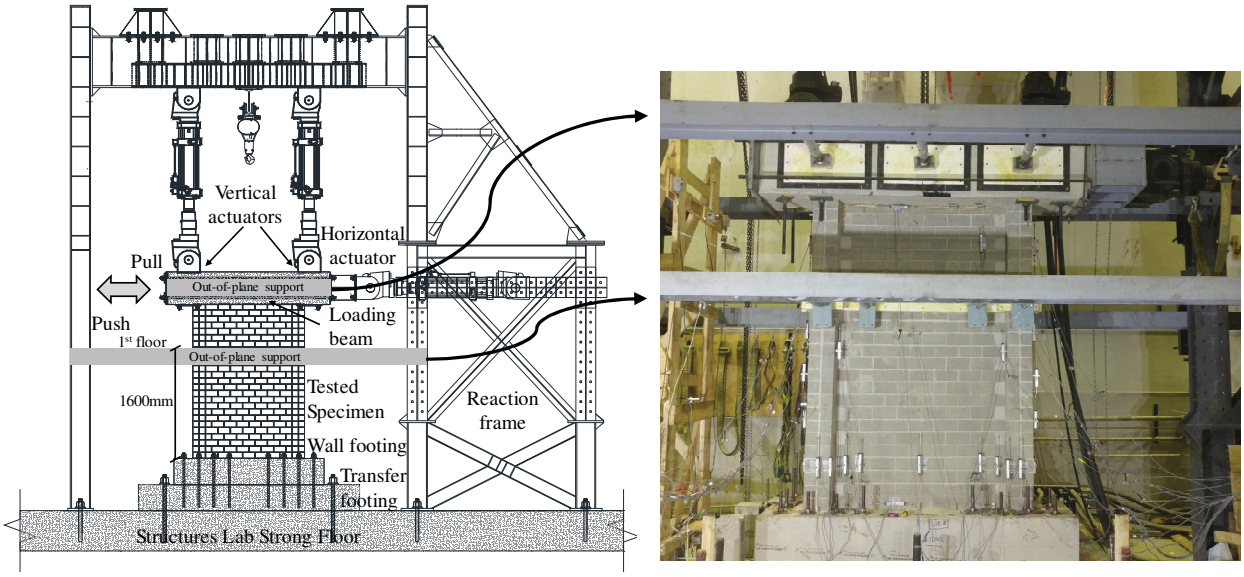

(a) (b)

Figure 3.5 Test setup: (a) elevation view; and (b) as-built photo

Figure 3.6 illustrates the estimation and application of the top moments. The top moments were calculated to compensate for the height difference between the tested specimens and the actual walls. A triangular distribution, corresponding to the first mode shape, was assumed for the lateral forces to simulate the seismic loads. Then, the base moment was estimated based on the application of the lateral force at the effective height (h_{eff}) of the full specimen. Thus, the top moment on the tested specimen was calculated such that it compensates for the lower base moment due to the application of the lateral force at the reduced height of the specimen (h_{tested}). First, the lateral displacements were applied at the top of the specimen at the middle of the top RC loading beam. The top RC loading beam was centered with the center of gravity of the wall to minimize the torsion due to the asymmetry of the walls' sections. Centering the loading beam with the shear

center of the wall was not feasible as it will create out-of-plane moments that could damage the specimen.

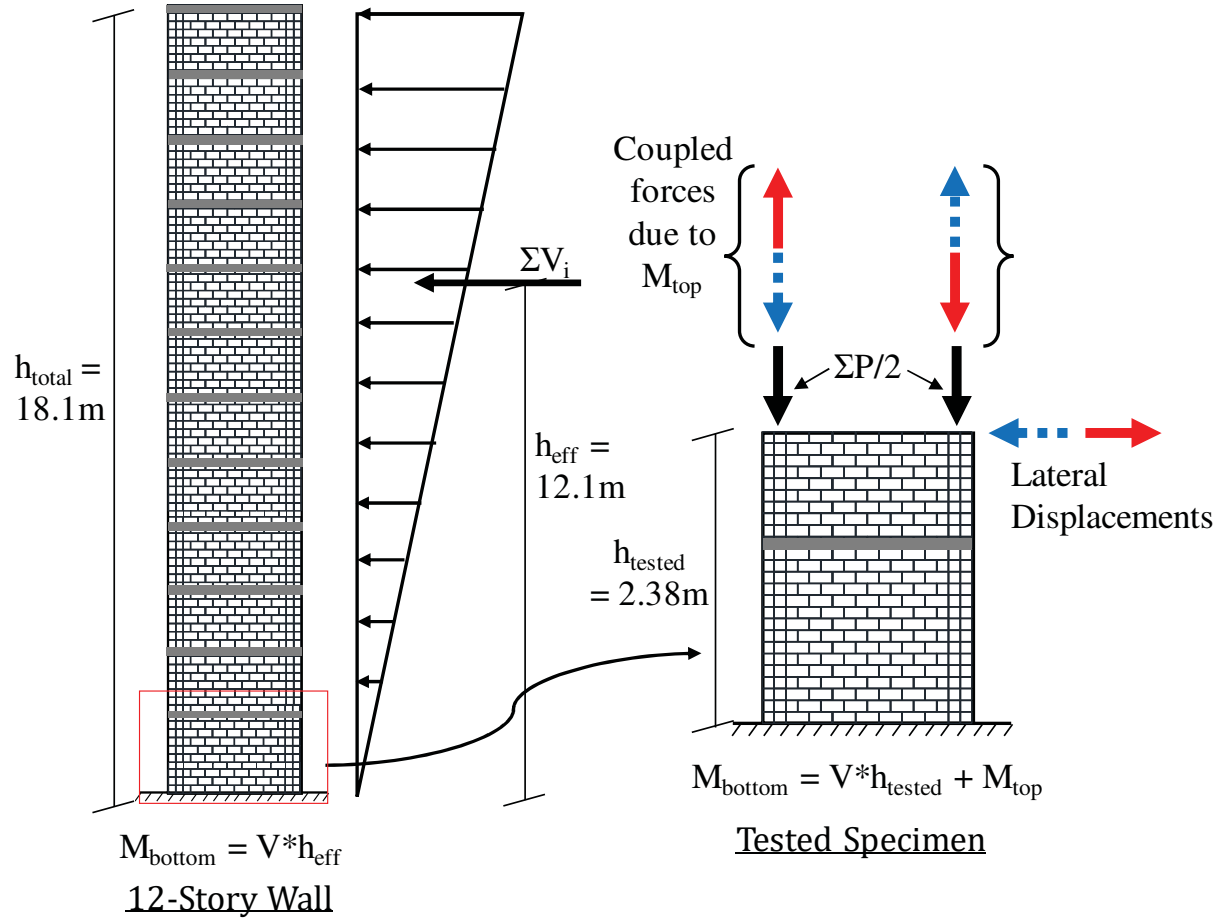

Figure 3.6 Estimation of the top moment on the tested specimen

The out-of-plane support system was designed with screw jacks from both sides attached to a strong beam (W250x45), as shown in Figure 3.5(b), to restrain any torsional rotation in the specimen. It is also acknowledged that the lateral force should be applied at the diaphragm (floor) level. However, as the tested specimens are flexure dominated and the shear response was insignificant, it was more important to ensure that the bottom moment in the tested wall is equivalent to that expected in the full specimen. In addition, due to the use of one lateral actuator, the applied shear represented the base shear and was constant along the height of the wall. This lateral load was transferred to the wall through the stiff top beam. At each displacement increment, the lateral resistance of the wall was measured using the horizontal actuator's load-cell. The measured lateral force was then used to calculate the coupling forces (i.e. push/pull) in the vertical actuators to apply the corresponding top moment. The applied top moments were more than four

times the bottom moment due to the applied lateral displacement (i.e. V x h_{tested}). The P-Δ effects were neglected as they were insignificant. However, the lateral resistance was corrected to include the horizontal force component from the vertical actuators, especially at high lateral displacements. It is noteworthy that the increase in the lateral force ranged from 9% to 11%.

The lateral displacements loading history used in testing the walls follows the fundamental requirements of quasi-static cyclic testing, the recommendations of FEMA 461 (2007) and ASTM E2126-12. In essence, the size of the displacement increment was carefully proportioned, and the loading was applied at a slow rate to allow ignoring the dynamic and strain-rate effects. FEMA 461 (2007) recommends a loading protocol for quasi-static cyclic testing of structural components that is based on increments of a damage state. In this study, the lateral displacement at the onset of the first yield in the outermost vertical reinforcement was selected as the damage level. The experimental lateral displacement at yield (Δ_y) was estimated by recording the lateral displacement corresponding to the yielding strain measurement in any of the strain gauges installed at the outermost vertical reinforcement located at the wall-foundation interface. The applied loading protocol consisted of displacement-controlled fully reversed loading cycles, twice at each displacement level. The walls were first loaded with the constant axial compressive stress, simulating gravity loads, in a force-controlled mode as shown in Figure 3.7(a). Afterwards, the lateral cyclic displacements were applied following the displacement-controlled loading history shown in Figure 3.7(b). The first portion of the loading history, pre-yield stage, consisted of small increments (i.e. 25%, 50% and 75%) of the yield displacement (Δ_y), estimated based on the measured local strains in the outermost vertical rebars at the wall-foundation interface. The pre-yield stage was required to capture the experimental lateral displacement at the onset of the first yield (Δ_y). Subsequently, in the post-yield stage, the loading history was defined as multipliers of the experimentally measured yield displacement (Δ_y). To sufficiently capture the post-peak response, the loading protocol displacement amplitudes were gradually increased until 20% strength degradation occurred, the loss of load-carrying capacity, or until the fracture of vertical rebars and substantial crushing of the grout core, whichever happened first.

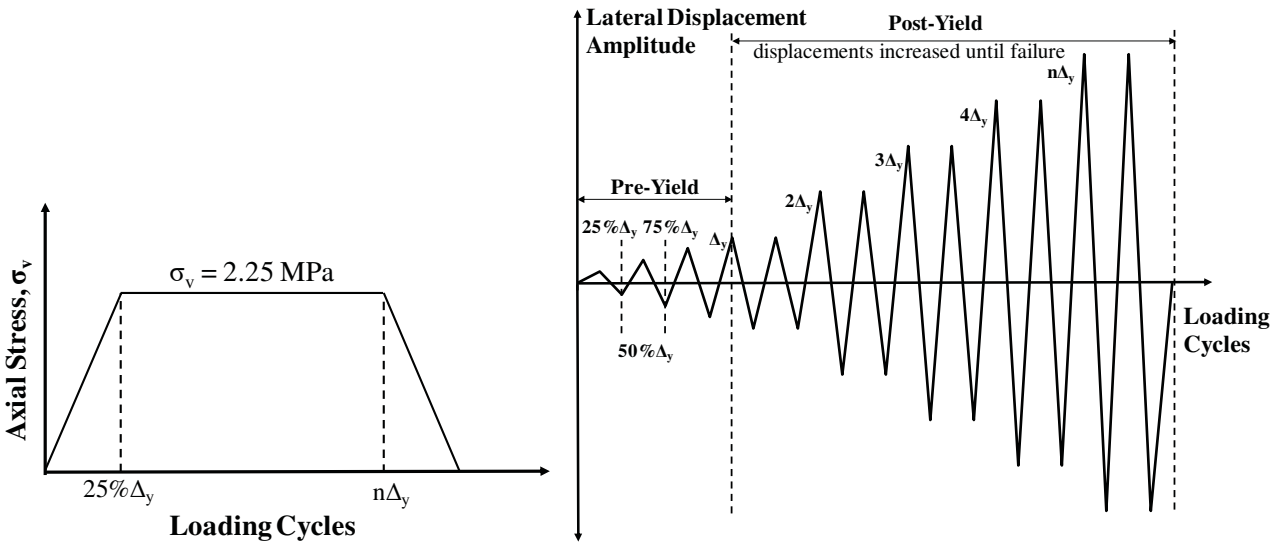

Figure 3.7 Loading protocol: (a) axial compressive stress; and (b) lateral displacements history

3.4 Experimental Results

3.4.1 Load-displacement response

Figure 3.8 presents the load-displacement hysteresis loops of the three tested specimens. The lateral forces shown in Figure 3.8 were adjusted to account for the horizontal force component applied by the vertical actuators, as mentioned previously. In addition, the lateral displacements are reported at the top of the tested specimen (Δ_T) as well as at the first-floor level (Δ_1). It can be seen that the three specimens had an almost linear elastic response until the onset of the first yield in the outermost vertical reinforcement. The linear response was accompanied with thin hysteresis loops reflecting a low-level of energy dissipation. At higher lateral displacements, the response of the walls started to become nonlinear after the yielding of vertical reinforcement and the horizontal flexural cracks. Fatter hysteresis loops were seen indicating the increase in the energy dissipated by the walls through the yielding of reinforcement and damage of masonry.

As depicted in Figure 3.8, the three specimens also had a stable ductile hysteretic response that is nearly symmetric in the push and pull directions. The symmetric response reflects the uniformity of the cross-sections. The walls sustained large inelastic deformations, beyond the yield displacement, without any significant degradation in lateral resistance. Additionally, the second loading cycle at each displacement level only resulted in limited degradation in the walls' lateral resistance and stiffness. The loops are almost overlapping, reflecting minor in-cycle and cyclic

degradation. Furthermore, the three walls had a hardening post-peak response until they reached the failure criteria. The peak and ultimate loads were almost identical for the three specimens. Therefore, the expected impact of the high axial compressive stress on the lateral resistance degradation was controlled by the presence of sufficient confinement in the compression zones of the walls.

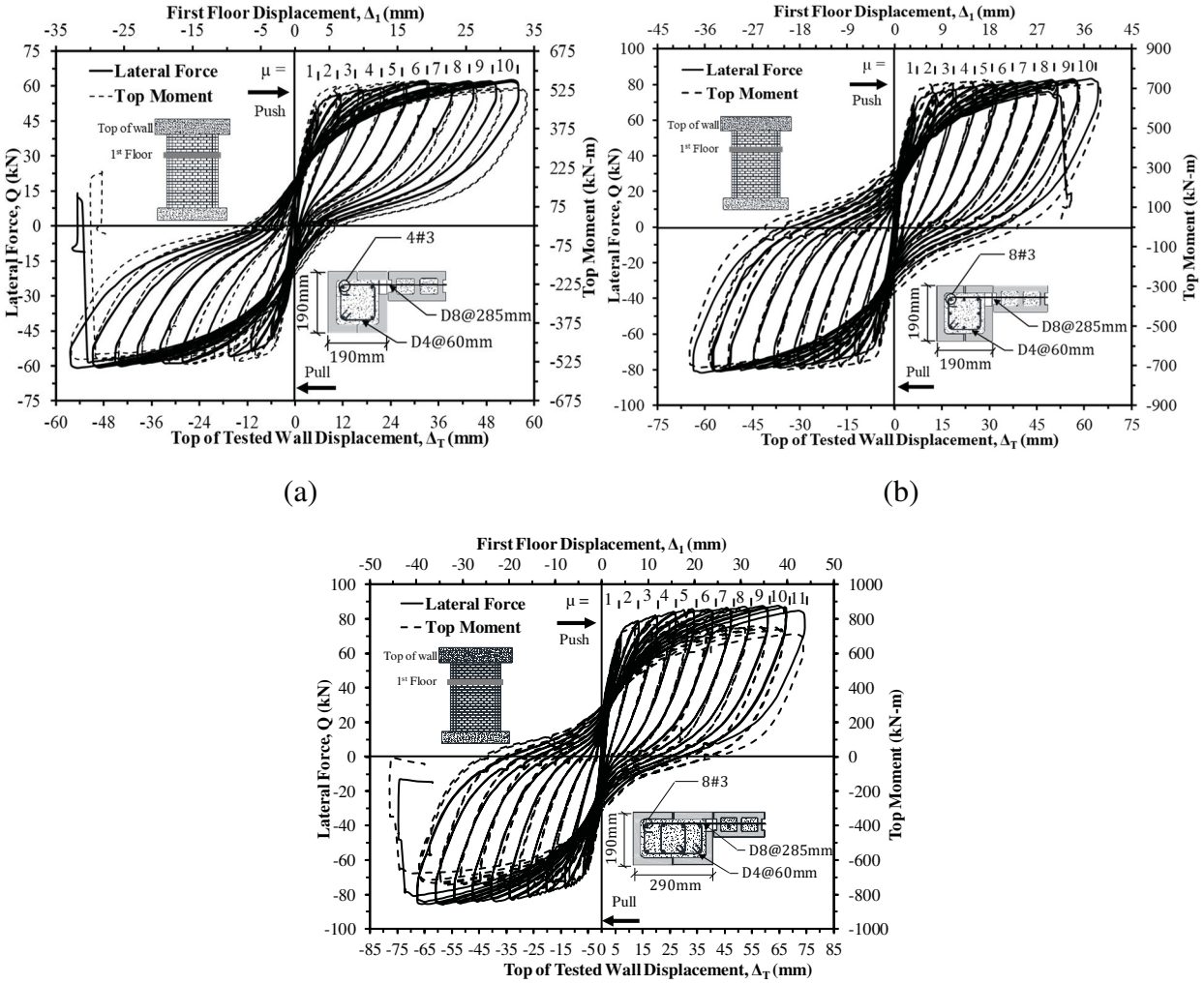

Figure 3.8 Lateral load-displacement response: (a) wall W7-C_4^{190}; (b) wall W8-C_8^{190}; and (c) wall W9-C_8^{290}

The load-displacement envelopes of the three specimens are shown in Figure 3.9. The top of the tested wall drift was calculated as the ratio between the displacements measured at the top of the specimen and the height of the tested specimen (h_{tested}). Wall W7-C_4^{190} had an average, for push and pull directions, measured lateral displacement at the onset of the first yield (Δ_y) of 5.60 mm

(0.24% drift), corresponding to a lateral force (Q_y) of 48.56 kN. Similarly, the average first yield displacement was 6.38 mm for wall W8-C_8^{190} and 6.75 mm for wall W9-C_8^{290}. The average lateral resistance at yield was 65.13 kN and 69.23 kN for walls W8-C_8^{190} and W9-C_8^{290}, respectively. It is worth noting that the difference between the lateral force and displacement at the first yield in push and pull directions was negligible for the three specimens. Doubling the amount of vertical reinforcement in the boundary elements of wall W8-C_8^{190} resulted in increasing the first yield displacement by 14% and the first yield force by 34% compared to wall W7-C_4^{190}. Besides, it increased the secant stiffness at the first yield by 19%. There was a marginal increase in the first yield displacement and force of W9-C_8^{290} compared to W8-C_8^{190} due to the increase in the boundary element's length.

3.4.2 Peak loads, ultimate loads, and corresponding displacements

As shown in Figure 3.9, wall W7-C_4^{190} had an average measured peak lateral load (Q_u) of 61.70 kN at a lateral displacement (Δ_{Qu}) of 54.84 mm. Specimen W8-C_8^{190} had a lateral resistance that is 34% higher than W7-C_4^{190} at a corresponding lateral displacement (Δ_{Qu}) equal to 61.79 mm. Similarly, wall W9-C_8^{290} had a lateral resistance that is 41% and 5% higher than walls W7-C_4^{190} and W8-C_8^{190}, respectively, at a lateral displacement of (Δ_{Qu}) 58.6 mm. Thus, the increase in vertical reinforcement was more effective in enhancing the lateral resistance of the walls compared to the increase in confined grout core size. The secant stiffness at ultimate loads was highest for wall W9-C_8^{290} reflecting the influence of the increase in vertical reinforcement and confined grout core size. However, the ratio between ultimate and first yield secant stiffness was similar for the three specimens with an average of 0.13. Wall W9-C_8^{290} failed at a lateral displacement of (Δ_u) 72.58 mm, which is 13% higher than W8-C_8^{190} and 29% higher than W7-C_4^{190}. The increase in the vertical reinforcement of W8-C_8^{190} increased its ultimate displacement (Δ_u) by 14% compared to W7-C_4^{190}. Therefore, the increase in the boundary elements' vertical reinforcement ratio and size were both capable of enhancing the ultimate lateral displacement capacity of the walls. This is because of the increase in the ultimate compressive strain sustained by the masonry extreme fibers and the reduction in the depth of the compression zone, which increased the ultimate curvature attained by the section. Thus, the ultimate displacement capacity was improved due to the increase in plastic deformations.

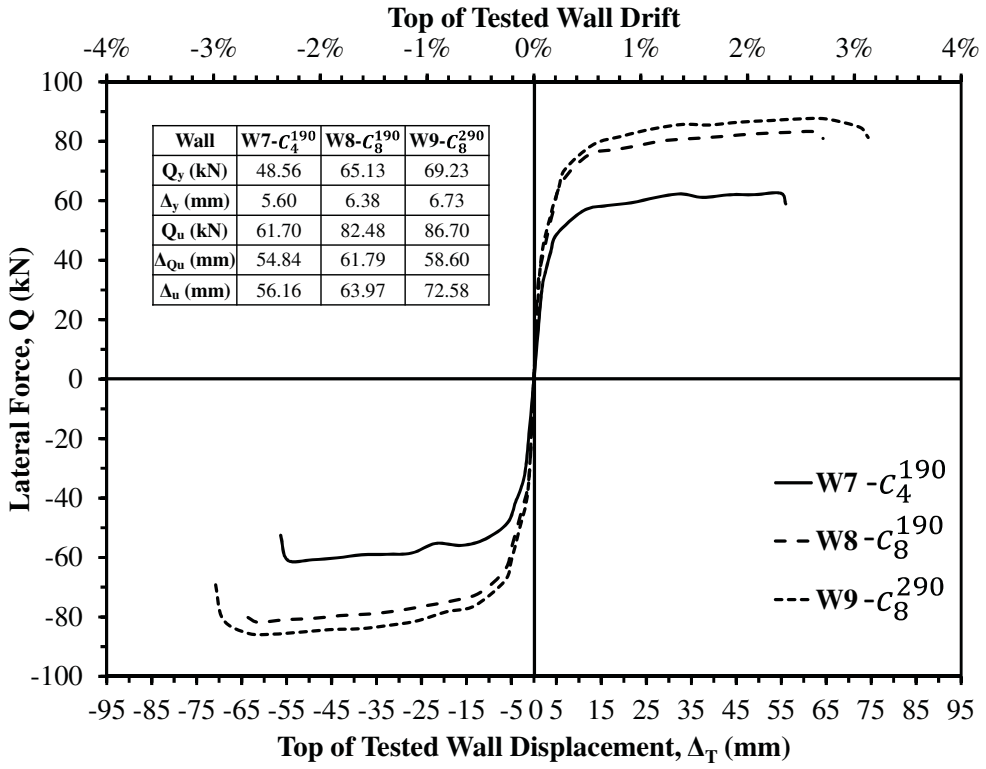

Wall	W7-C_4^{190}	W8-C_8^{190}	W9-C_8^{290}
Q_y (kN)	48.56	65.13	69.23
Δ_y (mm)	5.60	6.38	6.73
Q_u (kN)	61.70	82.48	86.70
Δ_{Qu} (mm)	54.84	61.79	58.60
Δ_u (mm)	56.16	63.97	72.58

Figure 3.9 Lateral load-displacement envelopes

3.4.3 Damage sequence

The three walls had a flexure dominated response reflected in the significant horizontal cracking along with the flexural yielding of vertical reinforcement, as illustrated in Figure 3.10. At the first yield displacement, the three specimens had few hairline horizontal flexural cracks along the bed joints on both sides of the wall. With the progression of loading history, the cracks propagated horizontally with larger widths. At higher lateral displacements, horizontal cracks were initiated in the boundary elements' blocks. This occurred at four times the first yield displacement (i.e. $4\Delta_y$) for wall W7-C_4^{190}, and $2\Delta_y$ for walls W8-C_8^{190} and W9-C_8^{290}. The first diagonal shear crack appeared in the first-floor at a lateral displacement corresponding to $5\Delta_y$ in wall W7-C_4^{190}, and at $3\Delta_y$ in walls W8-C_8^{190} and W9-C_8^{290}. With the increasing lateral displacements, the three specimens exhibited more horizontal cracks in the boundary elements' blocks along with the propagation of existing bed joint cracks. In addition, few more diagonal shear and step cracks appeared in walls W8-C_8^{190} and W9-C_8^{290} due to their increased lateral resistance.

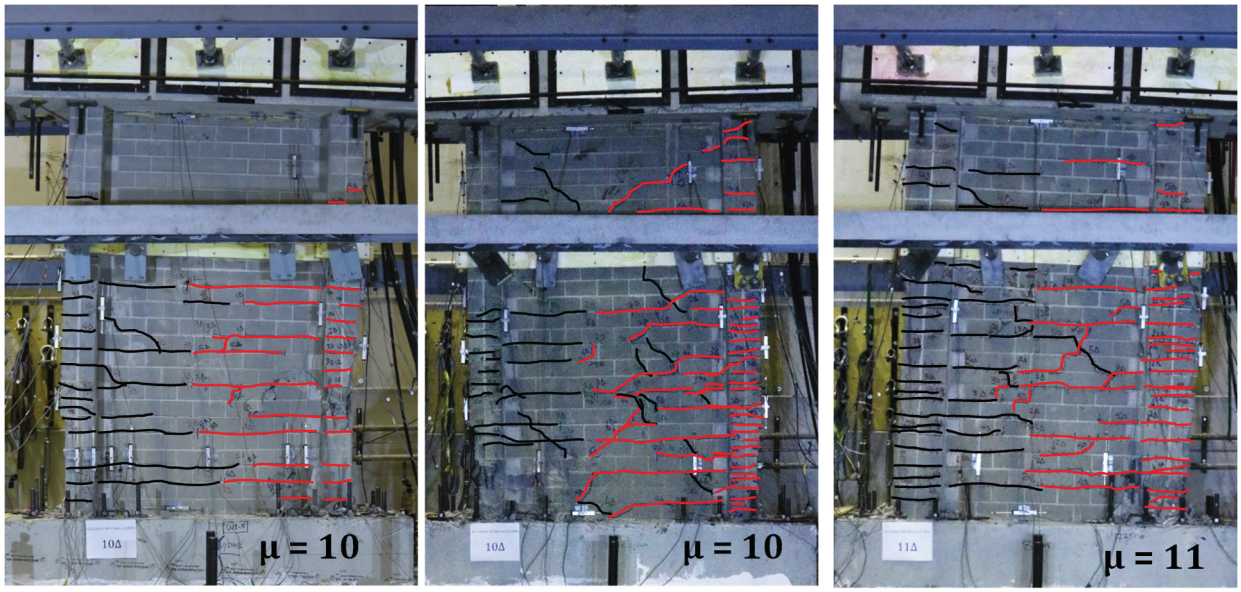

(a) (b) (c)

Figure 3.10 Damage and crack pattern: (a) wall W7-C_4^{190}; (b) wall W8-C_8^{190}; and (c) wall W9-C_8^{290}

Vertical cracking in the boundary elements was initiated at a lateral displacement corresponding to $6\Delta_y$ for walls W7-C_4^{190} and W9-C_8^{290}, whereas for wall W8-C_8^{190} it started at $7\Delta_y$. Following the initiation of the vertical cracks, the face-shell of the boundary elements' blocks started to spall in the subsequent loading cycles. However, the spalling of the face-shell had almost no impact on the lateral resistance of the walls. It occurred in wall W7-C_4^{190} after the lateral displacement of $6\Delta_y$ and resulted in a negligible (less than 2%) degradation in lateral capacity. Conversely, walls W8-C_8^{190} and W9-C_8^{290} continued to have a hardening post-peak response even after the spalling of the face-shell of the boundary elements' blocks. This is due to the enhanced detailing of the compression zones of walls W8-C_8^{190} and W9-C_8^{290}. As shown in Figure 3.10, majority of the cracking and damage was confined in the first-floor in specimen W7-C_4^{190}, while walls W8-C_8^{190} and W9-C_8^{290} had few more diagonal and horizontal cracks present on the top floor. This reflects that the height of the tested specimen was enough to represent the plastic hinge region where all inelastic deformations and damage are expected to concentrate.

3.4.4 Displacement ductility

Table 3.3 summarizes the measured and idealized displacement ductility values for the tested specimens at peak load and ultimate displacement. The measured displacement ductility at peak load (μ_{Qu}) was calculated as the ratio between the lateral displacement corresponding to the lateral

capacity (Δ_{Qu}) and the lateral displacement at the onset of the first yield (Δ_y) in the outermost vertical rebars. Likewise, the measured ultimate displacement ductility (μ_u) was calculated as the ratio between the lateral displacement corresponding to either 20% strength degradation or the loss of the wall load-carrying capacity (Δ_u) and the lateral displacement at the onset of the first yield (Δ_y) in the outermost vertical rebars. As shown in Table 3.3, the three walls were capable of attaining high displacement ductility values. The displacement ductility values measured at peak load (μ_{Qu}) ranged between 8.7 and 9.9. Additionally, the displacement ductility measured at ultimate displacement (μ_u) ranged between 10.0 and 10.8. Wall W9-C_8^{290}, which had the largest confined end zone, had the highest displacement ductility, measured at ultimate displacement, of 10.8.

Table 3.3 Summary of measured and idealized ductility values

	Measured		**Idealized - (Tomaževič, 1999)**		**Idealized - (Priestley et al., 2007)**	
Specimen	μ_{Qu}	μ_u	μ_{Qu}^{id}	μ_u^{id}	μ_{Qu}^{id}	μ_u^{id}
W7-C_4^{190}	9.9	10.1	8.0	8.2	7.8	8.0
W8-C_8^{190}	9.7	10.0	7.9	8.2	7.6	7.9
W9-C_8^{290}	8.7	10.8	7.2	8.9	7.0	8.6

The average load-displacement envelopes were idealized following two approaches to evaluate the idealized yield displacement and idealized displacement ductility. The first approach is as proposed by Tomaževič (1999) to idealize the inelastic response to an equivalent elastic-plastic system by having equal areas (i.e. equal energy absorption) under the load-displacement envelopes. This is achieved by extending the elastic line through the experimental first yield point and calculating an idealized lateral resistance ensuring that the area under the idealized bilinear curve is equal to the area under the actual load-displacement envelope. Figure 3.11 presents the average experimental and idealized, as suggested by Tomaževič (1999), load-displacement response curves for the three specimens. On average, the idealized lateral resistance was 3% lower than the experimentally measured peak load. Thus, the idealized ultimate secant stiffness was similar to the experimental values, and the ratio between idealized ultimate and yield secant stiffness values was 0.12. The idealized displacement ductility at ultimate displacement (μ_u^{id}), shown in Table 3.3, was 8.2 for walls W7-C_4^{190} and W8-C_8^{190}, and 8.9 for wall W9-C_8^{290}, which had the largest boundary element.

The second load-displacement idealization method was based on the recommendation of Priestley et al. (2007). This approach is based on a slightly more conservative estimate of the idealized yield displacement. The method assumes an idealized yield displacement at the intersection of a line extending from the origin having a slope equal to the initial secant stiffness at the first yield with a line tangent to the ultimate load. This approach resulted in marginally lower ductility values at ultimate displacement (μ_u^{id}) ranging between 8.0 and 8.6. It is interesting to highlight that the tested walls had comparable ductility values at peak loads (μ_{Qu}^{id}) and ultimate displacements (μ_u^{id}), whether idealized or average experimental values. This is attributed to the post-peak hardening response of the walls. Previously tested RM shear walls with boundary elements by Banting and El-Dakhakhni, (2012), (2014); and Shedid et al., (2010a), had a substantial difference between idealized ductility values at lateral resistance and ultimate displacement. This was because these walls utilized stretcher blocks in constructing the boundary elements, which limited the spacing of hoops to the standard height of the blocks. Besides, the confined concrete grout core was not uniform due to the presence of the webs of the stretcher blocks. Furthermore, in the walls reported in this study, the small difference between the response at peak load and ultimate displacement is due to the increased contribution from the flexure mechanism compared to the previously tested walls.

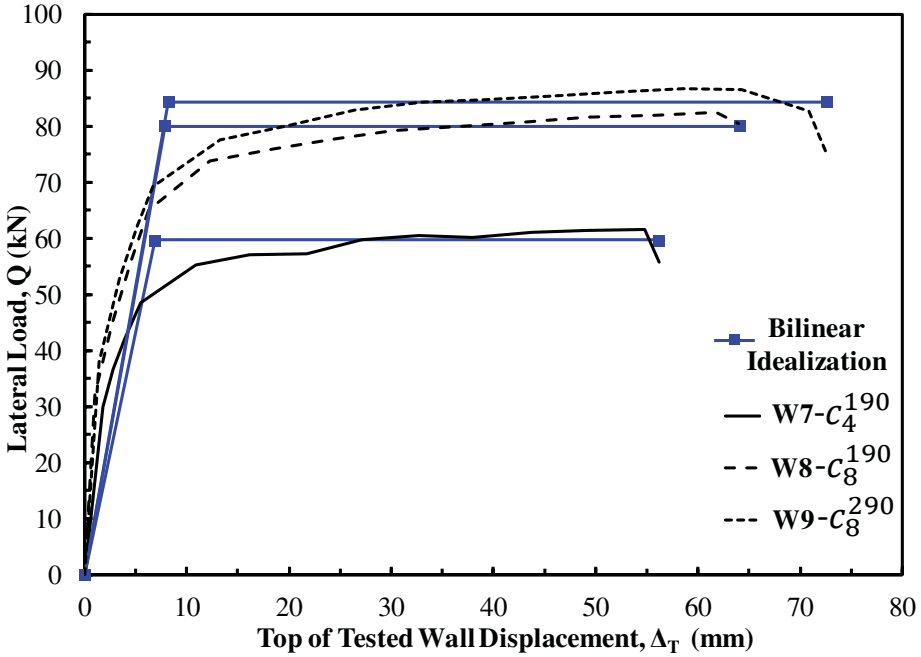

Figure 3.11 Average and elastic-plastic idealized lateral load-displacement envelopes

As a result, quantifying the ductility-related response modification factor (R_d) of the tested walls at either the peak load, prior to any degradation in strength, or at ultimate displacement would yield relatively high values. The ductility-related response modification factor (R_d) is calculated as the idealized displacement ductility, assuming the equal displacement concept applies. The increase in the boundary elements' vertical reinforcement did not affect the value of R_d, while there was an 8% increase when the confined grout core was larger (i.e. wall W9-C_8^{290} compared to W8-C_8^{190}). Consequently, increasing the size of the confined end zones (i.e. boundary elements) was relatively effective in enhancing the component ductility capacity. Based on the idealization of load-displacement response according to Tomaževič (1999), the average R_d would be 7.7 at peak load and 8.4 at ultimate displacement. The average R_d of previously tested RM shear walls with boundary elements constructed using the stretcher blocks (Banting and El-Dakhakhni, 2012, 2014; and Shedid et al., 2010a) was 3.9 and 6.9, at peak load and 20% strength degradation, respectively. Moreover, in the walls tested by Banting and El-Dakhakhni (2012), increasing the axial pre-compression ratio (P/f'_mA_g) from 3.3% to 9.8% resulted in reducing the calculated R_d by 47% (from 8.7 to 4.7). Thus, there is a significant enhancement in the structural performance of RM shear walls having end confined boundary elements built using the C-shaped blocks, compared to the use of the stretcher blocks. This is because the higher R_d would result in reduced seismic design forces and hence more optimized designs.

3.4.5 Failure mechanism

Although the three specimens were tested under high axial compressive stress, the walls achieved relatively high displacement ductility and failed in a flexural mode. Figure 3.12 depicts the final damage states of the three walls' boundary elements. Besides, Table 3.4 summarizes the lateral displacements corresponding to the main damage states. Walls W7-C_4^{190} and W8-C_8^{190} failed at a lateral displacement corresponding to $10\Delta_y$ due to substantial crushing in the boundary elements' grout core and buckling of several vertical rebars. Specimen W9-C_8^{290} reached the failure criteria at the lateral displacement level of $11\Delta_y$ due to fracture of vertical rebars caused by low-cycle fatigue and followed by substantial crushing in the grout core. The repeated buckling of the vertical rebars softened its material, reduced its fatigue life, and resulted in its fracture (Kunnath and Brown, 2004). In the three specimens, the crushing extended to the wall web, causing the buckling of the first vertical rebar in the web and resulting in loss of the load-carrying capacity.

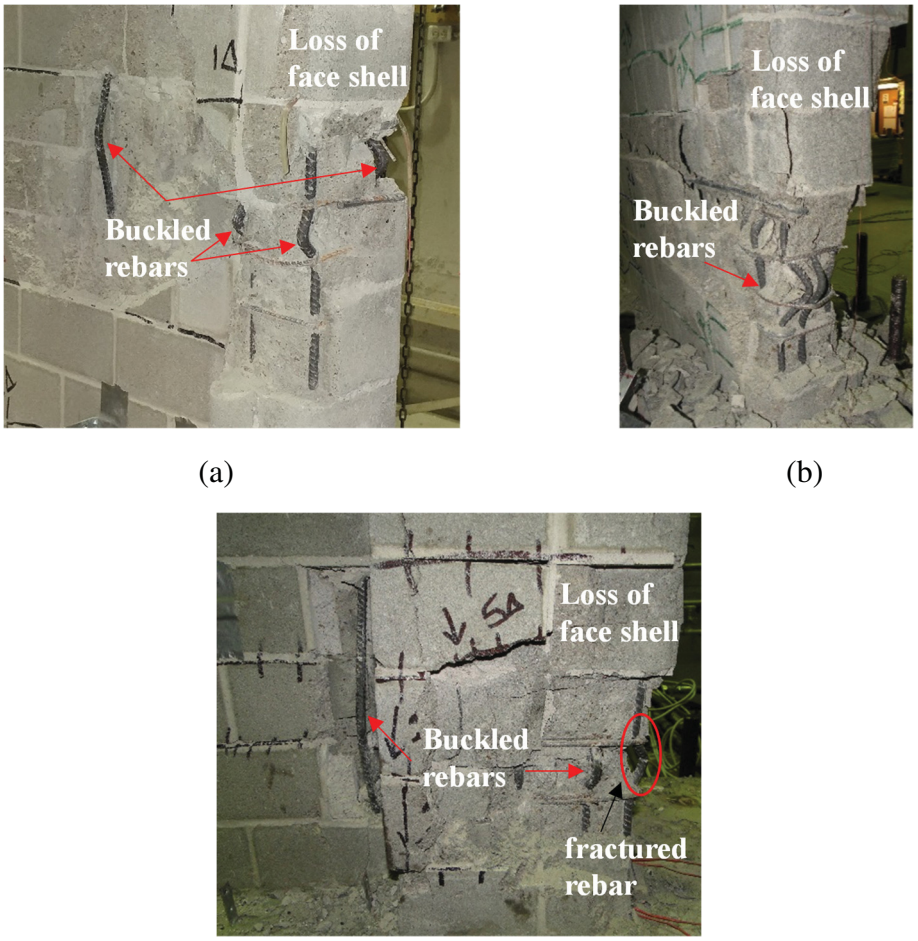

Figure 3.12 Boundary elements' final damage states: (a) wall W7-C_4^{190} at 10Δ_y; (b) wall W8-C_8^{190} at 10Δ_y; and (c) wall W9-C_8^{290} at 11Δ_y

Table 3.4 Summary of lateral displacements at different damage states

Specimen	Lateral Displacement (Top of Tested Wall Drift)		
	First horizontal crack in boundary elements' blocks	Face-shell spalling	Buckling/Fracture of rebars
W7-C_4^{190}	4Δ_y (0.94%)	6Δ_y (1.41%)	10Δ_y (2.35%)
W8-C_8^{190}	2Δ_y (0.54%)	7Δ_y (1.88%)	10Δ_y (2.68%)
W9-C_8^{290}	2Δ_y (0.57%)	7Δ_y (1.98%)	11Δ_y (3.11%)

3.4.6 Strains and curvatures

Using LVDTs L1-L2, L3-L4, and L5-L6 which were mounted on the extreme ends of the walls over a gauge length of 340 mm, 680 mm, and 1020 mm, respectively as previously shown in Figure 3.4(b), vertical deformations were measured. The measured vertical deformations were then used to estimate the average vertical compressive strains in the masonry extreme fibres (ε_m). Figure 3.13

presents the relations between the average masonry compressive strain (ε_m), average lateral force, and displacement ductility. It can be seen in Figure 3.13(a) that the three walls reached, without any strength degradation, compressive strain values that are much higher than the CSA S304-14 and TMS 402/602-16 specified maximum usable strain value, which is 0.0025 mm/mm. This observation is consistent for the three considered gauge lengths, which on average showed similar trends for the three walls.

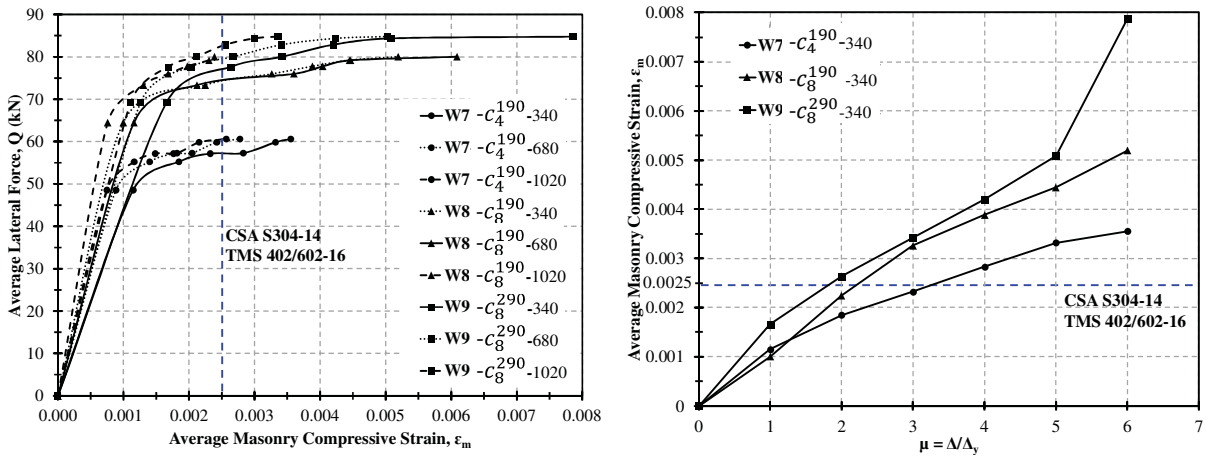

(a) (b)

Figure 3.13 (a) Average lateral force versus average masonry compressive strain; (b) average masonry compressive strain versus displacement ductility

It should be noted that the values shown in Figure 3.13 are the maximum values that were possible to measure and not the actual masonry crushing strain. This is because the LVDTs were attached to the face-shell of the boundary elements' blocks which typically spalled before the crushing of the grout core. Figure 3.13(b) illustrates the relationship between the average masonry compressive strain, measured over a gauge length of 340 mm, and the displacement ductility level. Wall W9-C_8^{290} with the largest confined grout core was capable of reaching higher compressive strains, at all ductility levels, compared to walls W7-C_4^{190} and W8-C_8^{190}. Similarly, the increased vertical reinforcement in the boundary elements of wall W8-C_8^{190} resulted in an increase in the attained compressive strains compared to wall W7-C_4^{190}. At the displacement ductility value of 6, the average measured compressive strain of wall W9-C_8^{290} was approximately 1.5 and 2.2 times that of walls W8-C_8^{190} and W7-C_4^{190}, respectively. It is worth noting that the sudden increase in the compressive strain of wall W9-C_8^{290} is possibly due to the initiation of the face-shell spalling and the sudden increase in the contribution of its confined grout core, which was larger than that

of the other two walls. Likewise, the average measured compressive strain of wall W8-C_8^{190} was 1.46 times that of wall W7-C_4^{190} at the ductility level of 6. Thus, increasing the boundary element's vertical reinforcement and the size of confined grout core were both influential in enhancing the ultimate masonry compressive strain and mitigating the impact of the high axial compressive stress.

Vertical deformations were measured on both sides of the walls over six segments using the twelve externally attached LVDTs. Then, the measured deformations were used to calculate the average vertical compressive (ε_m) and tensile (ε_s) strains. The average curvature (φ_i) was estimated over each of the six segments by dividing the sum of compressive and tensile strains measured on both sides of each segment by the wall's length (l_w), as shown in Eq. (3.1).

$$\varphi_i = \frac{\varepsilon_m + \varepsilon_s}{l_w} \tag{1}$$

The average curvature profiles of the three walls are presented in Figure 3.14. The curvature profiles are only shown up to the lateral displacement corresponding to $7\Delta_y$ due to the spalling of the blocks' face-shell, which resulted in losing the LVDT and discontinuation of measurements. It is evident that the three walls reached high curvature values without any substantial degradation in strength up to the displacement ductility value of 7. At the first yield, the average curvature (φ_y), over the first 340 mm segment, was similar for the three specimens. Wall W9-C_8^{290} had the highest average curvature value at yield (φ_y) of 2.88 (rad/mm x 10^{-6}), while the yield curvature of walls W7-C_4^{190} and W8-C_8^{190} was 2.49 and 2.61 (rad/mm x 10^{-6}), respectively. At a ductility factor of 5, the average measured curvature ductility over the first 340 mm segment was 32% higher for walls W8-C_8^{190} and W9-C_8^{290} compared to wall W7-C_4^{190}. The curvature ductility, calculated as the ratio between the measured curvature at a displacement ductility factor of 6 and the curvature at the first yield was 5.75, 6.80, and 7.19 for walls W7-C_4^{190}, W8-C_8^{190}, and W9-C_8^{290}, respectively. Consequently, there was a clear enhancement in the inelastic rotational capacity associated with the increase in the boundary elements' vertical reinforcement (W8-C_8^{190}) and size (W9-C_8^{290}).

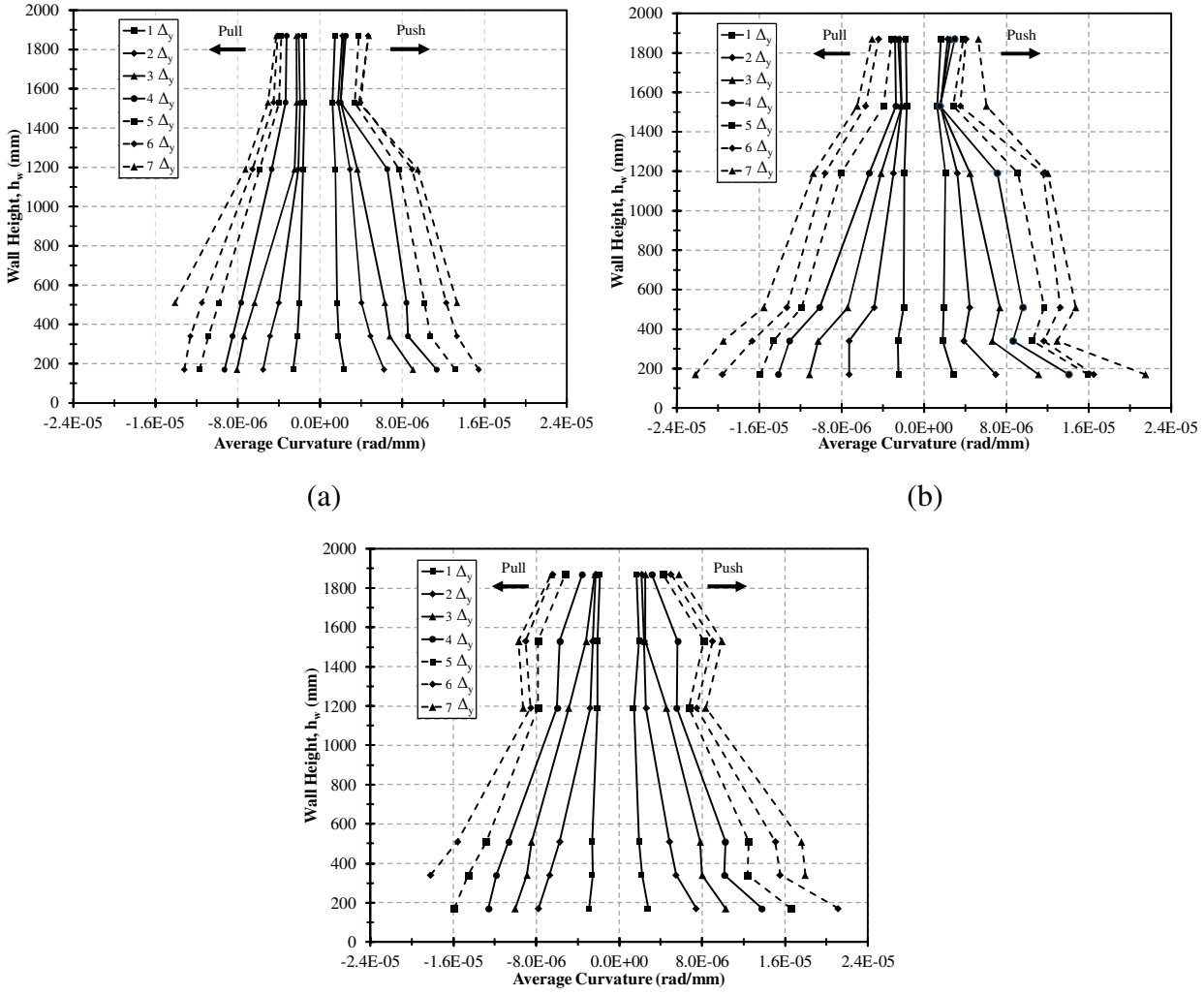

Figure 3.14 Average curvature profiles: (a) wall W7-C_4^{190}; (b) wall W8-C_8^{190}*;* and (c) wall W9-C_8^{290}

3.4.7 Energy dissipation capacity

The hysteretic energy dissipation capacity of structural components is typically quantified as the area inside the hysteresis loops. For the three tested specimens, Figure 3.15 is showing the dissipated hysteretic energy with respect to increasing displacement ductility levels. The dissipated energy values shown in Figure 3.15 were calculated as the area enclosed by the first hysteresis loop at each lateral displacement level. At the first yield, the three specimens had comparable energy dissipation capacities. With increasing lateral displacements, the energy dissipation capacity was linearly increasing, but with a much higher rate for walls W8-C_8^{190} and W9-C_8^{290}. Increasing the boundary elements' vertical reinforcement and size were both effective in improving the energy dissipation capacity. Walls W8-C_8^{190} and W9-C_8^{290} were capable of

dissipating significantly higher amounts of energy compared to wall W7-C_4^{190}, at all ductility levels. For instance, at the ductility factor of 6, the amount of energy dissipated by walls W8-C_8^{190} and W9-C_8^{290} was 1.9 and 2.0 times, respectively, higher than that of wall W7-C_4^{190}.

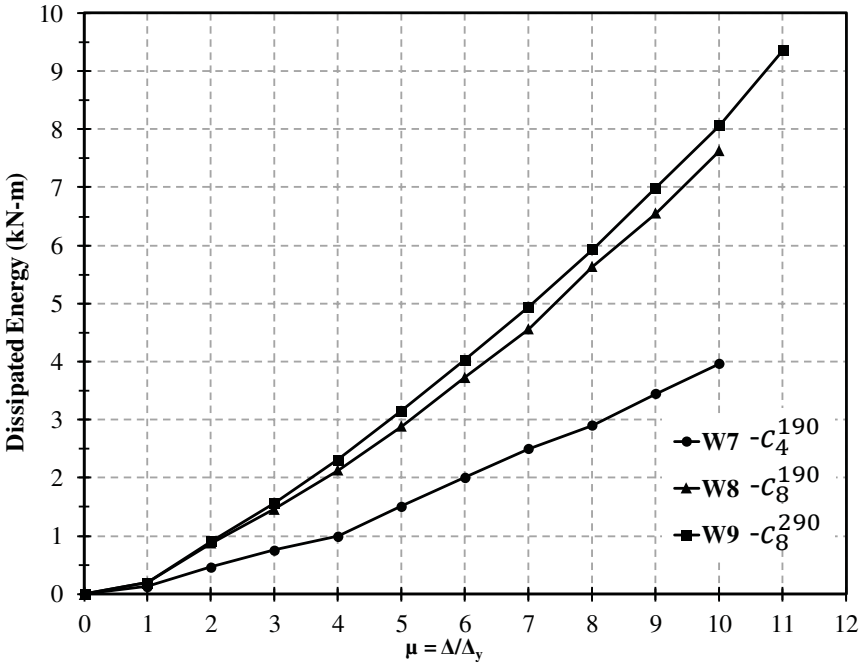

Figure 3.15 Energy dissipation capacity

The high axial compressive load on the test specimens is expected to limit their energy dissipation capacity. To quantify this effect, the energy dissipated by each specimen was compared to the input energy exerted by the three actuators. The energy dissipated ($E_{dissipated}$) was calculated as the area enclosed by the first hysteresis loop in each loading cycle, while the input energy (E_{input}) was calculated as the area under the skeleton of each loop as illustrated in Figure 3.16(a). The energy dissipation ratio was calculated as the ratio between $E_{dissipated}$ and E_{input} both calculated in the first cycle of loading at each imposed lateral displacement. Figure 3.16(b) shows the increase in energy dissipation ratios for the three specimens with the progression of loading history. The energy dissipation ratios are also summarized in Table 3.5. Overall, the three walls had reasonably high energy dissipation capacities reflecting the ability of detailing and confining the compression zones on mitigating the high axial load effects. Specimen W8-C_8^{190} had the highest energy dissipation ratios over the entire loading history because of the increase in its concentrated vertical reinforcement ratio compared to walls W7-C_4^{190} and W9-C_8^{290}. However, wall W9-C_8^{290} was able

to attain the highest energy dissipation ratio of 0.89 due to its increased boundary element length, which allowed the wall to undergo an additional loading cycle (i.e. μ = 11).

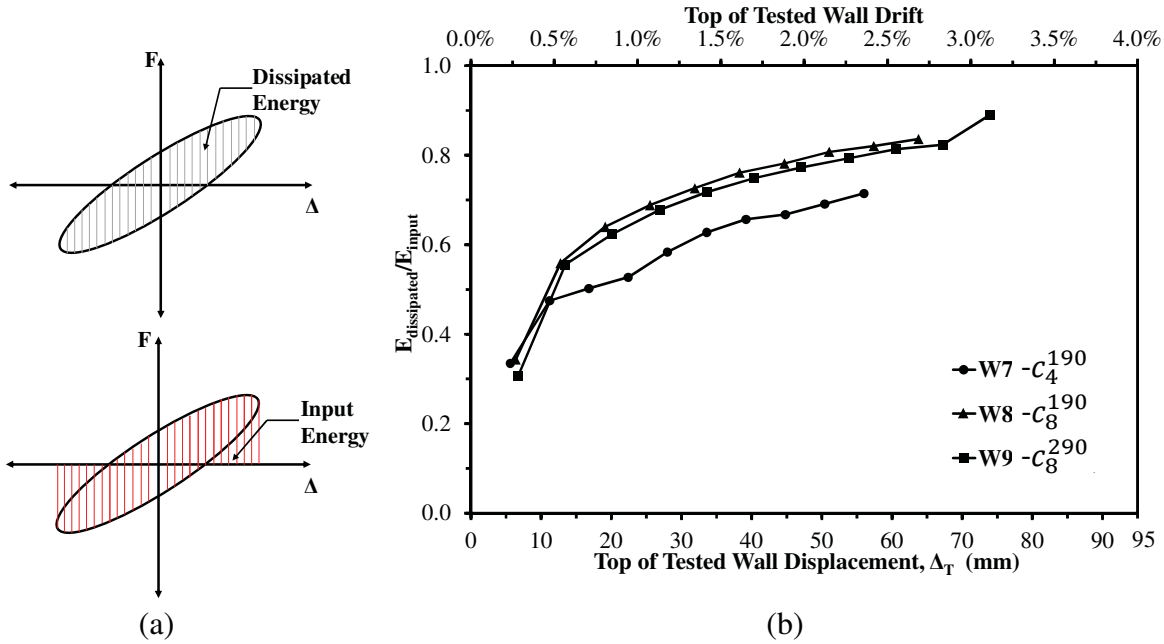

(a) (b)

Figure 3.16 (a) Evaluation of dissipated energy and input energy in one loading cycle; (b) Energy dissipation ratio with respect to top displacement

Table 3.5 Summary of energy dissipation and equivalent viscous damping ratios

	Energy Dissipation ($E_{dissipated}/E_{input}$)			**Equivalent Viscous Damping (ξ_{eq})**		
Lateral Displacement	**W7-C_4^{190}**	**W8-C_8^{190}**	**W9-C_8^{290}**	**W7-C_4^{190}**	**W8-C_8^{190}**	**W9-C_8^{290}**
$1\Delta_y$	33%	34%	31%	7.6%	7.5%	6.5%
$2\Delta_y$	47%	56%	56%	12.2%	15.5%	14.1%
$3\Delta_y$	50%	64%	62%	13.0%	16.5%	15.9%
$4\Delta_y$	53%	69%	68%	12.7%	17.7%	16.8%
$5\Delta_y$	58%	73%	72%	14.8%	19.2%	18.0%
$6\Delta_y$	63%	76%	75%	16.1%	20.2%	19.5%
$7\Delta_y$	66%	78%	77%	17.4%	21.0%	20.1%
$8\Delta_y$	67%	81%	79%	17.3%	22.4%	20.9%
$9\Delta_y$	69%	82%	81%	18.2%	22.7%	21.9%
$10\Delta_y$	71%	84%	82%	18.6%	23.8%	23.1%
$11\Delta_y$	-	-	89%	-	-	25.4%

3.4.8 Equivalent viscous damping

Quantification of the equivalent viscous damping (ξ_{eq}) of structural systems is crucial within the context of displacement-based designs. It is composed of elastic viscous damping (ξ_{el}) and hysteretic damping (ξ_{hyst}). Priestley et al. (2007) suggested a value of 5% for the elastic viscous damping (ξ_{el}) of RM buildings. The hysteretic damping (ξ_{hyst}) is evaluated experimentally using

the load-displacement hysteresis loops from quasi-static cyclic load tests. In this study, the approach proposed by Chopra (2007), given in Eq. (3.3), was used to evaluate the equivalent viscous damping (ξ_{eq}) by relating it to the ratio of the energy dissipated in a single hysteresis loop (E_D) and the elastic strain energy (E_s) calculated at the peak displacement of that loop.

$$\xi_{eq} = \xi_{el} + \xi_{hyst} \tag{3.2}$$

$$\xi_{eq} = \frac{1}{4\pi}\frac{E_D}{E_S} \tag{3.3}$$

Figure 3.17 shows the equivalent viscous damping of the three walls with respect to top displacements and displacement ductility. The three walls had increasing damping ratios with the increase in lateral drifts, especially after the yielding of vertical reinforcement. A trend similar to energy dissipation ratios is seen. At the first yield, the three specimens had similar damping ratios. However, at higher displacements and corresponding ductility levels, wall W8-C_8^{190} had the highest damping ratios.

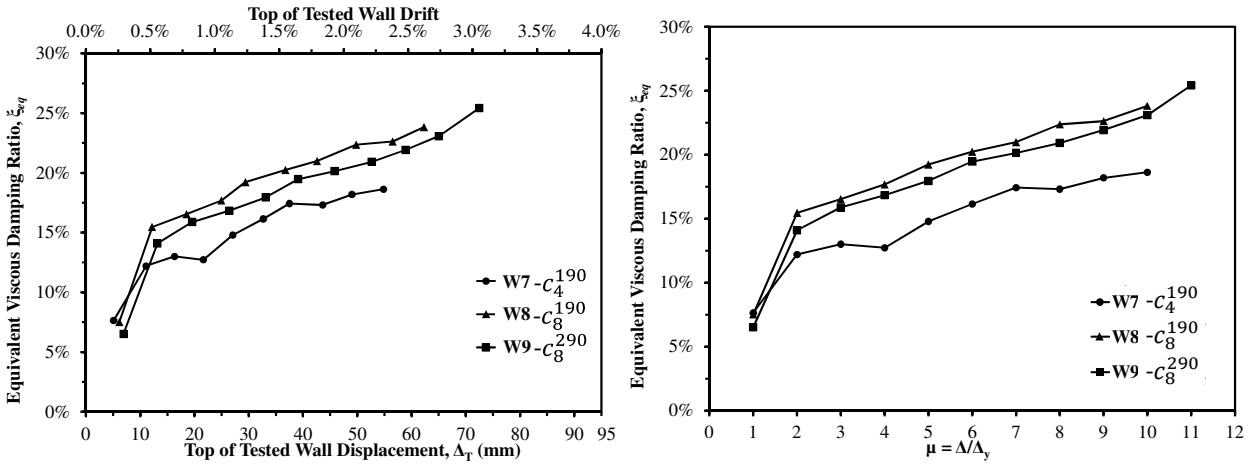

Figure 3.17 Equivalent viscous damping with respect to: (a) top displacement; and (b) displacement ductility

3.4.9 Lateral stiffness degradation

The high axial compressive load on the walls increases the initial stiffness and the rate of stiffness degradation. The degradation in the lateral stiffness of test walls was evaluated based on effective secant stiffness (K_e), which is also an essential parameter in the displacement-based design context. The average secant stiffness (K_e) at a loading cycle was calculated using Eq. (3.4)

as the slope of the line passing through the origin and intersecting with the hysteresis loop at the maximum (Q_{max}, Δ_{min}) and minimum peaks (Q_{min}, Δ_{min}).

$$K_e = \frac{Q_{max} - Q_{min}}{\Delta_{max} - \Delta_{min}} \tag{3.4}$$

The average secant stiffness at each loading cycle is normalized by the initial secant stiffness (K_i), calculated at 25% of Δ_y, and by the stiffness at yield displacement (K_y). The trends of normalized stiffness, K_e/K_i and K_e/K_y, of the tested specimens in dependence on top of the tested wall displacements and drifts, are illustrated in Figure 3.18. In general, there is a similar overall trend in the stiffness degradation of the three walls.

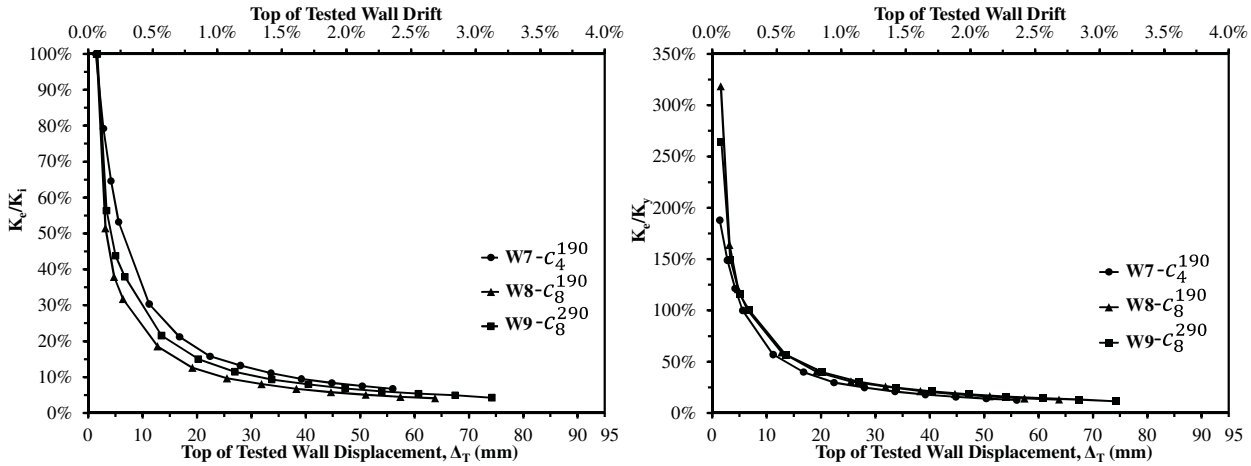

Figure 3.18 Lateral stiffness degradation: (a) effective stiffness normalized by initial stiffness; and (b) effective stiffness normalized by yield stiffness

The initial stiffness is highest for wall W8-C_8^{190} with the increased concentrated vertical reinforcement in the boundary elements and lowest for wall W7-C_4^{190}. The degradation in lateral stiffness was much steeper at initial loading stages. The initial stiffness (K_i), measured at 25% of the yield displacement (Δ_y), dropped by 47% at the first yield of W7-C_4^{190} (0.24% top of tested wall drift), 68% at the first yield of W8-C_8^{190} (0.27% top of tested wall drift), and 62% at the first yield of W9-C_8^{290} (0.28% top of tested wall drift). This confirms previous research findings (e.g. Banting and El-Dakhakhni, 2012) that axial load is a key parameter in the estimation of initial and effective stiffness. The large drop in the lateral stiffness of the walls at initial loading stages reflects an elongation in the natural period of vibration and a reduction in the attracted lateral force. Thus, it indicates an enhancement in structural performance associated with the improved boundary

elements' detailing. At higher lateral displacements, there was mild degradation in stiffness for the three walls indicating lesser elongation in the natural periods.

3.4.10 Residual displacements

The increase in the axial compression loads enhances the self-centring characteristics of the walls and reduces the residual displacements. The residual displacements indicate the level of structural damage and reflect the energy dissipation capacity of ductile structures. In this study, residual displacements were defined as the lateral displacements at the end of the first loading cycle corresponding to zero lateral force. They were estimated for the test specimens to evaluate the ability of detailing the end zones on maintaining the energy dissipation capacity under the high axial compressive load. Figure 3.19 presents the relations between the residual displacements, top lateral displacements, and ductility levels.

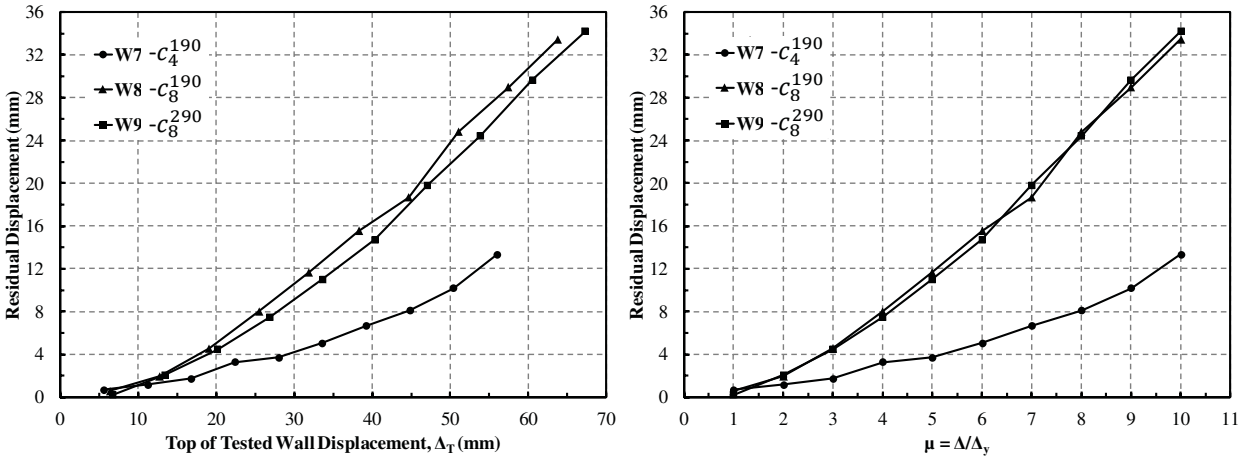

(a) (b)

Figure 3.19 Residual displacements in relation to: (a) top displacement; (b) displacement ductility

A similar relation of linearly increasing residual displacements with the increase in ductility levels is seen in the response of the three specimens. At yield, the three walls had negligible and similar values of residual displacements. At higher ductility levels, walls W8-C_8^{190} and W9-C_8^{290} sustained similar residual displacements that are much higher than those of wall W7-C_4^{190}. At failure, the residual displacements were 24%, 52%, and 51% of the total lateral displacement for walls W7-C_4^{190}, W8-C_8^{190}, and W9-C_8^{290}, respectively. Walls W8-C_8^{190} and W9-C_8^{290} were capable of sustaining higher residual displacements compared to wall W7-C_4^{190} due to the enhanced detailing in their end zones. The increased concentrated vertical reinforcement resulted in

increasing the energy dissipation capacity as higher number of rebars experienced more yielding (with buckling being delayed using the closely spaced hoops), which resulted in higher residual displacement as a by-product. This explains the increase in the energy dissipation capacity of walls W9-C_8^{290} and W8-C_8^{190} relative to W7-C_4^{190} and the trade-off in having a ductile response with fatter hysteresis loops. Therefore, the increase in the size of the confined grout core and boundary element's vertical reinforcement reduced the influence of the high axial load on the ductile response and energy absorption capacity.

3.5 Conclusions

The majority of previous studies focused on the response of rectangular low- to mid-rise RM shear walls. There is a limited number of tested RM shear walls with boundary elements. In addition, most of the previously tested RM walls with boundary elements were low-rise, subjected to low axial pre-compression ratios, less than 10%, and had limited confinement in the end zones due to the use of the standard concrete masonry stretcher blocks. Consequently, this paper presented an experimental investigation of the cyclic response of three high-rise fully grouted RM shear walls with boundary elements tested to failure under pseudo-static cyclic loading and a high constant axial compressive load. The walls were subjected to normalized axial stress ratios higher than 10%. The tested specimens were half-scale shear walls representing the plastic hinge region of typical walls in a 12-storey prototype building. The walls varied in the boundary elements' size (i.e. confined grout core size) and boundary element's vertical reinforcement. The experimental testing focused on assessing the ability of sufficiently detailing the compression zones to alleviate the impact of the high axial load on the walls' structural performance. Thus, the tested walls were designed to have enlarged boundary elements that were built using C-shaped concrete masonry blocks to overcome the limitations of the previous studies. The walls were constructed by the same certified mason using the same materials to minimize the influence of materials' variability on the findings. The following observations and conclusions are drawn based on the testing results:

1- It is recommended to use C-shaped masonry blocks to construct the wall's boundary elements. This would provide more design options to enhance the seismic detailing of the end zones.
2- To increase the lateral resistance of the walls, it is suggested to increase the concentrated vertical reinforcement in the boundary element. This would also increase the energy

dissipation capacity. Using the C-shaped blocks, it is possible to have different arrangements for the concentrated vertical reinforcement.

3- Increasing the size of the confined grout (i.e. boundary elements) mitigates the adverse effects of the high axial load and improves the displacement ductility.
4- The enhanced detailing in the end zones (increasing concentrated reinforcement and size of confined boundary elements) increased the ultimate masonry compressive strain and reduced the depth of the compression zone. As a result, the section's curvature ductility was improved, and the ultimate displacement capacity was increased. Besides, more rebars exhibited significant yielding, which increased the energy dissipation capacity and resulted in higher residual displacement.
5- The high axial load increased the rate of stiffness degradation of the test specimens. This confirms previous research findings that axial load is a key parameter in the estimation of initial and effective stiffness.
6- RM shear walls with boundary elements utilizing the suggested detailing enhancements are a potential competitive seismic force resisting system. The tested walls had an average ductility-related response modification factor (R_d) of 7.7 at peak load and 8.4 at ultimate displacement.

In closing, the presented results demonstrate the enhanced component-level structural performance of RM shear walls having enlarged boundary elements built using C-shaped blocks. It indicates the increased competitiveness of masonry buildings as an alternative construction method when utilizing this type of walls. More testing is still required to quantify and establish more confidence in its structural performance, considering a different and broader range of design parameters. Additionally, evaluating the system-level structural performance when utilizing the proposed RM shear walls with boundary elements is essential.

Chapter 4

In-Plane Cyclic Response of High-Rise Reinforced Concrete Masonry Structural Walls with Boundary Elements

4.1 Abstract

The majority of tested Reinforced Concrete Masonry (RCM) shear walls with boundary elements represented walls in low- to mid-rise buildings. In addition, these tested walls had continuous vertical reinforcement with no lap splices, which is impractical in multi-storey masonry buildings. Therefore, this study aims to evaluate the structural performance of high-rise RCM structural walls with boundary elements under reversed cyclic loading simulating seismic actions. This is achieved by constructing and testing four half-scale fully grouted RCM shear walls with boundary elements under constant axial load and quasi-static reversed cyclic loading. The walls were designed and constructed with similar geometry and material properties and were tested under the same level of axial compressive stress. The studied parameters are the wall's shear span-to-depth ratio, the type of boundary elements' masonry blocks (stretcher or C-shaped), and the lap splicing of vertical reinforcement in the plastic hinge region. The objective is to quantify the cyclic response of ductile RCM shear walls and to provide experimental evidence of its reliable structural performance for higher aspect ratios. Furthermore, the present study investigates the impact of the presence of lap splices in the plastic hinge region on the ductile response of high-rise RCM walls with boundary elements. The tested walls had an enhanced cyclic response due to its end zone confinement. The testing results demonstrated that the shear span significantly influences the distribution and layout of cracks, the lateral stiffness and resistance, and the post-peak response. Using the C-shaped blocks instead of the regular stretcher blocks in constructing the boundary elements enhanced the construction and performance of the walls. Lap splicing of vertical rebars increased the initial lateral stiffness, resulted in a higher rate of stiffness and strength degradation, and slightly limited the ultimate displacement ductility. However, with proper detailing of the splice and confinement of the end zones, the premature tensile bond failure was prevented.

4.2 Introduction

Reinforced Concrete Masonry (RCM) is a competitive alternative construction material for buildings. It features relatively rapid construction with reasonably built-in soundproofing and fire insulation characteristics. The most common Seismic Force Resisting System (SFRS) in masonry buildings is RCM structural walls. Significant research efforts have been performed in the past decade to enhance the structural performance of RCM shear walls. These research efforts were translated into the addition of the ductile RCM shear walls in the 2015 edition of the National Building Code of Canada (NBCC-15), which were given a higher ductility-related response modification factor (R_d) of 3. The Canadian masonry design standard (i.e. CSA S304-14) assigned special design and detailing requirements to the ductile walls to ensure its stable ductile response and to qualify for the higher R_d. In RCM shear walls, the ductile response can be achieved by integrating confined masonry boundary elements to the ends of the rectangular walls. Several research studies (Aly and Galal, 2019a, 2019b, 2019c) demonstrated the enhanced system-level performance of masonry buildings utilizing ductile RCM shear walls with boundary elements as the SFRS in a proposed hybrid structural system.

Previous experimental studies of RCM shear walls with boundary elements highlighted that there was a substantial enhancement in the overall seismic performance when end confinement was utilized. For instance, Shedid et al. (2010a) emphasized that there was a considerable improvement in the inelastic response of end-confined RCM shear walls compared to their rectangular counterparts. The displacement ductility of the walls with confined boundary elements was 106% higher than that of the rectangular walls. Similarly, the results of the quasi-static reversed cyclic testing by Banting and El-Dakhakhni (2012) confirmed that the presence of confinement in the boundary elements significantly enhanced the post-peak response of the walls. The considered parameters were the presence of inter-storey slabs, the continuation of boundary elements above the first-floor, and the level of axial loads. The results of that experimental study were used to establish the force- and displacement-based seismic performance parameters of RCM shear walls with boundary elements. It was demonstrated that boundary elements with two layers of vertical reinforcement and transverse reinforcement for confinement significantly improved the post-peak response. This was due to its ability to delay vertical rebars buckling and to provide confinement to the grout core. Thus, the masonry blocks face-shell spalling and vertical cracking did not result in a significant drop in strength. Failure of tested walls occurred mostly due to the

crushing of compression toes and fracture of vertical rebars at high drift ratios ranging between 2.4% and 3.7% for the different walls.

Banting and El-Dakhakhni (2014) also tested five half-scale RCM walls with boundary elements having varying heights, lengths, and vertical reinforcement ratios to establish the impact of boundary elements' confinement and provide prescriptive design requirements. Based on their experimental results, it was concluded that the force-based response of the walls was highly dependent on the horizontal extent of boundary elements. Additionally, the increase in the walls' aspect ratios resulted in increasing the experimentally measured plastic hinge length, curvature ductility, and displacement ductility. The results also suggested that an increase in vertical reinforcement ratio would adversely affect the displacement ductility of the wall. Furthermore, it was recommended to account for the shear deformations in the design, as it had a significant contribution to the walls' structural response.

Ahmadi et al. (2014) tested 30 fully grouted RCM shear walls under reversed cyclic loading as part of a research project to develop guidelines for the displacement-based seismic design of masonry buildings. They aimed to establish the trends between essential design parameters, such as aspect ratio, axial load level, vertical reinforcement ratio and configuration, and lap splices on the nonlinear load-displacement response of the walls. The researchers considered five aspect ratios ranging from 0.78 to 4.5, six axial load levels (0, 5%, 6.25%, 10%, 12.5% and 15% of gross compressive strength), different arrangements and ratios of vertical reinforcement, presence of lap splices in vertical reinforcement, and the use of green masonry blocks. The dimensions and reinforcement details of the tested walls were selected to result in a flexural dominant response. The selected axial load levels represented common values in typical masonry shear wall buildings. The researchers noted that, on average, the measured lateral resistance of the walls was 1.22 times the nominal capacity estimated using the provisions of the 2011 edition of the Masonry Standards Joint Committee (MSJC). This was close to the 1.25 factor used in capacity design to calculate the probable resistance. The ratio between the measured lateral capacity and estimated nominal resistance marginally decreased with the increase in axial load. However, there was no apparent impact from neither the aspect ratio nor the ratio of vertical reinforcement. It was concluded that the decrease in aspect ratio increases the initial stiffness, flexural capacity and the rate of strength degradation. Conversely, it decreases the ultimate drift capacity of the walls. Likewise, based on

their experimental results, it was indicated that the presence of lap splices in the vertical reinforcement adversely influenced the hysteretic response of the RCM walls. It increased the initial stiffness, reduced the lateral displacement at failure, and resulted in higher rate of strength deterioration. Furthermore, it reduced the energy dissipation capacity and caused more pinching in the hysteretic response. It also reduced the inelastic curvature and the plastic hinge length of the walls. Therefore, Ahmadi et al. (2014) suggested that more testing might be required to investigate the influence of lap splices on the response of RCM shear walls considering more design variables.

Nine RCM shear walls with varying lap splice lengths, bar sizes, and reinforcement arrangements were tested by Mjelde et al. (2009) under displacement-controlled reversed cyclic loading until failure. The tested specimens were fully grouted full-scale walls with an aspect ratio of 1.76 and were constructed in a running bond pattern. The objective was to evaluate the performance of splices in RCM under representative loading conditions and to verify the provisions of the 2005 edition of MSJC. The test results indicated that the lap splice failure caused a sudden longitudinal splitting in the masonry walls and resulted in a substantial drop in the resistance. It was also observed that lap splices with length equal to 48 times the longitudinal bar diameter (d_b) performed adequately when the rebars were in the centre of the masonry block cell, and horizontal reinforcement was provided. Offsetting the longitudinal bars in the cells adversely affected the performance even when longer splice lengths were used, up to $60d_b$. Thus, the researchers concluded that the lap splice design provisions should include guidelines for the cover. Besides, it was highlighted that MSJC-05 lap splice provisions were capable of predicting the performance of the lap splice of bars with small diameters and were excessively conservative for the larger diameters.

It can be seen that previous testing of RCM shear walls with confined boundary elements demonstrated their potential as a competitive SFRS for masonry buildings. However, the majority of tested walls were 2- to 3-storey high with continuous vertical reinforcement and were subjected to low or moderate axial compressive load levels. Therefore, there is a need for more testing to evaluate the in-plane cyclic response of this type of RCM shear walls, especially with higher aspect ratios and considering the effect of lap splicing the vertical reinforcement in the plastic hinge region. Lap splicing of vertical rebars is unavoidable in RCM shear walls due to the practical limitations involved with placing the blocks over the long continuous vertical rebars. There is

minimal evidence on the response of RCM shear walls with boundary elements having spliced vertical rebars as all existing studies were based on continuous reinforcement. Consequently, the actual performance of these walls will differ from the one observed during testing. Aaleti et al. (2013) highlighted that the presence of lap splices in plastic hinge regions would typically concentrate significant inelastic strains below and above the lap splice. Thus, it reduces the extent of plasticity and limits the plastic hinge rotational, ductility, and energy dissipation capacities.

4.3 Test Program

The experimental program reported in this study aims to quantify the in-plane cyclic response of high-rise RCM shear walls with boundary elements. It is part of a research project at Concordia University designed to develop innovative and resilient RCM structural systems.

4.3.1 Test specimens

The specimens of this study were selected to fill the currently existing research gap in the literature. In the previous studies (Banting and El-Dakhakhni, 2012, 2014; and Shedid et al., 2010a), most of tested RCM shear walls with boundary elements represented low to mid-rise walls, were tested under axial compressive stress values less than 10% of masonry gross compressive strength, had boundary elements built using the standard stretcher blocks, and had continuous vertical reinforcement. Consequently, the test walls investigate the effects of the shear span-to-depth ratio (*M/Vd*), the type of boundary elements' masonry blocks (stretcher or C-shaped), and the lap splicing of vertical rebars in the plastic hinge zone. In addition, the walls are high- and mid-rise and were tested under an axial compressive stress of 2.25 MPa to result in pre-compression ratios higher than 10%, based on the gross cross-sectional area. The characteristics of the walls are summarized in Table 4.1, and the walls' dimensions and reinforcement details are shown in Figure 4.1. The walls are designated with a unified ID that is based on the sequence of testing at Concordia University. Besides, the specimens are assigned an ID that reflects the studied parameter in this paper. For example, wall W10 is designated with $P^{4}_{M/Vd}$, which indicates that this wall has a shear span-to-depth ratio (*M/Vd*) of 4.4. The shear span-to-depth ratio was calculated using the effective height (h_{eff}), which was taken as two-third of the full specimen height based on the assumed triangular lateral load distribution. Similarly, wall W11 is given the ID of $P^{Stret.}_{BE}$ reflecting that this wall evaluates the impact of the type of masonry blocks used in the boundary elements and was built using stretcher (Stret.) blocks. Specimen W12 has the ID of $P^{Lap}_{V.Rft}$ to assess the impact

of lap splicing the vertical reinforcement in the plastic hinge region. Wall W7 is the reference (Ref) specimen and is used to investigate the effects of the varied parameters. The four specimens had the same wall length (l_w), web thickness, boundary element dimensions, and reinforcement ratios, as presented in Table 4.1.

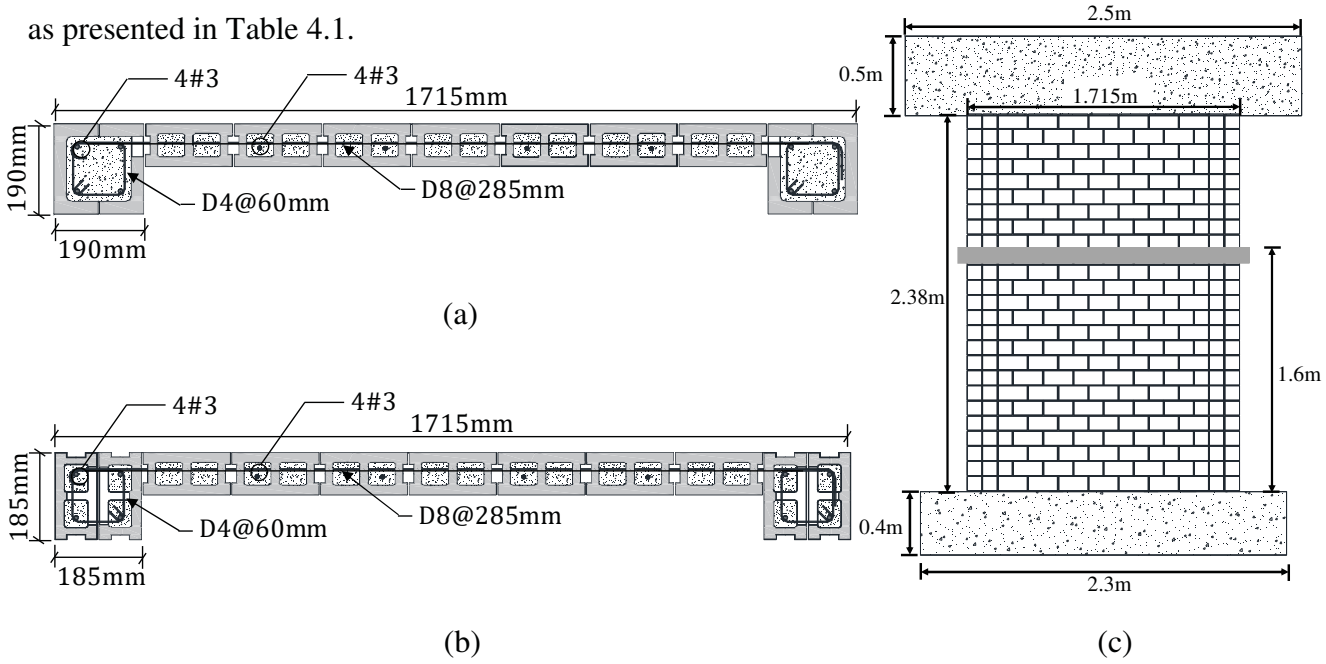

Figure 4.1 Test walls' dimensions and reinforcement details: (a) cross-section of walls W7- Ref, W10-$P^{4}_{M/Vd}$ and W12-$P^{Lap}_{V.Rft}$; (b) cross-section of wall W11-$P^{Stret.}_{BE}$; and (c) elevation view

The test specimens were slender walls designed to be flexural dominant. Moreover, the tested walls were half-scale fully grouted RCM shear walls representing the plastic hinge regions of 12-storey and 6-storey RCM structural walls with boundary elements. The full-scale heights were 36.2 m and 18.2 m for the 12-storey and 6-storey walls, which correspond to 18.1 m and 9.1 m half-scale heights, respectively. This was based on an assumed first-floor height of 3.2 m and a typical floor height of 3.0 m. The height of the tested (h_{tested}) specimens was 2.38 m, which represents an approximate upper-bound estimate of the plastic hinge height based on the detailing requirements of CSA S304-14 for the ductile walls. In addition, the walls had the first-floor located at 1.6 m from the bottom footing. The slab of the first-floor was represented by attaching Polytetrafluoroethylene (PTFE) sheets to the back and front sides of the wall. The 12-storey and 6-storey walls had effective height-to-length ratios (h_{eff}/l_w) equal to 7 and 3.5, respectively. Furthermore, the 12-storey walls (W7-Ref, W11-$P^{Stret.}_{BE}$, and W12-$P^{Lap}_{V.Rft}$) had a shear span-to-depth ratio (*M/Vd*) of 8.8, whereas the shear span-to-depth ratio (*M/Vd*) of the 6-stoery wall (W10-$P^{4}_{M/Vd}$) was 4.4.

Table 4.1 Characteristics of tested walls

Unified ID*	Wall Length (mm)	Common Parameters								Axial Stress (MPa)	Studied Parameters			
		Web			Boundary Element						Studied Parameter ID**	M/Vd***	Boundary Element Blocks	Vertical bars
		Thickness (mm)	Vertical bars	Horizontal bars	Length (mm)	Width (mm)	Vertical bars	ρ_v (%)	Confinement					
W7	1715	90	4#3	D8@285mm	190	190	4#3	0.79	D4@60mm	2.25	Ref	8.8	C-shaped	Continuous
W10	1715	90	4#3	D8@285mm	190	190	4#3	0.79	D4@60mm	2.25	$P^{4}_{M/Vd}$	4.4	C-shaped	Continuous
W11	1715	90	4#3	D8@285mm	185	185	4#3	0.83	D4@60mm	2.25	$P^{Stret.}_{BE}$	8.8	Stretcher	Continuous
W12	1715	90	4#3	D8@285mm	190	190	4#3	0.79	D4@60mm	2.25	$P^{Lap}_{V.Rft}$	8.8	C-shaped	Lap Splice

* Based on the wall ID tested at Concordia University
** Based on the parameters studied in this paper
*** $d = 0.8l_w$

The walls were designed and detailed according to the requirements of CSA S304-14 and TMS 406/602-16 for ductile and special walls, respectively. Additionally, the specimens were constructed by the same certified mason using materials with similar mechanical properties. The web region of the walls was constructed using half-scale depressed stretcher concrete blocks, Figure 4.2(a), and was reinforced vertically using four No. 3 (diameter = 9.525 mm and area = 71 mm^2) bars and horizontally using D8 (diameter = 8.11 mm and area = 51.61 mm^2) deformed wires spaced at 285 mm, as was shown in Figure 4.1(a) and (b). Additional D8-180° hooks were provided in the masonry courses with no continuous horizontal reinforcement to increase the shear flow resistance at the interface between the wall's web and boundary elements. The end details of the horizontal reinforcement followed the requirements of CSA S304-14. The continuous D8 wires had one end with 90° standard hook and the other end with 180° hook, while the additional D8 wires had standard 180° hooks. The web blocks were laid in a running bond pattern using 5 mm, half-scale of the typical 10 mm, mortar joints. The boundary elements of the walls, except wall W11-$P_{BE}^{Stret.}$, were built using C-shaped concrete masonry blocks that were cut to form the required dimensions, as illustrated in Figure 4.2(b).

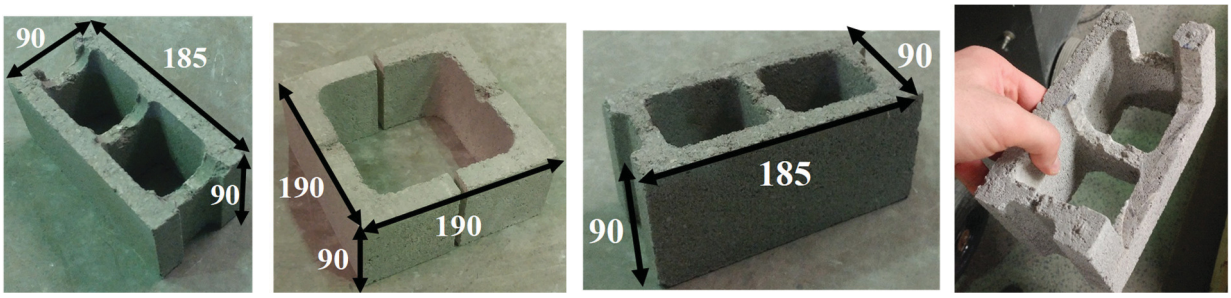

(a) (b) (c)

Figure 4.2 Half-scale concrete masonry units: (a) depressed stretcher blocks; (b) C-shaped blocks; and (c) standard and notched stretcher blocks (all dimensions are in millimetres)

The boundary element blocks were stack bonded using 5 mm mortar joints. The boundary elements of wall W11-$P_{BE}^{Stret.}$ were built using half-scale stretcher masonry blocks laid in a running bond pattern, with 5 mm mortar joints, to match the previously tested walls in the literature (Banting and El-Dakhakhni, 2012, 2014; and Shedid et al., 2010a). The mortar used in constructing the specimens was pre-bagged Type-S mortar. All boundary elements were reinforced vertically using four No. 3 rebars and confined with hoops of D4 (diameter = 5.73 mm and area = 25.8 mm^2) deformed wires spaced at 60 mm centre-to-centre. The provided area and spacing of hoops fulfilled

the buckling prevention requirements of CSA S304-14. In wall W11-$P_{BE}^{Stret.}$, the stretcher blocks used in constructing the boundary elements were depressed using the saw to allow placing the hoops at 60 mm. This was achieved by cutting the face-shell of one side and the middle web of the block, as shown in Figure 4.2(c). The construction process of the boundary elements of wall W11-$P_{BE}^{Stret.}$ was relatively challenging and more time consuming compared to the other walls. This was mainly because in this wall the hoops were installed during the construction, whereas for the other walls the boundary elements' steel cages were completed before placing the masonry blocks. Figure 4.3 shows the construction process of the first one-third of the test specimens. As can be seen, in wall W11-$P_{BE}^{Stret.}$ the hoops were fixed in every boundary elements' masonry course while the mason was placing the blocks. Conversely, in the other specimens which had C-shaped blocks in the boundary elements, it was possible to complete the steel cages before the wall construction.

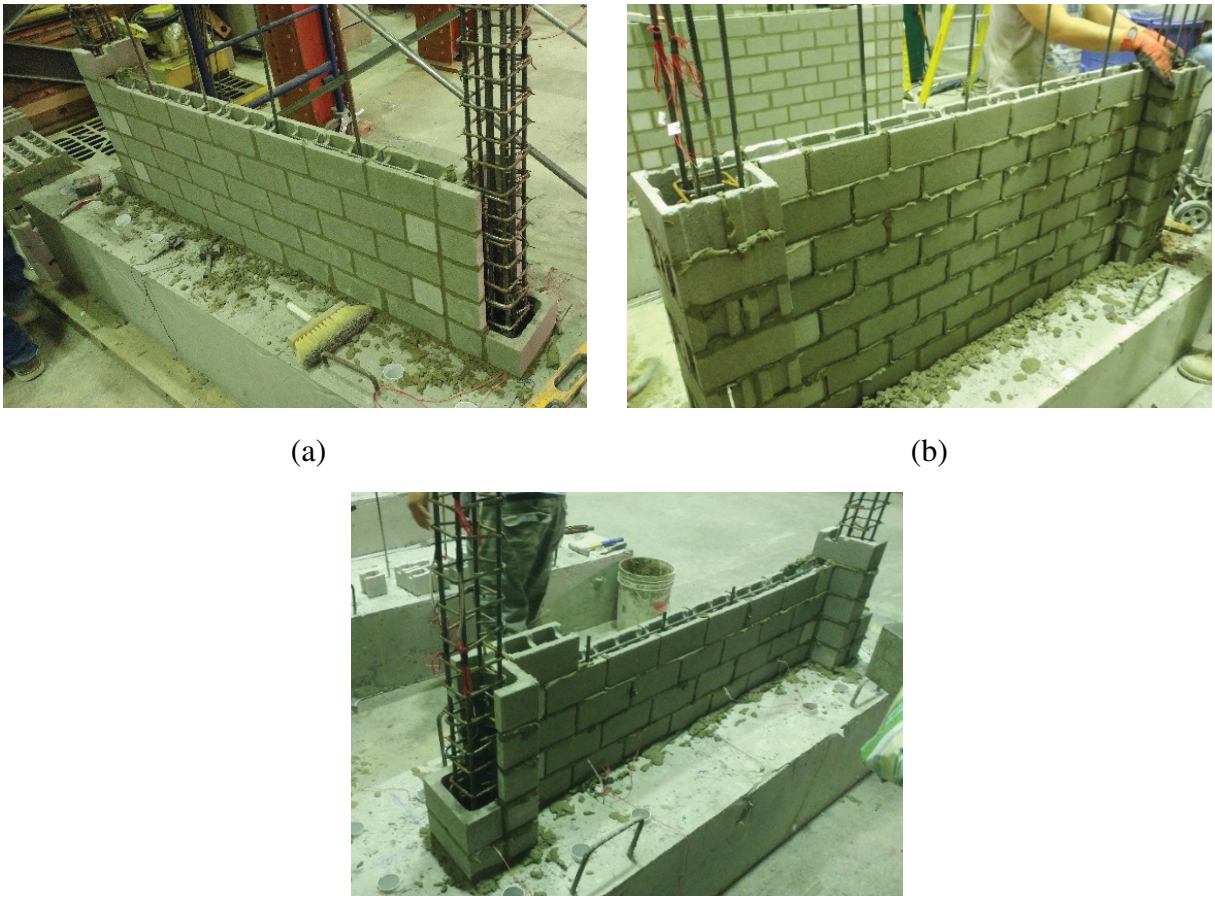

(a) (b)

(c)

Figure 4.3 Construction of first one-third: (a) wall W7- Ref and W10-$P_{M/Vd}^{4}$; (b) wall W11-$P_{BE}^{Stret.}$; and (c) wall W12-$P_{V.Rft}^{Lap}$

All walls were fully grouted using a high slump fine grout that was designed and mixed in the laboratory according to CSA A179-14. The webs were grouted using an ordinary strength grout, while for the boundary elements a high strength grout was used to enhance the axial compressive capacity of the walls and reduce the depth of the compression zone. The properties of the walls' top loading beam and bottom footing concrete, concrete masonry stretcher and C-shaped blocks, mortar, fine grout, masonry prisms, and steel reinforcement are summarized in Table 4.2. Wall W7-Ref was constructed in a different phase than the other walls. Consequently, some of its constituent materials had slightly different properties, as reported in Table 4.2. The deformed wires, D4 and D8, had no clear yield point and thus the yield strength (f_y) was defined at a strain of 0.2% as specified by ASTM A1064M-15.

The test walls, except W12-$P_{V.Rft}^{Lap}$, had continuous vertical reinforcement, as displayed in Figure 4.4(a). The vertical rebars were anchored with standard 90^o hooks in the top Reinforced Concrete (RC) loading beam and bottom RC footing. Specimen W12-$P_{V.Rft}^{Lap}$ had lap spliced vertical rebars in the web at the wall-foundation interface and in the boundary elements at the first-floor level, as shown in Figure 4.4(b). The locations of the splices were selected to enhance the construction process of this type of RCM shear walls. Splicing the web rebars at the foundation was necessary to ease placing the stretcher blocks, as illustrated in Figure 4.3(c). Nevertheless, in the boundary elements, it was possible to splice the rebars at the first-floor when the C-shaped blocks were used. This would potentially enhance the structural performance and minimize the possibility of bond failures in the extreme rebars. The lap splice was designed according to the provisions of CSA S304-14 and also met the requirements of TMS 402/602-16. In the plastic hinge region, CSA S304-14 clause 16.9.5.2 does not allow splicing more than 50% of the longitudinal reinforcement at any section. Additionally, CSA S304-14 clauses 16.8.5.5 and 16.9.5.5 require increasing the lap splice length by 1.5 in the plastic hinge region of moderately ductile and ductile walls, respectively. Accordingly, the lap splice length was taken as 1.5 times the calculated development length (l_d). Furthermore, as per clause 16.4.2, CSA S304-14 does not allow reducing the minimum lap length due to excess amount of flexural reinforcement, according to clause 12.4.2.6, when the reinforcement might yield due to seismic actions.

Table 4.2 Materials' properties

Material	Property	Value	No. of Samples	c.o.v*	Testing Standard
	Walls W10-$P^{4}_{M/Vd}$, W11-$P^{Stret.}_{BE}$ and W12-$P^{Lap}_{V.Rft}$				
Top beam concrete	Cylinder compressive strength, f_c	48.3 MPa	3	10.8%	ASTM C39M-15
Footing concrete	Cylinder compressive strength, f_c	41.0 MPa	3	4.8%	ASTM C39M-15
Boundary element C-shaped blocks	Compressive strength, f_b	27.6 MPa	4	5.6%	CSA A165-14 and ASTM C140-15
Boundary element stretcher blocks	Compressive strength, f_b	21.8 MPa	5	18.1%	CSA A165-14 and ASTM C140-15
Web stretcher blocks	Compressive strength, f_b	34.7 MPa	3	7.6%	CSA A165-14 and ASTM C140-15
Mortar cubes	Compressive strength, f_{mo}	15.1 MPa	10	16.6%	CSA A179-14 and ASTM C109M-13
Ordinary strength grout	Cylinder compressive strength, f_{gr}	31.0 MPa	7	11.1%	CSA A179-14
High strength grout	Cylinder compressive strength, f_{gr}	42.6 MPa	3	5.6%	CSA A179-14
Four-courses web blocks prisms	Masonry compressive strength, f_m	15.5 MPa	3	3.0%	CSA S304-14
	Specified compressive strength, f'_m	14.2 MPa			CSA S304-14
Four-courses boundary element (C-shaped blocks) prisms	Masonry compressive strength, f_m	27.2 MPa	3	16.0%	CSA S304-14
	Specified compressive strength, f'_m	17.3 MPa			CSA S304-14
Four-courses boundary element (stretcher blocks) prisms	Masonry compressive strength, f_m	13.5 MPa	5	11.0%	CSA S304-14
	Specified compressive strength, f'_m	9.4 MPa			CSA S304-14
D4 deformed wires	Yield strength, f_y	590 MPa	3	0.2%	ASTM A1064M-15
D8 deformed wires	Yield strength, f_y	535 MPa	3	1.7%	ASTM A1064M-15
No. 3 rebars	Yield strength, f_y	460 MPa	3	0.6%	ASTM A615M-15
	Ultimate strength, f_u	680 MPa	3	1.6%	ASTM A615M-15
	Wall W7-Ref				
Boundary element C-shaped blocks	Compressive strength, f_b	22.8 MPa	4	4.8%	CSA A165-14 and ASTM C140-15
Ordinary strength grout	Cylinder compressive strength, f_{gr}	31.3 MPa	9	9.5%	CSA A179-14
High strength grout	Cylinder compressive strength, f_{gr}	43.2 MPa	12	15.5%	CSA A179-14
Four-courses web blocks prisms	Masonry compressive strength, f_m	11.3 MPa	8	12.0%	CSA S304-14
	Specified compressive strength, f'_m	8.7 MPa			CSA S304-14
Four-courses boundary element (C-shaped blocks) prisms	Masonry compressive strength, f_m	25.5 MPa	5	8.0%	CSA S304-14
	Specified compressive strength, f'_m	19.0 MPa			CSA S304-14

* Coefficient of Variation

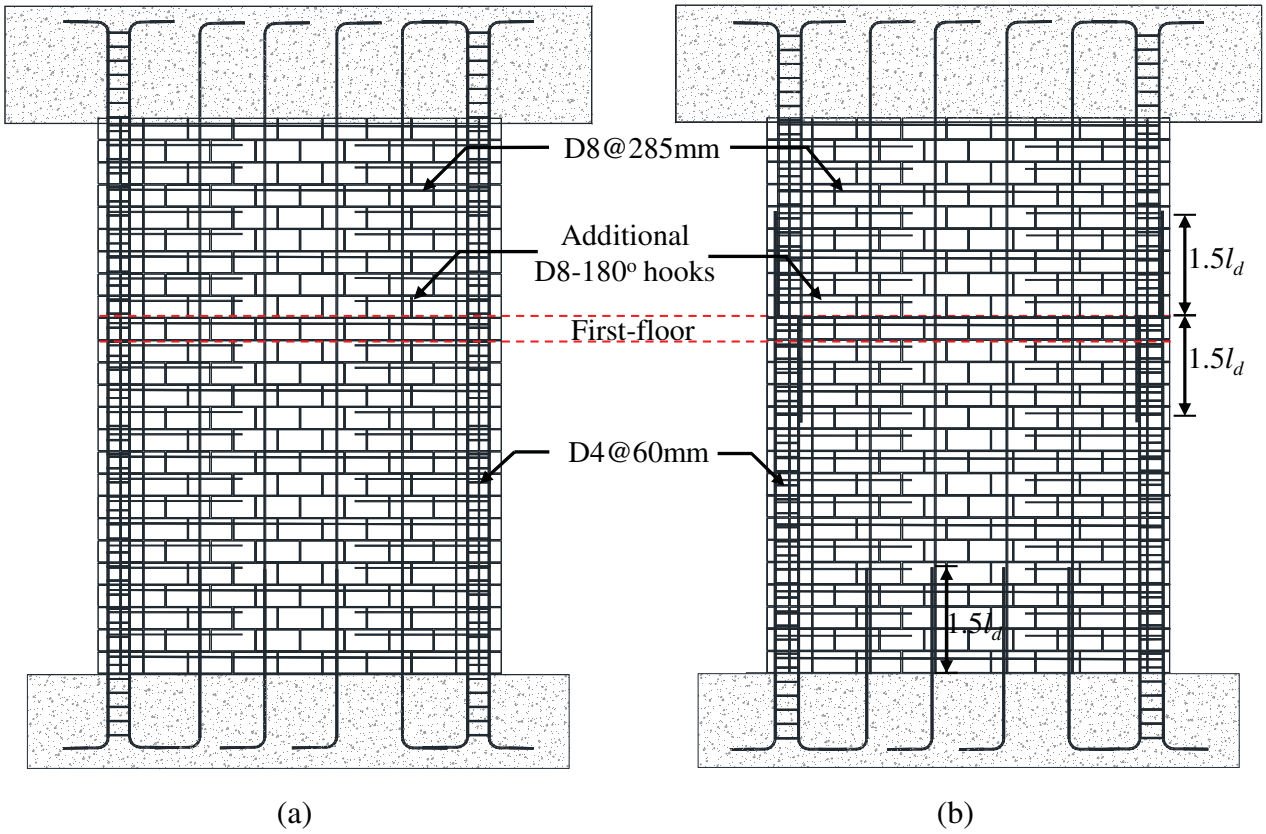

Figure 4.4 Elevation view of reinforcement details: (a) walls W7- Ref, W10-$P^{4}_{M/Vd}$, and W11-$P^{Stret.}_{BE}$; and (b) wall W12-$P^{Lap}_{V.Rft}$

4.3.2 Instrumentation

The response of the test walls was monitored using external and internal instrumentation. Externally, Linear Variable Displacement Transducers (LVDTs) and linear potentiometers were mounted on the test walls to measure the lateral, vertical, and diagonal deformations. As shown in Figure 4.5(a), the lateral displacements were measured using linear potentiometers P1-P4 and LVDT L27, which were attached to an independent reference frame. Potentiometers P1 and P2 were attached to the front and rear sides of the top loading beam, respectively. The applied displacement increments were calculated as the average of potentiometers' P1 and P2 readings and were corrected for any sliding displacements measured by potentiometer P5. The vertical deformations were measured using LVDTs L1-L12, which were attached to the walls ends, as displayed in Figure 4.5(a). Furthermore, LVDTs L20-L26 along with L14 and L17 were used to establish the horizontal strain gradients along the walls' length. LVDTs L16 and L14/L17 were used to monitor the uplift at the test walls' interfaces with the top loading beam and bottom footing, correspondingly. Likewise, the uplift between the walls' footings and the testing frame's transfer

footing was checked using the readings of potentiometers P6 and P7. Moreover, the sliding displacements, if any, between the specimen and top loading beam or bottom footing were measured using LVDTs L13 and L15, respectively. The slip displacements at the web and boundary elements interfaces were recorded using LVDTs L18 and L19. The linear potentiometers P8 and P9 were used to measure the diagonal shear displacements.

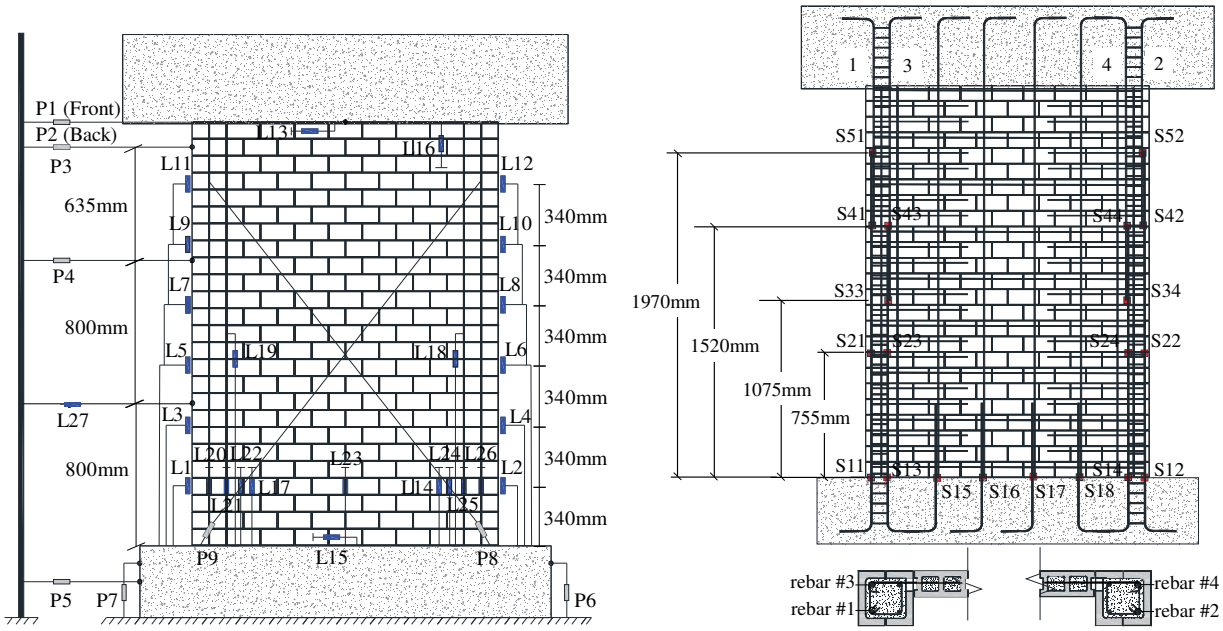

(a) (b)

Figure 4.5 Layout of instrumentation: (a) LVDTs and potentiometers (all walls); and (b) strain gauges of wall W12-$P^{Lap}_{V.Rft}$

Internally, a total of twenty 5-mm strain gauges were installed over the height of the four outermost vertical reinforcement in each specimen. Each of the four outermost rebars in the boundary elements of walls W7-Ref, W10-$P^{4}_{M/Vd}$, and W11-$P^{Stret.}_{BE}$ had five strain gauges attached at 40 mm into the bottom footing, at the wall-foundation interface, and over the height of the rebar. Wall W12-$P^{Lap}_{V.Rft}$ had the strain gauges mounted as indicated in Figure 4.5(b) to monitor the strains along the lap splice in the web and boundary elements. It should be noted that for the illustrative purposes of the strain gauges' locations, the rebars shown in the boundary elements in Figure 4.5(b) are the two outermost rebars. In addition to monitoring the local strains of the vertical rebars, the strain gauges were most importantly used to determine the yield load (Q_y) and displacement (Δ_y). The yielding point in each loading direction (i.e. push or pull) was defined as the point when

one of the strain gauges attached to the outermost vertical rebars at the wall-foundation interface reach the yield strain. A digital data acquisition system was used to record all measured forces, displacements, and strains.

4.3.3 Test setup and loading procedure

The walls were tested under constant axial compressive load, quasi-static reversed cyclic displacements, and top moment. As displayed in Figure 4.6, the testing setup consisted of a RC transfer footing post-tensioned to the strong floor of the laboratory, and three double acting hydraulic actuators attached to a steel reaction frame. Each specimen had a top RC loading beam and a bottom RC footing. The bottom footing was fixed to the testing frame's transfer footing using high-strength anchor bolts to represent a fixed boundary condition at the wall's base. The top loading beam was attached to the two vertical and the horizontal actuators while allowing the top rotations. As the tested specimens represented the plastic hinge regions of the walls, a top moment was applied along with the applied lateral displacements. The two vertical actuators were used to apply the axial compressive stress and top moments, whereas the lateral displacements were applied by the horizontal actuator. Out-of-plane displacements were restrained at the first-floor and the level of load application, as shown in Figure 4.6. Restraining the out-of-plane displacements at the first-floor was necessary to limit the height-to-thickness ratio of the test walls within the limits of CSA S304-14, clause 16. The slab of the first-floor was represented by attaching Polytetrafluoroethylene (PTFE) sheets to the back and front sides of the wall.

The walls were first loaded by the axial compressive stress, which simulated the service gravity loads and was kept constant throughout the test. This was achieved using the vertical actuators in a force-controlled mode. Subsequently, the lateral target displacements were applied to the test specimens by the horizontal actuator in a displacement-controlled mode. At each displacement increment, the measured lateral resistance was used to calculate the corresponding top moment to be applied as coupled forces by the vertical actuators in a force-control mode. The top moment was evaluated based on the difference between the height of the tested specimen and the effective height (h_{eff}) of the full wall. The lateral cyclic displacements' protocol followed the recommendations of the Federal Emergency Management Agency (FEMA 461, 2007) and the American Society for Testing and Materials (ASTM E2126, 2012). The loading protocol had two phases (pre- and post-yield) that consisted of fractions and increments of the first yield

displacement (Δ_y), respectively, as a representative damage state. In the pre-yield phase, the first yield displacement (Δ_y) was determined. This was accomplished by cycling the specimens to small target displacements that result in developing fractions (i.e. 25%, 50% and 75%) of the yield strain in the outermost vertical rebars located at the wall-footing interface. The displacements were gradually increased until the yield point was reached in both loading directions (i.e. push and pull). The experimental first yield displacement (Δ_y) was calculated as the average value of both directions.

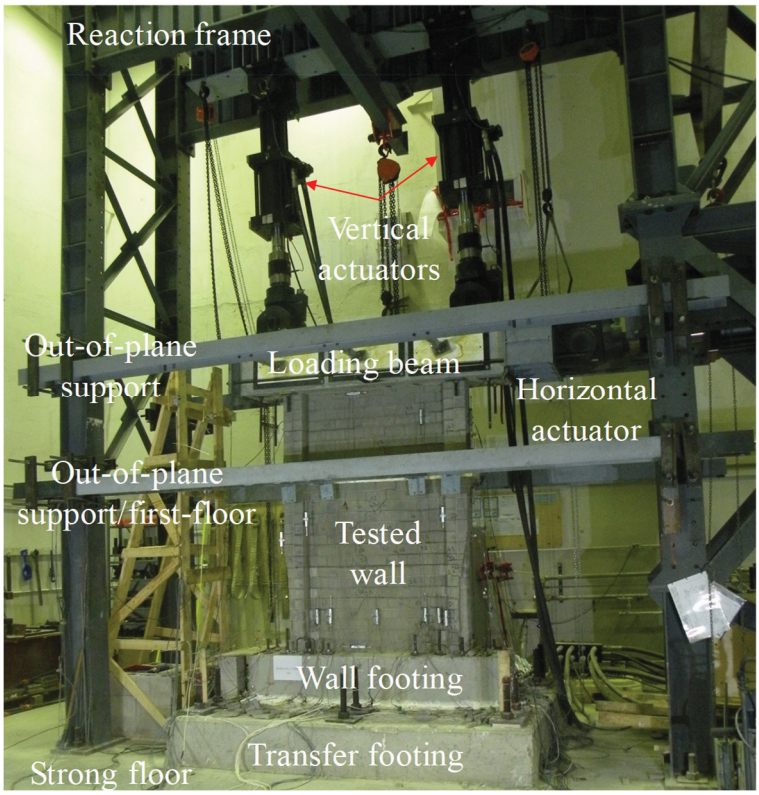

Figure 4.6 Testing setup

After that, in the post-yield phase, the target displacements were defined as multiples (i.e. 1, 2, 3, etc.) of the experimentally found first yield displacement (Δ_y). Besides, the post-yield displacements were fully reversed and were repeated twice to account for the strength and stiffness cyclic and in-cycle degradation. The post-peak response was captured by increasing the post-yield target displacements until the failure point was reached. In this study, the failure was defined as either a drop of more than 20% in the lateral resistance or the loss of the load-carrying capacity. The loss of the load-carrying capacity was reached when the walls lost the ability to resist the applied gravity loads. In testing the 6-storey wall, W10-$P^4_{M/Vd}$, the lower shear span-to-depth ratio

(M/Vd) was achieved by applying a lower top moment calculated based on the shorter effective height (h_{eff}) compared to that of the 12-storey walls.

4.4 Results and Discussion

The following subsections present and discuss the testing results of the four specimens. The focus is on evaluating the inelastic in-plane cyclic response of the walls. Additionally, the effects of the wall's shear span-to-depth ratio, the type of boundary elements' blocks, and the lap splicing of vertical rebars are quantified.

4.4.1 Hysteretic response and progression of damage

The hysteresis loops of the walls are given in Figure 4.7, and the average measured loads, curvatures, and displacements are summarized in Table 4.3. The lateral displacements are reported at two levels, at the first-floor (Δ_1) and the top of the tested wall (Δ_T). The Figure is also presenting the lateral resistance of the specimens along with the corresponding applied top moments. The measured lateral forces were corrected to include the horizontal force component applied by the vertical actuators. The walls had a symmetric cyclic response between the push and pull directions. The lateral loads and displacements at the first yield and the capacity were similar in both directions. The specimens had a flexural response seen in the yielding of outermost vertical reinforcing bars before the initiation of any diagonal or step cracks. Besides, the walls showed a ductile behaviour reflected in its ability to sustain large inelastic deformations without substantial loss of its load resisting capacity. This was also observed in the relatively wide hysteresis loops which reflected the high energy absorption capacity of the test walls.

Specimen W7-Ref had a lateral displacement, measured at the top of the tested wall, at first yield (Δ_y) of vertical reinforcement equal to 5.0 mm and -6.2 mm in the push and pull directions, respectively. This was corresponding to a lateral force (Q_y) of 48.78 kN and -48.34 kN, in the push and pull directions, respectively. At the first yield, there were few horizontal hairline cracks seen in the mortar bed joints. With the progression of loading history, the flexural cracks propagated horizontally with larger widths but remained in the mortar bed joints of the first-floor. At the lateral displacement level of $4\Delta_y$, horizontal cracking was initiated in the boundary elements' blocks. Furthermore, the first horizontal crack appeared in the bed joint above the first-floor's out-of-plane support level. More horizontal cracks occurred in the boundary elements' blocks and existing cracks propagated horizontally at the lateral displacement corresponding to $5\Delta_y$. In addition, the

first diagonal shear crack occurred at the lateral displacement level of $5\Delta_y$, and only a few shear cracks were observed afterwards until the failure of the specimen. Vertical cracks were initiated in the right boundary elements at $6\Delta_y$, and the face-shell of the blocks started spalling. At the lateral displacement of $7\Delta_y$, vertical cracking occurred in the left boundary element and the spalling of face-shell was initiated. Compression toes crushing along with vertical propagation of face-shell spalling were observed at the lateral displacement levels of at $8\Delta_y$ and $9\Delta_y$. While going to the lateral displacement corresponding to $10\Delta_y$, the wall reached its ultimate capacity of 62.55 kN and -60.86 kN in the push and pull directions, respectively. The wall had a hardening post-peak response. There was minor degradation in the lateral strength with the progression of the loading history until the failure of the specimen.

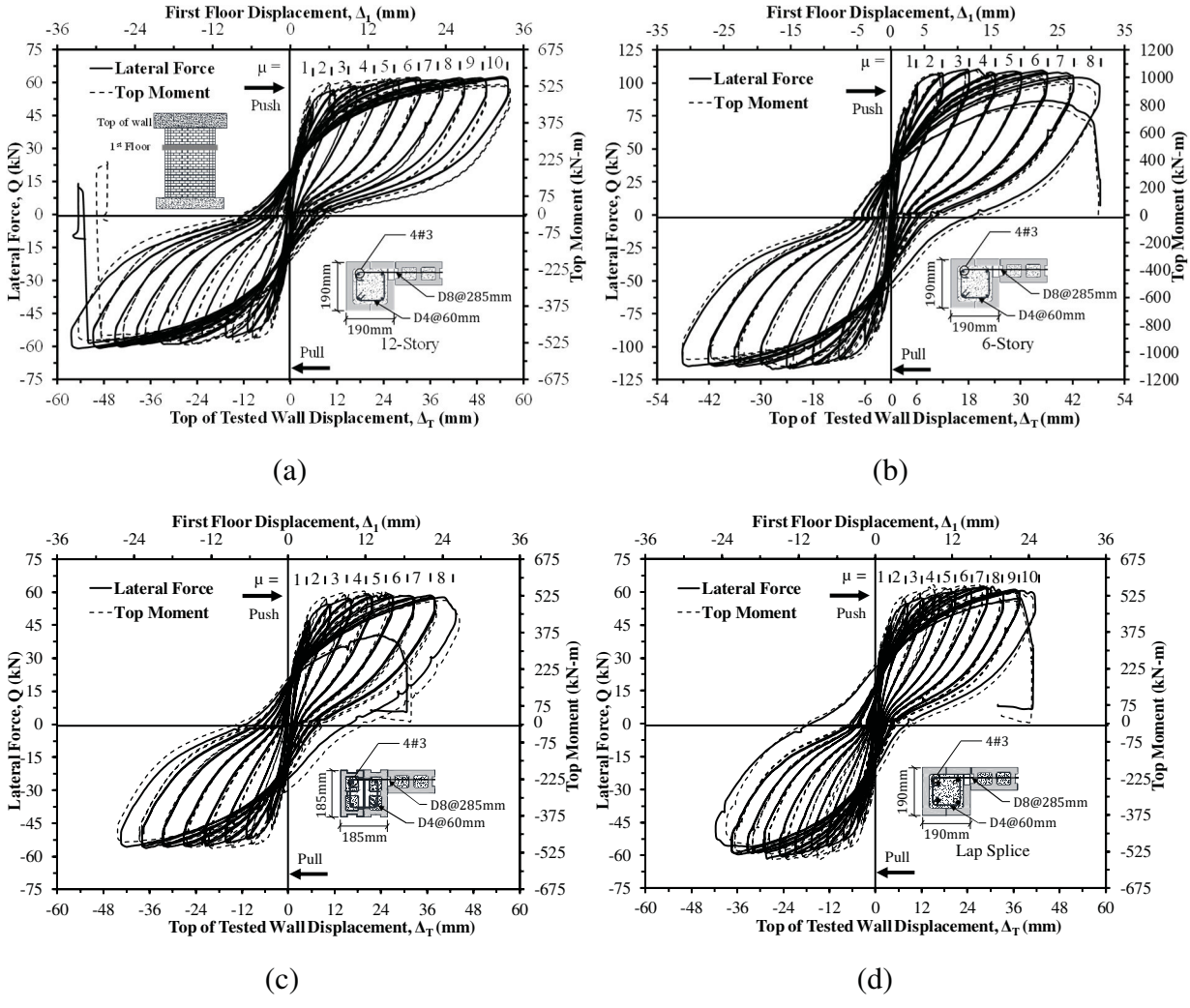

Figure 4.7 Load-displacement hysteresis loops: (a) wall W7- Ref; (b) wall W10-$P_{M/Vd}^{4}$; (c) wall W11-$P_{BE}^{Stret.}$; and (d) wall W12-$P_{V.Rft}^{Lap}$

The first yield in the outermost vertical reinforcement occurred in wall W10-$P^{4}_{M/Vd}$ at a lateral displacement (Δ_y), measured at the top of the tested wall, equal to ±6.0 mm in the push and pull directions. The lateral force at the first yield (Q_y) was 97.9 kN and -97.8 kN, in the push and pull directions, respectively. Few flexural cracks were seen in the mortar bed joints of the first-floor at the onset of the first yield. Besides, the first step crack in the mortar bed and head joints appeared at $1\Delta_y$. At the lateral displacement of $2\Delta_y$, there were longer horizontal cracks in the mortar bed joints and a larger step crack in the wall web. The first horizontal and diagonal cracks appeared above the first-floor at the lateral displacement of $3\Delta_y$. More flexural and shear cracks were observed with the incrementally increasing lateral displacements. At the peak of the lateral displacement of $4\Delta_y$, vertical cracks were initiated in the left boundary element. The wall also reached its ultimate resistance of 110.4 kN and -116.3 kN, in the push and pull directions, correspondingly at $4\Delta_y$. Face-shell spalling along with toe crushing occurred in the left boundary element at the lateral displacement corresponding to $5\Delta_y$, which caused a slight drop in the lateral resistance of the wall. At the loading cycle of $6\Delta_y$, more diagonal shear cracking occurred, and the first horizontal crack was seen in the left boundary element's blocks. Moreover, vertical cracking was initiated in the right boundary element. The face-shell of the right boundary element's blocks started spalling at the lateral displacement corresponding to $7\Delta_y$. While going to the lateral displacement of $8\Delta_y$, at the peak of the first push, there was lateral strength degradation due to the crushing of the grout core in the left boundary element. The degradation in the lateral resistance of wall W10-$P^{4}_{M/Vd}$ was more distinct compared to the reference wall, W7.

Table 4.3 Summary of average measured loads, curvatures and displacements

Wall	W7- Ref	W10-$P^{4}_{M/Vd}$	W11-$P^{Stret.}_{BE}$	W12-$P^{Lap}_{V.Rft}$
Q_y (kN)	48.56	97.86	45.45	44.69
Δ_y (mm)	5.60	6.00	5.40	4.15
φ_y (rad/mm)	2.49E-06	2.47E-06	2.27E-06	1.74E-06
Q_u (kN)	61.70	113.35	57.37	61.98
Δ_{Qu} (mm)	54.84	21.76	36.95	28.33
Δ_u (mm)	56.16	48.17	43.38	41.63

Wall W11-$P^{Stret.}_{BE}$ had the onset of the first yield at the lateral displacements of 5.6 mm and -5.2 mm in the push and pull directions, respectively. The corresponding lateral force (Q_y) was 46.53 kN in the push direction and -44.37 kN in the pull direction. At the onset of the first yield, there were only horizontal hairline cracks in a few of the mortar bed joints in the first-floor. More horizontal cracks occurred at the lateral displacement level corresponding to $2\Delta_y$. During the

loading cycle of $3\Delta_y$, few more flexural cracks were seen in the mortar bed joints along with the appearance of the first step crack in the wall web. Additionally, vertical cracking was initiated in the first two courses of the right boundary element. More cracking and propagation of existing cracks were seen with the increasing lateral displacements. Toe crushing and vertical cracking occurred in the left boundary element at $4\Delta_y$. While going to the first peak of the lateral displacement corresponding to $5\Delta_y$, there was a slight degradation in the lateral resistance resulting from the toe crushing in the left boundary element and the face-shell spalling of the right boundary element's blocks. At the end of the loading cycle of $5\Delta_y$, there was face-shell spalling in the left and right boundary elements. Furthermore, the first diagonal and horizontal cracks appeared on the top floor (i.e. above the first-floor's out-of-plane support). The first crack in the boundary element's blocks happened at the lateral displacement of $6\Delta_y$. In the first masonry course in the right boundary element, mortar accumulated and resulted in a weak plane in the grout core. A similar mortar accumulation was also observed in the ninth masonry course. This caused early face-shell spalling in that course due to the mortar cavity in the grout core. The presence of the mortar in the grout core could be attributed to the combination of scaling effects of the masonry blocks and the type of blocks that was used in constructing the boundary elements of this wall (i.e. stretcher blocks). The use of the stretcher blocks in the boundary elements, unlike the C-shaped blocks, resulted in having separate grout cores inside the cells of the blocks rather than a single uniform grout core. Thus, it is recommended, for this type of wall construction, to have cleanouts of the mortar joints at the first masonry course before grouting the walls to enhance the construction quality. This observation sheds light on the saying of Newmark and Rosenblueth (1971) that "earthquake effects on structures systematically bring out the mistakes made in design and construction even the minutest mistakes." No more cracking was seen after the loading cycle of $6\Delta_y$. At the peak of the second pull to the displacement of $7\Delta_y$, there were vertical cracks initiated in the left boundary element's grout core. The wall also reached its lateral resistance of 58.7 kN and -56.1 kN in the push and pull directions, respectively, at $7\Delta_y$. At the first peak of the push direction in the loading cycle of $8\Delta_y$, toe crushing occurred in the left boundary element and resulted in 13.8% degradation in lateral strength. In the pull direction, at the peak, the degradation in lateral resistance was only 3.7%.

Specimen W12-$P_{V.Rft}^{Lap}$ had the first yield in vertical reinforcement at the top of tested wall lateral displacements (Δ_y) equal to 3.8 mm in the push direction and -4.5 mm in the pull direction.

The lateral resistance at the first yield (Q_y) was 44.3 kN and -45.1 kN in the push and pull directions, respectively. At the end of the loading cycles corresponding to $1\Delta_y$ and $2\Delta_y$, there were only a few horizontal cracks in the mortar bed joints in the first-floor. At the lateral displacement corresponding to $3\Delta_y$, there were few more flexural cracks in the mortar bed joints of the first-floor and mainly horizontal propagation of previous cracks. The first diagonal shear crack appeared in the first-floor after the loading cycle corresponding to the lateral displacement of $4\Delta_y$. In addition, the first horizontal bed joint crack occurred on the top floor at the lateral displacement of $4\Delta_y$. The first crack in the boundary elements' blocks was observed after the loading cycle of $5\Delta_y$. At the lateral displacement of $6\Delta_y$, few more flexural and shear cracks were observed in the first-floor, and one more horizontal crack occurred on the top floor. At the first push peak of the loading cycle to $7\Delta_y$, vertical cracks were initiated in the right boundary element. After the second push, the face-shell of the boundary element's blocks spall in the first two courses. The wall reached its ultimate lateral capacity of 62.58 kN and -61.38 kN, in the push and pull directions, respectively, at the lateral displacement of $7\Delta_y$. More face-shell spalling happened in the right boundary element, up to the tenth masonry course, at the end of the loading cycle corresponding to $8\Delta_y$. Additionally, vertical cracking was initiated in the left boundary element along with face-shell spalling until the ninth masonry course. A slight drop of 2% occurred in the lateral resistance while going to the second push peak due to toe crushing and spalling of the face-shell in the left boundary element. Face-shells also spalled in the upper masonry courses of the right boundary element due to the presence of a mortar bulk in the grout core. At the lateral displacement of $9\Delta_y$, there was mainly toe crushing in the left and right boundary elements. At the first push peak in the loading cycle of $10\Delta_y$, there were vertical cracks in the grout core of the left boundary element in second and third masonry courses. This was associated with 8.9% degradation in the lateral strength in this loading cycle. Similarly, at the first pull peak, there was substantial vertical cracking in the right boundary element's grout core, which caused a 10.3% drop in the lateral resistance.

The final cracking patterns of the four specimens are illustrated in Figure 4.8. The damage and cracking were mostly concentrated in the first-floor, below the out-of-plane support, reflecting the sufficiency of the tested height in conservatively representing the plastic hinge regions. Besides, the four walls had a flexural dominant response with significant horizontal cracks and yielding of vertical reinforcing bars.

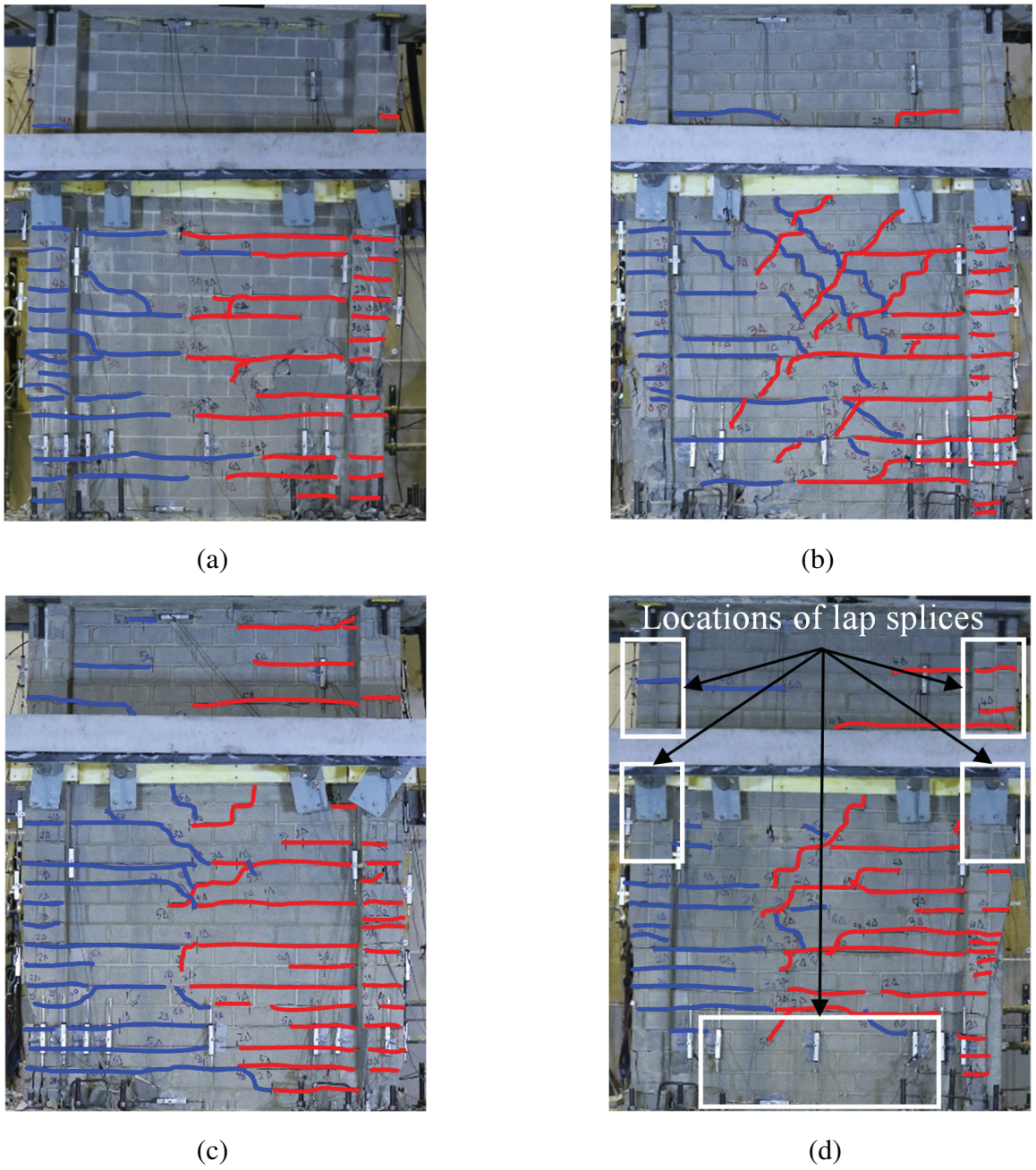

Figure 4.8 Final cracking pattern: (a) wall W7- Ref at μ = 10; (b) wall W10-$P^4_{M/Vd}$ at μ = 8; (c) wall W11-$P^{Stret.}_{BE}$ at μ = 8; and (d) wall W12-$P^{Lap}_{V.Rft}$ at μ = 10

In wall W10-$P^4_{M/Vd}$, the shear mechanism was more predominant as seen in the increased diagonal cracking compared to wall W7- Ref. In addition, the first shear crack occurred in W7-Ref at the lateral displacement of 5Δ_y, while in W10-$P^4_{M/Vd}$ it was observed at the loading cycle of 1Δ_y. This is attributed to the lower moment-to-shear ratio of W10-$P^4_{M/Vd}$ compared to that of W7-Ref, which increased the contribution of the shear mechanism to the overall response. The overall

cracking patterns of walls W11-$P_{BE}^{Stret.}$ and W7-Ref were comparable. Walls W7-Ref and W12-$P_{V.Rft}^{Lap}$ had also similar cracks. However, in specimen W12-$P_{V.Rft}^{Lap}$, the cracking in the web started above the lap splice (above the fifth masonry course), as shown in Figure 4.8(d). Furthermore, there were only a few cracks in the boundary elements at the first-floor location, where the rebars were lapped. This is because of the increased stiffness and flexural resistance in these locations due to the doubled rebars along the lap length. Hence, the damage in wall W12-$P_{V.Rft}^{Lap}$ was mainly concentrated above or below the lapped rebars.

The final damage states of the walls' boundary elements are presented in Figure 4.9. The four walls had flexural failure mechanisms that were initiated in the end zones. Wall W7-Ref failed at the loading cycle of $10\Delta_y$, during the second pull, due to buckling of several vertical rebars in the right boundary element, as shown in Figure 4.9(a). This was combined with crushing of the boundary element's grout core that extended to the wall's web and resulted in buckling of the first rebar in the web. The test was terminated due to the rapid drop in the load-carrying capacity of the wall. Specimen W10-$P_{M/Vd}^{4}$ failed while going to the peak of the second push to the lateral displacement of $8\Delta_y$. As illustrated in Figure 4.9(b), this was due to the buckling of vertical rebars in the second masonry course in the left boundary element. Subsequently, extensive crushing was observed in the grout core, which triggered buckling of the vertical rebars in upper masonry courses then propagation of crushing to the web region. This resulted in more than 20% degradation in the lateral resistance. Similarly, wall W11-$P_{BE}^{Stret.}$ failed while going to the second push peak of $8\Delta_y$ due to extensive crushing in the grout core and buckling of the vertical rebars in the left boundary element in two courses, as shown in Figure 4.9(c). The crushing also propagated to the wall's web and caused buckling of the first rebar. The test was stopped due to a sharp drop in the lateral capacity that was more than 20%. Wall W12-$P_{V.Rft}^{Lap}$ failed in the loading cycle of $10\Delta_y$ while going to second push peak due to buckling of vertical rebars and crushing of grout core in the left boundary element, as presented in Figure 4.9(d).

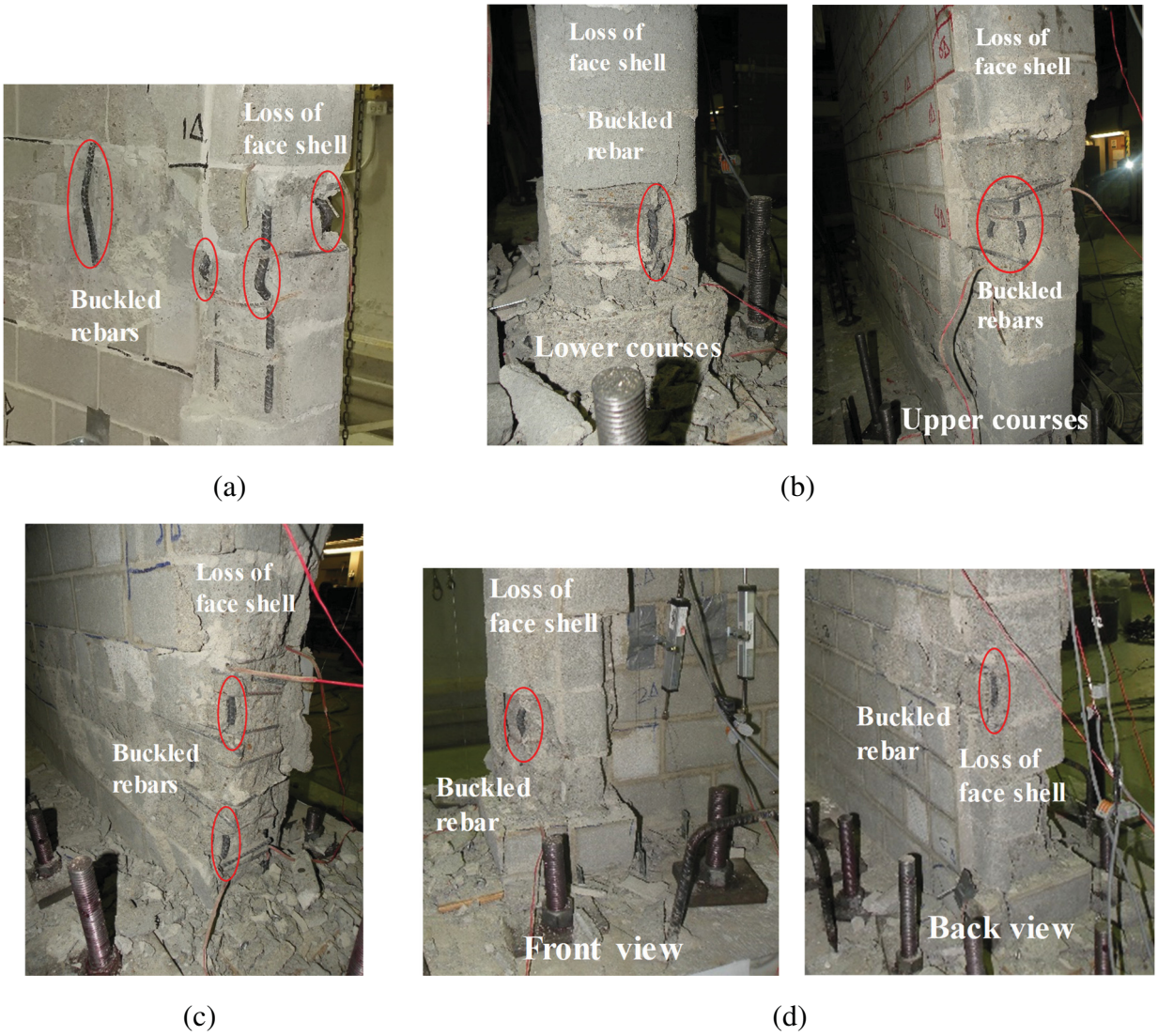

Figure 4.9 Final damage state: (a) right boundary element of wall W7- Ref at μ = 10; (b) left boundary element of wall W10-$P^{4}_{M/Vd}$ at μ = 8; (c) left boundary element of wall W11-$P^{Stret.}_{BE}$ at μ = 8; and (d) left boundary element of wall W12-$P^{Lap}_{V.Rft}$ at μ = 10

Unlike the other three walls which had the crushing extending to the web region and causing the buckling of the first rebar in the web, in W12-$P^{Lap}_{V.Rft}$ no crushing or buckling occurred in the web. This was because of the doubled web reinforcement over the length of the splice. The failure of this wall was because of its loss of the load-carrying capacity, and no tensile bond failure occurred in the lap splice. This is an essential enhancement in the structural performance of RCM shear walls with boundary elements when compared to their rectangular counterparts. Priestley and Elder (1982) tested slender rectangular RCM walls with lap spliced vertical rebars in the plastic hinge. The tested walls had a bond failure in the lapped tensile reinforcement at the end of

the testing. In wall W12-$P^{Lap}_{V.Rft}$, using the C-shaped blocks in the boundary elements, it was possible to locate the splices at the first-floor and provide sufficient confinement in the end zones. Therefore, the premature bond failure in the spliced extreme tensile rebars was prevented.

4.4.2 Experimental and idealized response

The experimental load-displacement envelopes were developed for the test specimens by connecting the peaks of the first loading cycle at each lateral displacement increment. The experimental envelopes were then idealized to an equivalent elastic-plastic system having the same energy absorption capacity, as suggested by Tomaževič (1999). The experimental and elastic-plastic load-displacement envelopes of the specimens are illustrated in Figure 4.10. Moreover, the idealized ultimate lateral load ($Q_{u\text{-}id}$), idealized lateral yield displacement ($\Delta_{y\text{-}id}$), and idealized displacement ductility ($\mu_{Qu\text{-}id}$ and $\mu_{\Delta u\text{-}id}$) values are shown in Table 4.4.

Table 4.4 Idealized response parameters

Wall	W7- Ref	W10-$P^{4}_{M/Vd}$	W11-$P^{Stret.}_{BE}$	W12-$P^{Lap}_{V.Rft}$
$Q_{u\text{-}id}$ (kN)	59.72	113.65	56.67	58.95
$\Delta_{y\text{-}id}$ (mm)	6.88	6.97	6.73	5.46
$\mu_{Qu\text{-}id}$	8.0	3.1	5.5	5.2
$\mu_{\Delta u\text{-}id}$	8.2	6.9	6.4	7.6

Figure 4.10(a) shows a comparison between the envelope curves of W7-Ref and W10-$P^{4}_{M/Vd}$. There was an evident influence from the reduction in the shear span-to-depth ratio on the response of wall W10-$P^{4}_{M/Vd}$. Wall W10-$P^{4}_{M/Vd}$ had a degrading post-peak response, whereas W7-Ref had a hardening response until failure. The shorter shear span triggered a higher contribution from the shear mechanism to the overall response and resulted in more shear cracking as was shown in Figure 4.8(b). In addition, it limited the contribution of vertical rebars' strain-hardening to the lateral resistance. The average ratio between peak load (Q_u) and yield load (Q_y) dropped from 1.27 in W7-Ref to 1.16 in W10-$P^{4}_{M/Vd}$. At the first yield in vertical rebars, wall W10-$P^{4}_{M/Vd}$ had almost twice the lateral capacity and a slightly higher, by 7%, lateral displacement compared to wall W7-Ref. The average lateral resistance of specimen W10-$P^{4}_{M/Vd}$ was approximately 84% higher than that of wall W7-Ref due to its increased lateral stiffness caused by the reduction in the shear span-to-depth ratio. There was also a significant reduction in the displacement at peak load of W10-$P^{4}_{M/Vd}$ compared to W7-Ref. Wall W10-$P^{4}_{M/Vd}$ had a lateral displacement at failure that was 2.21

times higher than the value at peak load, mainly due to its degrading post-peak response. The idealized lateral displacement at the first yield was similar for both walls, W7-Ref and W10-$P^4_{M/Vd}$. However, there was a substantial reduction in the idealized displacement ductility values of W10-$P^4_{M/Vd}$ at both, ultimate load and ultimate displacement due to the reduced moment to shear ratio. The idealized displacement ductility of wall W10-$P^4_{M/Vd}$ was lower by 61% and 15% at peak load and ultimate displacement, respectively, compared to W7-Ref. In wall W10-$P^4_{M/Vd}$, the significant difference between ductility at peak load and ultimate displacement is attributed to the degrading post-peak behaviour. The idealized displacement ductility at ultimate displacement ($\mu_{\Delta u\text{-}id}$) of W10-$P^4_{M/Vd}$ was 2.2 times higher compared to the value at peak load ($\mu_{Qu\text{-}id}$), while for the reference wall, the difference in the idealized ductility values between peak load and ultimate displacement was marginal.

The load-displacement envelopes of wall W11-$P^{Stret.}_{BE}$ are compared to those of the reference wall in Figure 4.10(b). Both specimens had similar lateral loads and displacements at the first yield in vertical reinforcement. Wall W11-$P^{Stret.}_{BE}$ had a slightly lower, by 7%, average ultimate load compared to W7-Ref. Furthermore, the lateral displacement at peak load and failure were 33% and 23% lower, respectively, for wall W11-$P^{Stret.}_{BE}$ relative to the reference specimen. Wall W11-$P^{Stret.}_{BE}$ had a 17% increase in its lateral displacement from peak load to failure load, whereas W7-Ref failed at a lateral displacement that was only 2% higher from the peak point. The idealized resistance of wall W11-$P^{Stret.}_{BE}$ was 5% lower than W7-Ref, while the idealized yield displacements were similar. Therefore, there was no clear impact from the type of blocks (stretcher or C-shaped) used in the boundary elements on the lateral resistance. However, the effect was evident on the displacement capacity. Although both specimens had the same level of confinement in the end zones, the average idealized displacement ductility was lower for wall W11-$P^{Stret.}_{BE}$ by 31% at peak load and 21% at ultimate displacement. Wall W11-$P^{Stret.}_{BE}$ had a strength degrading post-peak behaviour, which resulted in a 17% increase in its idealized ductility capacity from the peak to the failure point.

The impact of lap splicing the vertical rebars in the plastic hinge zone on the lateral load-displacement response is illustrated in Figure 4.10(c). At the first yield, the average lateral load was not affected; however, there was a 26% drop in the displacement caused by the increased

stiffness from doubling the vertical rebars along the splice length. The ultimate lateral resistance was also not impacted by the presence of the lap splice. The influence of the lap splice was more pronounced on the displacement capacity. Wall W12-$P_{V.Rft}^{Lap}$ had the peak load at a displacement 48% lower than that of wall W7-Ref. Similarly, at failure, the lateral displacement was lower by 26%. In specimen W12-$P_{V.Rft}^{Lap}$, the lateral displacement at failure was 47% higher than the peak load-displacement due to its degrading load-displacement response. Similar trends were seen in the idealized response. The idealized lateral resistance was similar for both specimens, but the idealized yield displacement was 21% lower for W12-$P_{V.Rft}^{Lap}$. The impact of the lap splice on the displacement capacity was more evident at the peak load. The average idealized displacement ductility, at ultimate load, ($\mu_{Qu\text{-}id}$) of W12-$P_{V.Rft}^{Lap}$ was 35% lower compared to the reference wall, W7, which had continuous vertical rebars. At ultimate displacement, the difference in idealized displacement ductility ($\mu_{\Delta u\text{-}id}$) values between walls W12-$P_{V.Rft}^{Lap}$ and W7-Ref was only 7%. Wall W12-$P_{V.Rft}^{Lap}$ had a degrading post-peak response which resulted in a significant difference between its ductility values at peak load and ultimate displacement. The idealized displacement ductility at the ultimate displacement ($\mu_{\Delta u\text{-}id}$) of wall W12-$P_{V.Rft}^{Lap}$ was 1.47 times higher than the value at ultimate load.

The differences in the test walls' performance at ultimate load and ultimate displacement is a result of the combination of two factors. Firstly, the contribution of the flexure mechanism (W10-$P_{M/Vd}^{4}$ Vs. W7-Ref) and, secondly, the use of the C-shaped blocks (comparing W11-$P_{BE}^{Stret.}$ to W7-Ref) in the boundary elements. The reduction in the shear span triggered more contribution from the shear mechanism, which resulted in a degrading post-peak response. On the other hand, the utilization of the C-shaped blocks enhanced the uniformity of the grout core in the boundary elements and reduced the possibility of having weak planes due to the accumulation of mortar. Thus, it improved the post-peak response as it was typically controlled by the performance of the grout core.

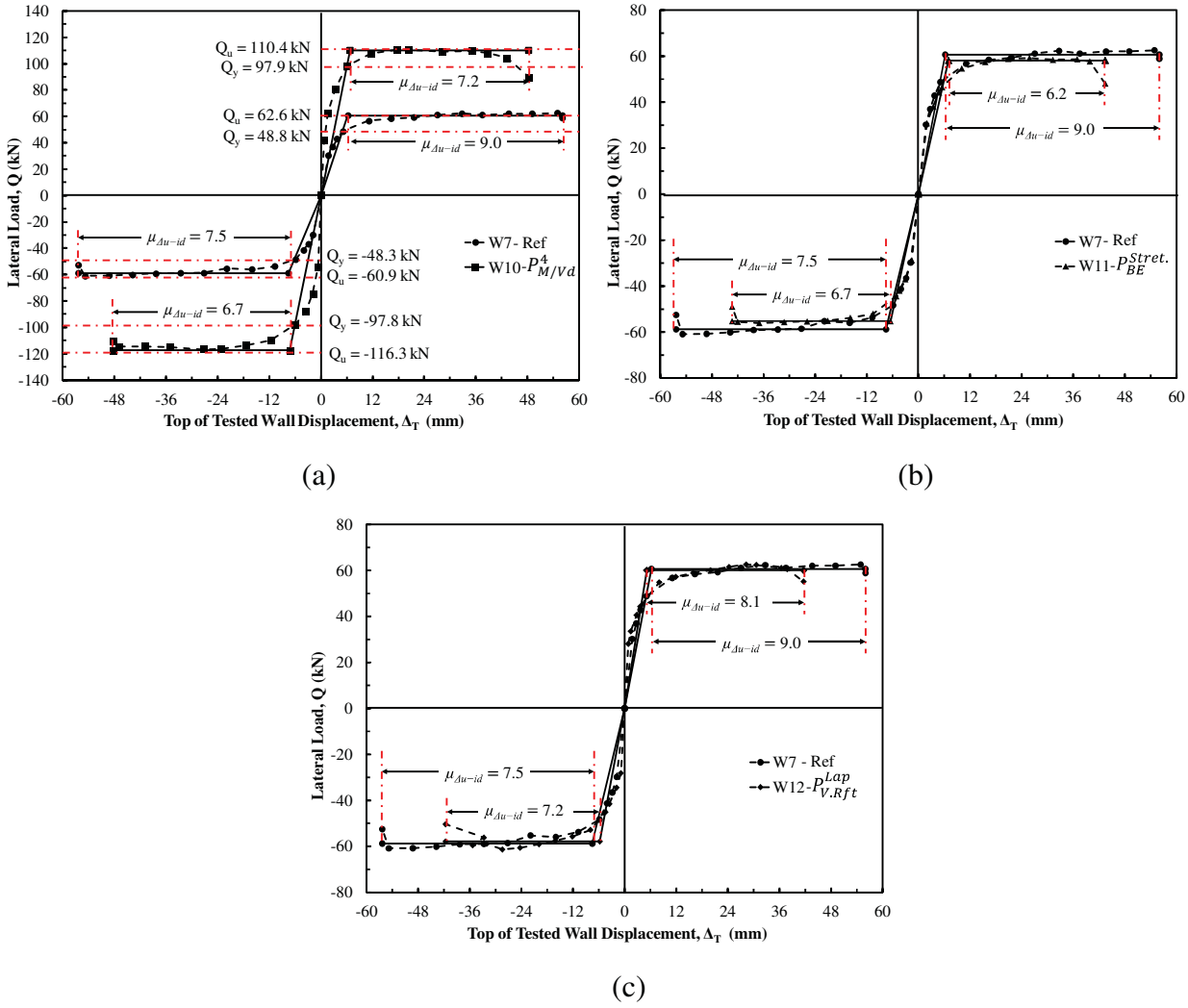

Figure 4.10 Experimental and elastic-plastic idealized lateral load-displacement envelopes: (a) walls W7- Ref and W10-$P^4_{M/Vd}$; (b) walls W7- Ref and W11-$P^{Stret.}_{BE}$; and (c) walls W7- Ref and W12-$P^{Lap}_{V.Rft}$

4.4.3 Stiffness degradation

The effective lateral secant stiffness (K_e) trends of the test specimens are shown in Figure 4.11(a) in relation to the applied lateral displacements and Figure 4.11(b) in dependence on the displacement ductility level. The initial (K_i), first yield (K_y), peak (K_{Qu}) and ultimate ($K_{\Delta u}$) secant stiffness values are also summarized in Table 4.5. The initial stiffness was evaluated at the first applied displacement increment of $0.25\Delta_y$. The presented values are the average between the push and pull directions and were calculated as the slope of the line connecting the peaks in the two loading directions (push and pull) of each applied displacement increment, as illustrated in Figure 4.11(a).

Table 4.5 Average measured lateral secant stiffness

Wall	W7- Ref	W10-$P^{4}_{M/Vd}$	W11-$P^{Stret.}_{BE}$	W12-$P^{Lap}_{V.Rft}$
K_i (kN-mm)	16.66	70.40	17.02	32.13
K_y (kN-mm)	8.86	16.44	8.52	11.08
K_{Qu} (kN-mm)	1.13	5.21	1.55	2.19
$K_{\Delta u}$ (kN-mm)	0.99	2.08	1.12	1.27

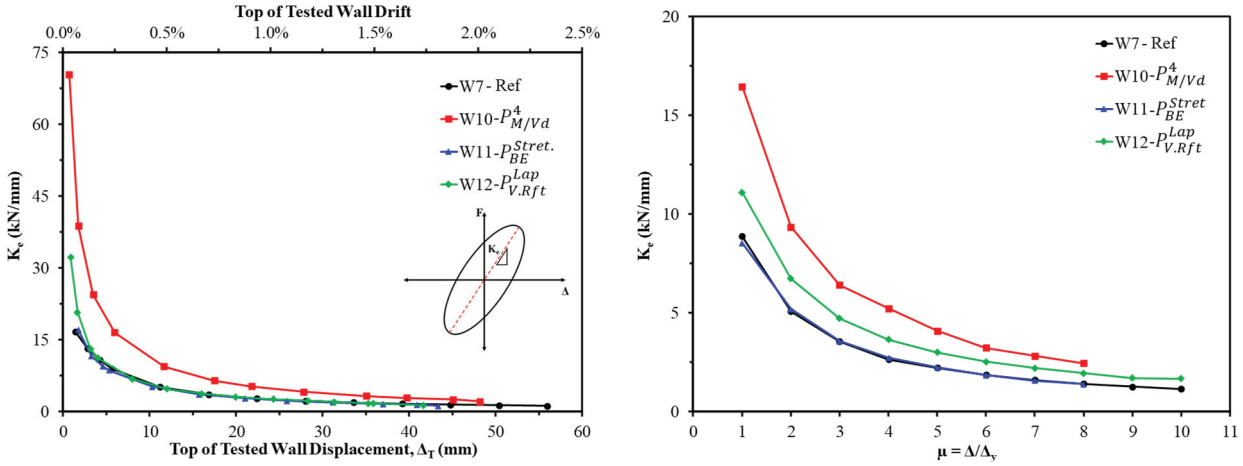

(a) (b)

Figure 4.11 Average lateral secant stiffness variation in dependence on: (a) applied top displacement; and (b) displacement ductility

The 6-storey wall, W10-$P^{4}_{M/Vd}$, had an initial lateral stiffness that is 4.2 times higher than the reference 12-storey wall. Furthermore, over the entire loading history, wall W10-$P^{4}_{M/Vd}$ had significantly higher stiffness values compared to W7-Ref, due to its lower shear span-to-depth ratio. At peak load and ultimate displacement, the stiffness values were also 4.6 and 2.1 times higher, respectively. As expected, there was no impact from the boundary elements' block type (W11-$P^{Stret.}_{BE}$) on the lateral stiffness. Wall W11-$P^{Stret.}_{BE}$ had similar initial and first yield stiffness values to those of specimen W7-Ref. Besides, with the gradually increasing displacement increments, both walls had comparable stiffness values. However, the stiffness of wall W11-$P^{Stret.}_{BE}$ was higher by 38% at the lateral capacity and 13% at the ultimate displacement, relative to the reference wall. The doubled vertical rebars over the splice length in wall W12-$P^{Lap}_{V.Rft}$ increased its initial stiffness (K_i) by 93% and its first yield stiffness (K_y) by 25%, compared to the reference wall, which had continuous vertical reinforcing bars. The lateral secant stiffness values over the entire loading protocol were also higher than those of wall W7-Ref. Specimen W12-$P^{Lap}_{V.Rft}$ had

94% and 27% increase, compared to W7-Ref, in its secant stiffness at ultimate load and ultimate displacement, respectively.

The lateral stiffness degradation patterns of the test specimens are compared in Figure 4.12 with respect to the applied top displacements and the displacement ductility demands. The values were normalized by the initial secant stiffness (K_i), measured at the lateral displacement increment of $0.25\Delta_y$. Wall W10-$P^4_{M/Vd}$ had the highest lateral stiffness degradation rate over the entire loading history. The lateral stiffness at first yield dropped to 23% of the initial stiffness. This was due to the higher contribution from the shear mechanism and the increased shear cracking compared to the other walls. The presence of the lap spliced vertical rebars in the plastic hinge region of wall W12-$P^{Lap}_{V.Rft}$ also resulted in an increased rate of stiffness degradation. Specimen W12-$P^{Lap}_{V.Rft}$ had a lateral stiffness at first yield that was only 34% of its initial stiffness. Walls W7-Ref and W11-$P^{Stret.}_{BE}$ had similar stiffness degradation trends. The stiffness at yield dropped to 53% and 50% of the initial values, for walls W7-Ref and W11-$P^{Stret.}_{BE}$, respectively. At ultimate load, all walls, except W11-$P^{Stret.}_{BE}$, had a lateral stiffness that was approximately 7% of the initial value. Wall W11-$P^{Stret.}_{BE}$ had a marginally higher ultimate stiffness that was 9% of its initial stiffness.

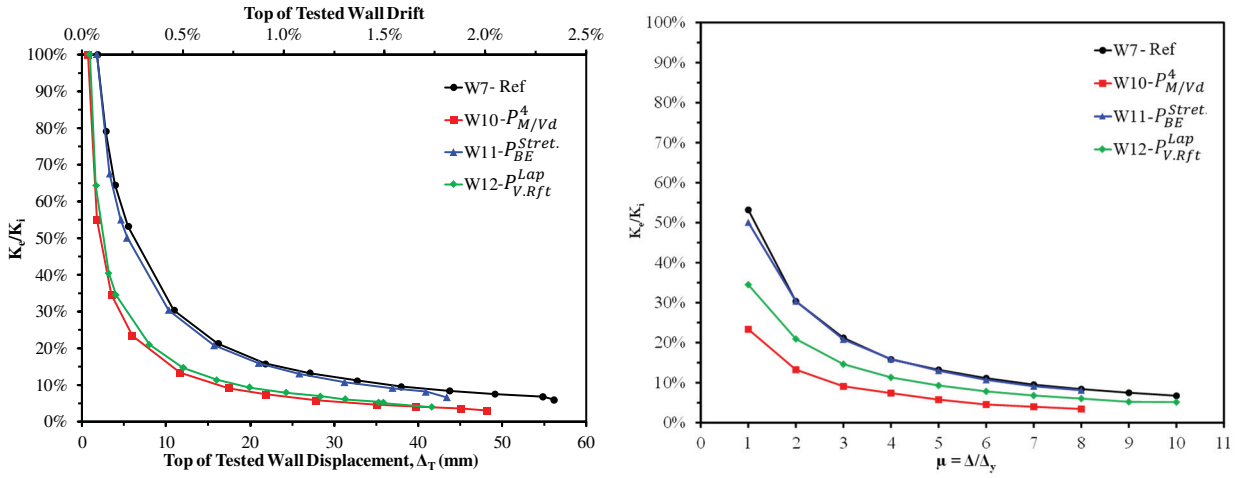

(a) (b)

Figure 4.12 Normalized lateral stiffness in relation to: (a) applied top displacement; and (b) displacement ductility

4.4.4 Axial strains and curvatures

The influence of the studied parameters on the average masonry compressive strain can be seen in Figure 4.13. The strains were calculated in the extreme ends of the walls over 340 mm, 680 mm,

and 1020 mm gauge lengths using the measurements of LVDTs L1-L6. Overall, in all the test specimens, the compressive strain trends were similar over the three gauge lengths. The four walls were able to reach high average compressive strains in the masonry extreme fibre, before any degradation in lateral resistance, much higher than the North American masonry design standards' (CSA S304-14 and TMS 406/602-16) design value of 0.0025, as shown in Figure 4.13(a). The highest masonry compressive strains were measured over the gauge length of 680 mm in wall W11-$P_{BE}^{Stret.}$ due to its delayed face-shell spalling in the upper masonry courses. As illustrated in Figure 4.13(b), the average masonry compressive strains were higher for walls W10-$P_{M/Vd}^{4}$ and W11-$P_{BE}^{Stret.}$, relative to the reference wall at all displacement ductility levels. On the other hand, the compressive strains sustained by specimen W12-$P_{V.Rft}^{Lap}$ were much lower than wall W7-Ref at all ductility demands. The doubled reinforcement over the length of the splice resulted in increasing the lateral stiffness of the wall, as discussed in the previous subsection, and hence reduced the compressive strains in the extreme masonry fibres.

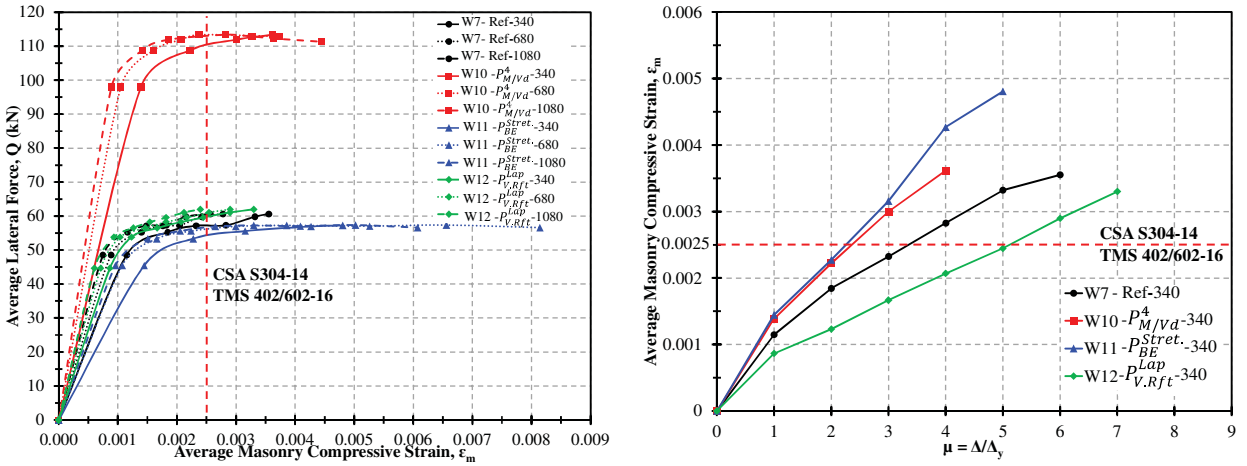

(a) (b)

Figure 4.13 Average masonry compressive strain: (a) relationship with average lateral force; and (b) relationship with displacement ductility

Figure 4.14 presents the vertical strains along the wall's length. The axial strains were calculated using the vertical deformations measured over a gauge length of 340 mm above the wall's foundation. The strain gradients are shown for the push and pull loading directions at the different ductility demand levels that were possible to measure before the spalling of the blocks' face-shell. The horizontal axis is displaying the normalized locations of the vertical strain measurements by the wall's length. The positive axial strains are compressive.

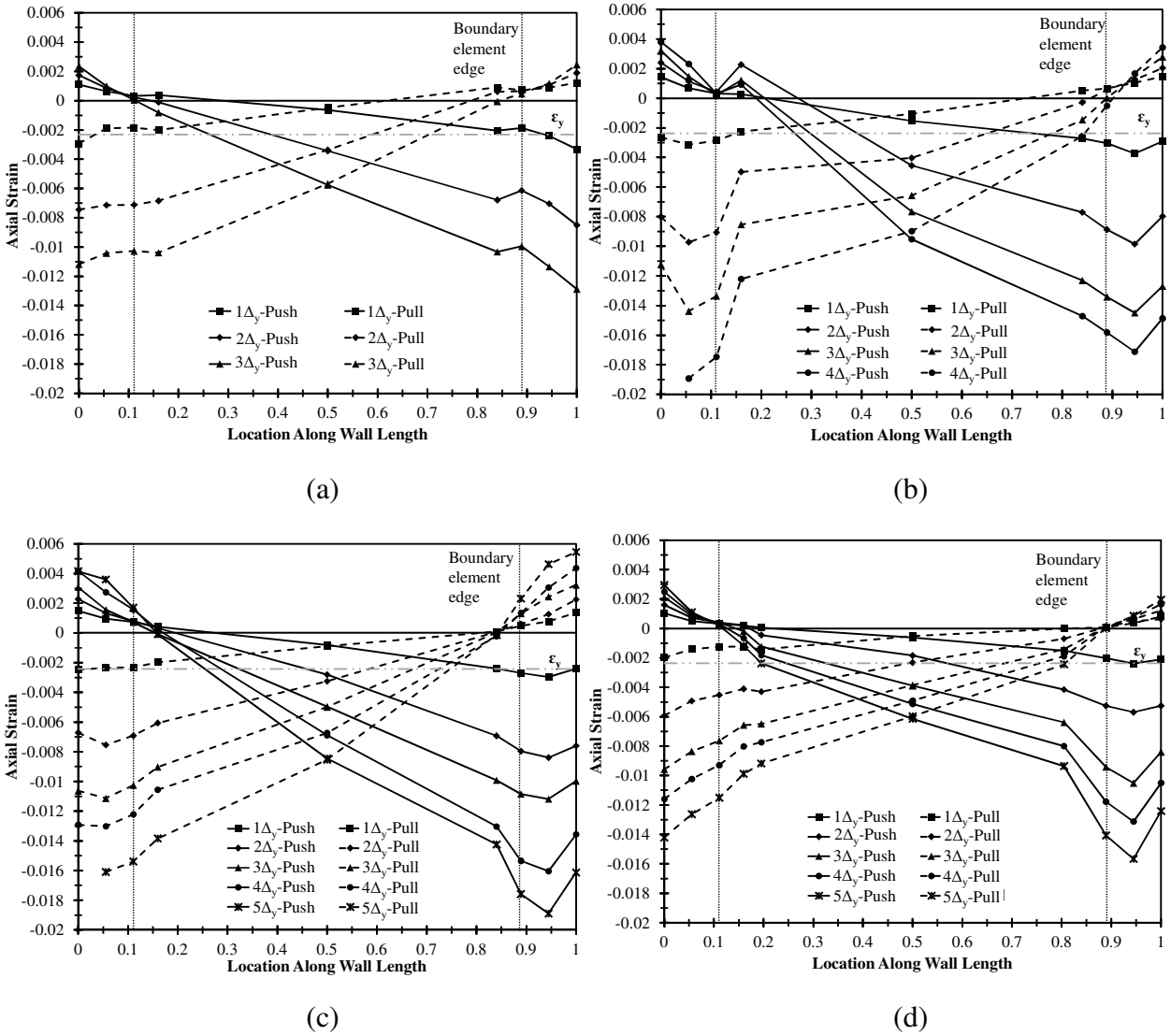

Figure 4.14 Horizontal strain profiles: (a) wall W7- Ref; (b) wall W10-$P^{4}_{M/Vd}$; (c) wall W11-$P^{Stret.}_{BE}$; and (d) wall W12-$P^{Lap}_{V.Rft}$

It can be seen that, at low lateral displacements, the strain gradients were reasonably linear and nearly symmetric in the push and pull loading directions. The neutral axis depths, measured from the extreme compression fibre to the point where the strain profile crosses the zero, were comparable in both loading directions. With the increasing ductility demands, slight nonlinearity was seen in the horizontal strain profiles, especially at the interface between the web and the boundary elements. However, overall, the plane section assumption seems to be valid for the tested walls.

The test walls' curvature profiles are given in Figure 4.15. The presented curvature values were calculated using the vertical deformations measured by LVDTs L1-L12, which were mounted on the walls' ends. The values were averaged over the six gauge lengths previously shown in Figure 4.5(a). The walls, except wall W12-$P^{Lap}_{V.Rft}$, had similar curvature values at the onset of the first yield in tension reinforcement.

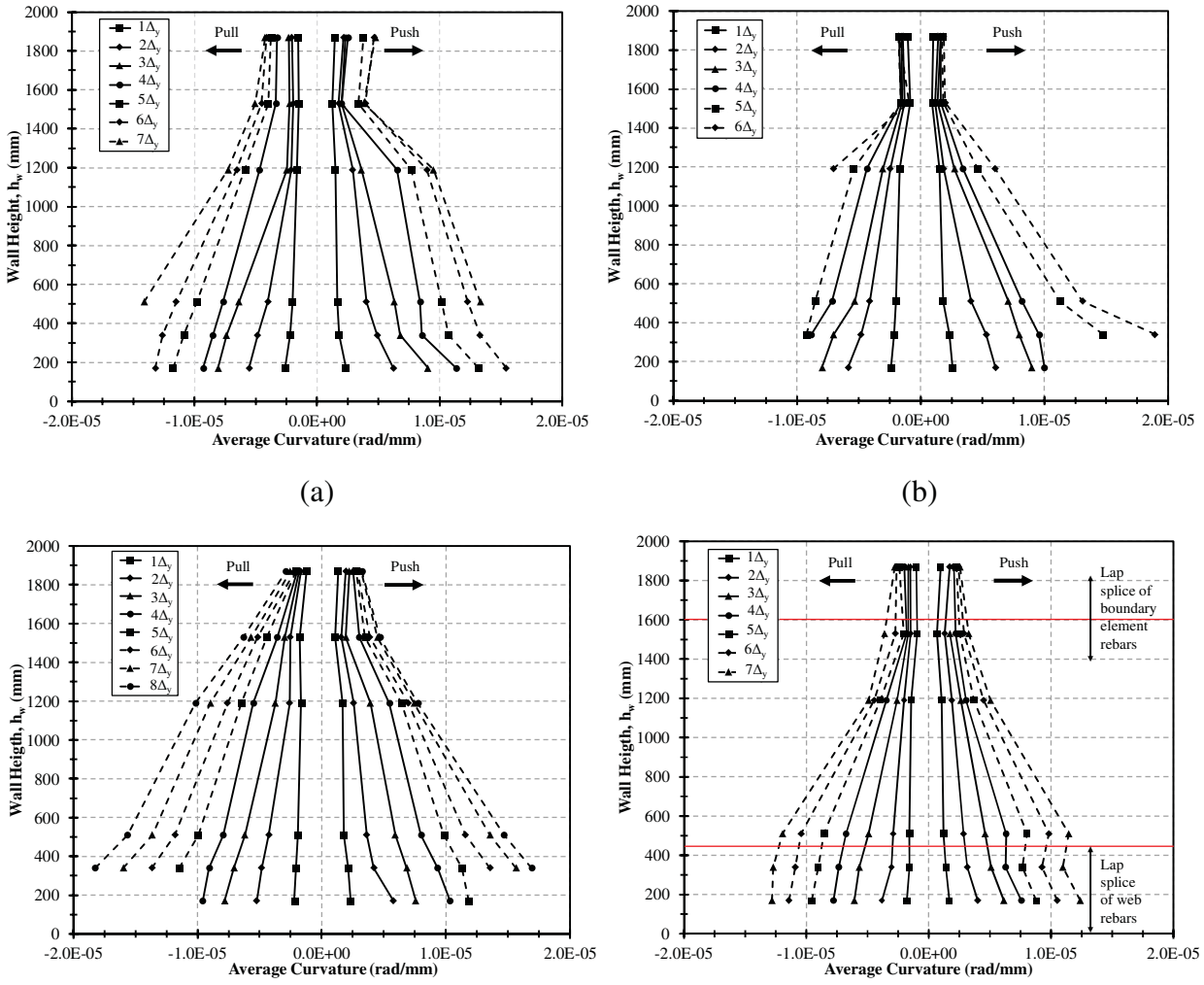

Figure 4.15 Average curvature profiles: (a) wall W7- Ref; (b) wall W10-$P^{4}_{M/Vd}$; (c) wall W11-$P^{Stret.}_{BE}$; and (d) wall W12-$P^{Lap}_{V.Rft}$

Specimen W12-$P^{Lap}_{V.Rft}$ had the lowest first yield curvature due to the presence of lap splices. Furthermore, the curvatures were lower in wall W12-$P^{Lap}_{V.Rft}$ at almost all ductility demands. For instance, at the ductility value of 4, wall W12-$P^{Lap}_{V.Rft}$ had the least curvature value (measured over

the first 340 mm gauge length) compared to the other walls, which had similar values. At the first-floor, where the boundary elements' rebars were lapped in specimen W12-$P^{Lap}_{V.Rft}$, the measured curvatures were lower compared to the reference wall (W7), as can be seen in Figure 4.15(d) and (a), respectively. Besides, at the location of splices in the web rebars (i.e. at wall-foundation interface), there was a substantial reduction in the slope of the curvature profiles at all ductility levels, relative to the reference wall with continuous rebars.

4.4.5 Shear and flexure displacements

The total top of wall displacement (Δ_T) is a combination of the contributions from flexure displacement (Δ_f), shear displacement (Δ_{sh}), and sliding displacement (Δ_{sl}). The flexure displacements at the top of the tested wall were calculated for the test specimens by double integration of the experimental curvature profiles that were shown in Figure 4.15. Then, the shear displacements were computed by subtracting the flexure and sliding displacements from the total displacement. The sliding displacements between the wall and the bottom foundation were measured using LVDT L15 and were found to constantly equal to zero for all the tested walls. The impact of the studied parameters on the contribution of flexure and shear displacements to the total displacement is evaluated in Figure 4.16(a) and (b), respectively. In general, there was no clear trend seen in the contribution of shear displacements with the increasing ductility demands. All the tested walls, except W10-$P^{4}_{M/Vd}$, had more than 80% of its lateral top displacement, at all ductility levels, due to the flexure component. This confirms the dominance of the flexural response. Conforming to previous observations, the reduction in the shear span of wall W10-$P^{4}_{M/Vd}$ increased the contribution of the shear displacements. The shear displacements of wall W10-$P^{4}_{M/Vd}$ contributed by 21% to the total displacement at the onset of the first yield, compared to 14.2% in wall W7-Ref. Besides, on average, over the entire loading history, the shear contribution in wall W10-$P^{4}_{M/Vd}$ was 26.3%, which is 65% higher than the reference wall. Similar contributions from flexure displacements were seen in walls W7-Ref and W11-$P^{Stret.}_{BE}$. The flexure component, on average, contributed by 84% and 85.7% to the total top of wall displacement of specimens W7-Ref and W11-$P^{Stret.}_{BE}$, respectively. A slightly higher contribution from the flexure displacements was observed in the specimen with the lap spliced vertical rebars. Wall W12-$P^{Lap}_{V.Rft}$ had, on average, 87.7% of its total displacement due to the flexure component. This could be attributed to its locally increased flexural resistance at the lap splice locations.

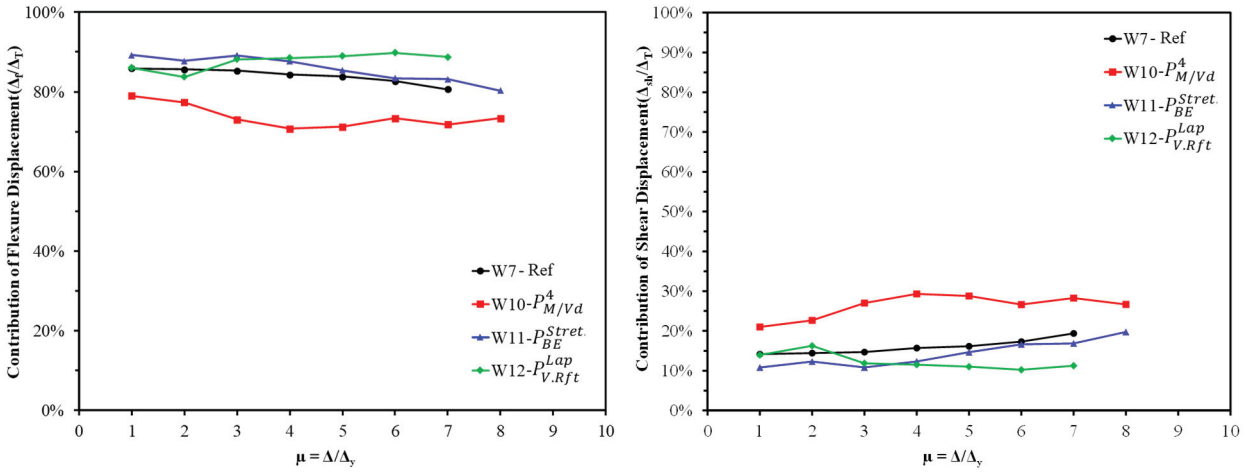

(a) (b)

Figure 4.16 Top of wall displacement components: (a) flexure contribution; and (b) shear contribution

4.4.6 Energy dissipation

The hysteretic energy absorption capacity reflects the walls' ductility level and the ability to dissipate the energy during seismic events. The dissipated energy (E_d) was calculated for the test specimens as the area enclosed by each hysteresis loop. The displayed E_d values in Figure 4.17 were evaluated at the first loading cycle of each applied displacement increment. Figure 4.17(a) presents the test walls dissipated energy values with respect to the increasing ductility demands. At the onset of the first yield (i.e. μ=1), the four walls had similar and low amounts of dissipated energy. At higher ductility values, the dissipated energy was higher due to the yielding of tensile reinforcement and cracking of masonry. As seen in Figure 4.17(a), wall W10-$P^4_{M/Vd}$ dissipated significantly larger energy at all the applied displacement increments compared to W7-Ref. This was due to its higher lateral resistance, which made the hysteresis loops larger. Conversely, specimens W11-$P^{Stret.}_{BE}$ and W7-Ref had similar values of E_d reflecting the negligible impact from the type of blocks used in the boundary elements. The presence of lap splices in the plastic hinge zone of wall W12-$P^{Lap}_{V.Rft}$ limited its energy dissipation ability, at all ductility levels, relative to the reference wall.

The dissipated hysteretic energy values (E_d) were normalized by the input energy (E_i) exerted by the three actuators to calculate the energy dissipation ratios (E_d/E_i). The input energy (E_i) at each displacement increment was calculated as the area under the skeleton of the first hysteresis loop to that displacement level. The normalized energy dissipation trends of the test specimens are

shown in Figure 4.17(b). The four walls had similar variations in E_d/E_i and were capable of dissipating significantly high amounts of the input energy. The dissipated energy ratios ranged from 33% to 40%, at the onset of the first yield. Although wall W10-$P^4_{M/Vd}$ had higher dissipated energy values compared to W7-Ref, the energy dissipation ratios were similar for both walls. However, since wall W10-$P^4_{M/Vd}$ had a degrading post-peak response, the energy dissipation ratio at the lateral resistance (μ=4) was only 59%, compared to 71% (at μ=10) for W7-Ref. At ultimate load, walls W11-$P^{Stret.}_{BE}$ and W12-$P^{Lap}_{V.Rft}$ had energy dissipation ratios of 68% and 63%, respectively. Therefore, the influence of the boundary elements' block type and lap splicing of vertical rebars was not substantial on the energy dissipation ratios.

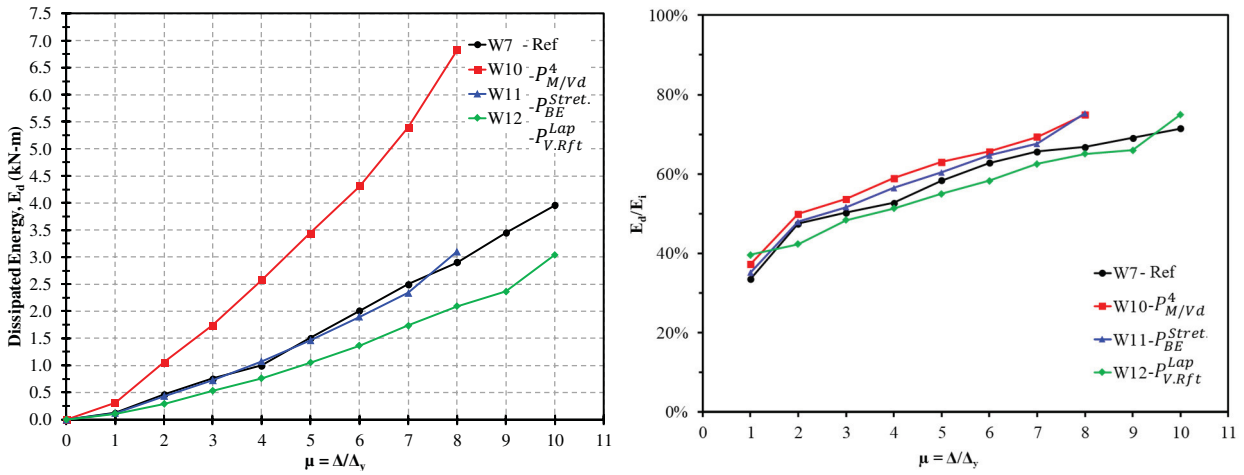

(a) (b)

Figure 4.17 Trends of energy dissipation with increasing ductility demands: (a) energy absorbed at the first cycle of each displacement increment; and (b) normalized energy dissipation capacity

The equivalent viscous damping ratios (ξ_{eq}) of the test walls are displayed in Figure 4.18. The shown values were calculated based on the method suggested by Chopra (2007) using Eq. (4.1), where E_d is the energy dissipated in a single hysteresis loop and E_s is the elastic strain energy of an equivalent elastic-perfectly plastic system. The elastic energy (E_s) was evaluated at the peak of the corresponding hysteresis loop.

$$\xi_{eq} = \frac{1}{4\pi}\frac{E_d}{E_s} \tag{4.1}$$

All walls had increasing damping ratios with the increase in lateral displacement demands. At the onset of the first yield, the walls had similar damping ratios, ranging between 7.6-8.5%, with

a slightly higher value of 10% for W12-$P^{Lap}_{V.Rft}$. At ultimate load, the equivalent damping ratios were 18.6% for W7-Ref, 16.6% for W10-$P^{4}_{M/Vd}$, 17.6% for W11-$P^{Stret.}_{BE}$, and 16% W12-$P^{Lap}_{V.Rft}$. The lower shear span-to-depth ratio slightly increased the damping ratios at the higher lateral displacements. The type of boundary elements' masonry blocks and the presence of the lap splices in vertical rebars had no evident impact on the damping ratios.

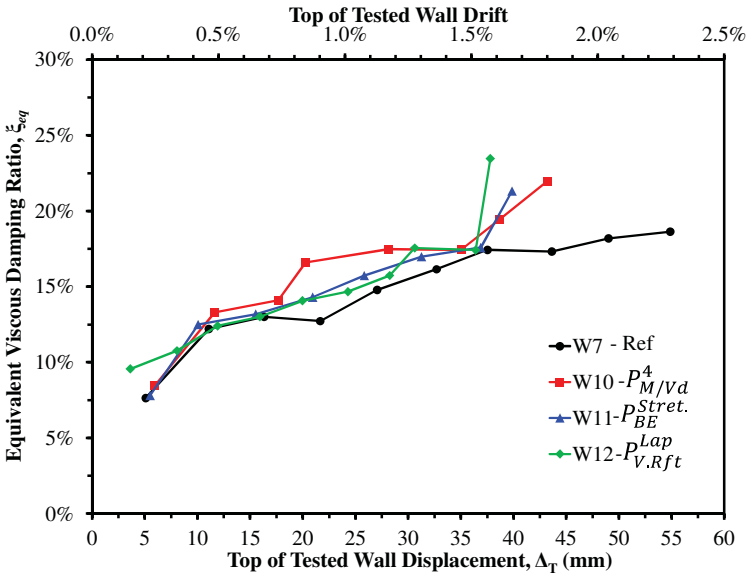

Figure 4.18 Variation of equivalent viscous damping ratios with increasing displacement demands

4.5 Summary and Conclusions

This study presented an evaluation of the in-plane cyclic response of high-rise RCM shear walls with boundary elements. The tested specimens were slender walls representing the plastic hinge of 12-storey and 6-storey walls. The walls were constructed at half-scale and were tested under constant axial load and quasi-static reversed cyclic loading to failure. The focus was on quantifying the influences of the wall's shear span-to-depth ratio, the type of boundary elements' masonry blocks, and the lap splicing of vertical rebars on the structural performance. The walls demonstrated a ductile performance dominated by flexure. All the walls had a symmetric and stable hysteretic response with wide loops indicating a high energy dissipation capacity. Besides, the walls sustained compressive strains in the masonry extreme fibres, before the initiation of strength degradation, higher than the design value of the North American masonry design standards. The failure mechanism in the four walls was initiated in the end zones due to buckling of longitudinal rebars and crushing of the grout core.

The reduction in the shear span-to-depth ratio increased the contribution of the shear mechanism. Thus, it resulted in more diagonal and step cracks and increased the relative contribution of shear displacements to the total displacement. Additionally, it increased the initial stiffness, lateral resistance, and the rate of stiffness and strength degradation. However, it limited the ultimate displacement capacity of the wall. The initial stiffness and lateral resistance of the 6-storey wall were 4.2 and 1.9 times higher, respectively than those of the 12-storey wall. Furthermore, the initial stiffness dropped by 77% at the first yield, compared to 47% in the 12-storey reference wall. The displacement ductility values were lower by 61% and 15% at peak load and ultimate displacement, respectively, when the shear span-to-depth ratio was reduced from 8.8 to 4.4. The contribution of the shear displacements to the total top displacement was on average 65% higher in the 6-storey wall. The amounts of dissipated hysteretic energy were higher in the 6-storey wall due to its increased lateral resistance, but the ratios of normalized energy dissipation by the input energy were comparable between the 12- and 6-storey walls.

The use of the C-shaped blocks, in lieu of the conventional stretcher blocks in forming the wall's boundary elements improved the construction process, time, and quality. However, it had no substantial impact on the cracking pattern, initial stiffness, stiffness degradation, lateral resistance, and energy dissipation capacity. Nonetheless, the use of the stretcher blocks in the wall's boundary elements limited the displacement capacity and resulted in a degrading post-peak response. The displacement capacity was reduced by 31% at peak load and by 21% at ultimate displacement when the stretcher blocks were used.

Lap splicing of vertical rebars in the plastic hinge affected the final cracking pattern. Only a few cracks were seen in the lap splice locations as a result of the locally increased flexural resistance, while the damage was concentrated above or below the spliced rebars. In addition, it increased the initial stiffness by 93% and the first yield stiffness by 25% compared to the similar wall with continuous rebars. The stiffness degradation rate was also higher. The wall with lap spliced longitudinal rebars had a 66% drop in its lateral stiffness at the first yield, whereas in the wall with no splices the drop was 47%. The effect of the lap splice on the lateral resistance was negligible; the wall was capable of attaining its ultimate capacity. However, lap splicing the vertical reinforcement limited the displacement capacity and increased the strength degradation. The displacement ductility was lowered by 35% and 7% at peak load and ultimate displacement,

respectively, when the rebars were spliced. The increased lateral stiffness from the lap splice restrained the compressive strains developed in the masonry extreme fibres. The dissipated hysteretic energy was also reduced when lap splices were present; however, the effect was lesser on the normalized energy dissipation values. Therefore, with the proper design of the lap splice as recommended by CSA S304-14 provisions and the presence of sufficient confinement in the end zones, the spliced rebars had a marginal impact on ultimate displacement and energy dissipation capacities. Besides, the premature tensile bond failure of extreme rebars was prevented.

Based on the test results, it is recommended to utilize the newly proposed C-shaped blocks in constructing the boundary elements of RCM shear walls. Special attention should be given to the shear resistance of walls with shorter shear spans to ensure their ductile response. Finally, lap splicing of vertical rebars in the plastic hinge is expected to slightly lower the ultimate displacement ductility and energy dissipation capacity of RCM shear walls with boundary elements. As it cannot be avoided, it should cautiously follow the current provisions of CSA S304-14 to minimize the adverse impacts and to prevent bond failures.

Chapter 5

Seismic Performance and Height Limits of Ductile Reinforced Masonry Shear Wall Buildings with Boundary Elements

5.1 Abstract

The National Building Code of Canada, NBCC-15 has recently added a new Seismic Force Resisting System (SFRS) category, ductile shear walls, for Reinforced Masonry (RM) buildings. Although it was assigned a higher ductility-related force modification factor compared to that of moderately ductile walls, NBCC-15 assigned the same building height limits for the ductile and moderately ductile RM walls. This study aims to assess (i.e. numerically) the seismic performance and collapse capacity of ductile RM buildings, having heights exceeding the code limit, built using ductile RM shear walls with boundary elements as the SFRS. The main objective is to propose height limits based on solid and objective seismic performance acceptance criteria. In this regard, six archetype buildings with varying heights are designed according to CSA S304-14 with ductile RM structural walls having confined boundary elements. The reference buildings are located in two regions representing the high and moderate seismicity levels of NBCC-15. The seismic performance is evaluated using nonlinear pseudo-static pushover and Incremental Dynamic Analyses (IDA). The quantification of seismic performance and collapse capacity is executed using the procedure outlined in FEMA P695. This research study contributes to the understanding of the seismic performance and collapse capacity of ductile RM shear wall buildings with boundary elements. It provides practical design recommendations to enhance the overall system performance. In addition, the study proposes a simple, yet efficient nonlinear numerical macro-modelling approach for RM shear walls. Finally, based on the findings of this study, it is suggested to assign a 70 m limit for the height of buildings in moderate seismicity regions and a 50 m limit for the buildings in regions with high seismic hazard.

5.2 Introduction and Background

Masonry buildings have been perceived incapable of achieving a ductile seismic response. This perception stems from the observed damage and response of unreinforced masonry during previous earthquake events (Bruneau and Yoshimura, 1996). For Reinforced Masonry (RM) shear walls to be ductile in a seismic event, it shall be capable of sustaining large reversible cycles of inelastic deformations without significant degradation in strength. This can be achieved by integrating confined masonry boundary elements at the ends of rectangular RM shear walls. RM shear walls constructed with boundary elements at the end zones demonstrated a significant enhancement in the wall's curvature ductility compared to that of RM rectangular walls (Banting and El-Dakhakhni, 2012, 2014; Ezzeldin et al., 2017, 2016; and Shedid et al., 2010b). Consequently, RM shear walls with boundary elements present a potential Seismic Force Resisting System (SFRS) for mid- and high-rise RM buildings. The addition of the confined boundary elements has a primary purpose of increasing the inelastic strain capacity of masonry. In addition, the increased thickness of the added boundary element stabilizes and reduces the depth of the compression zone. Therefore, as the boundary element's confinement increases, the ultimate compressive strain and ultimate curvature of the wall are significantly enhanced.

The enhancements in RM shear walls' ductility and displacement capacity due to the presence of confined boundary elements have been observed in the experimental study by Shedid et al. (2010a). That study highlighted that the proposed end configurations (flanged and confined boundary elements) significantly enhanced the overall seismic performance of RM walls with limited changes in masonry common construction methods. It was concluded that RM shear walls having end confinement are capable of attaining high ductility and energy dissipation capacities. This would result in reduced seismic design forces making RM a competitive alternative construction material (Shedid et al., 2010a).

Banting and El-Dakhakhni (2012) also presented an experimental investigation of RM shear walls with confined boundary elements. It was concluded that the newly proposed construction approach (addition of boundary elements) is capable of significantly enhancing the ductility and thus reducing the seismic design forces. Another experimental program was designed by Banting and El-Dakhakhni (2014) to establish prescriptive design requirements for the confinement of RM shear walls with boundary elements. Based on their experimental results, it was concluded that the

presence of boundary elements inhibited buckling of vertical rebars and delayed crushing of grout core in compression toes. Additionally, it prevented the sudden drop in strength at the onset of cracking and face-shell spalling. Therefore, the lateral confinement in boundary elements resulted in substantial improvement in the overall response of RM shear walls (Banting and El-Dakhakhni, 2014).

More recently, Ezzeldin et al. (2016) investigated the impact of adding boundary elements on the seismic collapse risk of RM shear walls. The results demonstrated that the addition of boundary elements increased the walls' period-based ductility and collapse capacity. It was found that RM walls with boundary elements satisfied the acceptance criteria of the Federal Emergency Management Agency (FEMA P695, 2009). The studied walls had collapse probabilities much lower than 20% at the Maximum Considered Earthquake (MCE). Therefore, it was concluded that higher seismic response modification factor (*R*) could be assigned for RM shear walls with boundary elements.

The 2015 National Building Code of Canada (NBCC-15) limits the application of each SFRS type to certain heights depending on the seismicity level of the building location. Table 5.1 summarizes the building height limits assigned in NBCC-15 to ductile and moderately ductile RM shear walls. Typically in building codes such as NBCC-15 and ASCE7-16, the SFRS restrictions such as height limits are derived from past experience and often from experimental or numerical studies of the seismic response (Filiatrault et al., 2013). Specified height limits are meant to prevent the development of highly localized inelastic deformation demand.

Table 5.1 NBCC-15 building height limits

			Height Limits			
			Seismicity [$I_E F_a S_a(0.2)$]			
Type of SFRS	**R_d**	**R_o**	< 0.2	≥ 0.2 to < 0.35	≥ 0.35 to ≤ 0.75	> 0.75
Ductile RM Shear Walls	3.0	1.5	No Limit	No Limit	60 m	40 m
Moderately Ductile RM Shear Walls	2.0	1.5	No Limit	No Limit	60 m	40 m

The possibility of high localized inelastic demand tends to increase as the height increases in regions with high seismicity (Filiatrault et al., 2013). A new category of RM shear walls (i.e. ductile) was recently added to NBCC in 2015 for RM structures designed and detailed according to the Canadian Standards Association (CSA) S304-14 "design of masonry Structures standard."

Ductile RM shear walls have special detailing requirements to ensure sufficient inelastic deformation capacity. Consequently, CSA S304-14 assigned a higher ductility-related force modification factor to ductile RM shear walls compared to that of moderately ductile RM walls. However, as shown in Table 5.1, ductile RM shear walls are assigned the same building height limits of moderately ductile RM walls. On the contrary, ductile Reinforced Concrete (RC) shear walls in NBCC-15 are assigned No Limit (NL) for the building heights regardless of the location's seismic hazard, whereas the moderately ductile RC walls are assigned a 60 m height limit when $I_E F_a S_a(0.2)$ is higher than 0.75. This could be attributed to the limited research concerned with the seismic performance and collapse capacity of ductile RM shear walls. In ASCE7-16, similar building height limits are assigned for special RM and RC shear walls for both building frame and load-bearing structural systems. In addition, the same seismic response modification factors are specified for special RM and RC shear walls in load-bearing systems. For building frame systems, a slightly lower force modification factor (R) of 5.5 is assigned for special RM shear walls while R of 6 is given for special RC shear walls. Several recent experimental and numerical studies of RM masonry structural walls with boundary elements highlighted its superior seismic performance and high collapse capacity, such as (Banting and El-Dakhakhni, 2012, 2014; Ezzeldin et al., 2017, 2016; and Shedid et al., 2010b). However, no study, up to the authors' knowledge, performed a validation of the NBCC-15 specified building height limits for ductile RM shear wall buildings based on seismic collapse performance.

In Canada, multi-storey masonry buildings were mainly utilized in regions with low seismic hazard. For instance, in 1970, a 24-storey apartment building (Place Louis Riel) was constructed in Winnipeg (Drysdale and Hamid, 2005). The building's structural system consisted of load-bearing reinforced masonry walls built using 200mm high strength concrete masonry blocks to resist vertical and lateral loads. In Hamilton, which is another region with low seismicity in Canada, high-rise unreinforced masonry apartment buildings up to 17-storey were constructed before the 1975 update to building code with the new seismic requirements (Drysdale and Hamid, 2005). After the building code update, the practice changed to utilize reinforced masonry construction, and up to 21-storey apartment buildings were constructed in the Hamilton region (Drysdale and Hamid, 2005). In regions with high seismic hazard the use of conventional reinforced masonry in multi-storey buildings will require long and thick walls making it an uneconomical and impractical alternative. Thus, the use of masonry in high seismicity regions was

limited to low-rise buildings and single-storey housing. However, based on the previously discussed research conducted in the last decade, it is evident that there is a great potential for RM shear walls with confined boundary elements as a practical alternative. This resulted in the recent addition of the ductile category for RM shear walls in NBCC-15.

The current study aims at evaluating the seismic performance and collapse capacity of ductile RM shear wall buildings with varying heights and located in moderate or high seismic hazard regions. The focus is on ductile RM shear walls with confined boundary elements. The primary objective is to propose building height limits that ensure satisfactory seismic response and low seismic collapse risk using FEMA P695 (2009) methodology. Therefore, this would demonstrate the potential of utilizing ductile RM shear walls in multi-storey buildings located in regions with moderate and high seismic hazards. This is achieved by designing six archetype ductile RM shear wall buildings with total heights exceeding the code specified limits. The buildings are located in Montréal and Vancouver, Canada, to represent the moderate and high seismicity levels of NBCC-15. A simplified macro-model is developed for RM shear walls using Seismostruct program (Seismosoft, 2016). The model is extensively calibrated and validated using available experimental data. Using the validated numerical model, nonlinear static and dynamic analyses are executed to evaluate the seismic performance. The dynamic analyses are performed using a series of ground motion records compatible with NBCC-15 design response spectrum for the corresponding building location. The selected records are obtained from the processed time series of Assatourians and Atkinson (Assatourians and Atkinson, 2010) and are scaled to match the target response spectrum at the natural period of each building. The collapse capacity is evaluated and quantified according to FEMA P695 methodology. Finally, height limits are proposed for ductile RM shear walls to ensure satisfactory seismic performance and low seismic collapse risk.

5.3 Selection and Characteristics of Archetype Buildings

The archetype buildings in the present study are selected such that it allows a comprehensive investigation of the height limits assigned by NBCC-15 to ductile RM shear walls. Given that the height limit is a function of the location seismicity (i.e. seismic hazard index in NBCC-15), the archetypes are assumed to be located in Montréal and Vancouver to represent regions with moderate and high seismic risks in Canada, respectively. For the moderate seismicity region (i.e. Montréal), the selected archetype buildings are 18-, 19-, and 20-storey buildings. The basis of this selection is to result in a total building height that is more than the code limit (i.e. more than 60 m

for the moderate seismicity regions). In addition, this selection range provides a high resolution of the impact of the number of floors on the seismic performance and collapse capacity. Similarly, for Vancouver, the high seismic risk region, the chosen archetypes have a number of floors varying between 12 and 14. Each selected building has a total height that is more than the 40 m limit assigned by the code for regions with high seismicity. The selected heights allow for careful investigation of the height effect on overall structural performance. Summary of the selected buildings' characteristics is shown in Table 5.2.

Table 5.2 Characteristics of the studied buildings

Archetype ID	Number of Stories	Proposed Location	$I_E F_a S_a(0.2)$	Seismicity	NBCC-15 Height Limit (m)	Total Height (m)
18S-M	18	Montréal, QC	0.595	Moderate	60	63
19S-M	19					66.5
20S-M	20					70
12S-V	12	Vancouver, BC	0.848	High	40	42
13S-V	13					45.5
14S-V	14					49

The selected archetypes are apartment buildings (i.e. residential occupancy) having the plan layout and isometric three-dimensional view shown in Figure 5.1. A generic layout is chosen to represent common load-bearing masonry buildings. The structural layout utilized in this study is a proposed hybrid load-bearing structural system for masonry buildings consisting of Primary (P) and Secondary (S) RM walls, as illustrated in Figure 5.1(a). The primary walls are ductile RM shear walls with boundary elements designed to resist all lateral forces and part of gravity loads. The ductile shear walls are located at the perimeter of the building to maximize its torsional resistance and control the axial load level. The secondary walls are termed gravity walls and are utilized in carrying the vertical forces from gravity loads. In addition, the gravity walls are designed to ensure deformation compatibility with the ductile walls at the maximum expected inter-story drift. A similar structural system of primary and secondary shear walls was introduced by Paulay and Priestley (Paulay and Priestley, 1992) and was adopted in the New Zealand Standard for the design of reinforced concrete masonry structures (NZS 4230-2004) (New Zealand Standard, 2004). Using this structural system layout, it is possible to control the level of axial load on the RM shear walls with boundary elements such that it does not adversely affect its ductility

and displacement capacity. Dimensional limitations are imposed on the gravity walls so that they remain elastic under the considered seismic design level.

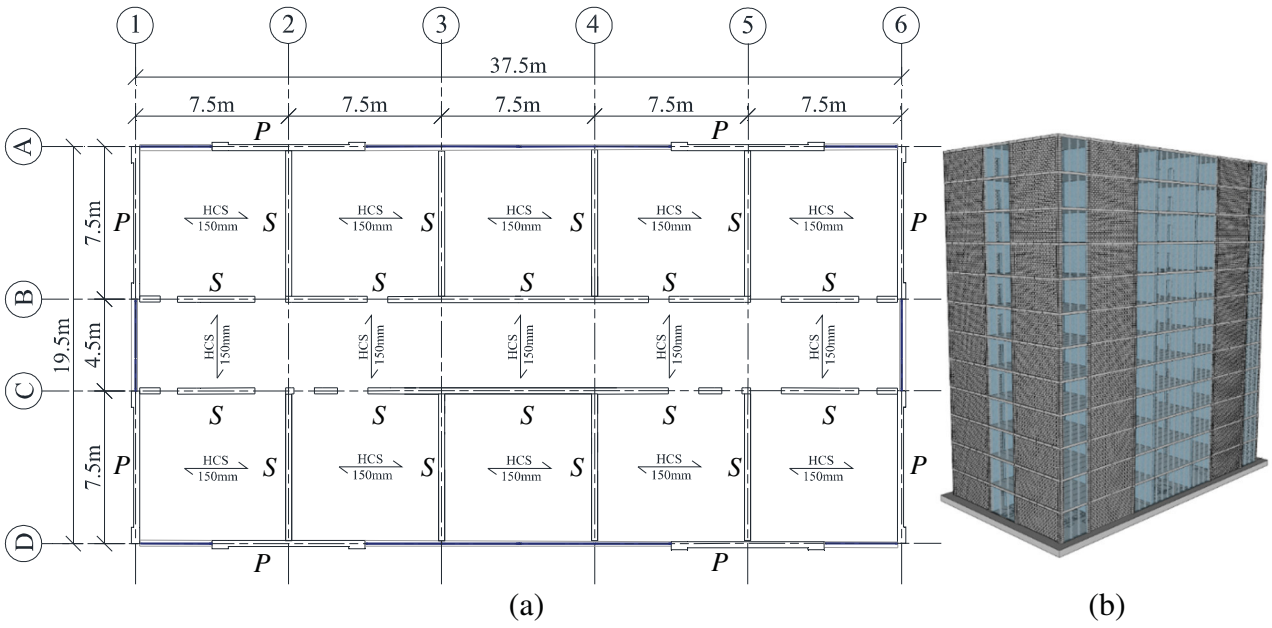

Figure 5.1 Archetype buildings: (a) typical floor plan view; and (b) three-dimensional isometric view of a 12-storey building

This is achieved by limiting the gravity walls total stiffness to one-quarter the stiffness of the longest ductile shear wall as recommended by Paulay and Priestley (1992) for primary walls. The stiffness of long or stiff gravity walls is controlled by introducing vertical separation joints at appropriate intervals. This type of joints follows the same details of movement joints, which are typical in reinforced concrete masonry buildings construction. The selection of this system in the present study is based on the results seen in a previous study; where all walls were ductile with boundary elements and part of the SFRS (Aly et al., 2017). The findings revealed very conservative seismic collapse capacity suggesting that there might be a potential for design optimization by reducing the number of ductile RM walls in the plan (Aly et al., 2017). The flooring system in this structural layout is composed of 150 mm thick precast prestressed Hollow Core Slabs (HCS) spanning for a maximum of 7.5 m. The layout of the HCS units was alternated in the plan to further control the level of axial load on the ductile RM shear walls. The total typical floor height is 3.5 m, which allows for 2.7 m clearance, 0.3 m for flooring, and 0.5 m for overhanging (Mechanical, Electrical, and Plumping) MEP services. The total heights of the reference buildings are summarized in Table 5.2.

5.4 Design of Archetype Buildings

The design loads are defined according to NBCC-15. The flooring load (including finishes and partitions) is considered as 1 kPa, and a load of 0.5 kPa is used for MEP services. For the estimation of earthquake design forces, the reference soil class C of NBCC-15 is assumed for the buildings' sites as it results in a soil modification factor F(0.2) of 1. This was necessary to result in an intermediate seismic hazard index in the moderate and high seismicity categories of NBCC-15 to represent the average of each group. As shown in Table 5.2, the seismic hazard index, $I_E F_a S_a(0.2)$, is 0.848 and 0.595 for the buildings located in Vancouver and Montréal, respectively. It can be seen that the seismic hazard index of Montréal is an intermediate value within the range of ≥ 0.35 and ≤ 0.75. Based on these seismic hazard indices, the assigned height limits as per NBCC-15 are 40 m for Vancouver and 60 m for Montréal. It is noteworthy that changing the soil class would result in slight changes in the seismicity index of the studied locations. However, as the value of PGA_{ref} is ranging from 0.3 to 0.4 for the selected locations, the changes will not be very significant. For instance, if site class D was assumed, the seismic hazard index will not be affected for Montréal and will be 6% lower for Vancouver. Nevertheless, for a site class B, the seismicity hazard index will be reduced by approximately 23% for both locations.

The seismic demands are calculated using the linear dynamic analysis procedure by the modal response spectrum method provided in Article 4.1.8.12 of NBCC-15. This method is selected as it is permitted for all reference buildings without restrictions on height or seismic hazard. The elastic response spectra of Vancouver and Montréal, along with the studied buildings, are shown in Figure 5.2. Three-dimensional finite element models of the archetype buildings are developed in ETABS program (CSI, 2015). The models are verified and used to estimate the seismic demands on walls based on the linear dynamic analysis procedure of NBCC-15. Wind loads are calculated based on NBCC-15. As expected, it did not govern over seismic loads for the buildings in Vancouver, Canada. However, for the high-rise buildings located in Montréal (i.e. more than 18-storey), the factored wind base shear governed the lateral demand over seismic forces. Although Montréal's seismicity is moderate, the design response spectrum is characterized by predominant high frequencies making it less severe on tall and flexible buildings. This is also evident in the shape of Montréal's response spectrum and the high ratio of S_a (0.2)/S_a (5.0). It should be noted that this occurred because the primary walls of the SFRS are ductile RM shear walls with ductility-related seismic response modification factor (R_d) of 3 and overstrength-related seismic response

modification factor (R_o) of 1.5. The buildings are designed and detailed in accordance with the special seismic design provisions provided in CSA S304-14, design of masonry structures standard, clause 16.

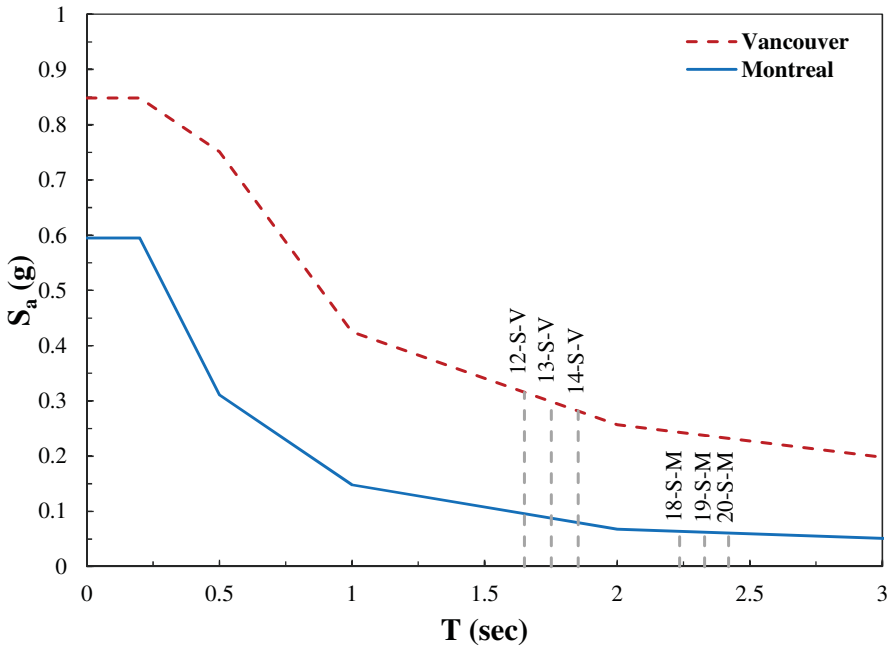

Figure 5.2 Elastic response spectra and archetype buildings

The gravity shear walls (i.e. the secondary walls) are designed using fully grouted standard concrete masonry stretcher blocks to resist axial forces from gravity loads, bending moments and shear forces from deformation compatibly. The walls are designed and detailed according to the recommendations given in NZS 4230-2004 clause 12 for secondary walls. To reduce the induced bending moments and shear forces on the gravity walls due to deformation compatibility, the length of the gravity walls is limited to a maximum of 1 m using vertical separation joints. Thus, the stiffness of the longest gravity wall is less than one-quarter that of the longest ductile wall. The induced actions on gravity walls are estimated at the maximum allowable inter-storey drift of 2.5%, as specified by NBCC2015. The stiffness (K) of the gravity walls is estimated in each floor using the model developed in ETABS program (CSI, 2015) by applying a unit force at the top and bottom of the walls in that floor. Then, shear forces (V) are evaluated by multiplying the estimated stiffness (K) by the maximum displacement corresponding to the 2.5% inter-storey drift limit. Finally, the resulting bending moments are estimated by multiplying the calculated shear force (V) by half of the wall height. The design bending moments included the moments induced by the

deformation compatibility and due to P-Δ effects. The bending moments resulting from P-Δ effects are calculated by multiplying the axial forces corresponding to the lateral load combination by the lateral deflection of the walls at the drift limit of NBCC-15. It is worth noting that these forces were not very significant as a result of the reduced stiffness of the gravity walls by the vertical movement joints spaced as suggested by NZS 4230-2004 clause 12. Conversely, the ductile shear walls (i.e. the primary walls) are designed using fully grouted standard concrete masonry stretcher blocks in the web, and fully grouted C-shaped pilaster block units in the boundary elements. A major challenge in designing multi-storey RM buildings is the need for higher specified compressive strength (f'_m), especially for the walls subjected to combined vertical and lateral loads (i.e. the primary walls). In this study, the primary walls have boundary elements made up of C-shaped pilaster block units. This provides flexibility in using higher grout strength, different number of vertical bars and closer spacing of lateral ties (hoops). Thus, it is possible to increase the overall axial load capacity of the boundary elements.

The concrete blocks in the gravity walls are assumed to have a compressive strength of 30 MPa. In addition, regular block filler with an average compressive strength of 20 MPa is assumed for the gravity walls' grout. Thus, the specified compressive strength (f'_m) according to Table 4 of S304-14 is 13.5 MPa for the gravity walls. For the ductile walls, a higher compressive strength was needed to satisfy the inelastic rotational demand, especially in the boundary elements. It was established by several researchers such as Drysdale and Hamid (1979), Khalaf (1996), Sarhat and Sherwood (2013), and Fortes et al. (2015) that increasing the block and grout compressive strengths would enhance the masonry prism compressive strength. It was also shown that the improvement is most effective when the grout and the blocks have close stiffness properties (Drysdale and Hamid, 2005). Therefore, in the ductile walls, a high compressive strength of more than 40 MPa is assumed for the boundary elements' pilaster blocks, and a 45 MPa is assumed for the compressive strength of the grout. It is allowed by CSA S304-14 to use higher specified compressive strength (f'_m) than the values shown in Table 4, of S304-14, when the concrete blocks have compressive strength that is higher than 30 MPa. The higher values can be determined by testing of masonry prisms. In this study, the approach outlined in Appendix B of NZS 4230-2004, which is based on the research of Priestley and Chai (1984), is used to calculate the specified compressive strength for the ductile walls based on the contributions from masonry and grout. Thus, the calculated compressive strength (f'_m) for the ductile walls' boundary elements is equal

to 35 MPa. For the ductile walls web region, the compressive strength (f'_m) is assumed similar to the gravity walls (i.e. 13.5 MPa).

Summary of the ductile RM shear walls with boundary elements design details (i.e. dimensions and reinforcement) is shown in Figure 5.3(a). Boundary element size and web stretcher blocks width are reduced every four floors to optimize the design, whenever possible. In addition to Figure 5.3(a), Table 5.3 summarizes the fundamental characteristics of the archetype buildings' ductile walls in the plastic hinge region.

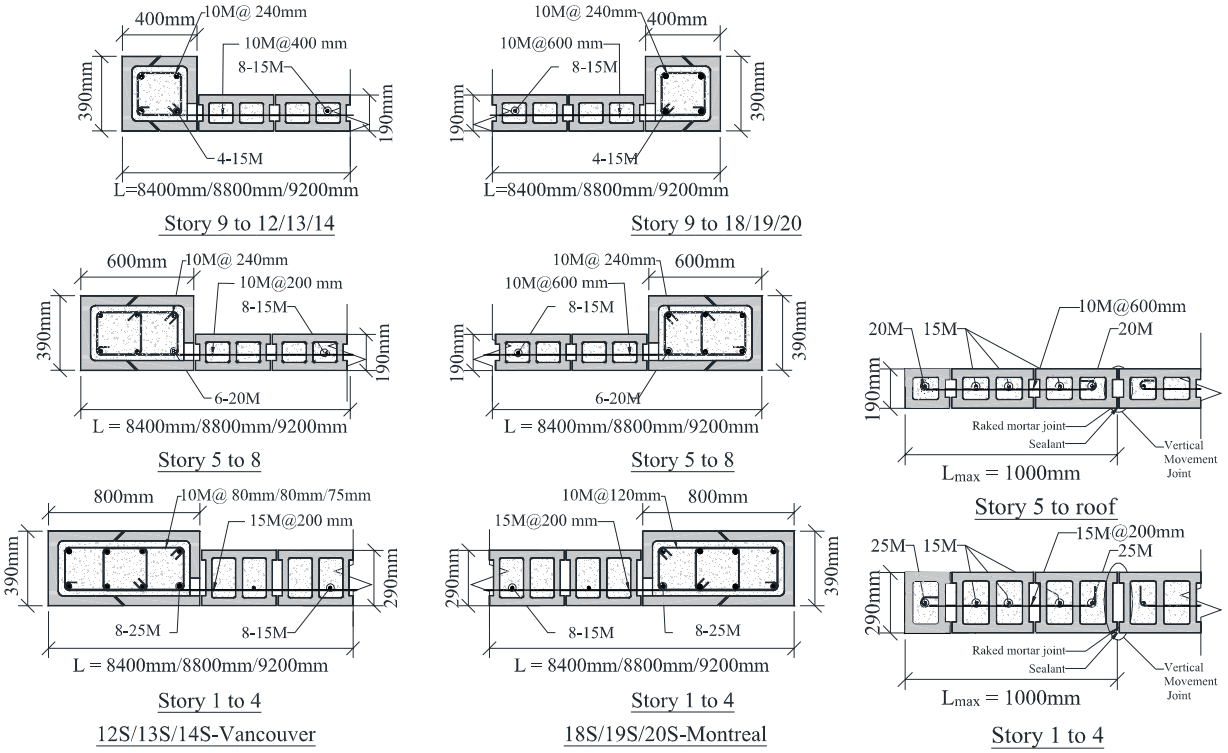

Figure 5.3 Dimensions and reinforcement details of: (a) ductile RM shear walls with boundary elements (Primary walls); and (b) gravity RM walls (Secondary walls)

These details are shown for the N-S ductile RM walls (i.e. the primary walls on axes 1 and 6) which are analyzed in the present study. The axial force (P_f) used in calculating the axial load ratio in Table 5.3 is calculated from the governing load combination, which included the earthquake load case. It can be seen that the axial pre-compression ratio ($P_f/A_g f'_m$) is ranging from 7.7% (building 12S-V) to 11.6% (building 20S-M). This axial load level is relatively low compared to that of the conventional masonry wall load-bearing alternative. This is mainly due to the utilized

hybrid structural layout, the selected arrangement for the HCS panels in the plan, and the use of higher compressive strength for the blocks and grout in the boundary elements. The dimensions and reinforcement details of the gravity RM walls are shown in Figure 5.3(b). In the first four stories, 300mm blocks are used to ensure sufficient resistance to the factored axial forces from gravity loads in addition to the shear forces and bending moments from the deformation compatibility. The blocks are reduced to 200mm for the top floors to optimize the design.

Table 5.3 Details of the studied RM shear walls with boundary elements

Archetype ID	l_w (mm)	h (mm)	Aspect Ratio	Configuration	ρ_v (%)	ρ_h^* (%)	$P/f'_m A_g$ (%)
18S-M	8400	63000	7.50		0.37	0.34	10.7
19S-M	8800	66500	7.56	End Confined	0.35	0.34	11.2
20S-M	9200	70000	7.61		0.34	0.34	11.6
12S-V	8400	42000	5.00		0.37	0.34	7.7
13S-V	8800	45500	5.17	End Confined	0.35	0.34	8.2
14S-V	9200	49000	5.33		0.34	0.34	8.7

*ρ_h is the ratio of horizontal web reinforcement

5.5 Nonlinear Numerical Modelling

Many researchers recently utilized distributed inelasticity beam-column element models to accurately simulate the response of RM structures, such as Abdel-Latif et al. (2015), Siyam et al. (2016), and Ezzeldin et al. (2016). In this study, a nonlinear finite element model is created for the reference buildings using Seismostruct program (Seismosoft, 2016). The RM shear walls are simulated using distributed inelasticity element models with fibre sections. A Displacement-Based (DB) beam-column element model is used with adequate meshing for the number of elements as well as section fibres to attempt to reproduce the nonlinear response. The adapted modelling technique is suitable for the application of this paper as the study involves a significant number of nonlinear static and dynamic analyses. The proposed model balances between reasonable accuracy and computational efficiency. The following subsections outline the utilized material, section, and element models.

5.5.1 Material models

The utilized modelling approach primarily depends on fibres' discretization to capture the flexural response of the structural members. Thus, the use of reliable material models is crucial. There is limited research concerned with the axial and cyclic compressive stress-strain behaviour of fully grouted concrete masonry. As a result, there are no available pre-defined constitutive

models for the response of grouted concrete masonry in most of the available numerical modelling programs such as Seismostruct (Seismosoft, 2016). In addition, previous research studies such as (Banting and El-Dakhakhni, 2014), (Drysdale and Khattab, 1995) and (Shing et al., 1990), demonstrated that the anisotropic characteristics of unreinforced masonry are substantially reduced when concrete masonry is fully grouted and well-detailed with horizontal and vertical reinforcement. Consequently, the nonlinear cyclic response of masonry is modelled using the uniaxial concrete material model proposed by Mander et al. (1988). Among the available concrete constitutive models, Mander et al. (1988) model was capable of simulating the nonlinear response of fully grouted masonry, which has an overall response similar to that of concrete. This is also in line with the findings of other research studies such as (Abdel-Latif et al., 2015) and (Hamzeh et al., 2018), where the response of grouted masonry was also modelled using Mander et al. (1988) concrete model.

In fully grouted concrete masonry, the hollow concrete blocks are filled with grout, which is a concrete mix having a very high slump. For the purposes of modelling the global response, the face-shell spalling in grouted masonry is assumed to be approximately represented by the cover spalling in concrete. It is essential to highlight that at the local level, face-shell spalling in grouted concrete masonry is not identical to the spalling of concrete cover. This is mainly because in grouted masonry, the unconfined portions include masonry face-shell as well as a concrete cover (outside the confined grout core), and the spalling occurs in both unconfined portions with larger chunks. Mander et al. (1988) material model is calibrated by five parameters, namely compressive strength (f'_m), tensile strength (f_t), modulus of elasticity (E_m), and strain at peak stress (ε_{mo}). For modelling validation, the values of these parameters are based on the material tests reported in the corresponding experimental studies. However, for the archetype buildings, the values are as per the design standard (i.e. CSA S304-14) recommendations and the assumed material properties for this study. Therefore, with the proper definition of these parameters, especially the peak stress (f'_m) and the corresponding strain (ε_{mo}), the material model would be capable of representing the global response of grouted masonry. The behavioural differences between concrete and fully grouted concrete masonry are accounted for by the proper definition of the material properties. This is also verified by comparing the simulated global response against the experimental results from testing of fully grouted RM shear walls. It should be noted that this material model might not be as effective for simulating the response of ungrouted or partially grouted masonry shear walls.

Mander et al. (1988) model that is implemented in Seismostruct program (Seismosoft, 2016) uses the cyclic response rules developed by Martinez-Rueda and Elnashai (1997). These rules define the inelastic strain and account for the increase in stiffness deterioration and strength degradation with the increase in strain levels (i.e. it considers the accumulation of damage). Consequently, it provides an unconditionally numerically stable concrete constitutive relationship with strength and stiffness degradation at any strain level. The model accounts for the confinement effect by assuming a constant confining pressure over the range of stress-strain. The stress-strain curve assigned to the confined portions is multiplied by the confinement factor, as proposed by Mander et al. (1988), which is defined as the ratio between confined and unconfined concrete compressive strengths.

The reinforcement nonlinear cyclic response is represented using the uniaxial stress-strain model derived by Menegotto and Pinto (1973). This model represents the cyclic response of reinforcement and is suited for structures that are subjected to loading histories with substantial reversals in loading cycles. It accounts for strain hardening, Baushinger effects, and pinching response in the hysteretic loops. The model defined in Seismostruct incorporates the isotropic strain hardening rules defined by Filippou et al. (1983). Menegotto and Pinto material model is known for its reliability, simplicity, and numerical stability (Carvalho et al., 2013). The model is calibrated based on material properties (i.e. modulus of elasticity, yield strength, and fracture/buckling strain) and other parameters to represent strain hardening, Baushinger effects, and pinching response. For validation of the numerical model, the reinforcement properties reported in the literature for each wall was used. Nevertheless, for the archetype buildings' numerical models, the reinforcement yield strength (f_y) and modulus of elasticity (E_s) are assumed to be 400 MPa and 200 GPa, respectively, as recommended by CSA S304-14.

5.5.2 Section model

In the fibre modelling approach utilized in this study, the cross-section is subdivided into several springs (i.e. fibres) acting in parallel. The corresponding uniaxial stress-strain relationships, as defined in the previous subsection, for masonry and reinforcement are assigned to the section fibres. Similar to previous studies, such as (Hamzeh et al., 2018), the boundary elements are discretized to differentiate between the confined (regions inside the confining hoops) and the unconfined (face-shell and concrete grout regions outside the confining hoops) portions of the cross-section. As such, the confinement effect on the stress-strain response is only taken into

consideration for the confined grout core in the boundary elements. The section fibres are then used to satisfy the equilibrium at each of the two integration sections for each element. The number of section fibres should be enough to ensure proper replication of the section stress-strain state. The ideal number of fibres mainly depends on the cross-section shape, material properties, and the expected degree of nonlinearity. Seismostruct user's manual (Seismosoft, 2016) recommends 100 fibres for cross-sections composed of a single material and 200 for more complex cross-sections. In this study, a sensitivity analysis is performed to estimate the optimum number of section fibres needed to accurately simulate the cross-section's stress-strain distribution and flexural response. Wall W2 from (Banting and El-Dakhakhni, 2014), details are shown in Table 5.4, is selected to investigate the impact of section fibres on the force-displacement response. The study is performed for numbers of fibres ranging from 200 to 700 with increments of 50 and 100.

Table 5.4 Summary of the details of walls used for the numerical model validation

Wall No. in Literature	Reference	l_w (mm)	h (mm)	Aspect Ratio	Configuration	ρ_v (%)	ρ_h (%)	$P/f'_m A_g$ (%)
W 1	(Shedid et al., 2010a)	1802	3990	2.21	Rectangular	1.17	0.30	6.6
W 2	(Shedid et al., 2010a)	1802	3990	2.21	Flanged	0.55	0.30	5.4
W 5	(Shedid et al., 2010a)	1802	2660	1.48	Flanged	0.55	0.60	5.4
W 6	(Shedid et al., 2010a)	1802	2660	1.48	End Confined	0.55	0.60	5.4
W 1	(Banting and El-Dakhakhni, 2012)	1803	3990	2.21	End Confined	0.56	0.30	3.3
W 2	(Banting and El-Dakhakhni, 2014)	1235	3990	3.23	End Confined	0.69	0.30	6.0

The resulting force-displacement responses from the different section fibres are shown in Figure 5.4. It is observed that there are no significant changes in the overall response when the number of fibres is increased beyond 200 (the value recommended by Seismostruct user manual). However, sometimes, the last loop is not captured. Additionally, the use of a large number of fibres (i.e. 600 or 700) did not result in any significant increase in the analysis time, but it ensured that the post-peak response is fully captured. Therefore, 700 fibres are used in the developed model to guarantee the proper reproduction of the stress-strain distribution and numerical convergence in most cases.

5.5.3 Element model

An inelastic DB beam-column element is used to model the RM shear walls. This finite element model type is capable of capturing material inelasticity and geometric nonlinearities (Seismosoft, 2016). It accounts for plasticity spread along member length and across its depth. For estimation of the nonlinear response, it assumes constant axial strain and linear curvature distribution. In

addition, the element's stiffness is estimated through the integration of moment diagrams with linear curvature interpolation (Carvalho et al., 2013). Therefore, there is a limitation in the capability of this finite element formulation in capturing highly inelastic behaviour where curvatures have higher-order nonlinear distributions along the element height. This issue is commonly resolved through proper element discretization and definition of the first member length as a function of plastic hinge length. For this reason, the choice of the number of elements and first member length is very critical when DB beam-column elements are used to model structural members.

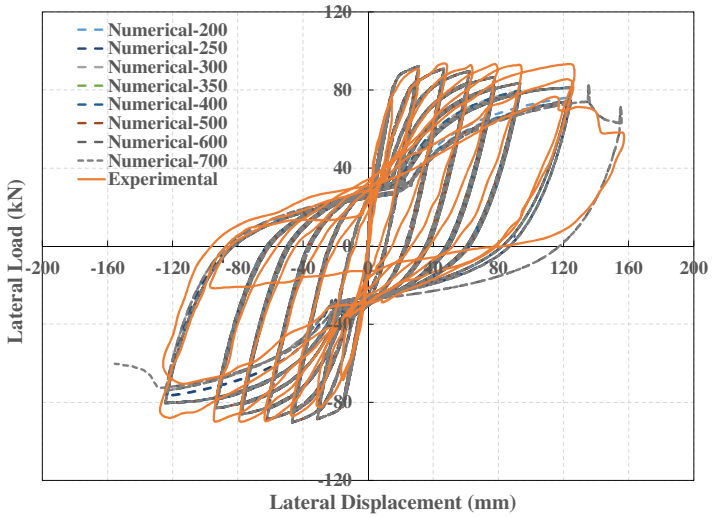

Figure 5.4 Experimental and numerical hysteresis loops of wall W2 (Banting and El-Dakhakhni, 2014) with varying number of fibres

In DB beam-column elements, the interpolation of displacement functions results in constraining the strain localization within a single element (Coleman and Spacone, 2001). Thus, in RM structural walls, the strain localization will be concentrated in the first element above the wall base. Therefore, it was highlighted by several researchers that the use of the plastic hinge length (l_p) for the first element above the wall's base produces accurate and objective results (e.g. Légeron et al. (2005), Calabrese et al. (2010), and Ezzeldin et al. (2016)). However, Calabrese et al. (2010), highlighted that localization and strain concentrations occur in the extreme integration point and not the extreme element. Therefore, the length of the extreme member could be twice the plastic hinge length ($2*l_p$), in the common case of two integration sections per element. This means that the length to each integration point will be equal to the plastification length (l_p). This regularization technique achieves an objective global response in cases where softening sectional

behaviour is present. Légeron et al. (2005) also recommended the utilization of elements with equal lengths. In addition, Seismostruct user manual recommends 4 to 6 elements for each structural member.

A sensitivity analysis is performed to investigate the validity of the proposed geometrical model for RM shear walls. The proposed model is illustrated in Figure 5.5. It consists of an extreme member (first element) with length equal to twice the plastic hinge length and five members with equal lengths. A total of 6 members are used for each structural wall to conform with the software manual recommendations (Seismosoft, 2016).

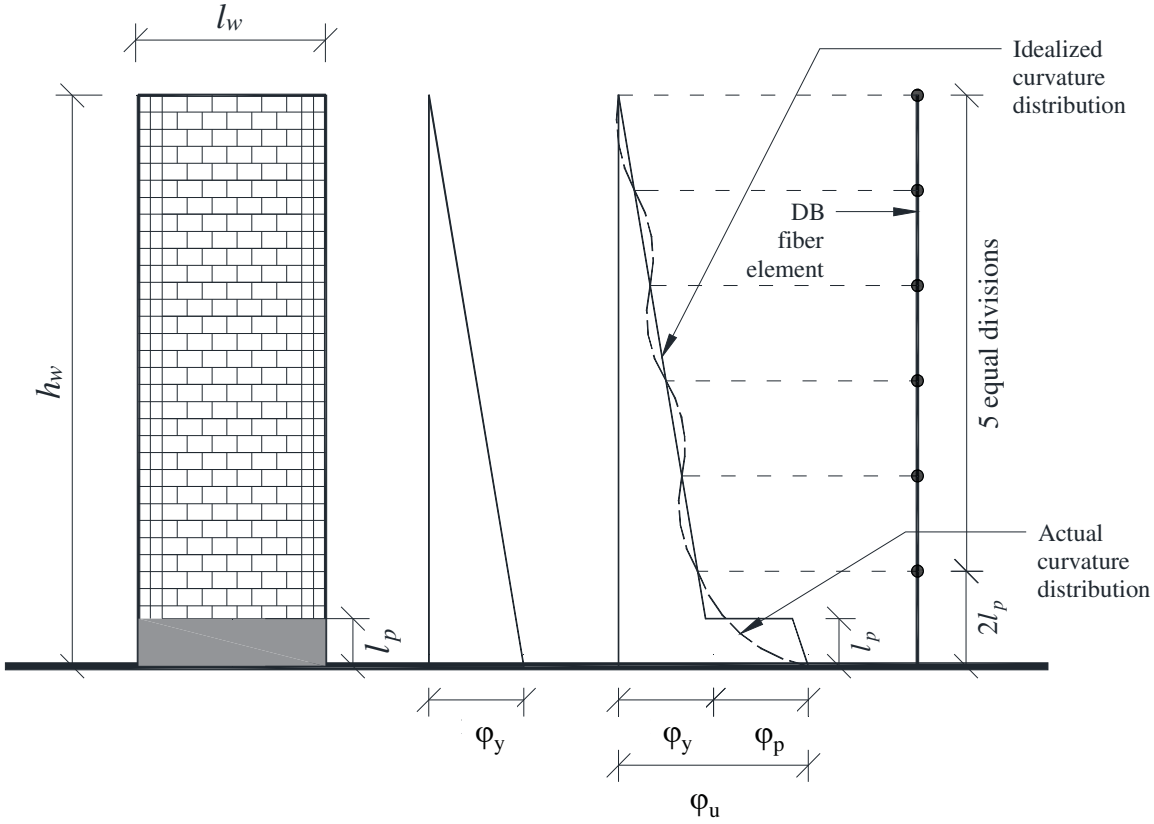

Figure 5.5 Schematic diagram of the proposed geometrical model for RM shear walls

The plastic hinge length is calculated using the expression derived by Bohl and Adebar (2011). This expression was developed based on numerical simulations of 22 cantilever RC structural walls using a validated nonlinear finite element model. The expression, Eq. (5.1), is a function of the wall's length (l_w), effective height (moment-to-shear ratio, z), and axial compresion (P). It results in plastic hinge lengths that are in good agreement with experimental results for RM shear

walls (Ezzeldin et al., 2016). In addition, it is one of the few available plastic hinge length formulas that account for the axial load effect on the inelastic displacement capacity of walls. Thus, it is deemed appropriate to be utilized in calculating the plastic hinge length for the proposed model.

$$l_p = (0.2l_w + 0.05z)\left(1 - \frac{1.5P}{f_c' A_g}\right) \leq 0.80L_w \tag{5.1}$$

The use of these recommendations is assessed against the ability of the modelling approach in producing objective results independent of the meshing size. It is commonly known that response simulations using DB beam-column elements are sensitive to the number and length of used elements. Figure 5.6 compares the resulting hysteresis loops of wall W2 from (Banting and El-Dakhakhni, 2014), details are shown in Table 5.4, using different numbers of elements and extreme element lengths against experimental results. It is clear from Figure 5.6(a) that using an extreme member (i.e. first element) having a length equal to twice the plastic hinge ($2l_p$) resulted in the best agreement with the experimental results.

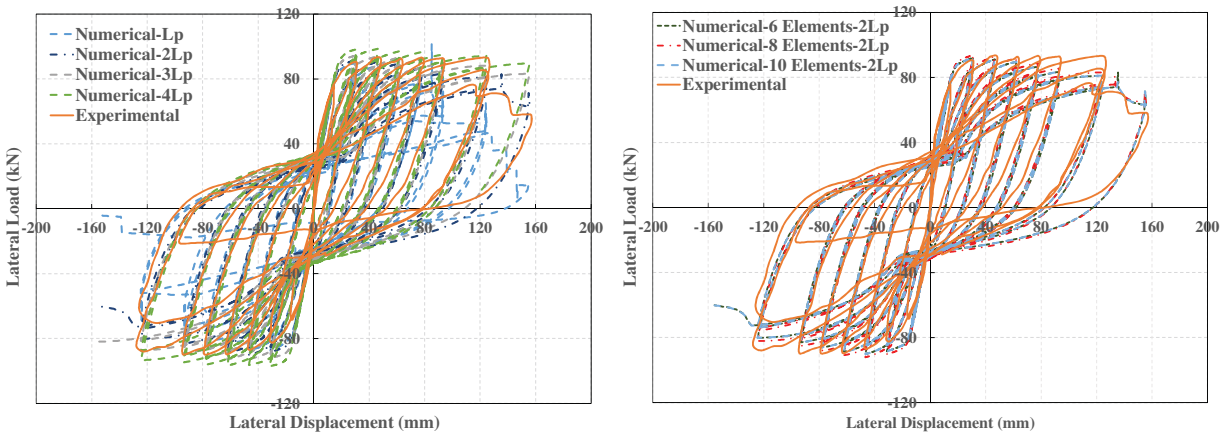

(a) (b)

Figure 5.6 Experimental and numerical hysteresis loops of wall W2 (Banting and El-Dakhakhni, 2014) with: (a) 6-elements and varying extreme member length; and (b) $2l_p$ extreme member length and a varying number of elements

It should be highlighted that the total number of elements was 6, as per the recommendation of Seismiostruct software manual, and only the length of the first element was changed. In addition, as shown in Figure 5.6(a), using the first element with length equal to plastic hinge length (l_p) results in underestimating the strength, stiffness, and hysteretic energy dissipation capacity. On the

contrary, the models with first elements' lengths that are longer than l_p overestimate the capacity and do not capture the strength and stiffness degradation.

For the same wall (W2), the predicted hysteresis response using an extreme member length of $2l_p$ and varying the total number of elements is presented in Figure 5.6(b). It can be seen that changing the number of elements did not result in any impact on the simulated numerical response using the proposed model. Without this regularization technique, it was observed that increasing the number of elements, when using a DB element formulation, underestimates the strength and results in sharp degradation. Conversely, a smaller number of elements would overestimate the strength and result in almost no post-peak degradation. Thus, the proposed geometrical model for RM shear walls using the suggested regularization technique (i.e. extreme member length equal to $2l_p$) is proven to be objective (i.e. non-sensitive to changes in number or length of elements).

5.6 Numerical Modelling Validation

The proposed nonlinear modelling approach, along with the calibrated material modelling parameters implemented in this study are validated against existing experimental test results of RM shear walls. The experimental data is obtained from (Shedid et al., 2010a), (Banting and El-Dakhakhni, 2012), and (Banting and El-Dakhakhni, 2014). Summary of the walls' details is given in Table 5.4. It should be noted that available experimental testing of RM shear walls with boundary elements is very limited as it is a relatively newly proposed construction technique for RM structures. Up to the authors' knowledge, only the studies by Banting and El-Dakhakhni (2012 and 2014) and Shedid et al. (2010a) included quasi-static cyclic testing of RM shear walls with confined boundary elements. To overcome the limited number of available experimental tests of RM shear walls with boundary elements, the modelling validation included walls that are rectangular, flanged, and end-confined. Validating the numerical model against walls with different cross-sectional configurations, aspect ratios, and axial stress levels ensures the accuracy, reliability, and robustness of the utilized modelling approach. The end confined walls selected to verify the accuracy and reliability of the proposed numerical model had aspect ratios ranging between 1.48 and 3.23, and axial pre-compression ratios ranging between 3.3% and 6.0%. A comparison between experimental and numerical load-displacement response of the walls is shown in Figure 5.7.

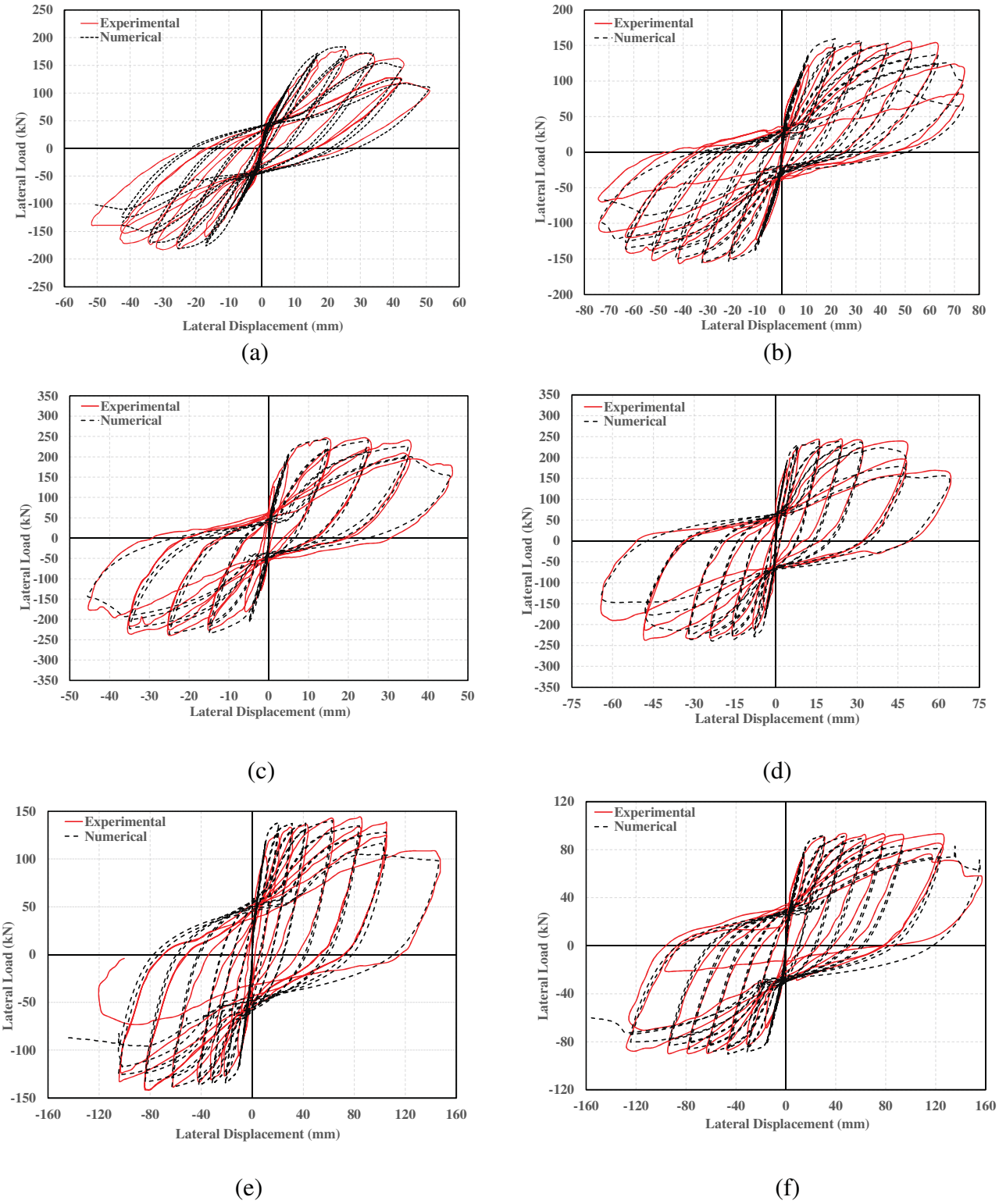

Figure 5.7 Experimental and numerical load-displacement response of: (a) rectangular wall W1 (Shedid et al., 2010a); (b) flanged wall W2 (Shedid et al., 2010a); (c) flanged wall W5 (Shedid et al., 2010a); (d) end confined wall W6 (Shedid et al., 2010a); (e) end confined wall W1 (Banting and El-Dakhakhni, 2012); and (f) end confined wall W2 (Banting and El-Dakhakhni, 2014)

It can be seen that the predicted hysteretic responses are in good agreement with the experimental results. The proposed nonlinear model for RM shear walls is capable of predicting

the initial stiffness, yield strength, ultimate strength, and drift capacity. The numerical predictions are, on average, within ±10% of the experimentally measured values. In addition, the model captured the loading and unloading branches and the post-peak response. The model is also capable of representing the level of pinching expected in RM structural walls. Among the considered end confined walls (W6, W1 and W2), it is observed that the accuracy of the simulated nonlinear response is enhanced for the wall with highest aspect ratio (i.e. W2). This could be attributed to the inability of the fibre beam-column elements in accurately capturing the shear deformations (Calabrese et al., 2010), which were reduced with the increase in aspect ratio. Thus, this modelling approach is deemed more suitable for flexural dominant walls with high aspect ratios. It should be noted that the walls considered in the present study have properties (e.g. configuration, vertical and horizontal reinforcement ratios), shown in Table 5.3, that are similar to those of the walls considered in validating the numerical model. However, due to the scarcity of tested RM shear walls with boundary elements in the literature, there are differences in the aspect ratios and levels of axial load between the studied walls and the modelling validation walls.

5.7 Nonlinear Pseudo-Static Analysis

Nonlinear pseudo-static pushover analysis is performed to verify the nonlinear model and evaluate the strength and deformation capacities of the archetype buildings. It is executed using the approach outlined in FEMA P695. The pushover analysis is performed under the gravity loads expected during seismic events as specified by FEMA P695 using the load combination in Eq 5.2.

$$1.05D+0.25L \tag{5.2}$$

D is the total dead load (self-weight and superimposed dead load) on the building, and L is the live load. The analysis results are used to create the lateral capacity (monotonic backbone) curves of the model buildings SFRS in the North-South (N-S) direction. Sample lateral capacity curves of two archetype buildings (20S-M and 14S-V) are shown in Figure 5.8. The system overstrength (R_o), from the pseudo-static analysis, is calculated as the ratio between maximum base shear capacity (V_{max}) and the design base shear. The calculated overstrength value is 1.68 for the 20-storey building in Montréal and 1.22 for the 14-storey building located in Vancouver. From the pushover curves, the normalized base shear capacities of the buildings are 3.3% and 5.9% for 20S-M and 14S-V, which corresponds to 2.14% and 3.50% roof drift ratios, respectively.

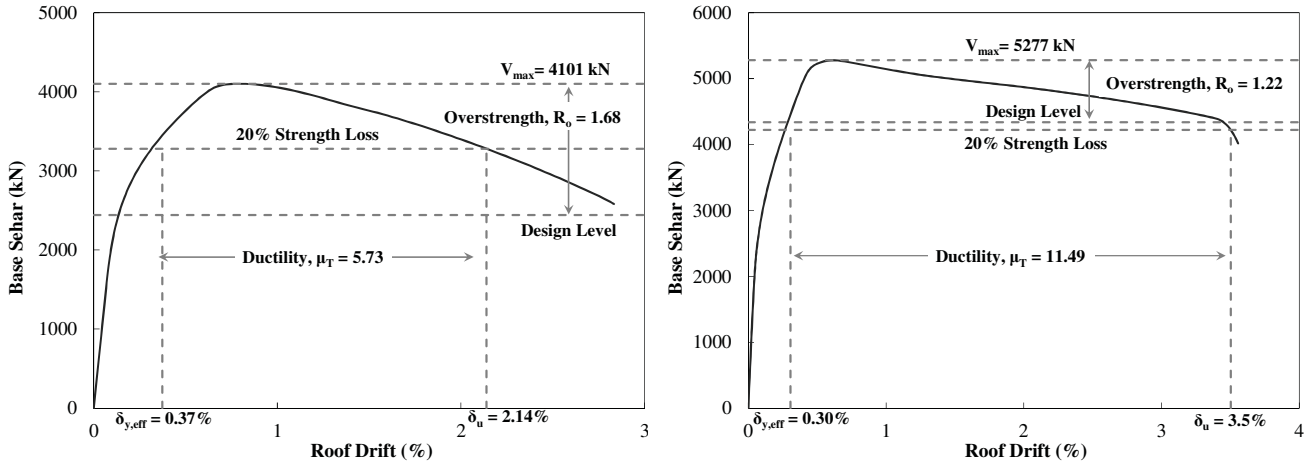

Figure 5.8 Pushover curves for N-S SFRS: (a) building 20S-M; and (b) building 14S-V

Examination of Figure 5.8 (a) and (b) confirms a clear ductile response for the two archetypes RM ductile shear wall buildings with confined boundary elements. It is apparent that the degradation in strength occurred gradually until 20% of the capacity is lost. The period-based ductility (μ_T), used to quantify the system ductility capacity, is calculated as the ratio between the ultimate roof displacement and the effective yield roof displacement. The ultimate displacement (δ_u) is calculated at the roof corresponding to 20% degradation in ultimate capacity. The effective yield roof displacement ($\delta_{y,eff}$) is evaluated as per FEMA P695 by correlating the fundamental mode of vibration's roof displacement of an idealized single degree of freedom to the roof displacement of the building. This can be calculated using Eq. (5.3).

$$\delta_{y,eff} = C_o \frac{V_{max}}{W} \left[\frac{g}{4\pi^2}\right] (\max\{T, T_1\})^2 \tag{5.3}$$

where T is the upper limit on the natural period (i.e. 2*T_a in NBCC-15 for shear walls), and T_1 is the natural period as calculated by modal analysis. C_o is a coefficient that correlates the roof displacement of an equivalent single degree of freedom system to the roof displacement of the building. As shown in Figure 5.8, the calculated period-based ductilities are 5.73 and 11.49 for buildings 20S-M and 14S-V, respectively. A summary of the pushover analysis results for the six reference buildings is illustrated in Table 5.5. As can be seen, there is a relative increase in the period-based ductility for the archetypes in performance group 2 compared to performance group 1. This might be attributed to the higher seismicity in Vancouver, which mandated the use of more stringent seismic detailing, such as closer spacing of boundary element hoops (for confinement).

In general, the high ductility seen in the reference buildings is due to the presence of the well detailed and confined boundary elements in the shear walls. The presence of confined boundary elements significantly enhanced the ultimate curvature and reduced the curvature at the onset of vertical reinforcement yielding. This resulted in a clear improvement in the system's displacement ductility. This enhancement in ductility because of RM shear walls with boundary elements is in agreement with the findings of others (Ezzeldin et al., 2016).

Table 5.5 Summary of pushover analysis results

Archetype ID	Static R_o	$\Delta_{y,eff}$ (%)	Δ_u (%)	V_{max}/W	μ_T
Performance Group 1-Moderate Seismicity					
18S-M	1.753	0.33%	2.41%	3.349%	7.28
19S-M	1.745	0.35%	2.25%	3.348%	6.46
20S-M	1.681	0.37%	2.14%	3.301%	5.73
Performance Group 2-High Seismicity					
12S-V	1.234	0.261%	2.07%	6.405%	7.92
13S-V	1.222	0.264%	3.24%	6.193%	12.30
14S-V	1.217	0.305%	3.50%	5.854%	11.49

Additionally, it can be observed that static overstrength (R_o) factors slightly decrease with the increase in the number of floors (natural period) in both performance groups. The inverse relationship between number of floors and overstrength factors was also observed by Mwafy (2011). However, the calculated overstrength factors are much lower for the archetypes in performance group 2, which are designed for the high seismicity. This is due to the low seismic design forces in Montréal for tall buildings, compared to Vancouver, which made the strength design controlled by factored wind forces calculated in accordance with NBCC-15. Therefore, the walls were designed to have higher capacity than required by seismic demand. It was also highlighted by Gogus and Wallace (2015) that the shear wall buildings designed for low seismicity had higher overstrength values compared to those designed for higher seismicity. In performance group 2, the average overstrength factor calculated based on the pseudo-static analysis is approximately 23% lower than the design code value for ductile RM shear walls. Nevertheless, as will be seen in next sections, there is a significant overstrength based on the nonlinear dynamic analyses results.

5.8 Selection and Scaling of Ground Motion Records

The ground motion records are selected following the intensity-based performance assessment approach outlined in FEMA P58-1 (Federal Emergency Management Agency, 2012). The

selection of ground motion records should guarantee a uniform and unbiased seismic response from the different records. For that purpose, the records are selected to ensure a close match between its geometric mean spectral shape and that of the target response spectrum over a specified period range between T_{min} and T_{max}. According to FEMA P58-1 (2012), T_{min} is taken as the least of $0.2T_1$ or $0.2T_2$, and T_{max} is the larger of $2T_1$ or $2T_2$. T_1 and T_2 are the first and second vibration modes' periods. In addition to the spectral shape or frequency content, the selected ground motion records should have fault mechanisms, event magnitudes, epicentral distance, and local site conditions similar to those expected at the structure's location.

The ratio of Peak Ground Acceleration (PGA) to Peak Ground Velocity (PGV) was studied by Tso et al. (1992) and found significant in measuring the frequency content or spectral shape, event magnitude, and epicentral distance of the records. Two levels of PGA/PGV were recommended; a high level of ratios more than 1.2 and a low level of ratios less than 0.8. The high PGA/PGV would simulate ground motions with high predominant frequencies, small to medium events' magnitudes, narrow band response spectra, short fault to source distance, short event duration, and short site period. On the other hand, the low ratio would reflect ground motions with low predominant frequencies, medium to high events' magnitudes, wide-ranging response spectra, long fault to source distance, long duration, and short site period.

In this study, the ground motions are selected from a database of processed artificial time series generated for Canada by Assatourians and Atkinson (2010). The selected records, their designations, events' magnitudes, and epicentral distances are tabulated in Table 5.6. For nonlinear time-history analyses, NBCC-15 recommends using the maximum response from three ground motion records or the mean response when using seven ground motion records or more. In general, the number of selected records should be sufficient to compute the median response, reduce the dispersion, and account for the record-to-record variability (Michaud and Leger, 2014). It was demonstrated by Michaud and Léger (2014) that using seven ground motion records with proper scaling is sufficient for calculation of the mean seismic response and its dispersion. In addition, FEMA P58-1 recommends using seven pairs of ground motions when there is a good match with the target response spectrum and eleven records or more when the match is weak. Therefore, for the archetype buildings located in western and eastern Canada, a total of 32 random horizontal

ground motions (16 pairs) are selected for each location to account for the record-to-record variability and evaluate the median collapse intensity.

Table 5.6 Unscaled input ground motions' characteristics

	Western Canada (Vancouver)			Eastern Canada (Montréal)		
No.	Designation	Event Magnitude	Epicentre Distance (km)	Designation	Event Magnitude	Epicentre Distance (km)
1	west6c1	6.5	8.8	east6c1	6	12.8
2	west6c1	6.5	8.8	east6c1	6	12.8
3	west6c1	6.5	11.2	east6c1	6	12.5
4	west6c1	6.5	11.2	east6c1	6	12.5
5	west6c1	6.5	13	east6c1	6	12.8
6	west6c1	6.5	13	east6c1	6	12.8
7	west6c1	6.5	13	east6c1	6	10.7
8	west6c1	6.5	13	east6c1	6	13.6
9	west6c2	6.5	21.6	east6c2	6	20.8
10	west6c2	6.5	21.6	east6c2	6	21.5
11	west6c2	6.5	26.3	east6c2	6	16.9
12	west6c2	6.5	26.3	east6c2	6	16.9
13	west6c2	6.5	31.1	east6c2	6	21.1
14	west6c2	6.5	31.1	east6c2	6	21.1
15	west6c2	6.5	18.7	east6c2	6	26.3
16	west6c2	6.5	18.7	east6c2	6	26.3
17	west7c1	7.5	16.4	east7c1	7	13.8
18	west7c1	7.5	16.4	east7c1	7	13.8
19	west7c1	7.5	10.2	east7c1	7	15.3
20	west7c1	7.5	10.2	east7c1	7	15.3
21	west7c1	7.5	17.1	east7c1	7	14.2
22	west7c1	7.5	17.1	east7c1	7	14.9
23	west7c1	7.5	21.6	east7c1	7	14.8
24	west7c1	7.5	21.6	east7c1	7	20.6
25	west7c2	7.5	47.4	east7c2	7	41.6
26	west7c2	7.5	47.4	east7c2	7	50.3
27	west7c2	7.5	50.7	east7c2	7	45.2
28	west7c2	7.5	50.7	east7c2	7	45.2
29	west7c2	7.5	100.4	east7c2	7	50.3
30	west7c2	7.5	100.4	east7c2	7	50.3
31	west7c2	7.5	100.4	east7c2	7	51.9
32	west7c2	7.5	100.4	east7c2	7	51.9

The selected records, summarized in Table 5.6, are for site class C, which is consistent with the assumed soil conditions for reference buildings' location. They correspond to strong ground motion earthquakes with magnitudes of 6.5 and 7.5 for western Canada, and 6.0 and 7.0 for eastern Canada. Sixteen of the records simulate near-fault earthquakes (≤ 15km site to fault distance), while the other sixteen simulate a far-fault scenario (> 15km site to fault distance). Near-fault ground motion records are characterized by small durations and high amplitudes. However, the far-fault records have long durations, but with relatively smaller amplitudes.

The selected records for the archetypes located in western Canada are representative of the types of earthquakes that contribute to the hazard in the west coast, which are crustal and in-slab subduction earthquakes (Atkinson, 2009). As shown in Figure 5.9(a), the PGA/PGV ratio is varying between the two ranges (i.e. >1.2 and <0.8). This demonstrates that the selected records well simulate the wide range of expected types of earthquakes with medium to large magnitudes in western Canada. On the other hand, Figure 5.9(b) shows that the PGA/PGV ratios of the selected records for eastern Canada are always above 1.2. Therefore, these selected input records are representative of the types of expected earthquakes in eastern Canada which are characterized by high predominant frequencies (Atkinson, 2009).

The selected ground motion records are scaled according to FEMA P58-1 (2012) suggested approach. This approach scales the amplitude of both components for each selected record by the ratio between $S(T_{avg})$ from the target design response spectrum and the record geometric mean spectral acceleration at T_{avg}. T_{avg} is the average of the first mode (T_1) and second mode (T_2) periods of vibrations. The geometric mean spectral acceleration of each record $S_{gm}(T_{avg})$ is calculated according to Eq. (5.4).

$$S_{gm}(T) = \sqrt{[S_x(T_{avg}) \times S_y(T_{avg})]} \quad (5.4)$$

It is worth mentioning that FEMA P695 (2009) methodology is based on ASCE7-10. FEMA P695 requires using ground motions that are scaled to match the MCE level. In ASCE7-10, the MCE level is different from the design level. The MCE corresponds to a very rare earthquake event having a 2% probability of being exceeded in 50 years, while the design level is based on two-third of the MCE. This brings the design level down to an event having a return period of 475 years (i.e. 10% probability of exceedance in 50 years). On the other hand, in NBCC-15 the design

response spectrum is the MCE, as it corresponds to a very rare event with 2475 years return period (i.e. 2% probability of exceedance in 50 years). This is a primary difference between the seismic design criteria given in the two codes. ASCE7-10 reduces the MCE to the design level by relying on the assumption that well designed and detailed lateral force resisting systems usually achieve at least 50% overstrength against seismic collapse. Therefore, in this study, scaling the ground motion records to match the design level of NBCC-15 is equivalent to matching the MCE level in ASCE7-10.

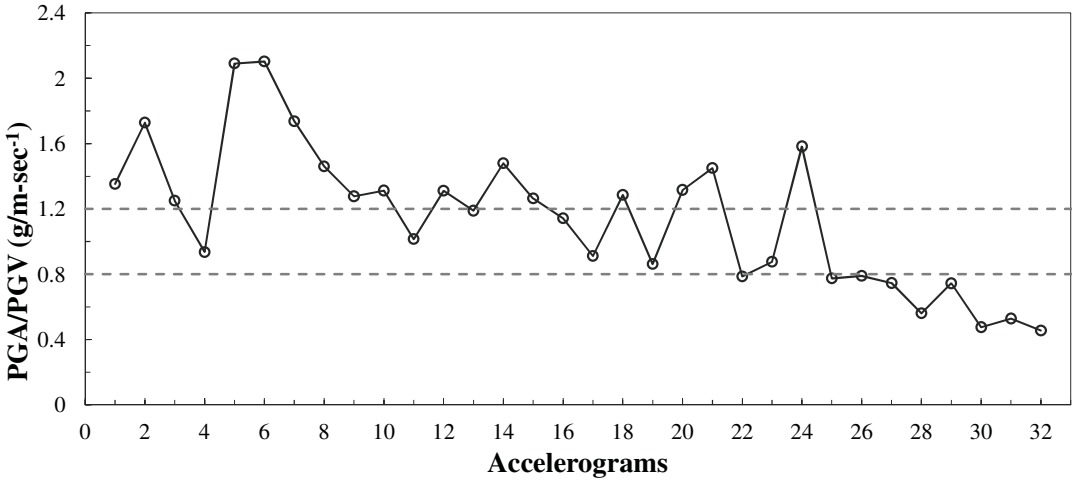

(a)

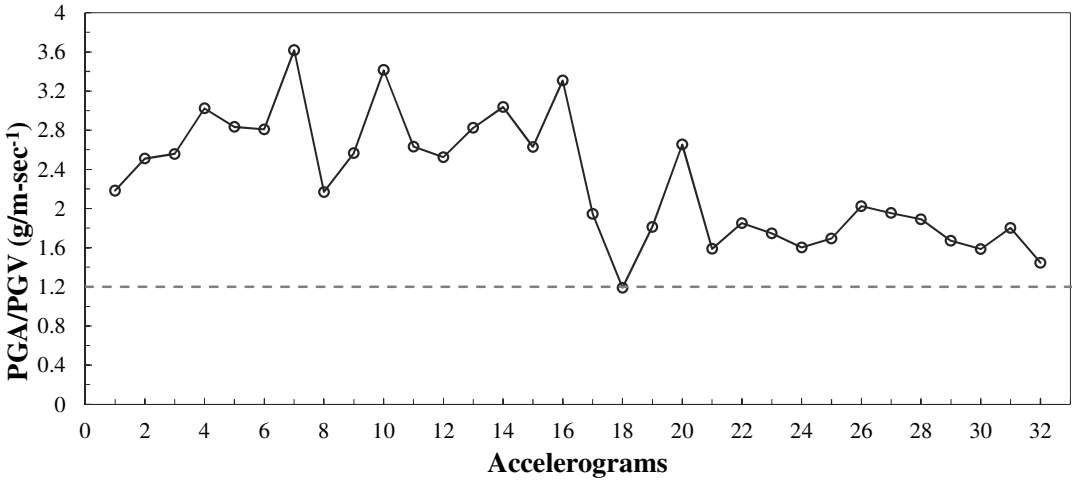

(b)

Figure 5.9 Input ground motions PGA/PGV ratios: (a) west Canada; and (b) east Canada

5.9 Nonlinear Dynamic Analyses

A series (more than 1900) of nonlinear response history analyses is performed to investigate the response of the reference buildings to ground motion excitations in N-S direction. To ensure the accuracy and stability of the dynamic equation of motion's numerical solution, the nonlinear response history analysis is performed with a small time-step that is at least one-half the input ground motion sampling time-step. In addition to the sampling time-step, nonlinear dynamic analysis is also sensitive to the utilized damping models. The total damping is composed of hysteretic damping and viscous damping. In general, hysteretic damping due to the reversed cyclic nature of earthquakes dissipates most of the energy. The hysteretic damping is explicitly accounted for in the modelling approach as fibre models' formulations are utilized for simulating the structural walls (Seismosoft, 2016). On the other hand, the minor contribution of non-hysteretic damping (elastic damping) to the energy dissipation is conservatively neglected. It is typically equivalently modelled using either mass proportional damping, stiffness proportional damping, or Rayleigh damping to account for the energy dissipation. Wilson (Wilson, 2001) recommended avoiding the equivalent modelling of damping in the computational model. This is due to the lack of detailed experimental and theoretical proof of its reliability and its possibility of resulting in a violation of the dynamic equilibrium (Wilson, 2001).

Each archetype building is subjected to the 32 previously selected, and scaled ground motion records with at least 10 successively increased Intensity Measure (IM) increments. This dynamic analysis approach is termed as IDA and is described in detail by Vamvatsikos and Cornell (2002). IDA allows systematic monitoring of the structure seismic response to ground motions at increasing intensities. Thus, it allows capturing the behaviour from elastic range until collapse is recognized in the structure. The IDA results are used to construct IDA curves or dynamic pushover curves. It is typically a plot relating an Engineering Demand Parameter (EDP) to an IM. In this study, peak inter-storey drift ratios are selected as the EDPs to represent the global performance of the building. This is consistent with the main objective of investigating the specified code (i.e. NBCC-15) limits on building heights. For the IMs, 5% damped spectral accelerations at the building's first mode period, S (T_1, 5%)/g, are selected. This allows representative and direct application of FEMA P695 (2009) methodology for the seismic performance evaluation. Additionally, the use of spectral accelerations as the IMs reduces the results' scatter (Vamvatsikos and Cornell, 2004). Figure 5.10 depicts the IDA response plots for the six reference buildings in

the N-S direction. Each point on the IDA curve typically represents the building response to a ground motion record at a certain intensity scaling factor (i.e. IM increment). The IDA results shown in Figure 5.10 are used to derive the collapse capacity and assess the seismic vulnerability of the archetype buildings.

For each of the studied buildings, the IDA curves are plotted for each group of ground motion (i.e. M6.0/6.5/7.0/7.5 and near-fault/far-fault) records to evaluate the possible impact of record-to-record variability on the seismic collapse performance. For the archetypes in eastern Canada (i.e. Montréal), there is no clear trend observed for the impact of event magnitude or ground motion characteristics on the buildings' seismic collapse capacity. This observation is consistent with the results reported in the study by Michaud and Léger (2014), which was also concerned with the seismic response of structures located in eastern North America. However, for the buildings located in the high seismicity region of Canada (i.e. Vancouver), the impact of ground motions variability was more evident. The results revealed that the collapse capacity could be sensitive to the characteristics of the used ground motions. Overall in the three archetype buildings located in Vancouver, the seismic collapse capacity is found to be slightly higher when calculated based on far-fault ground motions with magnitude of 6.5. When the event magnitude is 7.5, the collapse capacity is higher for the near-fault ground motion records. Therefore, this confirms the sensitivity of IDA results to the selection of ground motions, especially when the structures are located in regions with high seismicity such as Vancouver. A similar observation was also demonstrated by Vamvatsikos and Cornell (2002) and AlHamaydeh et al. (2017) regarding the sensitivity of IDA results to the selection of ground motion records. In the current study, the sensitivity of the seismic response to ground motions is accounted for by selecting a sufficient number of records (i.e. 32 ground motion records with varying characteristics) that represents the expected types of earthquakes.

5.10 Seismic Collapse Capacity Assessment

The methodology of FEMA P695 (2009) enables the modification of any design aspect, including the detailing requirements and height limits, of any proposed structural system. Thus, it is possible to test the proposed hybrid load-bearing layout detailing enhancements and recommend height limits for ductile RM shear walls with boundary elements by satisfying the seismic performance acceptance criteria of FEMA P695.

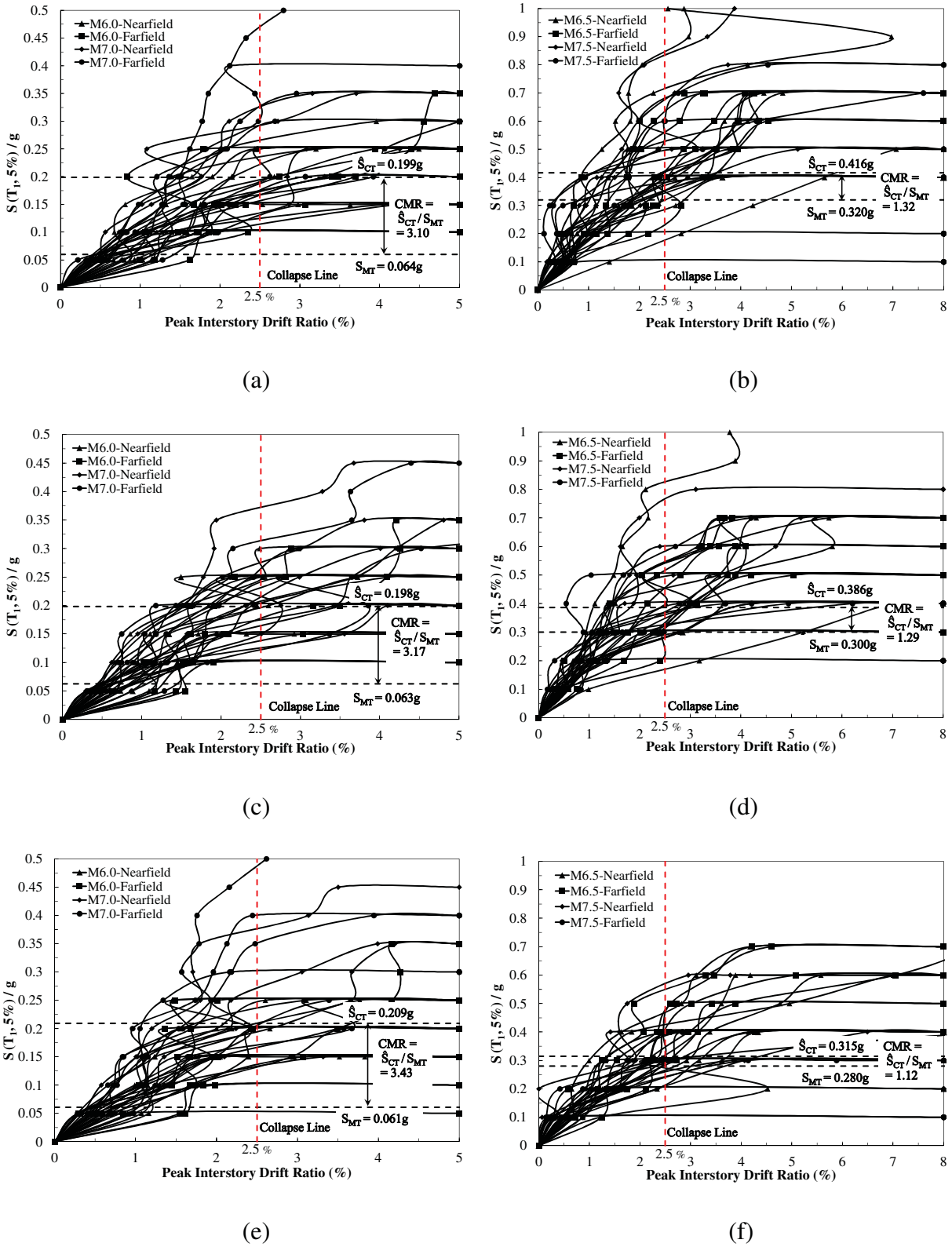

Figure 5.10 IDA curves of the SFRS in N-S direction: (a) building 18S-M; (b) building 12S-V; (c) building 19S-M; (d) building 13S-V; (e) building 20S-M; and (f) building 14S-V

To quantify the buildings' seismic collapse performance, it is required to estimate the median collapse intensity ($\hat{S}_{CT}$). The median collapse intensity is defined as the 5% damped spectral acceleration at the structure's natural period which results in 50% probability of collapse (i.e. when 50% of the records causes collapse). Based on FEMA P-58 (2012) and P695 (2009), the seismic collapse could be either simulated or non-simulated collapse. A simulated seismic collapse is when there is a dynamic instability or a side-sway collapse mechanism resulting from large lateral displacements. On the other hand, non-simulated seismic collapse is usually observed when a specific component limit state defined by the user is exceeded. For the objective of this study, it is most appropriate to assume that collapse is realized when there is a side-sway collapse mechanism being developed in the studied building. Therefore, seismic collapse is assumed when the peak inter-storey drift exceeds the NBCC-15 limit of 2.5% for buildings with normal importance. This value achieves the code's primary objective of protecting the life and safety of building occupants as the building responds to severe ground shaking. Thus, it is suitable to assess the code height limits for ductile RM shear wall buildings.

The calculated median collapse intensities ($\hat{S}_{CT}$) are evaluated from the IDA results and are shown in Figure 5.10 for the six archetype buildings. For the buildings located in Montréal, the median collapse intensities are 0.199g, 0.198g, and 0.209g for 18S-M, 19S-M, and 20S-M, respectively. The median collapse intensities of the archetypes located in Vancouver are 0.416g for building 12S-V, 0.386g for building 13S-V, and 0.315g for building 14S-V. These values are compared to the MCE level, or design level, spectral acceleration at the natural period of the building (S_{MT}) to calculate the Collapse Margin Ratio (CMR). The CMR is defined as the ratio between the median collapse intensity and MCE/design level spectral acceleration (i.e. $\hat{S}_{CT}/ S_{MT}$).

To develop the collapse fragility curves, IDA results are used to calculate the collapse probabilities at the different IM increments based on the previous definition of collapse. Then, those results are fitted using a Cumulative Distribution Function (CDF), assuming a lognormal distribution of the IM increments causing collapse. The parameters of the fragility fitting function, the median (θ) and dispersion (β), are estimated following the maximum likelihood method (Baker, 2015). In this method, the mean and the dispersion are estimated such that the resulting CDF ($\emptyset$) has the maximum likelihood of reproducing the observed analytical data points. The collapse fragility function, shown in Eq. (5.5), relates the probability of collapse to any given IM.

$$P\left(C \mid IM = x\right) = \emptyset\left[\frac{\ln\left(\frac{x}{\theta}\right)}{\beta}\right] \quad (5.5)$$

The fitted collapse fragility functions derived using the analytical IDA data points are then adjusted to account for the various uncertainty sources arising from the record-to-record variability (β_{RTR}), design requirements (β_{DR}), test data (β_{TD}), and numerical modelling (β_{MDL}). As these four parameters are assumed to be statistically independent, a lognormal standard deviation is calculated to define the total system's collapse uncertainty (β_{TOT}) using Eq. (5.6). This parameter is then used as the standard deviation of the adjusted fragility function.

$$\beta_{TOT} = \sqrt{\beta_{\mathrm{RTR}}^2 + \beta_{\mathrm{DR}}^2 + \beta_{\mathrm{TD}}^2 + \beta_{\mathrm{MDL}}^2} \quad (5.6)$$

For the current study, the record-to-record uncertainty (β_{RTR}) is calculated as 0.4 using Eq. (5.7), depending on the period-based ductility of the reference buildings.

$$\beta_{RTR} = 0.1 + 0.1\mu_T \leq 0.40 \quad (5.7)$$

Since the prescriptive design requirements are well-established and robust for RM shear walls in CSA S304-14, the uncertainty parameter due to design requirements (β_{DR}) is given a value of 0.2. This corresponds to medium completeness and robustness with high confidence in the design basis (i.e. a quality rating of (B) good). For the uncertainty due to test data (β_{TD}), a value of 0.2 is assigned based on medium completeness and high confidence. The used test data for modelling validation does not cover all possible range of parameters, but it is representative of common types of RM shear walls. Moreover, there was a good agreement between experimental results and numerical predictions. The utilized numerical modelling approach is capable of accurate simulation of the response of the archetype structures, but with few limitations. Hence, a value of 0.2 is assumed for the uncertainty due to modelling (β_{MDL}). This represents high capability of simulating collapse characteristics, but medium accuracy and robustness. The calculated total system collapse uncertainty parameter (β_{RTR}) is 0.529.

The collapse fragilities are further adjusted to account for the variations in the records' frequency content and the elongation in the structure's natural period that occurs prior to collapse. This adjustment is crucial for reliable estimation of seismic collapse capacities. FEMA P695 recommends a general and efficient method for adjusting the collapse capacity using the Spectral Shape Factor (SSF). This factor is estimated from Table 7-1 in FEMA P695 based on the

structures' natural period and the period-based ductility (μ_T). The Adjusted Collapse Margin Ratio (ACMR) is calculated by multiplying the CMR by the SSF. The analytical, log-normal fitted, and adjusted collapse fragility curves of the archetype buildings are shown in Figure 5.11. As shown, the uncertainty adjustments resulted in pushing the collapse fragility curves forward and making it relatively flatter. S_{CT} is the adjusted median collapse capacity.

As can be seen from Figure 5.11, the buildings located in Montréal (moderate seismicity) have flatter fragilities reflecting lower collapse probabilities compared to those of the buildings located in the high seismicity region (Vancouver). In addition, for the buildings located in Vancouver, it is evident that the increase in height resulted in an increase in collapse probability and a reduction in the seismic collapse capacity. Therefore, in regions with high seismic hazard, the increase in the number of floors results in increasing the seismic collapse risk. This trend is illustrated in Figure 5.12. Figure 5.12(a) shows an almost inverse linear relationship between the numbers of floors and the collapse fragility median (i.e. median collapse intensity). In contrast, the trend is not very clear between the fragility dispersion and the building's height, as illustrated in Figure 5.12(b).

The seismic performance and collapse capacity parameters of the six archetype buildings are summarized in Table 5.7. For the archetype buildings designed in Montréal, there is no clear trend seen in the median collapse intensity ($\hat{S}_{CT}$) neither when calculated at 2.5% peak inter-storey drift ratio nor at 2.0%. The three buildings have negligible collapse probabilities at the MCE or design level spectral accelerations, which are significantly lower than the recommended limits by FEMA P695 for acceptable seismic performance. In addition, the calculated seismic collapse capacities (CMRs) are more than 3 for all the buildings in performance group No. 1. This indicates a superior seismic performance characterized by a high reserve of collapse capacity. The calculated ACMRs are satisfying FEMA P695 acceptance criteria. This is achieved by having collapse probabilities at MCE lower than 20% for each building and lower than 10% for the performance group. It should be noted that the acceptable ACMR is based on the calculated total system collapse uncertainty (β_{RTR}) of 0.529. Even if a more stringent seismic collapse criteria (e.g. collapse assumed at 2.0% inter-storey drift) is imposed on the buildings in performance group No. 1, the buildings are still achieving the acceptance measures of FEMA P695 with substantial margins.

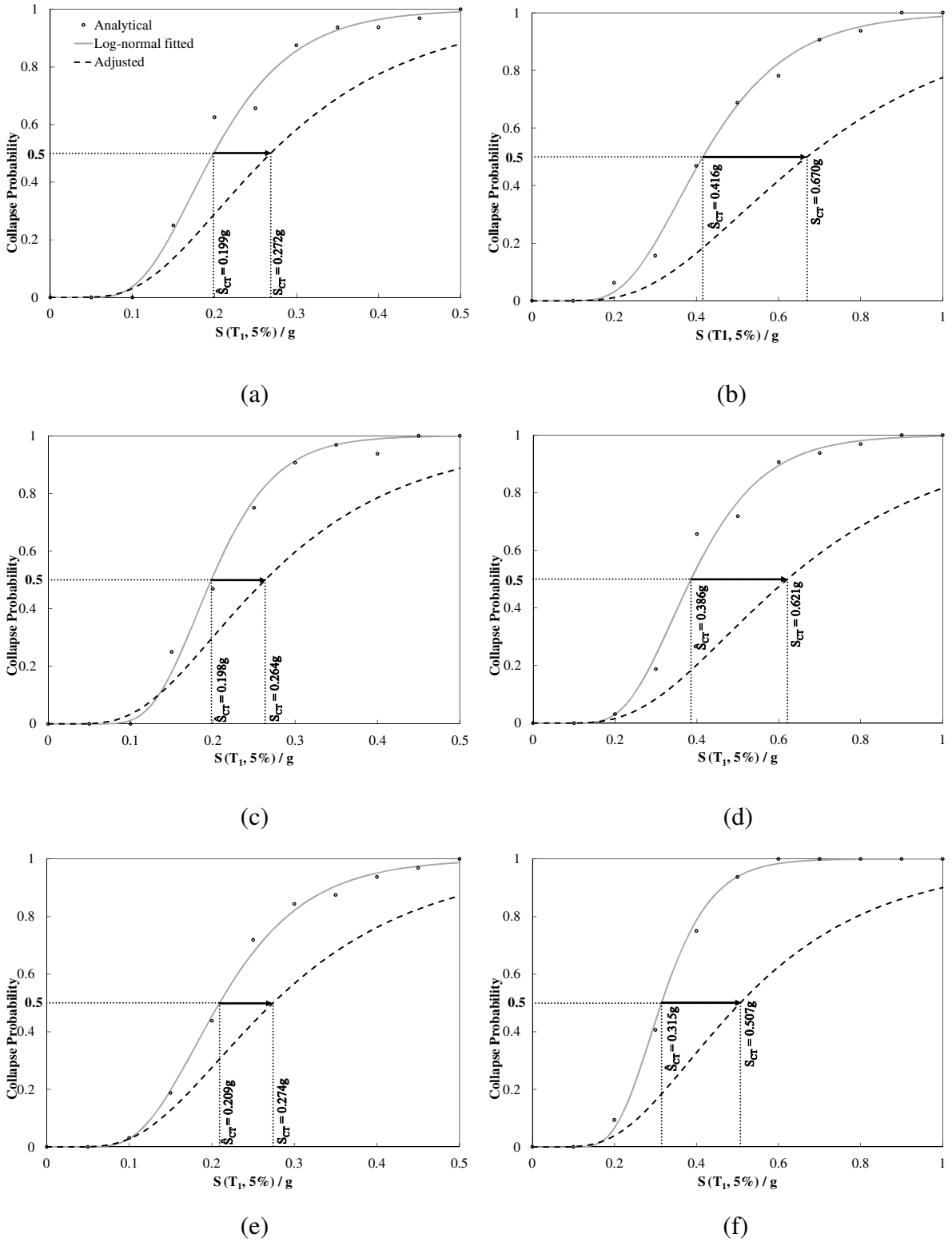

Figure 5.11 Collapse fragility curves for the SFRS in N-S direction: (a) building 18S-M; (b) building 12S-V; (c) building 19S-M; (d) building 13S-V; (e) building 20S-M; and (f) building 14S-V

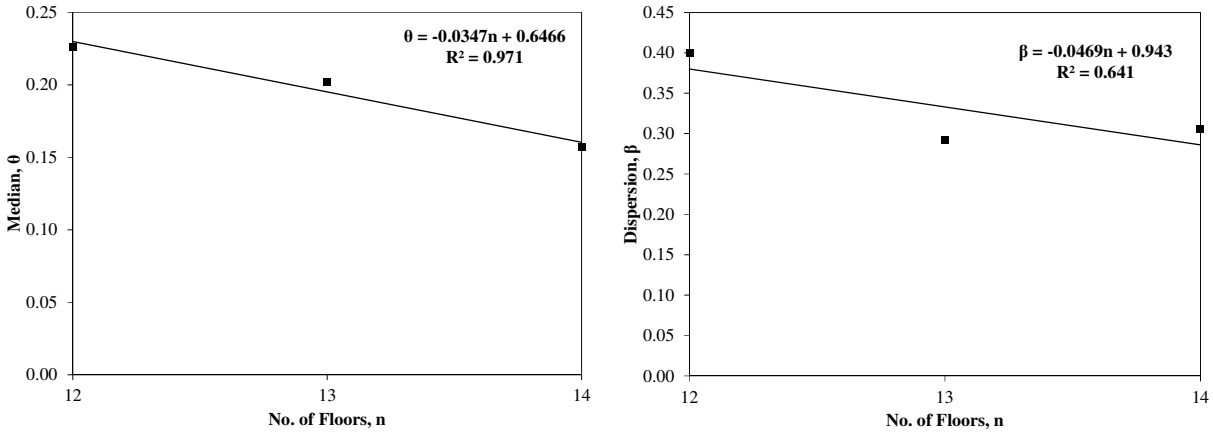

(a) (b)

Figure 5.12 Effect of building height on fragility parameters in high seismic regions with $I_E F_a S_a(0.2) > 0.75$ (Vancouver): (a) median; and (b) dispersion

The observed high overstrength and seismic collapse capacity of the three buildings designed in Montréal is possibly because factored wind loads governed the strength design over seismic forces. This is due to the use of ductile RM shears walls with boundary elements as the SFRS, which resulted in reducing the seismic demands. Moreover, the high predominant frequencies in Montréal's design response spectrum resulted in lower seismic forces on the archetype buildings with long natural periods. From the results shown in Table 5.7, it is concluded that performance group No. 1 completely satisfies the acceptance conditions for acceptable seismic performance and collapse capacity. Therefore, it is possible to relax the 60 m height limit imposed by NBCC-15. Furthermore, the proposed hybrid load-bearing plan layout of RM shear walls with boundary elements and RM gravity walls along with the detailing enhancements is proved to be a potentially attractive alternative to the conventional load-bearing walls system for RM buildings.

The buildings designed in Vancouver, the high seismic risk region, have collapse probabilities at MCE of 8.13%, 8.45%, and 13.11% for the 12-storey, 13-storey, and 14-storey buildings, respectively. As expected, the collapse probabilities are increasing with the increase in the building's height. This is also seen in the reduction in seismic collapse intensities ($\hat{S}_{CT}$) as the building's height increases. However, the probability of collapse at the MCE is always lower than 20% for each building and lower than 10% for the entire performance group, as required by FEMA P695. The calculated CMRs considering that the simulated seismic collapse occurs at a peak inter-storey drift of 2.5% is also decreasing with height.

Table 5.7 Summary of seismic performance and collapse capacity results for the archetype buildings

	Collapse Capacity Parameters									Acceptance Check	
Archetype ID	**S_{MT} (g)**	**$P(C|S_{MT})$**	**$\hat{S}_{CT}$ @ 2.5% IDR (g)**	**$\hat{S}_{CT}$ @ 2.0% IDR (g)**	**CMR @ 2.5%**	**CMR @ 2.0%**	**SSF**	**ACMR @ 2.5%**	**ACMR @ 2.0%**	**Accept. ACMR**	**Pass/ Fail**
Performance Group No. 1											
18S-M	0.064	0.23%	0.199	0.168	3.10	2.62	1.35	4.19	3.54	1.56	**Pass**
19S-M	0.063	0.26%	0.198	0.175	3.17	2.79	1.33	4.21	3.71	1.56	**Pass**
20S-M	0.061	0.20%	0.209	0.180	3.43	2.95	1.31	4.49	3.87	1.56	**Pass**
Mean Performance	-	0.23%	-	-	3.23	2.79	1.33	4.30	3.71	1.96	**Pass**
Performance Group No. 2											
12S-V	0.32	8.13%	0.416	0.360	1.32	1.14	1.61	2.12	1.84	1.56	**Pass**
13S-V	0.30	8.45%	0.386	0.341	1.29	1.14	1.61	2.08	1.84	1.56	**Pass**
14S-V	0.28	13.11%	0.315	0.266	1.12	0.94	1.61	1.80	1.52	1.56	**Pass**
Mean Performance	-	9.90%	-	-	1.24	1.08	1.61	2.00	1.73	1.96	**Pass**

This justifies imposing height limits on buildings located in regions with high seismic hazard since the increase in height results in a higher seismic collapse risk. Moreover, the adverse impact of height on seismic collapse risk highlights the potential need for period-dependent ductility-related seismic response modification factors. The objective of having period-dependent seismic response modification factors is to ensure a uniform distribution of the seismic collapse risk across the buildings that is also independent of the buildings' heights. Thus, taller buildings might mandate larger strength to enhance the seismic performance and reduce the seismic collapse risk. According to Table 5.7, the adjusted collapse capacities (ACMRs) for the three archetypes, of performance group No. 2, satisfy the performance objectives of FEMA P695, when the collapse is evaluated at 2.5% peak inter-storey drift. This is true for the individual buildings as well as for the performance group. Therefore, the 50 m building height limit assigned by NBCC-15 to buildings located in high seismic hazard regions can be safely increased. Moreover, similar to performance group No. 1, the utilization of the hybrid layout, as well as the proposed detailing enhancements resulted in a superior seismic performance and collapse capacity for the three buildings located in Vancouver.

Comparing the collapse capacity assessment results of the archetype buildings located in Montréal and Vancouver reveals very interesting findings. Firstly, the buildings designed in the moderate seismicity region (i.e. Montréal) have significantly lower probabilities of collapse at the MCE compared to those of the buildings located in Vancouver (high seismicity). Additionally, the ACMRs are much higher for the buildings located in Montréal compared to those located in Vancouver. This verifies that the seismic collapse risk increases with the increase in the seismic hazard index ($I_E F_a S_a(0.2)$). Furthermore, there is an inverse relationship between the number of floors and ACMR for the buildings designed in regions with high seismic hazard, as illustrated in Figure 5.13(a). On the contrast, as presented in Figure 5.13(b), for the buildings located in the moderate seismicity region, the ACMR increases with the increase in the number of floors. This is attributed to the fact that these buildings' strength design is governed by factored wind loads, which is increased with the building height. Figure 5.13 also reflects the significant overstrength and margin of safety against seismic collapse of the archetype buildings, especially those located in Montréal. This demonstrates that ductile RM shear wall buildings that utilize the proposed hybrid layout and detailing enhancements have an overall favourable structural performance.

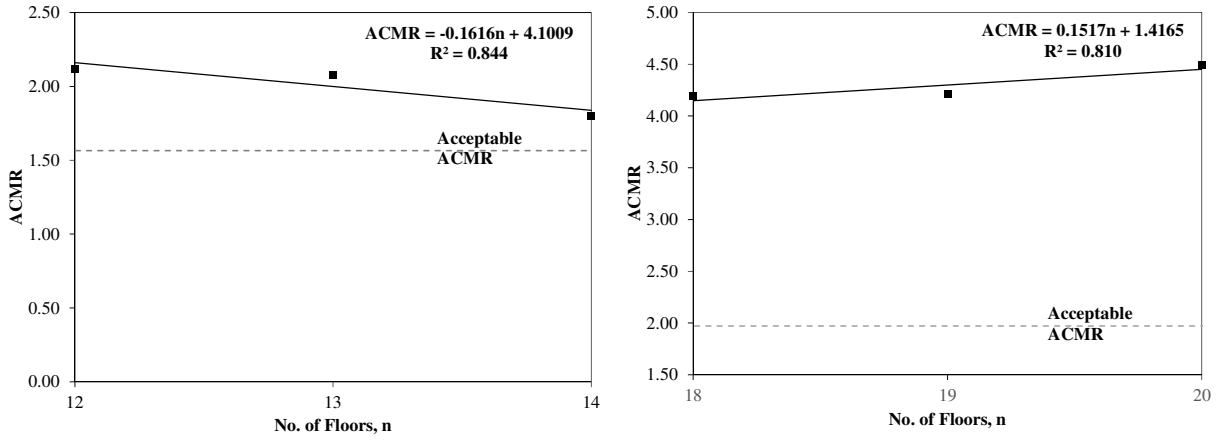

(a) (b)

Figure 5.13 Effect of building height on ACMR: (a) Vancouver [$I_E F_a S_a(0.2) > 0.75$]; and (b) Montréal [$0.35 \leq I_E F_a S_a(0.2) \leq 0.75$]

5.11 Proposed Height Limits

As mentioned earlier, NBCC-15 assigns the same height limits for ductile and moderately ductile RM shear walls. However, the results of this study demonstrate that ductile RM shear walls with boundary elements have an enhanced overall seismic response and high seismic collapse capacity. Therefore, based on the collapse assessment results, it is recommended to consider relaxing the height limits assigned to ductile RM shear wall buildings. The height limits are sensitive to the seismicity of the buildings' location. Hence, it is suggested, based on the studied cases, to change the height limit assigned to buildings in regions of moderate seismicity [$0.35 \leq I_E F_a S_a (0.2) \leq 0.75$] to 70 m instead of the current 60 m limit. This is because the buildings in this seismicity region showed a significantly high collapse capacity and very low collapse risk. As illustrated in Figure 5.13(b), the ACMR is increasing with the increase in number of floors (total height). Furthermore, the design of high-rise ductile RM shear wall buildings, similar to the considered cases, in the moderate seismic hazard regions will be mostly governed by factored wind loads. Structures are typically designed to remain elastic under wind loading, and the purpose of limiting the height is to control the possibility of inelastic damage concentration. On the other hand, in regions with high seismicity [$I_E F_a S_a (0.2) > 0.75$], it is possible to increase the current height limit to 50 m. This is if the acceptance criteria of the seismic performance and collapse capacity is based on 20% probability of collapse at the MCE, as suggested by FEMA P695. If a more stringent acceptance criterion is to be enforced, such as 10% probability of collapse at MCE,

the height limit can be conservatively increased to 45 m. Figure 5.14 shows the impact of the increase in height on the collapse probabilities at MCE along with the two possible acceptance objectives for the buildings in high seismicity regions. It is clear that the three archetype buildings satisfy FEMA P695 recommended acceptance criteria. The proposed height limits and the existing height limits of NBCC-15 are presented in Figure 5.15. For the high seismicity regions, it is decided to adopt the acceptance criteria of FEMA P695 as it is well-established criteria for the quantification of seismic performance.

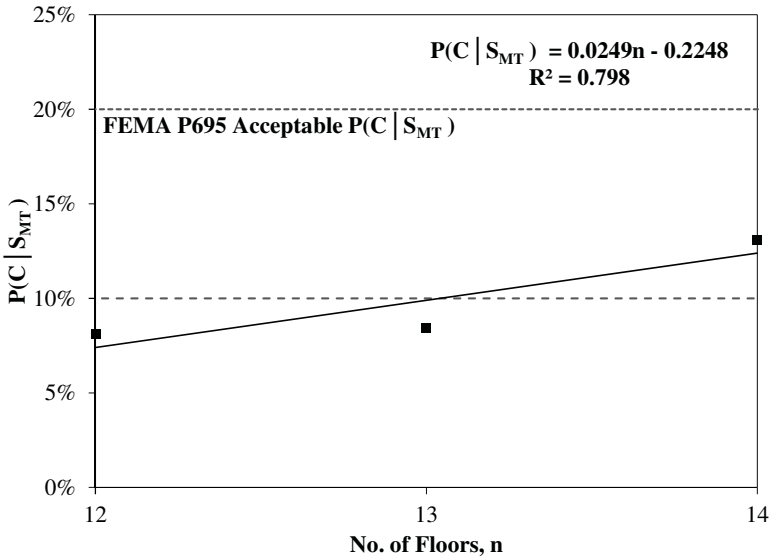

Figure 5.14 Effect of building height on the probability of collapse at MCE for buildings in regions with $I_E F_a S_a(0.2) > 0.75$

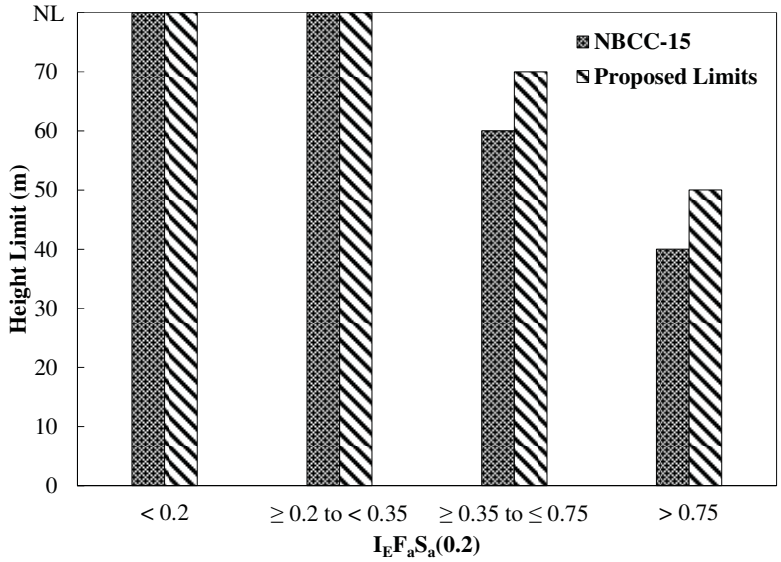

Figure 5.15 Proposed height limits for ductile RM shear wall buildings

5.12 Conclusions

This study was designed to assess the seismic performance of ductile RM shear wall buildings and propose height limits that are based on standard and objective acceptance criteria. Six archetype ductile RM shear wall buildings located in two regions in Canada representing the moderate and high seismicity levels of NBCC-15 were designed and studied. The studied archetype buildings had varying heights exceeding the NBCC-15 limits. A nonlinear numerical model was developed in Seismostruct (Seismosoft, 2016) program to simulate the seismic response of the archetype buildings. The seismic performance was evaluated using nonlinear pseudo-static and dynamic analyses based on FEMA P695 methodology.

Nonlinear pushover analysis results indicated a favourable response for ductile RM shear wall buildings with boundary elements. The resulting response from monotonic loading indicates reasonable strength and deformation capacities. Pushover curves reveal a significantly enhanced ductile response for the reference buildings, especially for the buildings located in the high seismic hazard region. IDA results also showed a favourable seismic performance for the reference buildings characterized by a high median collapse intensity ($\hat{S}_{CT}$) and low probabilities of collapse at the MCE. The developed collapse fragility curves confirmed the superior seismic performance and the high reserve of collapse capacity at the MCE level. The archetype buildings located in Montréal (moderate seismicity) had negligible probabilities of collapse at MCE and significantly high ACMRs. The strength design of the studied ductile RM shear wall buildings in Montréal was governed by factored wind loads. This resulted in significant overstrength and high seismic collapse capacity that was increasing with height. Conversely, the buildings located in Vancouver, a high seismic hazard region, had higher collapse probabilities at MCE, but within the acceptable limits of FEMA P695. ACMRs of the archetype buildings in Vancouver were lower than those of the buildings located in Montréal, but both performance groups satisfied FEMA P695 objectives. In general, dynamic analyses revealed higher overstrength than the suggested values based on pushover analysis results. In addition, the dynamic analyses results confirmed that the seismic collapse risk increases with the increase in the location's seismicity. Furthermore, in regions with high seismicity, collapse probabilities increase with the increase in the total building height.

This research study contributes to the understanding of the seismic performance and collapse capacity of ductile RM shear wall buildings with boundary elements. It emphasizes that the

addition of boundary elements using concrete C-shaped pilaster blocks provides great potential in enhancing the overall system ductility and seismic performance. It allows the use of several configurations of vertical reinforcements, closely spaced hoops for confinement, and the possibility of using high strength concrete grout. Additionally, the present study demonstrates that the use of the proposed hybrid load-bearing layout may present a practical and attractive alternative to conventional load-bearing wall systems. Utilizing these design enhancement recommendations, the findings of this study suggested that there is a potential to conservatively increase the height limits assigned by NBCC-15 to ductile RM shear walls. For RM shear wall buildings in moderate seismicity regions, $0.35 \leq I_E F_a S_a\,(0.2) \leq 0.75$, the height limit can be changed to 70 m instead of the 60 m limit. This recommendation is supported by the superior overall seismic performance and high collapse capacity of the considered buildings in performance group 1. For the buildings located in regions with high seismic hazard (i.e. $I_E F_a S_a\,(0.2) > 0.75$), it is recommended to raise the height limit to 50 m. The buildings, in performance group 2, with heights more than 40 m (the current limit by NBCC-15) had a satisfactory seismic performance that satisfies FEMA P695 objectives.

It should be noted that the current investigation is limited to ductile RM shear walls with boundary elements made from high strength C-shaped pilaster block units and grouted with high compressive strength grout. It utilized a proposed hybrid load-bearing layout system composed of primary and secondary walls, and seismic detailing enhancements to improve the overall system performance and reduce the seismic collapse risk. Finally, it should be highlighted that the numerical model established and utilized in this study was validated against the limited available experimental database of RM walls with boundary elements. Further validation of the numerical model can be performed to ensure the accuracy of its simulations once more data covering wider range of design parameters is available. The results of this study are limited to the considered cases including the design and modelling assumptions. It is recommended that more studies considering a broader range of design parameters should be conducted before generalizing the current recommendations for relaxing the height limits.

Chapter 6

Effect of Ductile Shear Wall Ratio and Cross-Section Configuration on the Seismic Behaviour of Reinforced Concrete Masonry Shear Wall Buildings

6.1 Abstract

Reinforced masonry buildings typically have load-bearing walls structural system. Thus, the reinforced masonry shear walls must be capable of resisting both vertical forces from gravity loads and lateral forces from seismic and wind loads. Typically, as the walls are subjected to high axial loads, ensuring the ductile response becomes challenging. A possible solution at the component-level would be the utilization of walls with confined ends (i.e. walls with boundary elements) to reduce the compression zone and increase the compression strain. Another solution, which is at the system-level, is the introduction of a hybrid structural system that is composed of two types of walls: (1) ductile walls with or without boundary elements to resist the lateral forces and part of vertical forces, and (2) gravity walls that resist only axial loads. This paper proposes a combination of both solutions (i.e. at component and system levels). Additionally, it utilizes a series of linear and nonlinear, static and dynamic analyses to evaluate and quantify the effect of cross-section configuration and ductile shear walls area to total floor area (i.e. ductile shear wall ratio) on the seismic response of masonry buildings. The numerical analyses are performed by a model developed using the Shear-Flexure Interaction Multiple-Vertical-Line-Element-Model (SFI-MVLEM) available in *OpenSees* modelling platform. The primary objective is to recommend a range of ductile shear wall ratios that optimize the design and overall performance. The study targets mid-rise and high-rise masonry buildings located in regions with moderate seismic hazard. The findings emphasized that utilizing the ductile walls with boundary elements in the proposed hybrid structural system resulted in favourable enhancements in the structural response and optimization of the design. In addition, the results demonstrated the possibility of vertically reducing and terminating the specially detailed boundary elements. Thus, promoting ductile reinforced concrete masonry shear wall buildings as a competitive building system.

6.2 Introduction

Multi-storey masonry buildings have been effectively utilized in regions with low seismic hazard, such as the 24-storey apartment building (Place Louis Riel) in Winnipeg (Drysdale and Hamid, 2005) and a 20-storey building in Brazil (Correa, 2016). However, the application in regions with moderate and high seismicity is still limited due to the challenges involved with conventional types of Reinforced Masonry (RM) shear walls and the typical wall load-bearing structural system. Historically, there was a perception that masonry buildings are vulnerable to earthquake excitations as they are incapable of achieving a ductile seismic response. This perspective was heavily influenced by the structural response and damage of unreinforced masonry structures during past earthquake events (Zhao and Wang, 2015). Bruneau and Yoshimura (1996) presented an assessment of the damage to masonry buildings after the Hyogo-ken Nanbu (Kobe) earthquake in 1995. The authors concluded that most of the unreinforced masonry buildings found in the earthquake site were severely damaged. However, they reported that the few RM buildings that existed in the Kobe area showed a satisfactory seismic response (Bruneau and Yoshimura, 1996). Masonry buildings designed properly following the capacity design philosophy are expected to have a ductile response and sustain large inelastic deformations during earthquake events. Several experimental tests of RM shear walls (e.g. Banting and El-Dakhakhni (2014) and Shedid et al. (2010)) confirmed its capability of achieving the ductile response. Furthermore, many analytical studies, such as those by Aly and Galal (2019c) and Ezzeldin et al. (2016), demonstrated the potential favourable structural performance from RM shear wall buildings when adequately designed and seismically detailed.

Priestley and Elder (1982) tested three slender concrete masonry shear walls to investigate the influence of axial load level, confinement plates, and lap splicing in potential plastic hinge zones on the walls' overall response to seismic loading. The tested walls were three stories high with an aspect ratio of 2.5, and all walls had lap splices in the vertical reinforcement at each floor slab. The walls were tested under reversed cyclic loading until failure with at least three full cycles at each displacement amplitude, which was a multiple of yield displacement. Walls 1 and 2 had a high axial load, whereas wall 3 was tested under low axial load. Wall 2 was the only wall with 600mm long stainless-steel confinement plates placed at each end of the wall in the second to eighth mortar joints. The utilization of the confinement plates resulted in a significant enhancement in the walls' seismic response. The presence of the confining plates in wall 2 effectively restrained the vertical

splitting. Hence, it resulted in a much lower extent of damage in the compression zone of wall 2 compared with that of wall 1. Besides, the plates confined the grout core and reduced the possibility of vertical bars buckling in the compression zone. Thus, tensile bond failures in the lap spliced extreme vertical bars were prevented. At the same levels of strength degradations, wall 2 was capable of attaining three times the cumulative ductility of wall 1. Those authors concluded that in general the presence of lap splices in plastic hinge regions is problematic and should be avoided as much as possible. Preventing lap splicing in the plastic hinge region would allow a greater spread of plasticity and consequently a reduction in peak compressive strains. It was also concluded that the use of confinement plates in the critical regions of the wall (i.e. compression zone in potential plastic hinge) significantly enhanced the response of slender concrete masonry walls to seismic loading. It allowed substantially higher peak compression strains and higher ductility capacity compared to unconfined walls.

The effect of different types of confinement reinforcement on the ductility and energy dissipation capacity of RM shear walls was assessed by Snook et al. (2005). Those authors tested nine cantilever masonry shear walls with two different aspect ratios under reversed cyclic loading and constant axial load representing seismic excitations. The walls had three types of confinement: steel confinement plates, seismic reinforcement combs, and polymer fibres mixed with the grout. The test results indicated that the use of these confinement techniques only modestly enhanced the displacement and energy dissipation capacities of the walls. Compared to the placement of confinement plates or seismic reinforcement combs in mortar joints, the addition of polymer fibres in the grout mix resulted in the highest increase in energy dissipation and drift capacities. Furthermore, mixing the fibres with the grout increased the shear resistance, which reduced the observed shear damage (i.e. the diagonal cracks and shear deformations) in the tested walls.

The enhancement in the system-level seismic performance of RM buildings having shear walls with boundary elements was quantified by Ezzeldin et al. (2017). That study presented the results of experimental testing of a two-storey one-third scale RM building with boundary elements. The building had four shear walls with boundary elements in the direction of loading and was tested under reversed cyclic loading until failure. It focused on assessing the influence of system-level aspects on the overall seismic performance and quantifying the impact of utilizing shear walls with boundary elements instead of the conventional rectangular walls. For this reason, the authors

compared their experimental results with the results of a previously tested building, by Ashour et al. (2016), having the same configuration, layout, and lateral resistance but with rectangular shear walls. The reported load-displacement response showed similar response between the two buildings until 0.9% drift ratio. After that, the building with boundary element walls showed less strength degradation and higher energy dissipation capacity. The building with confined boundary elements reached the failure criterion (i.e. 20% degradation in strength) at a higher drift ratio (2.2%) compared with the building with rectangular walls, which failed at 1.9% drift. Besides, Ezzeldin et al. (2017) highlighted that the presence of confined boundary elements delayed the fracture of vertical reinforcement and the crushing of grout core. Furthermore, the confined boundary elements resulted in improving the displacement capacity by postponing the strength degradation to higher drifts. The displacement ductility of the building with confined boundary elements was 20% and 40% higher than the building with rectangular walls at 20% and 50% strength degradation, respectively. The two buildings had similar energy dissipation capacities until 1.5% drift ratio. However, the presence of confined boundary elements resulted in 17% and 25% increases in the energy dissipation capacity at 2.2% and 3.5% drifts, respectively. Additionally, there was a 15% increase, on average, in the equivalent viscous damping of the building with shear walls having confined ends. Therefore, this would result in reduced seismic demands for the building with boundary elements as a result of the increased damping and energy dissipation capacity. Finally, the building with boundary elements had 60% reduction in the twist angle due to the increase in its torsional resistance and the associated reduction in the eccentricity between the centre of mass and centre of rigidity.

It is clear that there is a significant amount of effort done previously in coming up with a confinement technique or a cross-section configuration to enhance the overall performance of RM shear walls. However, it is essential to note that among the several confinement approaches proposed in the literature, only the integration of confined boundary elements is capable of enhancing the lateral stability of RM shear walls. Utilizing confinement plates (Priestley and Elder, 1982) or confinement combs (Shing et al., 1993) in the compression toes, or even adding fibre polymers in the grout mix (Snook et al., 2005) enhances the maximum usable compressive strain. Therefore, these techniques are capable of increasing the section's curvature ductility and thus enhancing the overall displacement ductility and energy dissipation capacity. Nevertheless, they do not offer any enhancement to the lateral stability issue encountered in RM shear walls with a

single layer of vertical reinforcement when subjected to large reversible cycles of inelastic strains in the plastic hinge region. The integration of a confined boundary element to the wall's ends with at least two layers of vertical reinforcement, and transverse reinforcement provides both an enhancement to the wall's lateral stability by delaying the onset of vertical reinforcement buckling and an improvement in ductility and energy dissipation capacity through confinement. It is a well-established concept that the utilization of confinement in the compression zones of the potential plastic hinge region reduces the compression strain-softening response of concrete.

The study presented herein is set up to propose a hybrid structural system composed of *ductile* shear walls and *gravity* shear walls for multi-storey RM buildings in regions with moderate seismic hazard. This is achieved by evaluating the effect of cross-section configuration (i.e. rectangular walls or walls with boundary elements) and ductile shear wall area to floor area (i.e. ductile shear wall ratio) on the seismic response of RM buildings having a varying number of floors (i.e. varying aspect ratios). The main objective is to recommend a structural system with ductile shear wall configurations and ratios that would optimize the design, cost, and structural performance. Furthermore, the study compares the efficiency of utilizing ductile rectangular RM shear walls versus ductile RM shear walls with confined boundary elements. It aims to highlight when the application of walls with boundary elements would be most optimal. Finally, it investigates the possibility of terminating the confined boundary elements vertically to further optimize the design of RM buildings. The intent is to recommend options for the vertical extent of boundary elements in ductile RM shear walls that would result in structurally safe and optimized designs. The study utilizes the Canadian Standards Association (CSA) S304-14 (CSA, 2014) for the design and detailing of the model buildings. It targets mid- and high-rise RM buildings in regions of moderate seismic hazard. The outcomes of this study could also be used as aids for preliminary force- and displacement-based designs of RM shear wall buildings having the proposed layout of *ductile* and *gravity* shear walls.

6.3 Proposed Structural Layout

The proposed structural layout for RM shear wall buildings was put together to mitigate the known adverse effects of the high axial load on RM shear walls in typical load-bearing building systems. It was inspired by implicit recommendations in CSA S304-14 (CSA, 2014) and Masonry Standard Joint Committee (MSJC, 2013), and specific recommendations in New Zealand Standard

(NZS) 4230-2004 (NZS, 2004). According to CSA S304-14 clause 16.3.4.2, masonry shear walls can be divided into walls that are part of the *main* Seismic Force Resisting System (SFRS) and walls that are considered *minor*. This is achieved by ensuring that the stiffest wall in the main SFRS is capable of attracting and resisting 90% of the lateral force due to seismic actions. Those walls shall be designed and detailed to resist 100% of the resulting seismic forces. Minor walls shall not have enough stiffness to attract more than 2.5% of the total seismic force or 50% of the average shear force in main SFRS walls. Minor walls shall be designed to remain elastic or have sufficient nonlinear capacity to maintain its gravity load-carrying capacity while undergoing earthquake-induced deformations (i.e. satisfy the deformation compatibility). Furthermore, as per MSJC-2013 clause 7.3, masonry elements can be classified into *participating* and *nonparticipating* elements. Participating elements are the masonry components designed and detailed to resist all lateral forces such as shear walls, column piers, pilasters, beams, and coupling elements. On the contrary, nonparticipating elements do not contribute to the system's lateral strength or stiffness and shall be isolated from the lateral force resisting system. However, for these masonry elements, their isolation joints and connectors shall be designed to sufficiently resist the maximum storey drifts.

CSA S304-14 and MSCJ-2013 provided general guidelines for the classification of the structural components according to their resistance of vertical and lateral forces. However, according to NZS 4230-2004 clause 12.4, RM shear walls could be classified into *primary* and *secondary* walls. This was proposed for structures containing walls more than needed to resist the seismic design actions. In such cases, it is a rational decision to divide the system into *primary* shear walls resisting all lateral forces and part of gravity loads, and *secondary* walls resisting only gravity loads. Dimensional limitations are imposed on secondary walls to prevent them from exceeding the yield displacement. This is possibly achieved by limiting the walls' lateral stiffness and locating the primary walls such that the eccentricity between the centre of mass and centre of rigidity is minimized. The stiffness of secondary walls shall account for both flexure and shear deformations. If flexure deformations are dominant, then the length of secondary walls shall be limited to one-half that of the longest primary wall. However, when shear deformations dominate, the length of the longest secondary wall shall be limited to one-quarter that of the primary wall with equal thickness. To achieve this, long and stiff secondary walls shall be divided into more flexible segments using separation or isolation joints. The contributions from both primary and

secondary walls shall be accounted for when calculating the system's natural period. However, the ductility factor should be solely based on the primary walls' characteristics.

Based on the recommendations from the three international masonry design standards (i.e. CSA S304-14, MSJC-13, and NZS 4230-2004, the hybrid structural layout defined in this study was composed of *ductile* shear walls and *gravity* walls. The ductile walls follow a similar definition to that of main walls, participating elements, and primary walls, whereas the gravity walls follow the definition of minor walls, nonparticipating elements, and secondary walls. However, the main difference between the suggested layout and that defined by NZS 4230-2004 is that the current layout is based on utilizing ductile RM shear walls with boundary elements as the main SFRS. Besides, proposed design recommendations are implemented to mitigate the adverse impact of gravity axial loads and enhance the overall structural performance. Thus, the proposed system is a combination of system-level and component-level solutions. This structural system layout gives options to control the level of axial load on the critical walls that would provide the necessary ductility for the building. As such, it would be possible to reduce the axial load's adverse impacts on the ductility and energy dissipation capacity of the system. The ductile shear walls would be designed to resist all lateral forces and part of gravity forces, while the gravity walls would be resisting only vertical gravity forces and induced lateral forces due to deformation compatibility and P-Δ effects. The gravity walls should not have sufficient lateral stiffness to attract any lateral forces. As recommended by CSA S304-14, gravity walls should not be capable of attracting more than 2.5% of the total lateral force. This could be achieved by utilizing vertical separation or isolation joints in long gravity walls based on the prescriptive requirements given in NZS 4230-2004 for secondary walls. The vertical separation joints are common in RM buildings and would follow the detailing of typical movement joints. Thus, the application of the proposed layout would be practical in RM buildings without the need for adopting any new construction or detailing knowhow. Figure 6.1(b) illustrates the proposed structural in-plan arrangement for the ductile and gravity walls. The ductile walls can be either rectangular or end confined, whereas the gravity walls would ideally be of rectangular cross-section and conventional (i.e. non-seismic) detailing. Locating the ductile walls at the perimeter of the building results in a lower share from gravity axial forces and increases the building's torsional resistance. Besides the walls were placed symmetrically to minimize the eccentricity between the centre of mass and centre of rigidity.

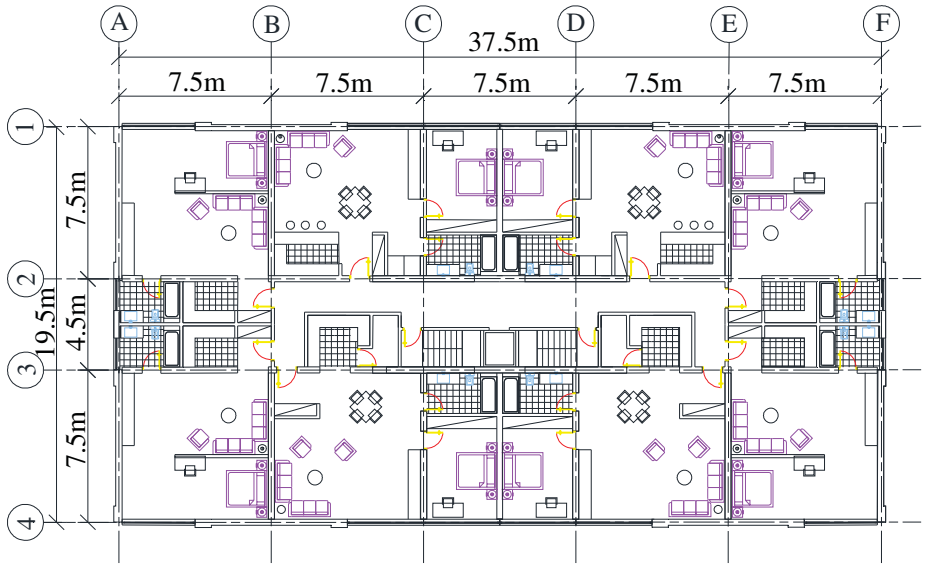

(a)

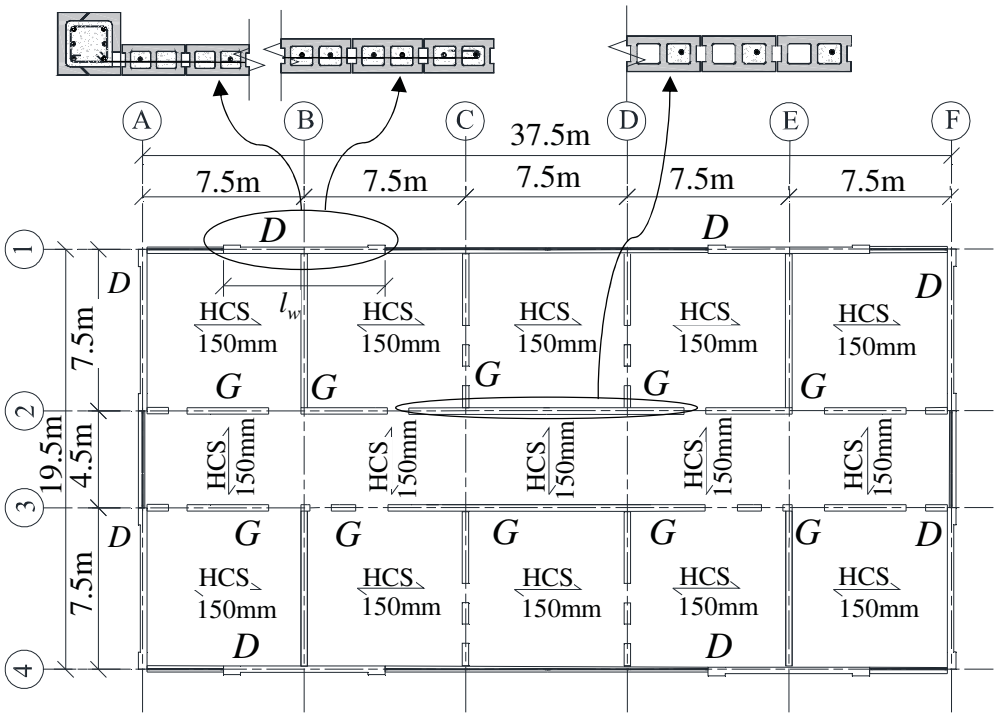

(b)

Figure 6.1 (a) Architectural plan layout; and (b) Proposed structural layout of Ductile (D) and Gravity (G) shear walls for RM buildings

6.4 Model Buildings' Selection and Design

In this study, twelve archetype buildings were selected to represent typical mid- and high-rise RM shear wall buildings located in a region with moderate seismicity. The model buildings were

assumed to be located in Québec City, Québec, which is a region of relatively high seismicity in eastern Canada. It is characterized by a seismic hazard index [i.e. $I_E F_a S_a(0.2)$] of 0.493 calculated based on NBCC-15. The selected buildings were based on the architectural plan layout presented in Figure 6.1(a). This is a conceptual architectural layout plan representative of masonry apartment buildings having corridor walls, exterior walls, and unit separation walls. Figure 6.1(b) shows the buildings' structural plan layout, which consists of ductile and gravity walls, as discussed previously. It can be seen that the proposed hybrid structural system is applicable to typical masonry buildings. The buildings varied in the number of floors, ductile shear wall configuration, and ratio defined as the total ductile shear wall area in one direction divided by the total floor area. Table 6.1 presents the details of the selected model buildings in this study.

Table 6.1 Model buildings' characteristics

Building No.	Building ID.	Number of storeys	Shear wall configuration	Shear wall length, l_w (m)	Ductile shear wall ratio (%)
1	6S-Rect-4.4m	6	Rectangular	4.4	0.70
2	6S-Rect-5.4m			5.4	0.86
3	6S-Rect-6.4m			6.4	1.02
4	6S-Rect-9.2m			9.2	1.46
5	6S-BE-2.4m		End confined	2.4	0.34
6	6S-BE-3.4m			3.4	0.45
7	6S-BE-4.4m			4.4	0.55
8	6S-BE-5.4m			5.4	0.65
9	12S-BE-4.4m	12	End confined	4.4	0.79
10	12S-BE-6.8m			6.8	1.17
11	12S-BE-8.4m			8.4	1.43
12	12S-BE-9.2m			9.2	1.56

The studied buildings are given the designation shown in Table 6.1, which reflects the number of floors (**6**-**S**torey or **12**-**S**torey), ductile shear wall's configuration (**Rect**angular or **B**oundary **E**lement), and ductile shear wall's length. To vary the ductile shear wall ratio, it was decided to fix the walls' arrangement and only change the wall's length. This is in-line with the objective of optimizing the ductile shear wall ratio and highlighting the advantages of having a hybrid layout composed of ductile and gravity shear walls. The locations of the ductile walls were cautiously selected to minimize their share of axial forces from gravity loads to allow sufficient inelastic rotation capacity. Furthermore, the floors were made up of precast pre-stressed Hollow Core Slabs (HCS), which is a typical flooring system utilized in RM shear wall buildings. Therefore, by alternating the orientation of the HCS units, it was possible to further control the level of axial load

on the ductile RM shear walls. The buildings had a typical floor height of 3.5 m, which makes the total building height 21 m for the 6-storey buildings and 42 m for the 12-storey buildings.

The model buildings were designed and detailed in accordance with the NBCC-15 requirements, which refer to CSA S304-14 for the design of masonry buildings. The design loads included vertical forces from dead, live, and snow loads and lateral forces from either wind or seismic actions, whichever governs. The dead loads included the self-weight of structural components and the additional weight of non-structural components, which was taken as 1.5 kPa to account for finishes, partitions, and other utilities. The live load was based on the specified loads in NBCC-15 for the residential occupancy, as the reference buildings were assumed to be apartment buildings. Roof snow load was calculated as per NBCC-15 based on the provided climate design data for the considered location (i.e. Québec City). For the selected location and the considered buildings' heights, seismic actions governed the lateral design forces over wind loads. The seismic loads were estimated following a linear dynamic analysis procedure using the seismic design data given in NBCC-15 Appendix C and based on the modal Response Spectrum Analysis (RSA) method. Detailed three-dimensional linear elastic models (based on finite element formulations) were created for the studied buildings in ETABS (CSI, 2015) program. Stiffness modifiers were used as recommended by CSA S304-14 to account for cracking effects on the lateral stiffness of the shear walls. The models were verified, and the seismic demands were calculated based on the modal RSA method outlined in NBCC-15. The use of the linear dynamic analysis procedure is permitted by NBCC-15 and ASCE7-16 for all buildings without restrictions on total height, seismicity, or system irregularities. It provides a more representative distribution of seismic forces over the building height compared with the equivalent static force procedure, accounts for accidental torsional effects, and optimizes the design base shear.

All ductile shear walls were detailed to satisfy CSA S304-14 provisions to qualify for a ductility-related seismic response modification factor (R_d) of 3 and an overstrength-related seismic response modification factor (R_o) of 1.5. The ductile shear walls were made up of reinforced fully grouted standard concrete masonry blocks. However, the gravity walls were partially grouted with vertical separation joints to control and limit their lateral stiffness. They were designed to resist vertical forces from gravity loads and lateral forces due to maximum inter-storey drifts (i.e. to satisfy deformation compatibility with ductile walls). For the ductile walls with boundary

elements, C-shaped pilaster block units were used to form the enlarged boundary elements at the walls' ends. Having confined boundary elements at walls' ends to enhance the ductility is a well-established construction technique in Reinforced Concrete (RC) shear walls. However, in RM, with the available conventional construction techniques, it might not be feasible to benefit from the boundary elements. This is because in typical planar RM shear walls, there is no sufficient space to provide several layers of vertical reinforcement and closely spaced hoops to confine the compression zones. Utilizing the C-shaped blocks provides flexibility in selecting the size of the boundary elements, enhancing the specified masonry compressive strength (f'_m), and using several layers of longitudinal reinforcement with closely spaced, as needed, hoops for buckling prevention and confinement. Compared to the alternative confinement schemes of providing embedded stainless steel plates (Priestley and Elder, 1982) or seismic combs (Shing et al., 1993) in mortar bed joints, having boundary elements in compression zones gives more room for enhancing the overall structural response. For instance, it allows using blocks and grout with higher compressive strength. Thus, it would be possible to benefit from an increase in the specified masonry compressive strength (f'_m). Drysdale and Hamid (1979), Khalaf (1996), Sarhat and Sherwood (2013), and Fortes et al. (2015) have shown that increasing the compressive strength of grout results in increasing the masonry prism compressive strength (f'_m), especially when the stiffness properties are close between the grout and masonry units. In addition, based on NZS 4230-2004 Appendix B, which was developed based on the work of Priestley and Chai (1984), it is possible to calculate the design compressive strength based on contributions from masonry and grout compressive strengths. Enhancing the masonry compressive strength, especially in the ductile shear walls, would improve the structural performance and reduce the required shear wall ratio.

Figure 6.2 along with Table 6.2 summarize the model buildings ductile shear walls cross-sectional dimensions and reinforcement details. For the 12-storey buildings, the ductile walls cross-sectional dimensions were grouped and optimized every four floors. Only the boundary elements' lengths and web thickness were reduced. The walls' in-plane length was kept constant, and the reduction in boundary element length was gradual to avoid resulting in a vertical stiffness structural irregularity. The reduction in boundary elements' vertical extent will be analyzed and discussed in detail in the following sections. In the 6-storey buildings with rectangular walls, the ductile walls' thickness and reinforcement were reduced every three floors. However, for the 6-storey buildings with boundary element walls, the cross-sectional dimensions were kept constant

over the building's height. Nevertheless, similar to the 12-storey buildings, termination of boundary elements vertically is assessed in subsequent sections.

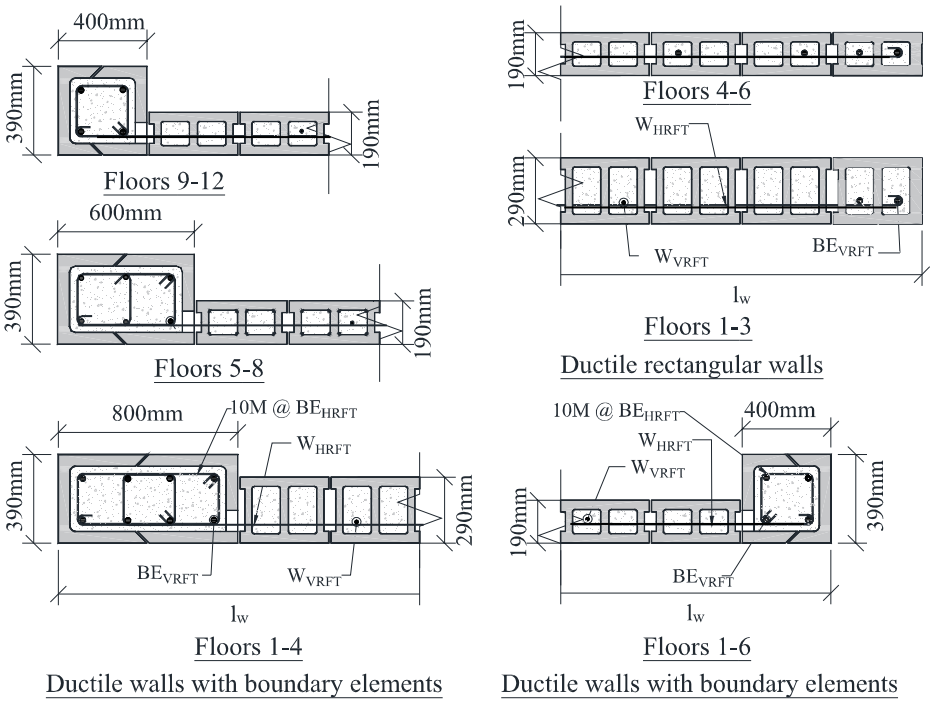

(a) (b)

Figure 6.2 Geometry, reinforcement details, and notation of the model buildings' ductile shear walls: (a) 12-storey buildings; and (b) 6-storey buildings

Table 6.2 Summary of model buildings' ductile shear walls reinforcement details

	Floors 1-3 and 1-4				Floors 4-6 and 5-12			
Building ID.	**BE_{VRFT}**	**BE_{HRFT}**	**W_{VRFT}**	**W_{HRFT}**	**BE_{VRFT}**	**BE_{HRFT}**	**W_{VRFT}**	**W_{HRFT}**
6S-Rect-4.4m	20M	NA*	4-15M	10M@200mm	15M	NA*	4-15M	10M@600mm
6S-Rect-5.4m	15M		5-15M	10M@200mm	15M		5-15M	10M@600mm
6S-Rect-6.4m	15M		6-15M	10M@200mm	15M		6-15M	10M@600mm
6S-Rect-9.2m	15M		10-15M	15M@200mm	15M		10-15M	10M@200mm
6S-BE-2.4m	15M	85mm	2-15M	10M@200mm	15M	240mm	2-15M	10M@200mm
6S-BE-3.4m	15M	90mm	3-15M	10M@200mm	15M	240mm	3-15M	10M@600mm
6S-BE-4.4m	15M	90mm	4-15M	15M@200mm	15M	240mm	4-15M	10M@600mm
6S-BE-5.4m	15M	90mm	4-15M	10M@200mm	15M	240mm	4-15M	10M@600mm
12S-BE-4.4m	15M	90mm	4-15M	15M@200mm	15M	240mm	4-15M	10M@600mm
12S-BE-6.8m	15M	90mm	6-15M	10M@200mm	15M	240mm	6-15M	10M@600mm
12S-BE-8.4m	20M	90mm	8-15M	15M@200mm	15M	240mm	8-15M	10M@400mm
12S-BE-9.2m	20M	90mm	8-15M	15M@200mm	15M	240mm	8-15M	10M@400mm

*Not Applicable

6.5 Finite Element Model

6.5.1 Model description

The use of beam-column (i.e. line-element model along the centreline of the wall) element models to simulate shear walls' response produces reasonably accurate simulations. However, it does not capture the shear deformations and the shift in the neutral axis along the wall's cross-section during the loading history. The simulation of shear response using empirical models defined independently from the flexural modelling parameters results in an uncoupled response between nonlinear shear and flexure. The analytical predictions based on uncoupled response might underestimate the vertical compressive strains for slender walls and overestimate lateral load capacity for walls with low and moderate aspect ratios (Kolozvari et al., 2015a). In this study, a state-of-the-art macro-modelling approach is utilized to simulate the nonlinear response of the RM shear walls. The RM shear walls are modelled using the Shear-Flexure Interaction Multiple-Vertical-Line-Element-Model (SFI-MVLEM) developed by Kolozvari et al. (2015a) and available in *OpenSees* (McKenna et al., 2000) modelling platform. This element is capable of capturing the nonlinear shear response and the coupled shear-flexure interaction. It also captures the changes in neutral axis depth along the wall's length. Figure 6.3 illustrates the geometry of the idealized nonlinear numerical model for RM shear walls based on SFI-MVLEM.

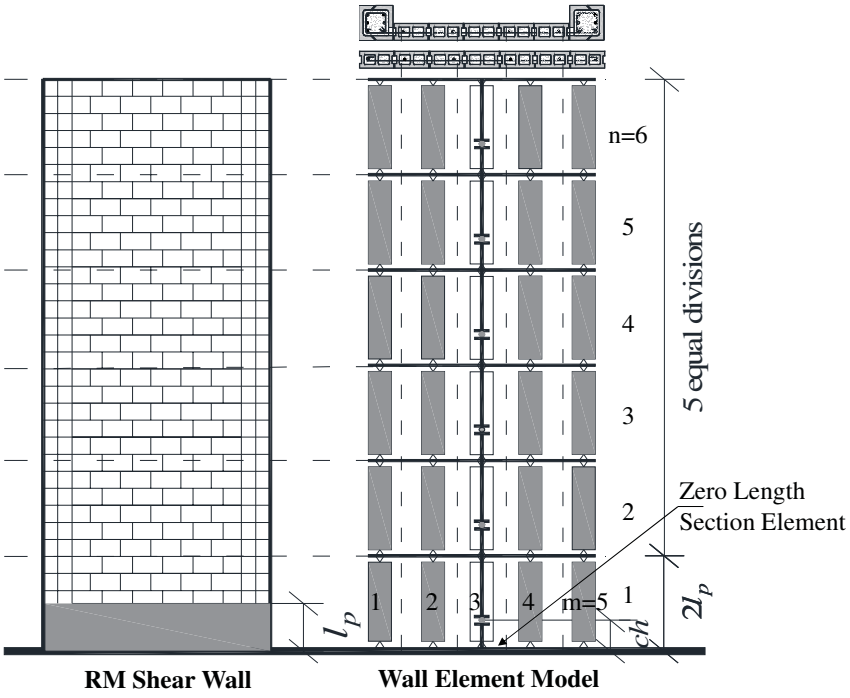

Figure 6.3 Numerical idealization of RM shear walls using SFI-MVLEM

The RM shear wall is idealized into six elements (n = 6) of vertical SFI-MVLEM elements over the wall height with a first element having a length equal to twice the plastic hinge length (i.e. $2l_p$). The plastic hinge length (l_p) can be calculated using the equation derived by Bohl and Adebar (2011) as it was specifically developed for structural walls, and it results in lengths close to the experimental results. Using twice the plastic hinge length as the length of the extreme element is in line with the recommendations in the literature, such as by Calabrese et al. (2010) and Aly and Galal (2019c) to ensure an objective and accurate response simulations. Each of the six elements is composed of five (m = 5) parallel RC panel elements, as recommended by Kolozvari et al. (2015b), and two rigid top and bottom beams. The RC panel element is comprised of concrete, vertical and horizontal reinforcement. The relative rotation between the top and bottom rigid beams is lumped at a height equal to *ch,* referred to as the centre of relative rotation. The value of c was taken equal to 0.4, as suggested by Vulcano et al. (1988) and Orakcal and Wallace (2006). The constitutive RC panel response due to reversed cyclic loading is idealized by the Fixed Strut Angle Model (FSAM), which was extended by Orakcal et al. (2012) to include shear aggregate interlock effects. The implemented shear resistance mechanism included shear aggregate interlock effects and reinforcement bars dowel action to represent the shear resistance along cracks (Kolozvari et al., 2015a). Shear aggregate interlock effects were simulated using a simple friction-based model that depends on a shear friction coefficient (η) and the normal stress perpendicular to the crack. Similarly, the steel reinforcement dowel action was represented by a simple linear-elastic constitutive model depending on a stiffness coefficient (α), the shear strain in the wall horizontal plane, and the elastic steel modulus.

There are two major limitations associated with this element model. First, the element is incapable of capturing the substantial strength degradation observed experimentally at the end of reversed cyclic loading tests of structural walls. This is due to the inability of the element model in simulating failure modes such as fracture or buckling of vertical reinforcement, out-of-plane instability, and sliding shear failure at the wall base. The second drawback of the SFI-MVLEM model is that it was not calibrated using a wide range of wall geometries, reinforcement ratios, and arrangement and axial load ratios. This is mainly for the shear resistance mechanism parameters (η and α). In the present study, to account for the failure modes represented by fracture and buckling of vertical reinforcement, the (MinMax) material model available in *OpenSees* (McKenna et al., 2000) was utilized. The fracture strain was given a value of 0.045, based on the

calibration study performed against several walls as discussed in following sub-sections. Additionally, to account for the failure modes associated with crushing of masonry or grout core, the masonry/concrete constitutive model was calibrated against experimental data to estimate the parameter (ε_{cr}), which is a non-dimensional critical post-peak strain needed to define a tangent line until the spalling strain. Furthermore, the developed model was extensively calibrated and validated against a range of experimental results from cyclic testing of several RM walls with different configurations, axial load levels, aspect ratios, and reinforcement ratios. The effects of strain penetration were also accounted for in the modelling approach by including a zero-length element section at the wall base. The reinforcement bars in this section were assigned Bond_SP01 material in *OpenSees* (McKenna et al., 2000) with the bar stress versus bar slip relation developed by Zhao and Sritharan (2007).

6.5.2 Constitutive material models

The predicted stiffness and load-deformation properties for the RM shear wall at any level of applied deformation will depend on the RC panel constitutive model, the assigned tributary areas of concrete and reinforcement, and their constitutive material models. In the SFI-MVLEM, the uniaxial stress-strain relationship of reinforcing steel was represented using the nonlinear hysteretic model of Menegotto and Pinto (1973), and the concrete uniaxial response along the fixed struts' direction was modelled using Chang and Mander (1994) stress-strain constitutive relationship. In this study, Chang and Mander (1994) concrete stress-strain constitutive relationship was calibrated to simulate the response of fully grouted masonry. This was achieved by using the proper peak compressive strength (f'_m), strain at peak compressive stress (ε_{mo}), and the modulus of elasticity (E_m) based on the experimental values reported in the literature for the walls used in validating the numerical model. For the validation models, the compressive strength (f'_m) reported in each experimental study was used, whereas for the numerical models of the studied buildings the assumed design values were used. The strain at compressive strength (ε_{mo}) was taken as 0.0015, the ultimate/crushing strain (ε_{mu}) was assumed to be 0.0025, and the initial tangent modulus (E_m) was estimated as $1000f'_m$ (in MPa). The other non-dimensional parameters were defined to refine the simulated response against the experimental results. The shape parameters in tension and compression (r_t and r_c) were taken as 1.5 and 10 for end confined walls, and as 1.2 and 15 for unconfined walls, respectively. Moreover, the non-dimensional critical strains in tension and compression (x_{crp} and x_{crn}) were taken as 1000 and 0.935, respectively.

Similarly, the utilized steel stress-strain material model in the validation models (i.e. Menegotto and Pinto (1973) nonlinear hysteretic model) was calibrated based on the reported material properties for the walls' reinforcing steel. However, the reinforcing steel material properties used in the studied buildings' nonlinear numerical models were based on the recommended values in the design standard (i.e. CSA S304-14). Thus, for the studied buildings' models, the reinforcement yield strength (f_y) was assumed to be 400 MPa, and the modulus of elasticity (E_s) was assumed to be 200 GPa. A value of 0.015 was assigned to the strain hardening parameter. The initial curvature parameter (R_0) was given a value of 20, and the curvature degradation parameters (cR_1 and cR_2) were assigned 0.975 and 0.25, respectively. For the isotropic hardening parameters, the default values of 0 and 1 were taken for the tension parameters (a_1 and a_2) and the compression parameters (a_3 and a_4).

6.5.3 Model sensitivity, calibration, and validation

The sensitivity of SFI-MVLEM along with the strain penetration zero-length element section and the utilized response regularization techniques were assessed for RM shear walls. It is essential to minimize the sensitivity of the model response simulations to the various modelling parameters. The choice of an extreme member having a length equal to twice the length of the plastic hinge was proven to reduce the dependence of the response results on the number of elements (n) used. Table 6.3 summarizes the characteristics of the RM shear walls used to validate the numerical model and asses its sensitivity to the modelling parameters.

Table 6.3 Details of the RM shear walls utilized for validating the numerical model

Wall No.	Wall No. in Literature	Authors	Configuration	l_w (mm)	h_w (mm)	AR[a]	ρ_v[b]	Axial Stress (MPa)	No. of Floors
W1	Wall 2-2014	Banting and El-Dakhakhni (2014)	End Confined	1235	3990	3.23	0.69%	0.89	3
W2	Wall 1-2012	Banting and El-Dakhakhni (2012)	End Confined	1803	3990	2.21	0.56%	0.45	3
W3	Wall 6-2010	Shedid et al. (2010a)	End Confined	1803	2660	1.48	0.56%	0.89	3
W4	Wall 1-2010	Shedid et al. (2010a)	Rectangular	1803	3990	2.21	1.17%	1.07	3
W5	Wall 4-2010	Shedid et al. (2010a)	Rectangular	1803	2660	1.48	1.17%	1.07	2

[a] Aspect Ratio
[b] Vertical reinforcement ratio

The numerical model was validated against the experimental results from the quasi-static cyclic loading tests of RM shear walls with different configurations, Aspect Ratios (AR), reinforcement ratios and arrangements provided by Banting and El-Dakhakhni, (2012, 2014); and

Shedid et al. (2010a). Furthermore, the shear resistance mechanism parameters (η and α) were calibrated for end confined and rectangular RM shear walls. The calibrated values for the shear friction coefficient (η) and the dowel action stiffness parameter (α) were found to be 0.1 and 0.05, respectively, for end confined RM walls and 0.2 and 0.1, respectively, for rectangular RM walls. Due to the limited space and for brevity, only samples of the simulated hysteretic responses are presented in this paper.

Figure 6.4 displays the sensitivity of the numerical lateral force-displacement response of W1 (i.e. Wall 2-2014), from Banting and El-Dakhakhni, (2014), to the number of elements (n) over the wall's height. It can be seen that when using the first element with a length equal to twice the plastic hinge, the simulated response was not significantly affected by the number of vertical elements. Thus, by utilizing this simple response regularization technique, which accounts for the strain localization phenomenon, it is possible to increase the objectivity of the response predictions and reduce the scatter in results.

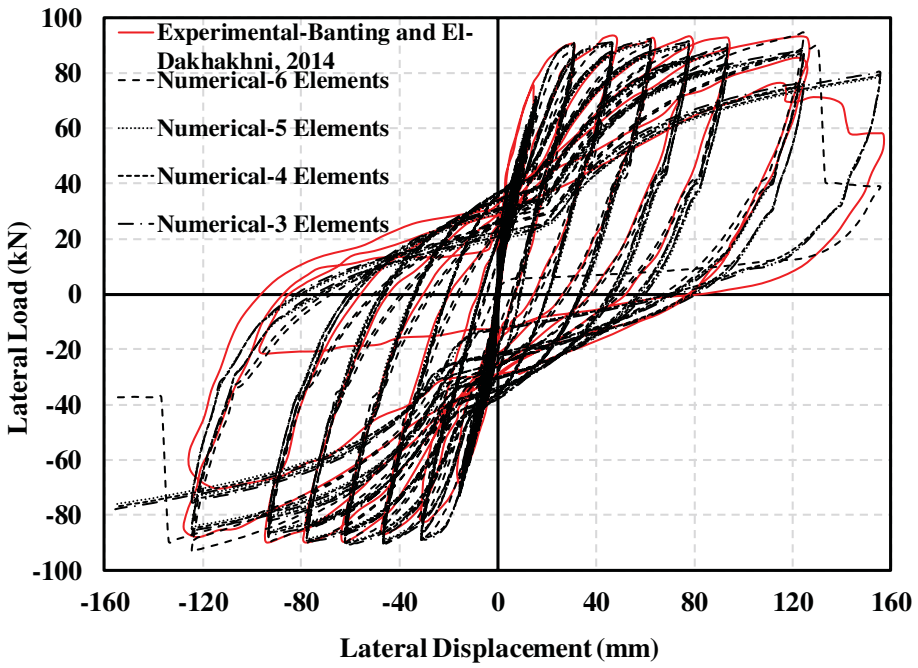

Figure 6.4 Numerical model sensitivity to the number of elements for W1

Figure 6.5 compares the experimental and numerical predictions of the hysteretic response of the walls summarized in Table 6.3. These walls had varying cross-sectional configurations, aspect ratios, vertical reinforcement ratios, and axial stress. The comparison shows reasonable agreement

between the experimental load-displacement loops and the numerical predictions. The model was capable of capturing the essential behavioural features of the cyclic response of RM shear walls, such as the pinching behaviour and the cyclic degradation in strength and stiffness as the loading history progresses. Furthermore, the numerical model captured, with acceptable accuracy, the experimentally measured lateral load capacity and lateral stiffness at most drift levels. Numerically predicted lateral load capacity and lateral stiffness were on average within ±15% of experimental values.

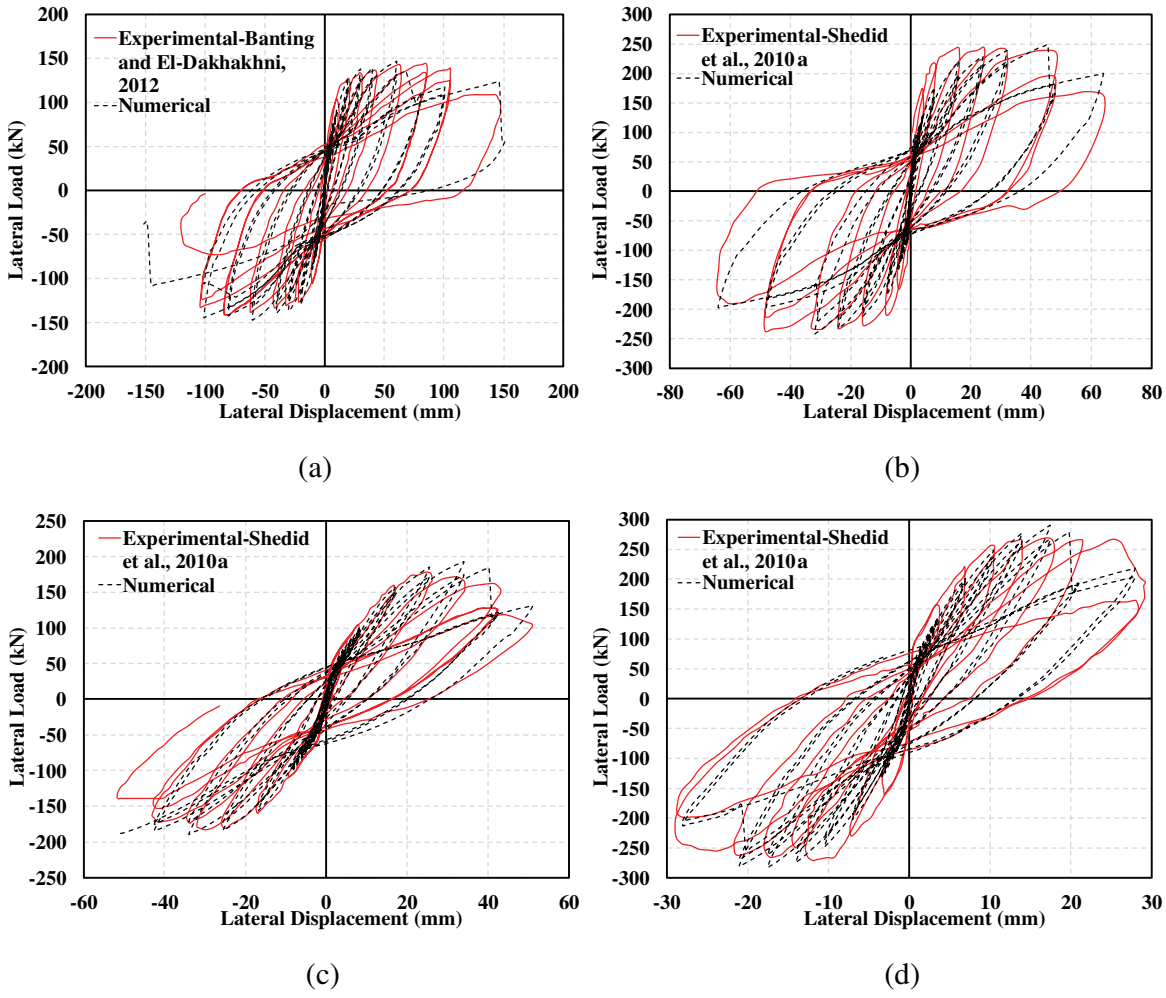

Figure 6.5 Experimental and numerical lateral load-displacement relationships of: (a) W2-end confined; (b) W3- end confined; (c) W4-rectangular; and (d) W5-rectangular

6.5.4 Archetype buildings' numerical models

The studied buildings were modelled in *OpenSees* (McKenna et al., 2000) using the validated modelling approach to simulate the response of the ductile RM shear walls. The gravity walls were implicitly modelled using a leaning column approach to account for P-Δ effects on the lateral

stiffness and strength of the buildings. As the studied buildings had a symmetric plan layout in both orthogonal directions, torsional modes of vibration were not dominant. Thus, a two-dimensional model was deemed sufficient to simulate the global response with reasonable accuracy. Although three-dimensional modelling might be the ideal choice, it would be very computationally demanding for the inelastic time-history simulations given the number of studied buildings and the number of selected input ground motions. A schematic representation of the model buildings' numerical model is presented in Figure 6.6.

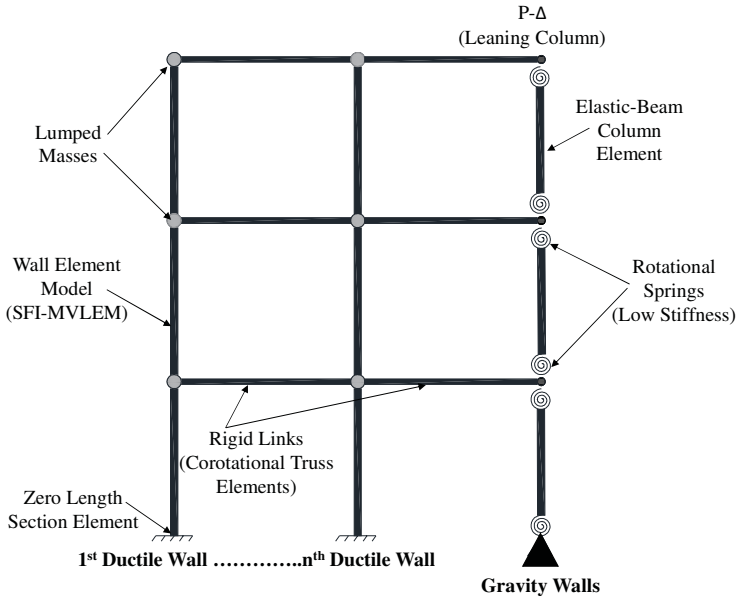

Figure 6.6 Schematic diagram of the archetype buildings' two-dimensional numerical models

It should be noted that the lumped masses were located at the floors' levels, regardless of the first element length, which was twice the plastic hinge length for the reasons discussed previously. The buildings' nonlinear models created in *OpenSees* (McKenna et al., 2000) were verified by comparing their dynamic characteristics against the design models, created in ETABS (CSI, 2015) and hand calculations. Table 6.4 compares the first mode of vibration periods obtained from ETABS and *OpenSees*. It can be seen that the un-cracked (elastic) natural periods from ETABS are within 1-16% of those estimated by *OpenSees* for the buildings with different configurations and ductile shear wall ratios. The numerical models in *OpenSees* had a slightly higher lateral stiffness due to the effective inclusion of the rebars in the calculations. The difference was higher for the buildings with walls having boundary elements as the *OpenSees* nonlinear models included the confinement effect on strength (i.e. increasing f'_m) and ductility.

Table 6.4 Verification of the numerical models' dynamic characteristics

Building ID.	T_1 (Elastic)-ETABS	T_1 (Elastic)-OpenSees	Difference (%)
6S-Rect-4.4m	1.11	1.14	2
6S-Rect-5.4m	0.85	0.86	2
6S-Rect-6.4m	0.68	0.68	1
6S-Rect-9.2m	0.43	0.42	1
6S-BE-2.4m	1.80	1.60	12
6S-BE-3.4m	1.24	1.07	15
6S-BE-4.4m	0.93	0.79	16
6S-BE-5.4m	0.74	0.63	16
12S-BE-4.4m	2.94	2.63	11
12S-BE-6.8m	1.75	1.55	12
12S-BE-8.4m	1.36	1.24	9
12S-BE-9.2m	1.22	1.12	9

6.6 Numerical Study

The study utilized linear dynamic, nonlinear static, and nonlinear dynamic analyses to evaluate and quantify the effect of ductile shear wall ratio, cross-section configuration and boundary element vertical extent on the global structural response of typical RM buildings. The linear dynamic analysis was performed based on the modal RSA method of NBCC-15 using the models developed in ETABS (CSI, 2015). Nonlinear static analysis (i.e. pushover) was performed for each of the archetype buildings to verify the nonlinear model and evaluate the buildings' lateral stiffness, strength, and ductility. The analysis was executed using the verified nonlinear numerical model generated in *OpenSees* (McKenna et al., 2000). The nonlinear static analysis results are also used to investigate the overstrength of the studied buildings. The nonlinear dynamic analysis utilized the Nonlinear Time-History Analysis (NTHA) method, which involves the determination of structural response by numerically integrating the equation of motion.

Due to the natural variability in ground motions' characteristics and the sensitivity of nonlinear response simulations, a sufficient number of representative input motions shall be used to capture the realistic dispersion of structural response. For that reason, the NTHA was performed using 12 pairs of ground motion accelerograms (i.e. a total of 24 individual records). The selected number of ground motions exceeds NBCC-15 recommendation of using 11 ground motion records for NTHA of buildings. As the studied buildings were located in eastern Canada (Québec City), which has a limited number of recorded natural ground motions, artificial ground motions were utilized in the present study. The input ground motion records were selected from the artificial time series database generated by Assatourians and Atkinson (2010) for Canada. Thus, these ground motion

accelerograms match the recommendations of most building codes (including NBCC-15) of utilizing spectrum-compatible ground motions in NTHA. The details of the selected input records are given in Table 6.5, and the unscaled response spectra are presented in Figure 6.7.

Table 6.5 Unscaled input ground motions' details (Assatourians and Atkinson, 2010)

No.	Designation	Event Magnitude	Epicentre Distance (km)
1-X	east6c1	6	12.8
1-Y	east6c1	6	12.8
2-X	east6c1	6	12.5
2-Y	east6c1	6	12.5
3-X	east6c1	6	12.8
3-Y	east6c1	6	12.8
4-X	east6c2	6	20.8
4-Y	east6c2	6	20.8
5-X	east6c2	6	16.9
5-Y	east6c2	6	16.9
6-X	east6c2	6	21.1
6-Y	east6c2	6	21.1
7-X	east7c1	7	15.3
7-Y	east7c1	7	15.3
8-X	east7c1	7	14.9
8-Y	east7c1	7	14.9
9-X	east7c1	7	14.8
9-Y	east7c1	7	14.8
10-X	east7c2	7	41.6
10-Y	east7c2	7	41.6
11-X	east7c2	7	45.2
11-Y	east7c2	7	45.2
12-X	east7c2	7	50.3
12-Y	east7c2	7	50.3

The ground motion accelerograms were scaled following the procedure of the seismic performance assessment of buildings, FEMA P58-1 (2012). The procedure requires scaling each of the selected records by a factor calculated according to Eq. (6.1), where $S(T_{avg})$ is the design spectral acceleration at the average of first and second modes periods; and $S_{gm}(T_{avg})$ is the ground motion record's geometric mean spectral acceleration calculated following Eq. (6.2), where $S_x(T_{avg})$ and $S_y(T_{avg})$ are the spectral accelerations at T_{avg} of the X and Y components of the ground motion, respectively.

$$Scale\ factor\ = \frac{S(T_{avg})}{S_{gm}(T_{avg})} \tag{6.1}$$

$$S_{gm}(T_{avg}) = \sqrt{[S_x(T_{avg}) \times S_y(T_{avg})]} \quad (6.2)$$

Using the scaled ground motions, a series of nonlinear dynamic analyses were performed for each of the model buildings to establish the trends between ductile shear wall ratios and important structural response parameters.

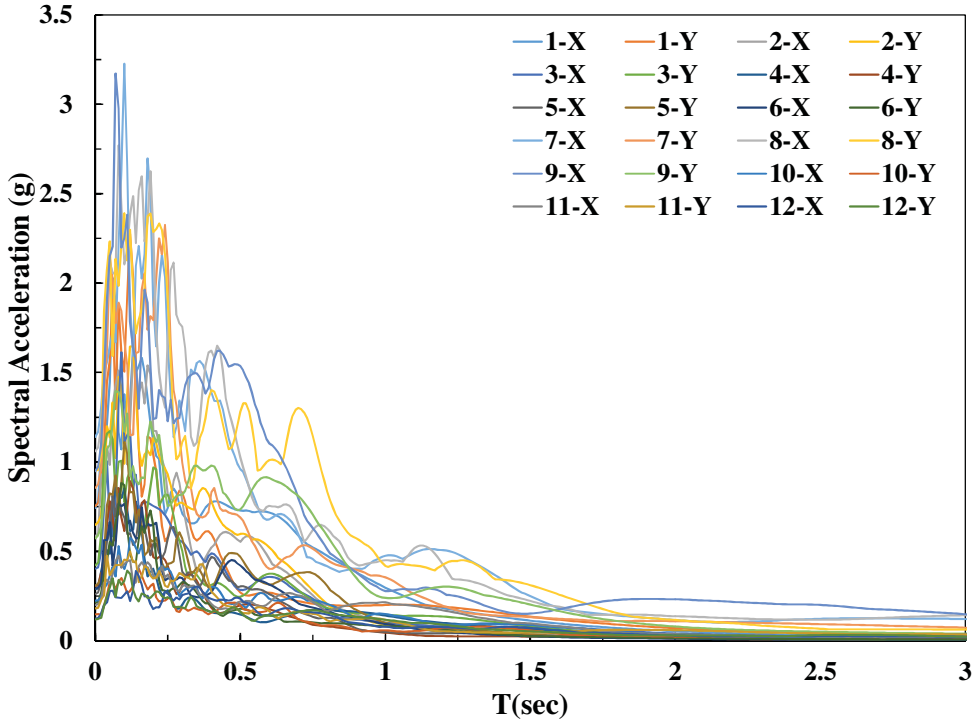

Figure 6.7 Unscaled response spectra of the selected ground motions (Assatourians and Atkinson, 2010)

6.7 Results and Discussion

6.7.1 Inter-storey drifts and base shear demand trends

The results of the linear and nonlinear dynamic analyses were used to establish the relations between peak inter-storey drift ratios and ductile shear wall ratios. From RSA, the peak inter-storey drift was directly found for each ductile shear wall ratio, configuration, and building height. The NTHA results were post-processed to calculate the peak inter-storey drift from each input ground motion. Then the mean was used to represent the peak inter-storey drift ratio from the selected suite of ground motions. Using the mean to represent the structure deformation response is in agreement with NBCC-15 recommendations. Figure 6.8 illustrates the impact of ductile shear wall ratios on the peak inter-storey drift of the 6-storey model buildings. Conforming to engineering intuition and consistent with the previous research results of Burak and Comlekoglu

(2013), the increase in the ductile shear wall ratio resulted in an apparent reduction in the peak inter-storey drift ratios. This is applicable for both configurations of ductile RM shear walls (i.e. rectangular walls and walls with boundary elements).

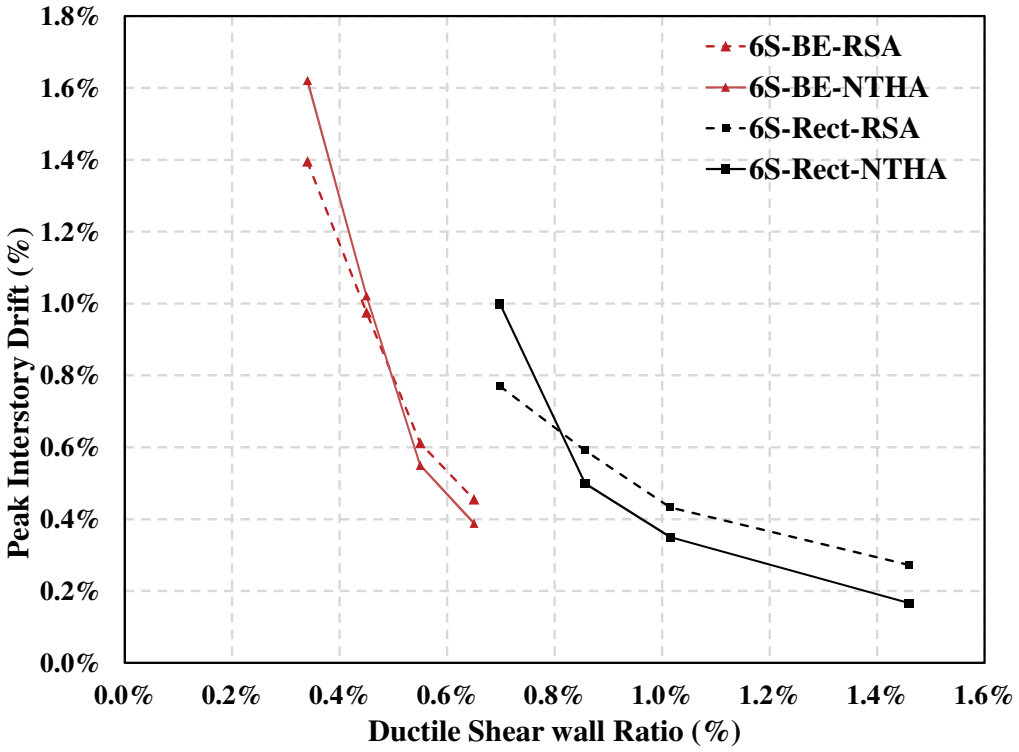

Figure 6.8 Effect of ductile shear wall ratio on peak inter-storey drift ratios of 6-storey buildings

Similar to the 6-storey model buildings, Figure 6.9 shows the impact of the ductile shear wall ratio on the peak inter-storey drifts of the 12-storey archetype buildings. The trend between ductile shear wall ratios and inter-storey drift ratio is seen in both the 6-storey and the 12-storey model buildings based on the results of the linear (RSA) and nonlinear (NTHA) dynamic analyses. However, this relation between the ductile shear wall ratio and peak inter-storey drift ratio is not typically obvious. This is because the increase in the ductile shear wall area would result in increasing the lateral stiffness of the building. A stiffer building is expected to attract higher seismic demands, which might result in a higher response, such as higher drift ratios or higher base shears. In Figure 6.8, the initial increase in the ductile shear wall ratio for the 6-storey buildings, beyond what was just needed to satisfy the design code (i.e. CSA S304-14) strength, stiffness, and ductility requirements, resulted in a sharp drop in peak drift ratios. This is attributed to the higher increase in the building's stiffness compared to the increase in its seismic mass and the forces'

demand. Afterwards, it is evident from Figure 6.8 that excessively increasing the ductile shear wall ratio beyond a specific value has less impact on the peak inter-storey drifts. This value was 0.55% for the walls with boundary elements and 1.02% for the walls with a rectangular configuration. For the 12-storey buildings, as seen in Figure 6.9, a similar trend is observed. The initial increase in ductile shear wall ratio beyond what was required to meet the code requirements resulted in a rapid drop in peak inter-storey drift. However, after a ductile shear wall ratio of 1.17%, the increase in the shear wall area compared to floor area only had a mild impact on inter-storey drifts.

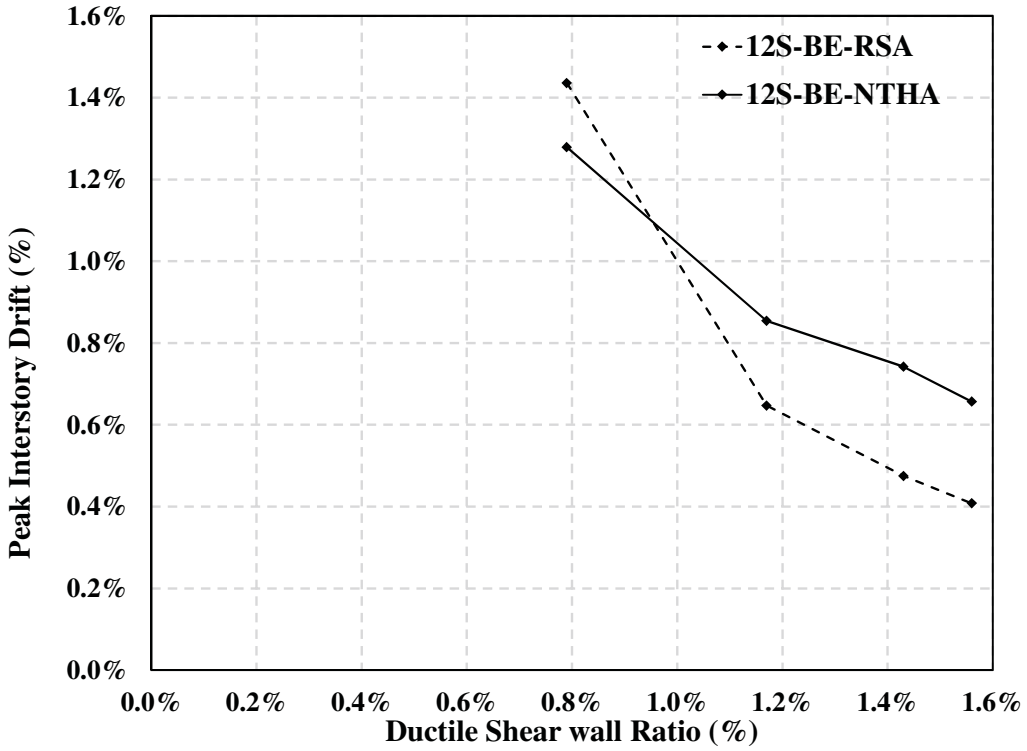

Figure 6.9 Effect of ductile shear wall ratio on peak inter-storey drift ratios of 12-storey buildings

From Figure 6.8, it can be seen that the minimum ductile shear wall ratio to satisfy the design code strength, drift, and ductility requirements for the 6-storey buildings was 0.70% for rectangular walls and 0.34% for end confined walls. This corresponds to peak inter-storey drift ratios of 1.62% and 1.00% for end confined and rectangular walls, respectively, based on NTHA. For rectangular walls, the governing condition was to satisfy the ductility requirements. It was not possible to ensure that the rectangular shear wall section had enough inelastic rotational capacity to achieve the ductile response with ductile shear wall ratios less than 0.70% (i.e. rectangular walls that are 4.4 m long). For the shear walls with boundary elements, the wall section was able to attain

sufficient inelastic rotational capacity with ductile shear ratios as low as 0.34%, corresponding to 2.4 m long walls. This is due to the presence of the confined boundary elements, which reduced and stabilized the compression zone, and delayed the onset of vertical reinforcement buckling. Thus, the maximum usable masonry compressive strain was increased, and the section's curvature ductility was enhanced (i.e. higher inelastic rotational capacity was attained). Therefore, a lower ductile shear wall ratio would be typically required when ductile shear walls with confined boundary elements are utilized instead of ductile rectangular shear walls. Furthermore, utilizing ductile shear walls with boundary elements as the main seismic force resisting components will make it possible to design RM buildings with optimized shear wall ratios making RM a competitive alternative construction material. As demonstrated in Figure 6.8, the drop in peak inter-storey drifts is much sharper for the end confined walls relative to the rectangular walls. This is attributed to the significant increase in lateral stiffness when the thicker boundary elements are further apart due to the increase in total wall's length.

For the 12-storey building, as illustrated in Figure 6.9, the minimum shear wall ratio to ensure the code requirements was 0.79%, which corresponds to 4.4 m long walls. It is noteworthy that it is very challenging to design 12-storey RM buildings with ductile rectangular shear walls. This is because of the difficulty in satisfying the inelastic rotational capacity requirement specified by CSA S304-14 for the ductile walls. It is much effective and perhaps practical to utilize RM shear walls with boundary elements in mid- and high-rise buildings in regions with relatively high seismicity, such as Québec City. This further supports the previous observation that utilizing ductile end confined RM shear walls would promote the competitiveness of RM buildings. It is clear that with the proposed structural layout, the shear wall ratio provided to ensure satisfying the code requirements will be significantly reduced. The trade-off will be an increase in gravity walls ratio, which will not have a substantial impact on neither the structural performance nor the cost as they do not mandate any special detailing.

Using the equivalent static lateral force procedure of NBCC-15, the resulting peak inter-storey drift ratios were found to be on the conservative side. The drift predictions were found to range between 1.4 and 2.3 times the RSA or NTHA results, respectively, for 6-storey buildings having ductile rectangular shear walls. For the 6-storey buildings with ductile walls having boundary elements, a similar range of conservativeness from 1.6 to 2.7 was observed between the static and

dynamic analysis methods. Similarly, using the NBCC-15 equivalent static lateral force procedure to design the 12-storey buildings would be very conservative. It was found that, at the lowest studied ductile shear wall ratio, the static analysis displacement predictions can be up to 3.3 or 3.7 times higher than the linear or nonlinear dynamic analyses results, respectively. It is important to note that all drift ratios, from RSA or NTHA, were less the 2.5% limit specified by NBCC-15 for buildings with normal importance. Thus, for high-rise RM buildings having ductile and gravity walls, it would be justifiable to utilize linear dynamic analysis in lieu of static analysis. This would produce designs that are not very conservative but are within the code prescribed requirements.

As previously mentioned, the impact of ductile shear wall ratio on the structural response is not apparent in most cases. Figure 6.10 illustrates the influence of increasing the ductile shear wall ratio, by increasing the length of walls, on the base shear demand from NTHA for the 6- and 12-storey buildings with rectangular and end confined walls. The vertical axis corresponds to the ratio between the base shear at a particular ductile shear wall ratio (V) and the base shear at the highest ductile shear wall ratio (V_{max}) for each building configuration. The 50th percentile was used to represent the natural variability in base shears from the individual ground motion records. It is evident in Figure 6.10 that increasing the ductile shear wall ratio is resulting in higher base shear demand due to the previously mentioned reasons, regardless of the buildings' aspect ratio or the walls' configuration. However, opting to utilize the end confined configuration for the 6-storey buildings would reduce the required ductile shear wall ratio to satisfy the design code requirements and provide more options for optimizing the design. It is interesting to note that unlike inter-storey drifts, excessively increasing ductile shear wall ratios remains influential in increasing the base shear demands. Base shear demands estimated using the equivalent static force procedure do not reflect the same trends seen in Figure 6.10. This is because they are typically based on the empirically estimated natural period, which is based on the building height and type of structural system. Alternatively, the linear dynamic analysis method is capable of reflecting the changes in base shear demands due to changes in the building's lateral stiffness. The outcomes of this study, as depicted in Figures 6.8-6.10, provide reasonable estimates of the required ductile shear wall ratios for limiting inter-storey drifts. Thus, it can be utilized as aids for preliminary designs of RM buildings, with ductile and gravity shear walls, based on force-based, displacement-based, or performance-based design approaches.

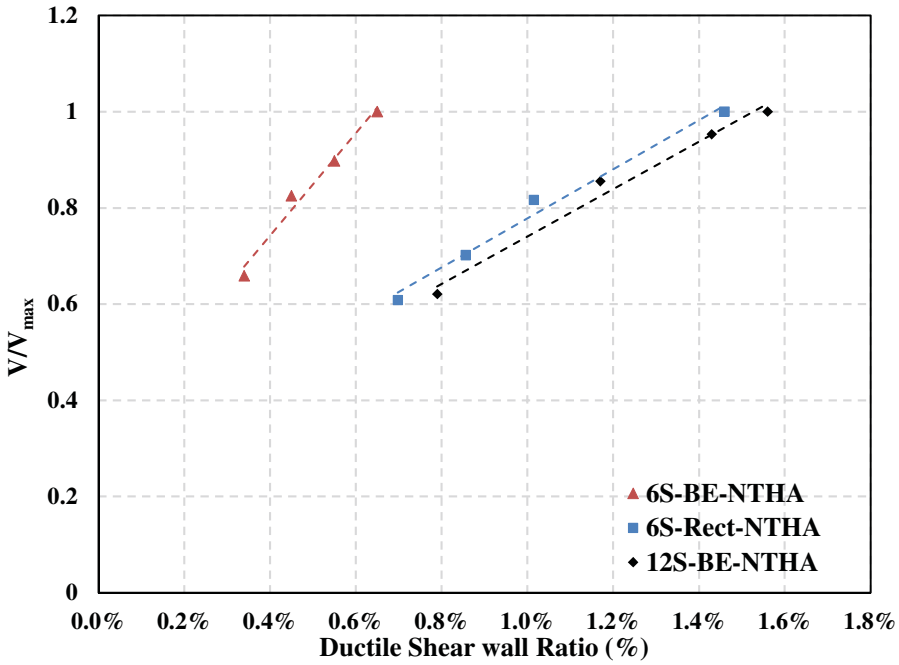

Figure 6.10 Influence of ductile shear wall ratio on base shear demand

The pushover analysis results were compared with the design capacity of the studied buildings to assess the overstrength and get an estimate of the overstrength-related response modification factor (R_o). Table 6.6 presents the estimated R_o values for the 12 buildings. For the 6-storey buildings with rectangular ductile walls, the average overstrength factor was 2.46. A higher average value of 3.8 was seen for the 6-storey buildings with end confined ductile walls. For the 12-storey buildings, the average was 3.24, which is marginally lower than the 6-story buildings. It is noteworthy that there was no clear trend between the increase in the ductile shear wall ratio and the estimated overstrength-related response modification factor. These results demonstrate that the 1.5 value provided by NBCC-15 for the overstrength-related response modification factor (R_o) of ductile RM shear walls is on the conservative side and can be safely applied to the proposed structural layout. In ASCE7-16, special RM shear walls, equivalent to ductile walls in Canadian standards, are assigned an overstrength factor (Ω_o) equal to 2.5 regardless of whether the building system is bearing wall or building frame.

Table 6.6 Overstrength-related response modification factors (R_o) of the archetype buildings

Building ID.	Static R_o
6S-Rect-4.4m	2.38
6S-Rect-5.4m	2.43
6S-Rect-6.4m	2.61
6S-Rect-9.2m	2.44
6S-BE-2.4m	3.96
6S-BE-3.4m	4.03
6S-BE-4.4m	4.11
6S-BE-5.4m	3.10
12S-BE-4.4m	3.30
12S-BE-6.8m	3.51
12S-BE-8.4m	3.12
12S-BE-9.2m	3.04

6.7.2 Boundary elements' vertical extent

The masonry design standard CSA S304-14 requires extending the boundary elements vertically over the entire wall height. Otherwise, it requires performing "rational analysis" to assess the influence of the changes in strength and stiffness on the structural performance of the walls. In MSJC-13, the need for boundary elements is evaluated based on either a displacement-based or a stress-based approach. Following the displacement-based approach, boundary elements are required when the neutral axis depth exceeds a critical value. In essence, confined boundary elements are required when the maximum compressive strain in extreme fibres exceeds the usable maximum masonry compressive strain. Based on this approach, it is allowed to terminate the boundary elements vertically beyond the larger of the wall length (l_w) or ($M_u/4V_u$). The objective of MSJC-13 provisions is to ensure that the boundary element extends vertically beyond a conservative estimate of the plastic hinge length. Alternatively, following the stress-based approach, boundary elements shall extend vertically when the maximum compressive stress due to factored loads at extreme fibres exceeds 20% of the masonry compressive strength (f'_m). It is permitted to vertically terminate the boundary elements when maximum stresses are less than 15% of f'_m.

In this study, the boundary elements cross-sectional dimensions and reinforcement details were kept constant for 6-storey buildings but were reduced for the 12-storey buildings. Maintaining the same cross-sectional dimensions and the special reinforcement details of boundary elements over 12-storey and higher buildings is neither economical nor practical. Thus, it was essential in this

study to investigate the possibility of terminating or reducing the boundary elements over the height of the building. This was achieved by comparing the NTHA results of the buildings with different options for the vertical extent of the boundary elements. Then, nonlinear static analysis (i.e. pushover) was performed to investigate the impacts of reducing the boundary element cross-sectional dimensions and reinforcement on critical global and local response parameters. Table 6.7 presents a description of the alternatives considered for the boundary elements' vertical extent in the studied 6-storey and 12-storey RM shear wall buildings.

Table 6.7 Alternatives for the boundary elements' cross-sectional dimensions (length and width) over the buildings' height

<table>
<tr><th>Building ID.</th><th>6S-BE-3.4m-1</th><th>6S-BE-3.4m-2</th><th>12S-BE-4.4m-1</th><th>12S-BE-4.4m-2</th><th>12S-BE-4.4m-3</th><th>12S-BE-4.4m-4</th></tr>
<tr><td>Ductile Shear Wall Ratio</td><td colspan="2">0.45%</td><td colspan="4">0.79%</td></tr>
<tr><td>Story 12
Story 11
Story 10</td><td rowspan="3"></td><td rowspan="3"></td><td>400x390mm</td><td>Terminated</td><td>Terminated</td><td>Terminated</td></tr>
<tr><td>Story 9
Story 8
Story 7</td><td rowspan="2">600x390mm</td><td rowspan="2">600x390mm</td><td rowspan="2">400x390mm</td><td rowspan="2">Terminated</td></tr>
<tr><td>Story 6
Story 5
Story 4</td><td>400x390mm</td><td>Terminated</td></tr>
<tr><td>Story 3
Story 2
Story 1</td><td>400x390mm</td><td>400x390mm</td><td>800x390mm</td><td>800x390mm</td><td>800x390mm</td><td>800x390mm</td></tr>
</table>

These alternatives were determined to ensure that the boundary element is at least extending vertically beyond the plastic hinge region. For a conservative estimate of the plastic hinge height, the CSA S304-14 upper estimate was used. In addition, the chosen alternatives for vertically reducing or terminating the boundary elements were carefully checked such that no vertical stiffness (e.g. soft storey) irregularity is formed. NBCC-15 and ASCE7-16 both define the vertical stiffness irregularity as a 70% reduction in the lateral stiffness of the SFRS in a floor compared to any adjacent floor or 80% reduction in lateral stiffness compared to the average stiffness of the three adjacent floors. Among the studied RM buildings, the archetypes with ductile shear wall ratios of 0.45% and 0.79% were selected to represent the 6-storey and 12-storey buildings,

respectively. The intent was to start with a reasonably optimized design in terms of the provided in-plan area of ductile shear walls and assess the possibility of further optimization vertically.

The impact of the boundary elements' vertical extent on the structural response of the studied buildings is summarized in Table 6.8. For the two groups of buildings (6-and 12-storey), it is evident that terminating or reducing the boundary elements vertically after the critical plastic hinge region had a negligible impact on the elastic (un-cracked) natural period of vibration (T_1). For the 6-storey building, terminating the boundary elements after the 3rd floor resulted in increasing the 50th percentile peak inter-storey drift ratio, based on NTHA, by 14%. However, for the 12-storey buildings, the impact on peak inter-storey drifts from the four alternatives for the boundary element vertical extent was minor.

Table 6.8 Impact of boundary elements' vertical extent on the structural response

Building ID.	Boundary Element	T_1 (Elastic) (sec)	Peak Inter-storey Drift
6S-BE-3.4m-1	Continuous	1.24	1.02%
6S-BE-3.4m-2	Discontinued at 4th floor	1.28	1.16%
12S-BE-4.4m-1	Continuous-Reduced	2.94	1.28%
12S-BE-4.4m-2	Discontinued at 9th floor	2.94	1.35%
12S-BE-4.4m-3	Discontinued at 10th floor	2.97	1.29%
12S-BE-4.4m-4	Discontinued at 7th floor	3.09	1.29%

A more detailed insight on the influence of the boundary elements' vertical extent on the distribution of inter-storey drifts is presented in Figure 6.11(a) and (b) for the 6-storey and 12-storey buildings, respectively. It is observed that in the 6-storey buildings terminating the boundary element at the 4th floor resulted in a sharp and sudden increase in inter-storey drifts in the floors above. Nonetheless, this increase is not very significant, by 14%, and the values are still well below the 2.5% limit of NBCC-15 for buildings with normal importance. For the 12-storey buildings, as illustrated in Figure 6.11(b), there is a more significant variation in the inter-storey drifts' distribution over the building height compared with the 6-storey buildings, even for the reference building (i.e. 12S-BE-4.4m-1). This is because the reference 6-storey building (i.e. 6S-BE-3.4m-1) had a continuous boundary element over the building's height. Thus, the impact of terminating the boundary element was very evident in the inter-storey drifts' distribution of building 6S-BE-3.4m-2. However, this was not the case in the 12-storey buildings. The reference building 12S-BE-4.4m-1 had a reduced boundary element over the building height. It would have been barely economical or practical to have the boundary element extend vertically over the entire building's

height with the same cross-sectional dimensions and reinforcement details. Among the four alternatives for the boundary elements' vertical extent in 12-storey buildings, option 3 (12S-BE4.4m-3) seems to have the least impact on inter-storey drifts' distribution. This alternative had a boundary element length that was gradually reduced by 200mm every three floors and then was discontinued at the 10th floor. On the other hand, reducing the boundary element's cross-sectional dimensions and reinforcement every four floors and then terminating it at 9th floor (i.e. building 12S-BE-4.4m-2) resulted in the most substantial variation in the distribution of inter-storey drifts. Similar to 6-storey buildings, all the studied alternatives for the boundary elements' vertical extent of 12-storey buildings resulted in peak inter-storey drifts that are well below the NBCC-15 limit. Therefore, if a sufficient ductile shear wall ratio is provided to satisfy the design code provisions, gradually reducing and eventually discontinuing the boundary element would be possible without violating the code drift limit or resulting in substantial variation in the building's strength or stiffness.

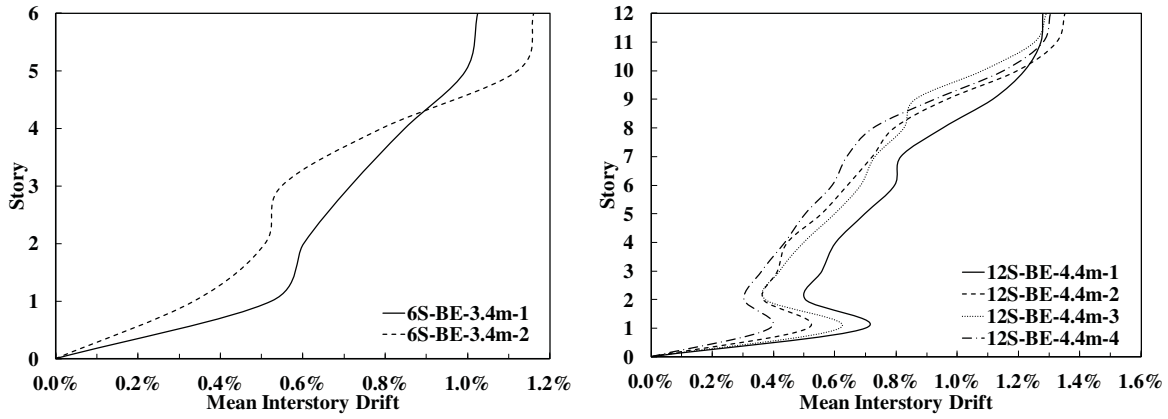

(a) (b)

Figure 6.11 Impact of boundary elements' vertical extent on inter-storey drifts' distribution: (a) 6-storey buildings; and (b) 12-storey buildings

The influence of reducing and discontinuing the boundary elements on the local response of the ductile walls is shown in Figures 6.12 and 6.13 for the 6-storey and 12-storey buildings, respectively. Figures 6.12 and 6.13 present the variation in the distribution of extreme fibres' vertical strains resulting from the inelastic static (i.e. pushover) and dynamic analyses. It is observed that there is a difference in the location of the critical section resulting from the static and dynamic analysis, especially in 12-storey buildings. In 6-storey buildings, when the boundary element was kept constant over the building's height, the critical section was located at the base,

based on both pushover analysis and NTHA. However, when the boundary element was terminated at the 4th floor, there was a sudden rise in extreme fibres' vertical strains. This is seen from the static and dynamic analyses, but more evident in the dynamic analysis results. For the 12-storey buildings, there was a similarly sharp increase in extreme fibres' vertical strains at the floors where boundary elements were either reduced or terminated. From the alternative boundary elements' vertical extents studied, the 3rd option of terminating the boundary element at the 10th floor after a smooth reduction in length seems to result in the least variation in vertical strains' profile. These results support the previously mentioned statement that with a sufficient in-plan ductile shear wall area, progressively reducing and discontinuing the boundary element is feasible.

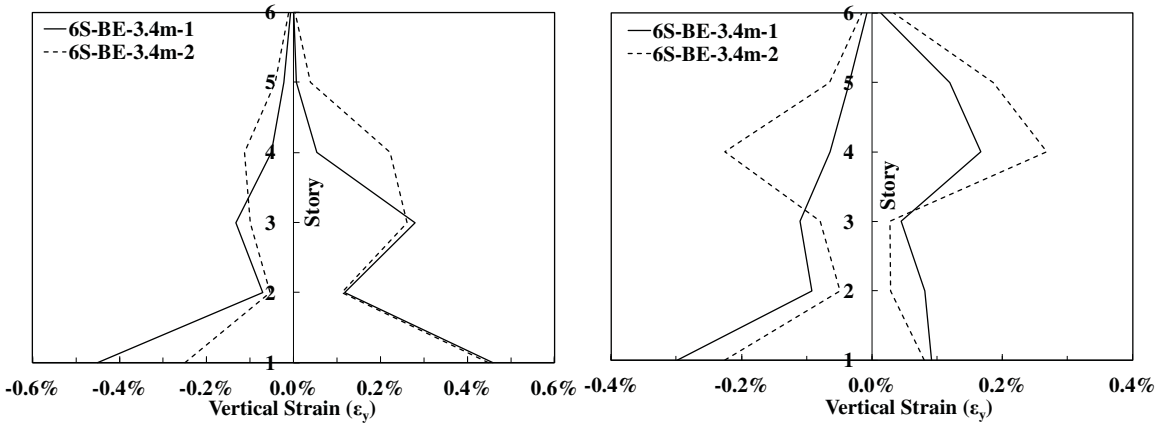

(a) (b)

Figure 6.12 Influence of boundary elements' vertical extent on the vertical strains' distribution of 6-storey buildings: (a) nonlinear static analysis results; and (b) nonlinear dynamic analysis results

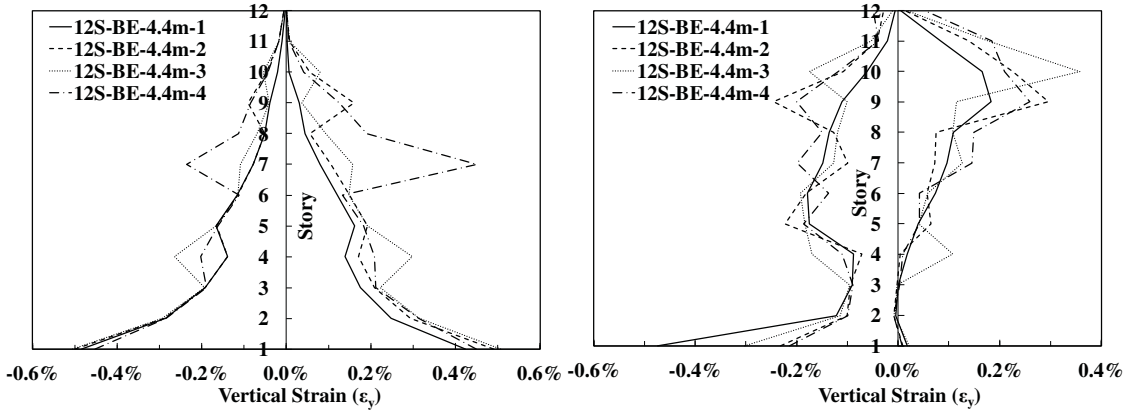

(a) (b)

Figure 6.13 Influence of boundary elements' vertical extent on the vertical strains' distribution of 12-storey buildings: (a) nonlinear static analysis results; and (b) nonlinear dynamic analysis results

6.8 Conclusions

In this study, a hybrid structural layout for RM shear wall buildings is proposed to enhance the system and component-level structural performance. The layout is composed of *ductile* and *gravity* RM shear walls. The influence of the in-plan ductile shear wall ratio on the overall structural response was investigated. This was achieved by designing and detailing 12 RM shear wall buildings having a varying number of floors, shear walls' configurations, and ductile shear wall ratios. Then, a series of inelastic static and dynamic analyses were performed using validated numerical models to quantify the influence of ductile shear wall ratios and cross-section configurations on the seismic behaviour. On the basis of the results of this numerical study and its idealized assumptions, the following conclusions can be made:

1- Compared to conventional load-bearing wall layouts, the introduced structural layout of ductile and gravity walls significantly reduced the required ductile shear wall ratios for RM buildings with varying number of floors. Ductile shear wall ratios less than 0.8% were required for the studied 6-storey and 12-storey buildings, whereas conventional load-bearing wall systems would typically require 2-3% shear wall ratios.

2- Opting for utilizing shear walls with boundary elements in lieu of ductile rectangular walls resulted in almost 50% reduction in the required ductile shear wall ratio for the studied 6-storey buildings. For the studied 12-storey buildings, it was only possible to use ductile walls with boundary elements to avoid having excessively large ductile shear wall ratios, which would result in highly uneconomical designs.

3- The results demonstrated that excessively increasing the ductile shear wall ratios is not very useful in enhancing the overall structural performance. Therefore, the choice of the ductile shear wall ratio and cross-section configuration shall be based on satisfying the pre-defined performance objective. The studied ranges of ductile shear wall ratios can be utilized as starting points for preliminary displacement-based designs of RM buildings having ductile and gravity shear walls.

4- The use of the equivalent static lateral force method of NBCC-15 to design mid- or high-rise masonry buildings utilizing the proposed structural layout would be satisfactory, but conservative. Alternatively, utilizing the linear dynamic analysis method would produce safe and optimized designs, especially for high-rise buildings.

5- It is possible to safely optimize the vertical extent of the boundary elements when sufficient ductile shear wall ratios are provided. However, it is crucial to keep the reduction in the boundary element's cross-sectional dimensions and reinforcement gradual to avoid having a vertical stiffness irregularity (e.g. soft storey). This is important to avoid the concentration of inelastic deformations at higher floors, which would result in premature structural failure. It was demonstrated in this study that reducing the boundary element's length by increments of 200mm every three floors until it was completely discontinued, produced the most favourable structural response in terms of the least variation in extreme fibres' vertical strains and inter-storey drifts.

In summary, the results presented herein demonstrate the effectiveness of utilizing the proposed plan layout of ductile walls with boundary elements and gravity walls for RM buildings. Proper selection of the location and total in-plan area of the ductile walls would allow reducing and discontinuing the boundary elements over the building's height. This study is limited to 6- and 12-storey buildings utilizing the proposed structural layout. Further experimental and analytical research is still needed to evaluate the possibility of providing detailing provisions to mitigate the effects of terminating the boundary elements outside the critical plastic hinge region.

Chapter 7

Summary, Conclusions, and Recommendations

7.1 Summary

This thesis includes experimental and numerical research work aiming to enhance the structural performance and competitiveness of Reinforced Concrete Masonry (RCM) buildings. The main objective was to recommend solutions at the component and system levels to improve the overall seismic response of masonry buildings. The components' (RCM shear walls with boundary elements) structural response was first quantified through experimental testing of large-scale specimens with varying design and detailing parameters. Then, a hybrid structural system composed of ductile and gravity walls was proposed for masonry buildings. Nonlinear numerical analyses were performed to evaluate the enhancements in structural performance and to propose representative building height limits for this system.

Six half-scale fully grouted RCM shear walls with boundary elements were designed, constructed, and tested to investigate the enhancements in the component's response when utilizing the proposed set of design and detailing recommendations. The tested large-scale specimens varied in the boundary element's length, the boundary element's vertical reinforcement ratio, the wall's shear span-to-depth ratio, the type of masonry blocks (stretcher or C-shaped) used in constructing the boundary elements, and the presence of lap splices in the vertical rebars of the plastic hinge region. The walls were tested to failure under a high axial compressive stress, quasi-static reversed cyclic displacements, and top moments. The level of axial compression load represented the expected gravity loads in mid- and high-rise masonry buildings. The specimens were slender walls representing the plastic hinge zones in the structural walls of 6- and 12-storey typical reinforced masonry buildings. The testing results were used to investigate the effects of axial load and end zone detailing on the inelastic response of RCM shear walls with boundary elements. In addition, the results were used to quantify the in-plane cyclic response of the walls, considering the varied parameters. Based on the analysis of the tests' results, design and detailing recommendations and guidelines were given to enhance the component-level structural performance.

The seismic performance and collapse risk of multi-storey masonry buildings were investigated by numerical modelling and nonlinear analyses of six archetype buildings. The buildings utilized a hybrid structural system composed of ductile RCM shear walls with boundary elements and gravity walls, which were conventional rectangular RCM walls. Besides, the buildings had varying heights that exceeded the limits assigned in NBCC-15 to the ductile type of RCM shear walls and were located in two regions, Montréal and Vancouver, representing the moderate and high seismicity categories, respectively. A numerical macro-model was developed in Seismostruct program and was validated against existing experimental data. The model was capable of simulating the nonlinear response of slender RCM shear walls with reasonable accuracy. Using the validated model, nonlinear pseudo-static and dynamic time-history analyses were performed on the reference buildings. Based on the results of the time-history analyses, the seismic collapse capacity of the buildings was quantified and used to assess the potential for increasing the assigned height limits by NBCC-15 for ductile RCM shear walls. Higher height limits were proposed based on the analyzed archetype buildings with ductile RCM shear walls with boundary elements.

A more in-depth analysis was performed to ease the adoption of the proposed hybrid structural system of *ductile* and *gravity* walls by the masonry design industry. This was done by evaluating the effects of the in-plane ductile shear wall ratios and cross-section configurations on the seismic response of RCM shear wall buildings. The analysis was performed utilizing a numerical model developed in *OpenSees* using the SFI-MVLEM to account for the nonlinear shear-flexure interaction and to increase the accuracy of the simulated response. The model was also validated against available experimental data of RCM shear walls. Twelve RCM shear wall buildings were designed with varying heights, ductile shear walls' configurations, and ductile shear wall ratios. The buildings were modelled using the validated modelling approach in *OpenSees*. Subsequently, nonlinear static and dynamic response history analyses were performed to evaluate the impact of the ductile shear wall ratios and cross-section configurations on the structural performance. Finally, the possibility of optimizing the design by reducing the size and terminating the boundary elements over the buildings' heights was investigated.

7.2 Conclusions

The findings of this research contribute to the understanding of the seismic performance and collapse capacity of RCM shear wall buildings with boundary elements. Additionally, the outcomes promote and facilitate the adoption of the proposed hybrid structural system by the masonry industry. The results of the experimental testing provide a new benchmark to further calibrate and enhance existing numerical models for simulating the nonlinear response of slender RCM shear walls. It is also used to develop design and detailing guidelines to enhance the structural performance of the ductile type of RCM shear walls. Furthermore, the results provide valuable data points that would aid the development of prescriptive design provisions for ductile RCM shear walls with boundary elements in the upcoming editions of CSA S304 and TMS 402/602. The results of the numerical simulations were used to recommend representative height limits for ductile RCM shear walls with boundary elements. Besides, the results were used to provide system-level design recommendations to enhance the seismic performance and optimize the structural design. The following subsections outline the main conclusions at the component and system levels based on the results of the experimental testing and numerical analyses, respectively.

7.2.1 Conclusions at the component-level drawn from the experimental testing results

- RCM shear walls with boundary elements built using C-shaped blocks were capable of sustaining high axial compression ratios, higher than 10% of the gross compressive strength, without limiting its ultimate lateral displacement capacity.
- The use of the C-shaped blocks permitted providing sufficient detailing, vertical and transverse reinforcement, in the compression zones. Therefore, the impact of the high axial pre-compression ratio on the structural performance was minimized.
- With sufficient confinement in the end zones, the degradation in lateral resistance was negligible, and the impact of face-shell spalling on the lateral capacity was marginal. Besides, the displacement ductility and hysteretic energy dissipation capacity were not limited by the increase in the axial compressive load.
- The tested walls demonstrated an overall enhanced post-peak response and failed in a flexural mode due to the improved detailing in the compression zones.

- The average ductility-related response modification factor, R_d, at peak load and ultimate displacement was 7.7 and 8.4, respectively, for the walls with different end zone (boundary element) detailing. Thus, in line with previous research, the results highlight the possibility of increasing the response modification factors of RCM shear walls with boundary elements in the next editions of the masonry design codes and standards, NBCC, CSA S304, ASCE7, and TMS 402/602.
- The evaluation of the in-plane cyclic response of RCM shear walls with boundary elements, considering the different design and detailing parameters, demonstrated their improved hysteretic response, even with the presence of lap splices in vertical rebars.
- RCM shear walls with boundary elements sustained high compressive strains in the masonry extreme fibres, before any degradation in lateral resistance, suggesting the possibility of increasing the design value in North American masonry design standards.
- The shorter shear span triggered higher contribution from the shear mechanism, resulted in more diagonal and step shear cracks, increased the strength degradation, and increased the contribution of shear displacements to the total displacement. As a result, it is essential to design the walls to have sufficient shear capacity to ensure the ductile response.
- The utilization of C-shaped blocks instead of the stretcher blocks in the boundary elements enhanced the quality of the construction process and improved the structural performance.
- Building the boundary elements using C-shaped blocks reduced the potential of having weak planes caused by the accumulation of mortar from the joints. Besides, it allowed the completion of the boundary elements' reinforcement cages before the construction of the walls.
- Lap splicing the longitudinal reinforcing bars in the plastic hinge region had a controlled impact on the displacement ductility and energy dissipation capacity.
- With C-shaped blocks in the boundary elements, the premature tensile bond failure at the lap splice was prevented. This was due to locating the splices, in outermost rebars, at the first-floor instead of the wall-foundation interface and the presence of sufficient confinement in the boundary elements.

Therefore, it is concluded, at the component-level, that RCM shear walls with boundary elements built using C-shaped blocks offer a practical and competitive SFRS.

7.2.2 Conclusions at the system-level drawn from the numerical analyses results

- Masonry buildings utilizing the proposed hybrid structural system of ductile RCM shear walls with boundary elements and conventional gravity walls had an enhanced seismic performance and reduced seismic collapse risk.
- The results of the pushover analysis highlighted the improvement in the strength and deformation capacity. Furthermore, the nonlinear response history analyses confirmed the enhanced seismic performance of the buildings with RCM shear with boundary elements.
- The studied buildings had high collapse capacities at the Maximum Considered Earthquake (MCE) that met the requirements of FEMA P695 for satisfactory seismic performance. Consequently, it is suggested to increase the height limits assigned by NBCC-15 to ductile RCM shear walls.
- For RCM shear wall buildings in moderate seismicity regions, $0.35 \leq I_E F_a S_a\,(0.2) \leq 0.75$, the height limit can be changed to 70 m instead of the current 60 m limit.
- For the buildings located in regions with high seismic hazard (i.e. $I_E F_a S_a\,(0.2) > 0.75$), it is recommended to raise the height limit from 40 m to 50 m.
- It is suggested that more studies considering different design parameters are conducted to further increase the height limits.
- Relative to the conventional load-bearing layout, the structural layout of ductile and gravity walls substantially reduced the required ductile shear wall ratios to meet the requirements of the design code and standard (NBCC-15 and CSA S304-14).
- In the introduced structural system, the utilization of the ductile RCM shear walls with boundary elements instead of the ductile rectangular walls further reduced the required ductile shear wall ratios and hence economized the design.
- The studied ranges of ductile shear walls ratios can be utilized as starting points for preliminary designs of RCM buildings having ductile and gravity shear walls.
- To further optimize the design of RCM buildings having shear walls with boundary elements, vertical extents were recommended for the boundary elements. Preliminarily,

a gradual reduction of the boundary element's cross-sectional dimensions and reinforcement was suggested to avoid resulting in a vertical stiffness irregularity.

- The results of the studied building's layout demonstrated that, when an adequate ductile shear wall ratio is provided, a reduction of 200 mm in the boundary element's length every three floors until it is totally discontinued resulted in the most preferred structural performance.

Thus, the conclusions of this research, at the system-level, present RCM buildings utilizing the proposed structural system with ductile walls with boundary elements as an efficient alternative building system.

7.3 Recommendations for Future Work

Innovative research is a continuous improvement process. Therefore, it is essential to utilize the findings of this research to further improve the seismic response and competitiveness of RCM buildings. To build on the results of the experimental and numerical research presented in this thesis, the following points are recommended:

1- Testing of several RCM shear walls with boundary elements having lap spliced vertical rebars considering different lengths and configurations for the splices.
2- Performing shake table testing on RCM shear walls with boundary elements and buildings utilizing this type of wall. This is essential to evaluate the dynamic effects and the performance of this system under representative demands.
3- Experimental testing, pseudo-static and pseudo-dynamic, of RCM buildings having the proposed hybrid structural system of ductile RCM shear walls with boundary elements and conventional masonry gravity walls.
4- Assessment, experimentally and numerically, of the impacts of the design and detailing of the gravity walls on the seismic performance and collapse capacity of RCM buildings utilizing the proposed hybrid structural system.
5- Enhancing the accuracy of the numerical modelling of RCM shear walls by overcoming the highlighted limitations. This can also be achieved by developing a material (stress-strain) model that is specific to grouted masonry instead of utilizing the available concrete material models. Furthermore, the vertical component of the ground motions could be considered in the nonlinear time-history analyses, to account for its effects on the axial load

in the ductile shear walls. This would also result in a more representative simulation of the expected response from the proposed structural layout.

6- Evaluating the cyclic stress-strain behaviour of RCM boundary elements to better represent the response under earthquake excitations. This would allow including the cyclic loading effects in the developed stress-strain model for RCM boundary elements.

7- Quantifying the compressive stress-strain response of RCM boundary elements considering the strain gradient (i.e. combined axial and flexure) and axial load level effects to simulate the actual loading in shear walls.

References

Aaleti, S., Brueggen, B. L., Johnson, B., French, C. E., and Sritharan, S. (2013). Cyclic response of reinforced concrete walls with different anchorage details: experimental investigation. *Journal of Structural Engineering*, *139*, 1181–1191.

Abdel-Latif, A., Okail, H., Shedid, M., and Abdelrahman, A. (2015). Modelling of reinforced masonry structural walls under lateral loads. In *12th North American Masonry Conference*. Denver, Colorado, United States of America.

Ahmadi, F., Hernandez, J., Sherman, J., Kapoi, C., Klingner, R. E., and McLean, D. I. (2014). Seismic performance of cantilever-reinforced concrete masonry shear walls. *Journal of Structural Engineering*, *140*(9), 04014051.

Alemdar, B. N., and White, D. W. (2005). Displacement, flexibility, and mixed beam-column finite element formulation for distributed plasticity analysis. *Journal of Structural Engineering*, *131*(12), 1811–1819.

AlHamaydeh, M., Aly, N., and Galal, K. (2017). Impact of seismicity on performance and cost of RC shear wall buildings in Dubai, United Arab Emirates. *Journal of Performance of Constructed Facilities*, *31*(5), 1–14.

Aly, N., Ashour, A., and Galal, K. (2017). Seismic performance and height limits of ductile reinforced masonry shear wall buildings with boundary elements. In *13th Canadian Masonry Symposium*. Halifax, Nova Scotia, Canada.

Aly, N., and Galal, K. (2019a). Effect of ductile shear wall ratio and cross-section configuration on the seismic behavior of reinforced concrete masonry shear wall buildings. *Journal of Structural Engineering (accepted-in press)*.

Aly, N., and Galal, K. (2019b). Influence of ductile shear wall ratio on the seismic performance of reinforced concrete masonry shear wall buildings. In *13th North American Masonry Conference* (pp. 1462–1474). Salt Lake City, Utah, United States of America: The Masonry Society.

Aly, N., and Galal, K. (2019c). Seismic performance and height limits of ductile reinforced masonry shear wall buildings with boundary elements. *Engineering Structures*, *190*, 171–188.

American Society for Testing and Materials (ASTM). (2012). *Standard Test Methods for Cyclic (Reversed) Load Test for Shear Resistance of Vertical Elements of the Lateral Force Resisting Systems for Buildings, E2126-12*. West Conshohocken, PA, United States of America.

American Society for Testing and Materials (ASTM). (2013). *Standard Test Method for Compressive Strength of Hydraulic Cement Mortars (Using 2-in. or [50-Mm] Cube Specimens), C109M-13*. West Conshohocken, PA, United States of America.

American Society for Testing and Materials (ASTM). (2015). *Standard Test Methods for Sampling and Testing Concrete Masonry Units and Related Units, C140-15*. West Conshohocken, PA, United States of America.

American Society for Testing and Materials (ASTM). (2015). *Standard Specification for Carbon-Steel Wire and Welded Wire Reinforcement, Plain and Deformed, for Concrete, A1064M-15*. West Conshohocken, PA, United States of America.

American Society for Testing and Materials (ASTM). (2015). *Standard Test Method for Compressive Strength of Cylindrical Concrete Specimens, C39M-15*. West Conshohocken, PA, United States of America.

American Society for Testing and Materials (ASTM). (2015). *Standard Specification for Deformed and Plain Carbon-Steel Bars for Concrete Reinforcement, A615M-15*. West Conshohocken, PA, United States of America.

American Society of Civil Engineers/Structural Engineering Institute (ASCE/SEI). (2008). *Minimum design loads for buildings and other structures (ASCE7-08)*. Reston, Virginia, United States of America.

American Society of Civil Engineers/Structural Engineering Institute (ASCE/SEI). (2010). *Minimum design loads for buildings and other structures (ASCE7-10)*. Reston, Virginia, United States of America.

American Society of Civil Engineers/Structural Engineering Institute (ASCE/SEI). (2016). *Minimum design loads for buildings and other structures (ASCE7-16)*. Reston, Virginia, United States of America.

Ashour, A., El-Dakhakhni, W., and Shedid, M. (2016). Influence of floor diaphragm–wall coupling on the system-level seismic performance of an asymmetrical reinforced concrete block building. *Journal of Structural Engineering*, *142*(10), 04016071.

Assatourians, K., and Atkinson, G. (2010). Database of processed time series and response spectra data for Canada: an example application to study of 2005 MN 5.4 Riviere du Loup, Québec, earthquake. *Seismological Research Letters*, *81*(6), 1013–1031.

Atkinson, G. (2009). Earthquake time histories compatible with the 2005 national building code of Canada uniform hazard spectrum. *Canadian Journal of Civil Engineering*, *36*(6), 991–1000.

Baker, J. W. (2015). Efficient analytical fragility function fitting using dynamic structural analysis. *Earthquake Spectra*, *31*(1), 579–599.

Banting, B., and El-Dakhakhni, W. (2012). Force- and displacement-based seismic performance parameters for reinforced masonry structural walls with boundary elements. *Journal of Structural Engineering*, *138*(12), 1477–1497.

Banting, B., and El-Dakhakhni, W. (2014). Seismic performance quantification of reinforced masonry structural walls with boundary elements. *Journal of Structural Engineering*, *140*(5), 1–15.

Banting, B., and El-Dakhakhni, W. (2014). Normal strain-adjusted shear strength expression for fully grouted reinforced masonry structural walls. *Journal of Structural Engineering*, *140*(3).

Bedeir, H., Shedid, M., Okail, H., and Hamdy, O. (2017). A force-based macro-model for reinforced concrete masonry walls subjected to quasi-static lateral loading. In *13th Canadian*

Masonry Symposium. Halifax, Nova Scotia, Canada.

Bohl, A., and Adebar, P. (2011). Plastic hinge length in high-rise concrete shear walls. *ACI Structural Journal*, *108*(2).

Bolhassani, M., Hamid, A. A., Johnson, C., Moon, F. L., and Schultz, A. E. (2016). New design detail to enhance the seismic performance of ordinary reinforced partially grouted masonry structures. *Journal of Structural Engineering*, *142*(12), 1–15.

Bruneau, M., and Yoshimura, K. (1996). Damage to masonry buildings caused by the 1995 Kobe earthquake. *Canadian Journal of Civil Engineering*, *23*, 797–807.

Burak, B., and Comlekoglu, H. G. (2013). Effect of shear wall area to floor area ratio on the seismic behavior of reinforced concrete buildings. *Journal of Structural Engineering, ASCE*, *139*(11), 1928–1937.

Calabrese, A., Almeida, J. P., and Pinho, R. (2010). Numerical issues in distributed inelasticity modeling of RC frame elements for seismic analysis. *Journal of Earthquake Engineering*, *14*(S1), 38–68.

Carvalho, G., Bento, R., and Bhatt, C. (2013). Nonlinear static and dynamic analyses of reinforced concrete buildings - comparison of different modelling approaches. *Earthquakes and Structures*, *4*(5), 451–470.

Chang, G. A., and Mander, J. B. (1994). Seismic energy based fatigue damage analysis of bridge columns: Part I—Evaluation of seismic capacity. *NCEER Technical Rep. No. NCEER-94-0006, State Univ. of New York, Buffalo, NY, 222*.

Chopra, A. K. (2007). *Dynamics of structures: Theory and applications to earthquake engineering* (3rd Ed.). Upper Saddle River, NJ: Pearson Prentice Hall.

Coleman, J., and Spacone, E. (2001). Localization issues in force-based frame elements. *Journal of Structural Engineering*, *127*(11), 1257–1265.

Correa, M. R. S. (2016). A 20-storey high masonry building in Brazil — design problems and adopted strategies. In *16th International Brick and Block Masonry Conference* (pp. 623–628). Padova, Italy.

Canadian Standards Association (CSA). (2014). *Mortar and Grout for Unit Masonry, A179-14*. Toronto, Ontario, Canada.

Canadian Standards Association (CSA). (2014). *CSA Standards on Concrete Masonry Units, A165-14*. Mississauga, Ontario, Canada.

Canadian Standards Association (CSA). (2004). *Design of Concrete Structures, A23.3-04*. Mississauga, Ontario, Canada.

Canadian Standards Association (CSA). (2004). *Design of Masonry Structures, S304.1-04*. Mississauga, Ontario, Canada.

Canadian Standards Association (CSA). (2014). *Design of Masonry Structures, S304-14*. Mississauga, Ontario, Canada.

Computers and Structures Inc. (CSI), ETABS 2015, https://www.csiamerica.com/products/etabs. (2015). Berkeley, California, United States of America.

Dhanasekar, M., and Shrive, N. G. (2002). Strength and deformation of confined and unconfined grouted concrete masonry. *ACI Structural Journal*, *99*(6), 819–826.

Drysdale, R. G., and Hamid, A. A. (1979). Behavior of concrete block masonry under axial compression. *ACI Journal*, *76*(6), 707–721.

Drysdale, R. G., and Hamid, A. A. (2005). *Masonry Structures Behaviour and Design* (Canadian edition). Canada Masonry Design Centre, Mississauga, Ontario, Canada.

Drysdale, R. G., and Khattab, M. M. (1995). In-plane behavior of grouted concrete masonry under biaxial tension-compression. *ACI Structural Journal*, *92*(6), 653–664.

El-Sokkary, H., and Galal, K. (2018). Material quantities of reinforced masonry versus reinforced concrete shear walls. In *Fifteenth International Conference on Structural and Geotechnical Engineering: Advances in construction materials-research and applications*. Cairo, Egypt: Ain Shams University.

Ezzeldin, M., El-Dakhakhni, W., and Weibe, L. (2017). Experimental assessment of the system-level seismic performance of an asymmetrical reinforced concrete block – wall building with boundary elements. *Journal of Structural Engineering*, *143*(8), 1–13.

Ezzeldin, M., Wiebe, L., and El-Dakhakhni, W. (2016). Seismic collapse risk assessment of reinforced masonry walls with boundary elements using the FEMA P695 methodology. *Journal of Structural Engineering*, *142*(11), 1–14.

Federal Emergency Management Agency (FEMA). (2007). FEMA 461, Interim Testing Protocols for determining the seismic performance characteristics of structural and nonstructural components. Prepared for the Federal Emergency Management Agency, Prepared by the Applied Technology Council, Washington D.C., United States of America.

Federal Emergency Management Agency (FEMA). (2009). FEMA P695, Quantification of Building Seismic Performance Factors. Prepared for the Federal Emergency Management Agency, Prepared by the Applied Technology Council, Washington D.C., United States of America.

Federal Emergency Management Agency (FEMA). (2012). FEMA P58-1, Seismic Performance Assessment of Buildings - Methodology. Prepared for the Federal Emergency Management Agency, Prepared by the Applied Technology Council, Washington D.C., United States of America.

Filiatrault, A., Tremblay, R., Christopoulos, C., Folz, B., and Pettinga, D. (2013). *Elements of earthquake engineering and structural dynamics* (third edit). Québec, Canada: Presses internationales Polytechnique.

Filippou, F. C., Povpov, E. P., and Bertero, V. V. (1983). Effects of bond deterioration on hysteretic behavior of reinforced concrete joints. *Earthquake Engineering Research Center*. University of California, Berkeley.

Fortes, E. S., Parsekian, G. A., and Fonseca, F. S. (2015). Relationship between the compressive

strength of concrete masonry and the compressive strength of concrete masonry units. *Journal of Materials in Civil Engineering*, *27*(9).

Gogus, A., and Wallace, J. (2015). Seismic safety evaluation of reinforced concrete walls through FEMA P695 methodology. *Journal of Structural Engineering*, *141*(10), 1–17.

Hamid, A. A., and Chandrakeerthy, S. R. (1992). Compressive strength of partially grouted concrete masonry using small scale wall elements. *The Masonry Society Journal*, 11(1), 75–85

Hamzeh, L., Ashour, A., and Galal, K. (2018). Development of fragility curves for reinforced-masonry structural walls with boundary elements. *Journal of Performance of Constructed Facilities*, *32*(4).

Jiang, H., and Kurama, Y. (2010). Analytical modeling of medium-rise reinforced concrete shear walls. *ACI Structural Journal*, *107*(4), 400–410.

Kelln, R. D., and Feldman, L. R. (2015). Bar size factors for lap splices in block walls subjected to flexure. *Canadian Journal of Civil Engineering*, *42*(8), 521–529.

Khalaf, F. M. (1996). Factors influencing compressive strength of concrete masonry prisms. *Magazine of Concrete Research*, *48*(175), 95–101.

Kikuchi, K., Yoshimura, K., Yoshida, K., Tanaka, A., Urasaki, H., Kijima, Y., and Mizumasa, N. (2004). Experimental study on seismic capacity of reinforced fully grouted concrete masonry walls. In *13th World Conference on Earthquake Engineering*, (1880). Vancouver, B.C., Canada.

Kolozvari, K., Orakcal, K., and Wallace, J. W. (2015a). Modeling of cyclic shear-flexure interaction in reinforced concrete structural walls. I: theory. *Journal of Structural Engineering*, *141*(5).

Kolozvari, K., Tran, T. A., Orakcal, K., and Wallace, J. W. (2015b). Modeling of cyclic shear-flexure interaction in reinforced concrete structural walls. II : experimental validation. *Journal of Structural Engineering*, *141*(5).

Kunnath, S. K., and Brown, J. (2004). Low-cycle fatigue failure of reinforcing steel bars. *ACI Materials Journal*, *101*(6), 457–466.

Légeron, F., Paultre, P., and Mazars, J. (2005). Damage mechanics modeling of nonlinear seismic behavior of concrete structures. *Journal of Structural Engineering*, *131*(6), 946–955.

Mander, J. B., Priestley, M. J. N., and Park, R. (1988). Theoretical stress-strain model for confined concrete. *Journal of Structural Engineering*, *114*(8), 1804–1826.

Martinez-Rueda, J. E., and Elnashai, A. S. (1997). Confined concrete model under cyclic load. *Materials and Structures*, *30*(3), 139–147.

McKenna, F., Fenves, G., and Scott, M. (2000). Open system for earthquake engineering simulation (*OpenSees*). University of California, Berkeley, California. United States of America.

Menegotto, M., and Pinto, P. E. (1973). Method of analysis for cyclically loaded RC plane frames

including changes in geometry and non-elastic behavior of elements under combined normal force and bending. In *proceedings of IABSE Symposium on Resistance and Ultimate Deformability of Structures Acted on by Well Defined Loads* (pp. 15–22). International Association for Bridge and Structural Engineering, Zurich, Switzerland.

Michaud, D., and Leger, P. (2014). Ground motions selection and scaling for nonlinear dynamic analysis of structures located in Eastern North America. *Canadian Journal of Civil Engineering*, *41*(3), 232–244.

Mjelde, J. Z., McLean, D. I., Thompson, J. J., and McGinley, W. M. (2009). Performance of lap splices in concrete masonry shear walls. *The Masonry Society Journal*, *27*(1), 35–54.

Masonry Standard Joint Committee (MSJC-05). (2005). *Building Code Requirements for Masonry Structures. TMS 402/ASCE 5/ACI 530*. Reston, VA, United States of America.

Masonry Standard Joint Committee (MSJC-11). (2011). *Building Code Requirements for Masonry Structures. TMS 402/ASCE 5/ACI 530*. Reston, VA, United States of America.

Masonry Standard Joint Committee (MSJC-13). (2013). *Building Code Requirements for Masonry Structures. TMS 402/ASCE 5/ACI 530*. Reston, VA, United States of America.

Mwafy, A. (2011). Assessment of seismic design response factors of concrete wall buildings. *Earthquake Engineering and Engineering Vibration*, *10*(01), 115–127.

National Building Code of Canada (NBCC). (2015). Institute for Research in Construction. Ottawa, Ontario, Canada: National Research Council of Canada.

Newmark, N. M., and Rosenblueth, E. (1971). *Fundamentals of Earthquake Engineering*. Englewood Cliffs, New Jersey: Prentice Hall.

New Zealand Standard (NZS). (2004). *Design of Reinforced Concrete Masonry Structures, NZS 4230*. Wellington, New Zealand.

Obaidat, A. T. (2017). Compressive behaviour of C-shaped reinforced masonry boundary elements. Ph.D. Thesis, Concordia University, Montreal, Canada.

Obaidat, A. T., Ashour, A., and Galal, K. (2018). Stress-strain behavior of C-shaped confined concrete masonry boundary elements of reinforced masonry shear walls. *Journal of Structural Engineering*, *144*(8), 1–15.

Orakcal, K., Ulugtekin, D., and Massone, L. M. (2012). Constitutive modeling of reinforced concrete panel behavior under cyclic loading. In *15th World Conference on Earthquake Engineering,* Lisbon, Portugal.

Orakcal, K., and Wallace, J. W. (2006). Flexural Modeling of Reinforced Concrete Walls-Experimental Verification. *ACI Structural Journal*, *103*(2), 196–206.

Orakcal, K., Wallace, J. W., and Conte, J. P. (2004). Flexural Modeling of Reinforced Concrete Walls-Model Attributes. *ACI Structural Journal*, *101*(5), 688–698.

Park, R., and Paulay, T. (1975). *Reinforced Concrete Structures*. John Wiley and Sons, Inc.

Paulay, T., and Priestley, M. J. N. (1992). *Seismic design of reinforced concrete and masonry*

buildings. John Wiley and Sons, Inc.

Priestley, M. J. N., Calvi, G. M., and Kowalsky, M. J. (2007). *Displacement based seismic design of structures*. Pavia, Italy: Istituto Universitario di Studi Superiori (IUSS).

Priestley, M. J. N., and Chai, Y. H. (1984). Prediction of Masonry Compression Strength Part 1. *New Zealand Concrete Construction*, *28*, 11–14.

Priestley, M. J. N., and Elder, D. M. (1982). Cyclic loading tests of slender concrete masonry shear walls. *Bulletin of the New Zealand National Society for Earthquake Engineering*, *15*(1), 3–21.

Pugh, J. S., Lowes, L. N., and Lehman, D. E. (2015). Nonlinear line-element modeling of flexural reinforced concrete walls. *Engineering Structures*, *104*, 174–192.

Sarhat, S. R., and Sherwood, E. G. (2013). The prediction of compressive strength of grouted hollow concrete block masonry based on the contribution of its individual components. In *12th Canadian Masonry Symposium*. Vancouver, B.C., Canada.

Seismosoft. (2016). SeismoStruct 2016 - A computer program for static and dynamic analysis of framed structures. Available from http://www.seismosoft.com.

Shedid, M., El-Dakhakhni, W., and Drysdale, R. (2010a). Alternative strategies to enhance the seismic performance of reinforced concrete-block shear wall systems. *Journal of Structural Engineering*, *136*(6), 676–689.

Shedid, M., El-Dakhakhni, W., and Drysdale, R. (2010b). Characteristics of rectangular, flanged, and end-confined reinforced concrete masonry shear walls for seismic design. *Journal of Structural Engineering*, *136*(12), 1471–1482.

Shedid, M., and Drysdale, R., El-Dakhakhni, W. (2008). Behavior of fully grouted reinforced concrete masonry shear walls failing in flexure: experimental results. *Journal of Structural Engineering*, *134*(11), 2032–2044.

Shedid, M., El-Dakhakhni, W., and Drysdale, R. (2011). Seismic response modification factors for reinforced masonry structural walls. *Journal of Performance of Constructed Facilities*, *25*(2), 74–86.

Shedid, M., El-Dakhakhni, W., and Drysdale, R. (2009). Behavior of fully grouted reinforced concrete masonry shear walls failing in flexure: Analysis. *Engineering Structures*, *31*(9), 2032–2044.

Shegay, A. V., Motter, C. J., Elwood, K. J., Henry, R. S., Lehman, D. E., and Lowes, L. N. (2018). Impact of axial load on the seismic response of rectangular walls. *Journal of Structural Engineering*, *144*(8), 1–32.

Shing, P. B., Brunner, J. D., and Lotfi, H. R. (1993). Evaluation of shear strength of reinforced masonry walls. *The Masonry Society Journal*, *12*(1), 61–76.

Shing, P. B., Klamerus, E., Spaeh, H., and Noland, J. L. (1988). Seismic performance of reinforced masonry shear Walls. In *9th World Conference on Earthquake Engineering*. Tokyo-Kyoto,

Japan.

Shing, P. B., Schuller, M., and Hoskere, V. S. (1990). In-plane resistance of reinforced masonry shear walls. *Journal of Structural Engineering*, *116*(3), 619–640.

Shing, P., Carter, E., and Noland, J. (1993). Influence of confining steel on flexural response of reinforced masonry shear walls. *The Masonry Society Journal*, *11*(2), 72–85.

Siyam, M., Konstantinidis, D., and El-Dakhakhni, W. (2016). Collapse fragility evaluation of ductile reinforced concrete block wall systems for seismic risk assessment. *Journal of Performance of Constructed Facilities*, *30*(6), 1–14.

Snook, M., McLean, D., McDaniel, C., and Pollock, D. (2005). Effects of confinement reinforcement on the performance of masonry shear walls. In *14th Canadian Masonry Symposium*. Banff, Alberta, Canada.

Su, R. K. L., and Wong, S. M. (2007). Seismic behaviour of slender reinforced concrete shear walls under high axial load ratio. *Engineering Structures*, *29*(8), 1957–1965.

The Masonry Society (TMS). (2016). *Building Code Requirements and Specifications for Masonry Structures, TMS 402/602-16*. Longmont, Colorado, United States of America.

Tomazevic, M. (1999). *Earthquake resistant design of masonry buildings*. London: Imperial College Press.

Tso, W. K., Zhu, T. J., and Heidebrecht, A. C. (1992). Engineering implication of ground motion A / V ratio. *Soil Dynamics and Earthquake Engineering*, *11*, 133–144.

Vamvatsikos, D., and Cornell, C. A. (2002). Incremental dynamic analysis. *Earthquake Engineering and Structural Dynamics*, *31*(3), 491–514.

Vamvatsikos, D., and Cornell, C. A. (2004). Applied incremental dynamic analysis. *Earthquake Spectra*, *20*(2), 523–553.

Vulcano, A., Bertero, V. V., and Colotti, V. (1988). Analytical modeling of R/C structural walls. In *9th World Conference on Earthquake Engineering,* (pp. 41–44). Tokyo-Kyoto, Japan.

Wilson, E. (2001). *Static and dynamic analysis of structures*. Berkeley, California, United States of America: Computers and Structures Inc.

Yuen, Y., and Kuang, J. (2014). Axial compression effect on ductility design of reinforced concrete structural walls. In *Second European Conference On Earthquake Engineering and Seismology*. Istanbul, Turkey.

Zhang, Y., and Wang, Z. (2000). Seismic behavior of reinforced concrete shear walls subjected to high axial loading. *ACI Structural Journal*, *97*(5), 739–750.

Zhao, J., and Sritharan, S. (2007). Modeling of strain penetration effects in fiber-based analysis of reinforced concrete structures. *ACI Structural Journal*, *104*(2), 133–141.

Zhao, Y., and Wang, F. (2015). Experimental studies on behavior of fully grouted reinforced-concrete masonry shear walls. *Earthquake Engineering and Engineering Vibration*, *14*(4), 743–757.

Appendix A

Supplemental Information to the Experimental Work (Chapters 3 and 4)

This Appendix provides photos for the construction process of the walls, photos for the damage states of the tested walls, and additional Figures and Tables for the experimental results. Furthermore, it presents photos for the construction of the concrete masonry prisms, photos for the testing of the walls' constituent materials, and additional results for the materials' testing.

A.1 Construction of RCM Shear Walls with Boundary Elements

(a) (b)

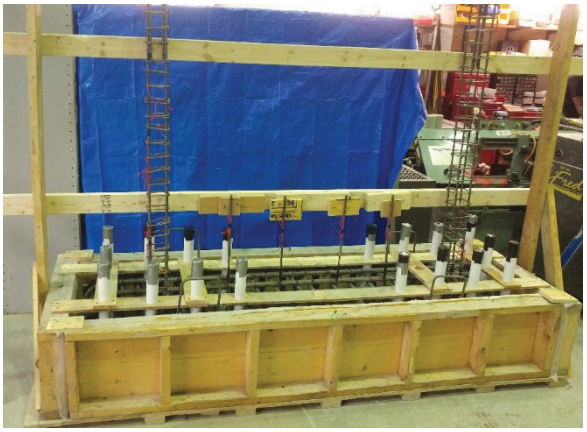

(c)

Figure A.1 Bottom footings' formwork and reinforcement: (a) walls W7, W8, W9 and W10; (b) wall W11; and (c) wall W12

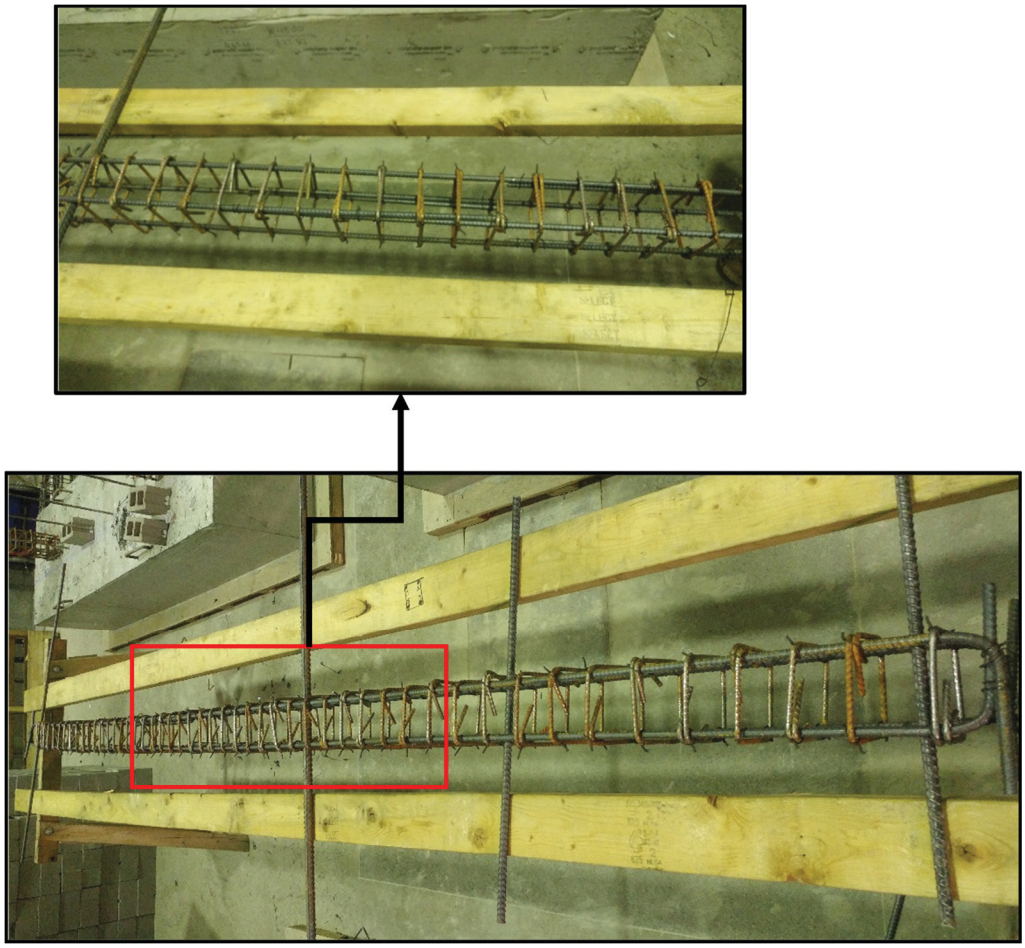

Figure A.2 Boundary elements' reinforcement cages with lap splices for wall W12

(a)

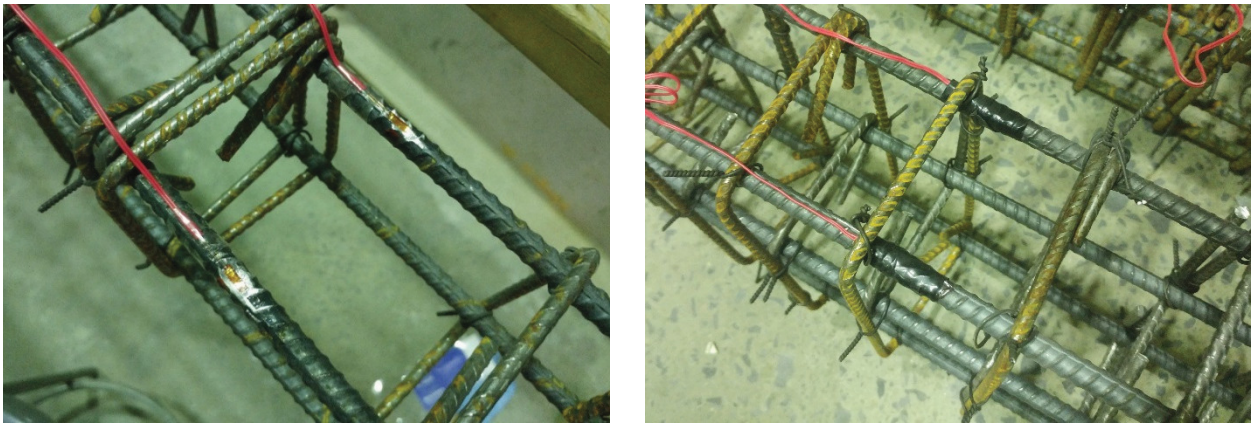

(b) (c)

Figure A.3 Installation of strain gauges: (a) grinding and smoothing the rebar surface; (b) attaching the strain gauges; and (c) protection of the strain gauges

(1) Laying 1st masonry course

(2) Laying 2nd & 3rd masonry course

(3) Laying 4th & 5th masonry course

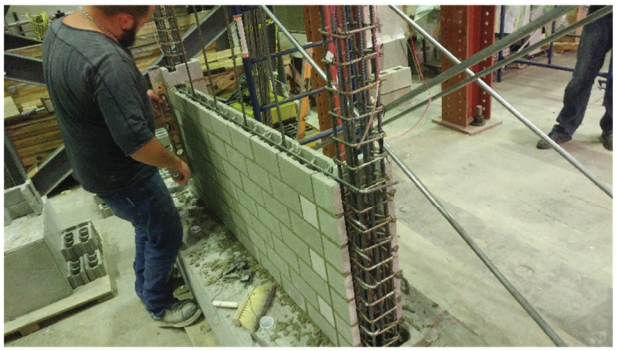

(4) Inserting horizontal reinforcement

(5) Completing 1/3 of the wall height

(6) Strapping & grouting of 1st one-third

Figure A.4 Typical construction process of the first one-third of walls

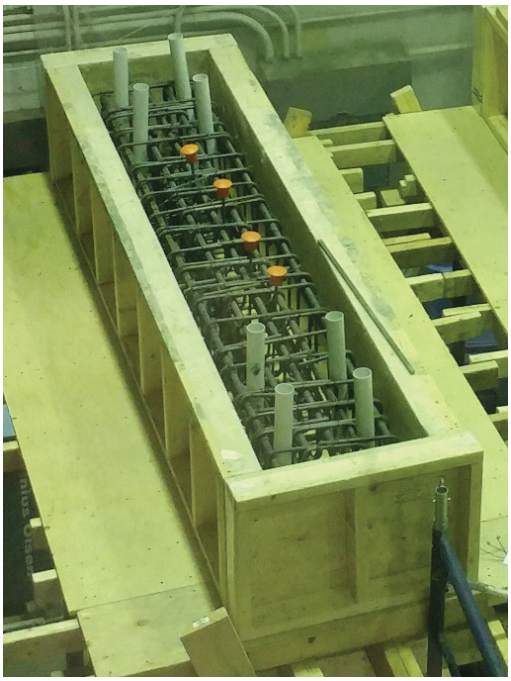

Figure A.5 Top footings' formwork, reinforcement and concrete

Table A.1 Mix proportions of grout

Grout Type	Water	Cement	Fine Aggregate (Sand)	Plasticizer
Ordinary Strength Grout	0.79 kg	1 kg	4 kg	Not used
High Strength Grout	0.52 kg	1 kg	2.65 kg	Not used

Table A.2 Compressive strength of grout trial mix

Grout Type	Sample No.	Slump (mm)	7-Days Compressive Strength (MPa)	28-Days Compressive Strength (MPa)
Ordinary Strength Grout	1	280	14.01	-
	2		-	23.18
	3		-	22.02
	Average		-	22.60
	c.o.v		-	2.57%
High Strength Grout	1	240	31.97	-
	2		-	45.3
	3		-	42.47
	Average		-	43.89
	c.o.v		-	3.22%

A.2 Additional Experimental Results

Figures A6-A11 present additional photos of the final damage states of the tested walls. It is worth highlighting that, as can be seen in the Figures, the vertical joint of the stack pattern in the boundary elements did not have a substantial impact on the overall performance of the walls. There was a relatively good bond between the C-shaped blocks in the boundary elements and the grout core. Furthermore, the spalling of the C-shaped blocks was initiated at high ductility factors and did not significantly affect the post-peak response, as discussed previously. However, the stack pattern was problematic during the grouting of the walls. It mandated strapping the boundary elements to avoid the spalling of the C-shaped blocks during the grouting of the boundary elements. Nevertheless, having the stack pattern in the boundary elements eased the construction of the blocks, allowed having rectangular boundary elements, and permitted the completion of the boundary elements' reinforcement cage before constructing the boundary elements.

Figure A.6 Final damage state and failure of wall W7

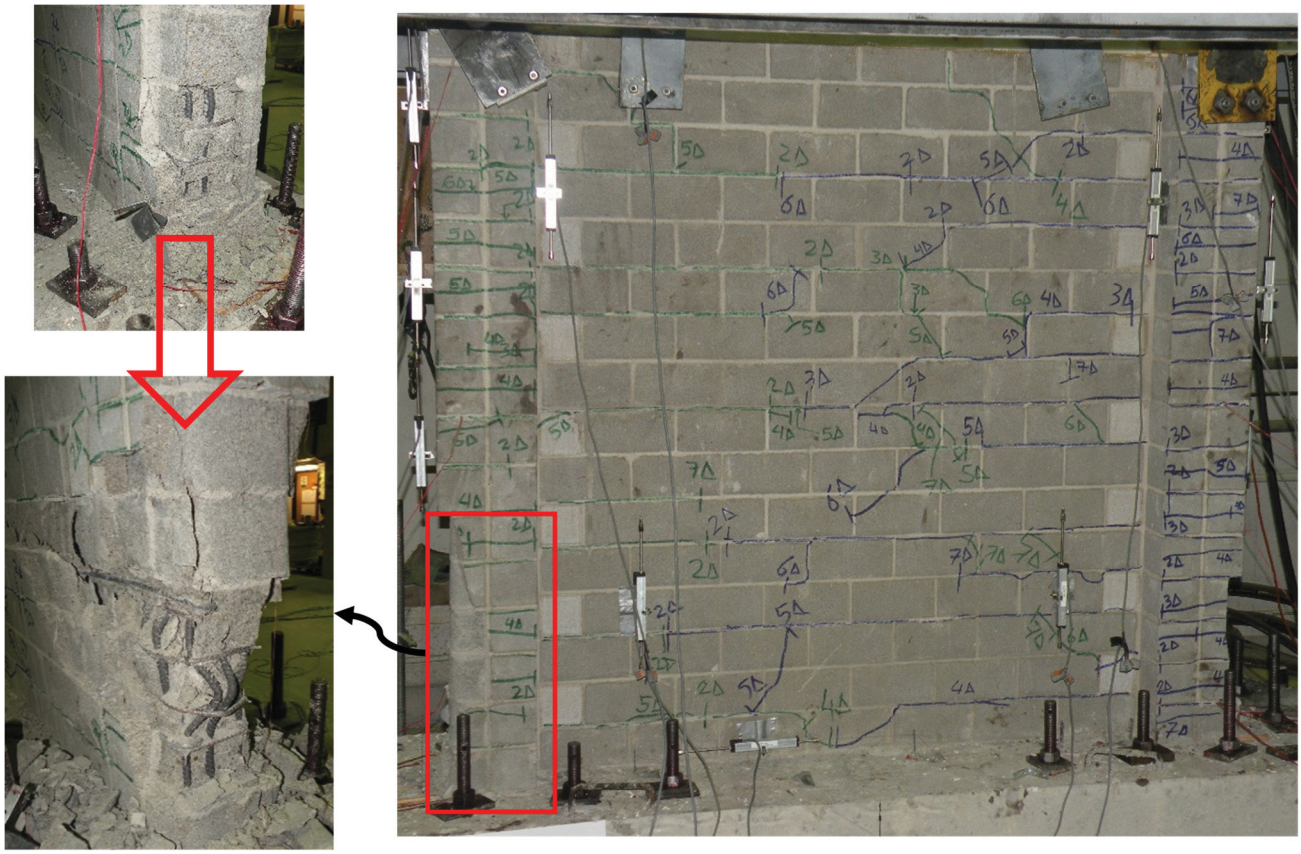

Figure A.7 Final damage state and failure of wall W8

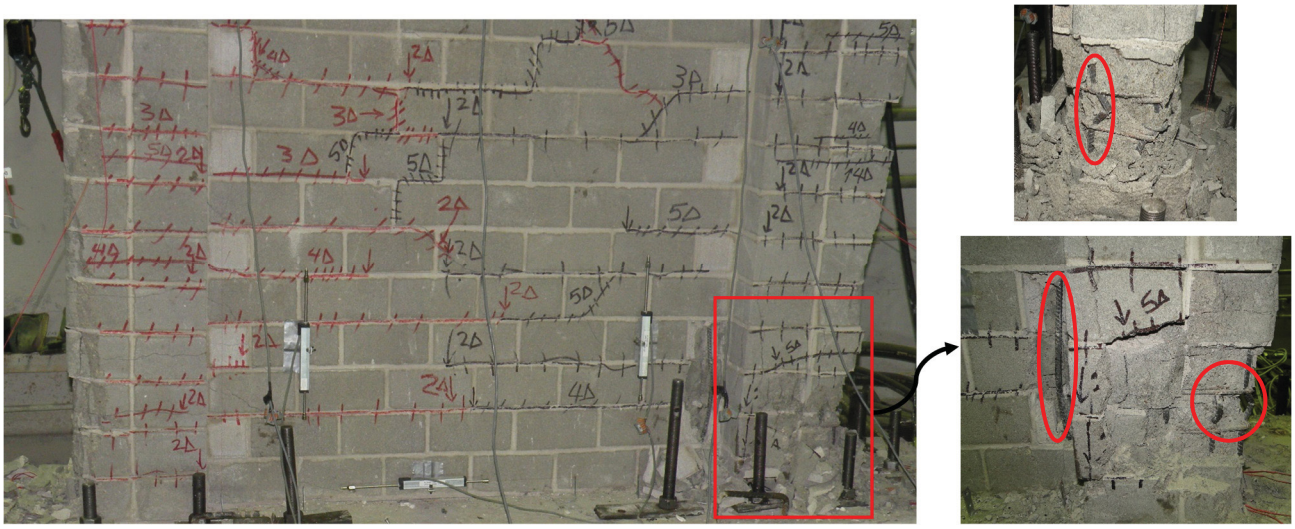

Figure A.8 Final damage state and failure of wall W9

(a) (b)

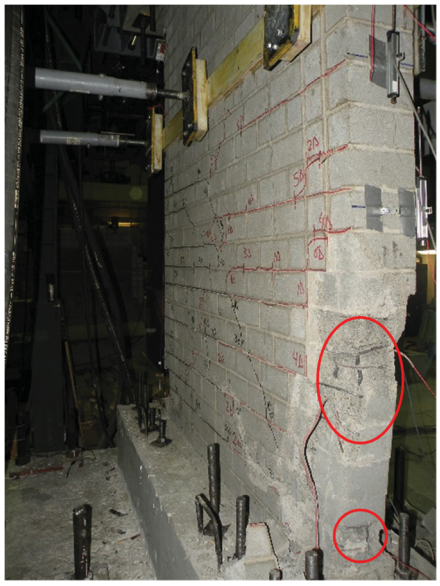

(c)

Figure A.9 Final damage state and failure of wall W10: (a) front view; (b) back view; and (c) side view of left boundary element

(a)

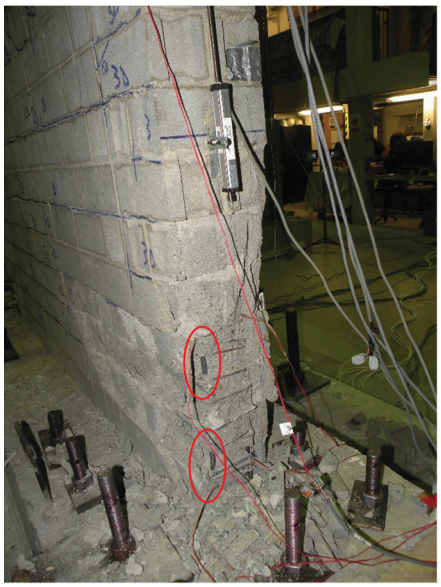

(b)

Figure A.10 Damage states of wall W11: (a) mortar accumulation in the right boundary element after face-shell spalling at μ = 6; and (b) side view of left boundary element at μ = 8

(a) (b)

(c)

Figure A.11 Final damage state and failure of wall W12: (a) front view; (b) back view; and (c) left boundary element

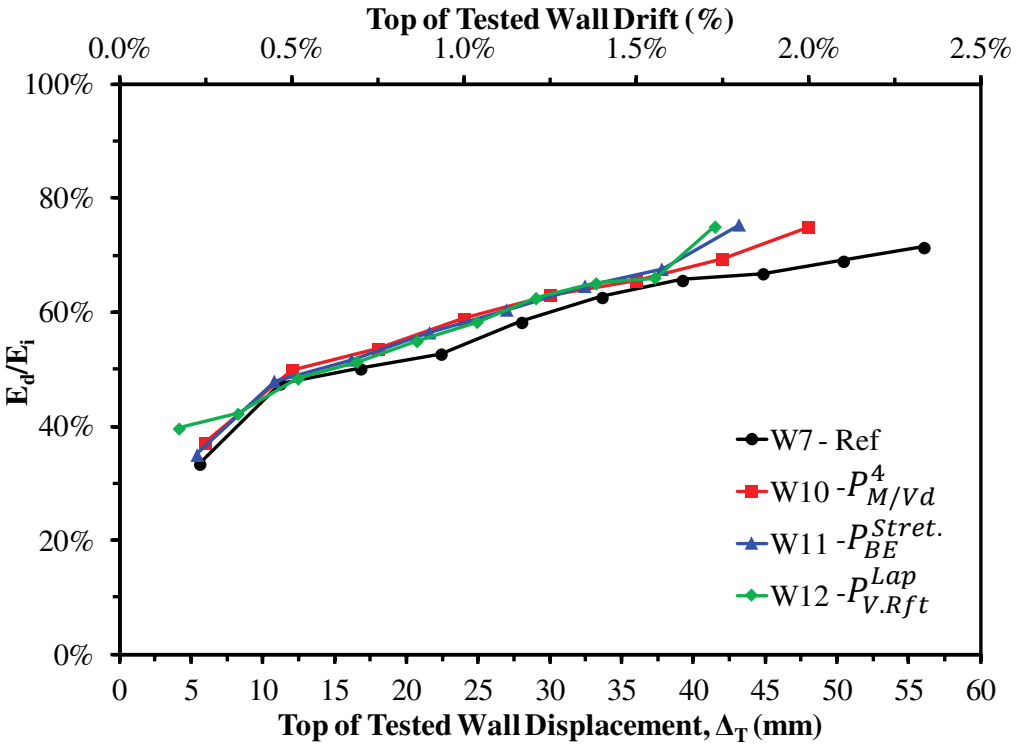

Figure A.12 Energy dissipation ratio with respect to top displacement

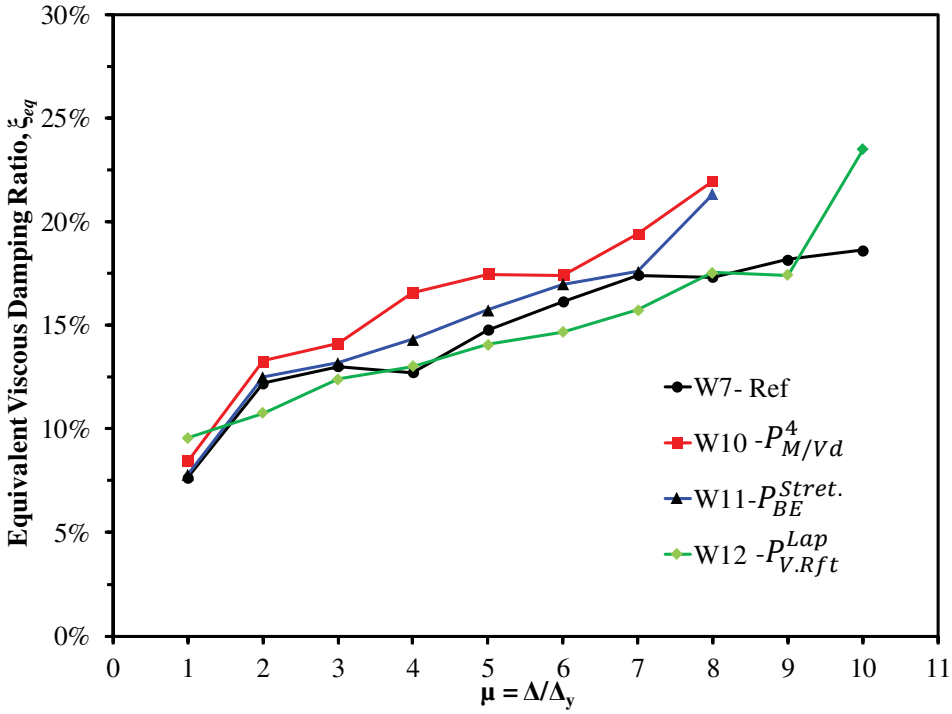

Figure A.13 Variation of equivalent viscous damping ratios with increasing ductility demands

Table A.3 summarizes the predicted and measured lateral loads and displacements of the six tested walls. The measured values were taken as the average between the two loading (push and pull) directions. The predicted lateral loads and displacements were calculated according to CSA S304-14 flexural resistance provisions using the measured material properties and without using any material strength reduction factors. In addition, the calculated ultimate loads were nominal values, without using the 1.25 factor which accounts for the strain hardening to calculate the probable resistance. The contribution of the compression reinforcement to the lateral resistance was also accounted for, but only for the rebars that were sufficiently tied using the confinement hoops. The yield and ultimate loads were underestimated, especially for wall W9 which had the largest confined grout core. This could be attributed to the increase in lateral resistance due to the confinement effect. Overall the prediction of capacities based on the application of the beam analysis theory and using the equations of CSA S304-14, including the tied compression reinforcing bars was acceptable and conservative. The predictions of lateral displacements at first yield in vertical reinforcement were also on the conservative side, except for wall W12. This is due to the impact of doubling the longitudinal rebars at the lap splices locations in wall W12, which was not accounted for in the predictions.

Table A.3 Predicted and measured lateral loads and displacements

	Predicted			**Measured**			**Predicted/Measured**		
Unified ID	**Q_y (kN)**	**Δ_y (mm)**	**Q_u (kN)**	**Q_y (kN)**	**Δ_y (mm)**	**Q_u (kN)**	**Q_y (kN)**	**Δ_y (mm)**	**Q_u (kN)**
W7	45.7	5.18	52.2	48.6	5.60	61.7	0.94	0.93	0.85
W8	59.5	5.32	67.8	65.1	6.38	82.5	0.91	0.83	0.82
W9	57.9	5.16	69.0	69.2	6.73	86.7	0.84	0.77	0.80
W10	90.8	4.69	104.8	97.9	6.00	113.4	0.93	0.78	0.92
W11	42.3	5.67	47.3	45.4	5.40	57.4	0.93	1.05	0.82
W12	45.4	5.04	52.4	44.7	4.15	62.0	1.02	1.21	0.85

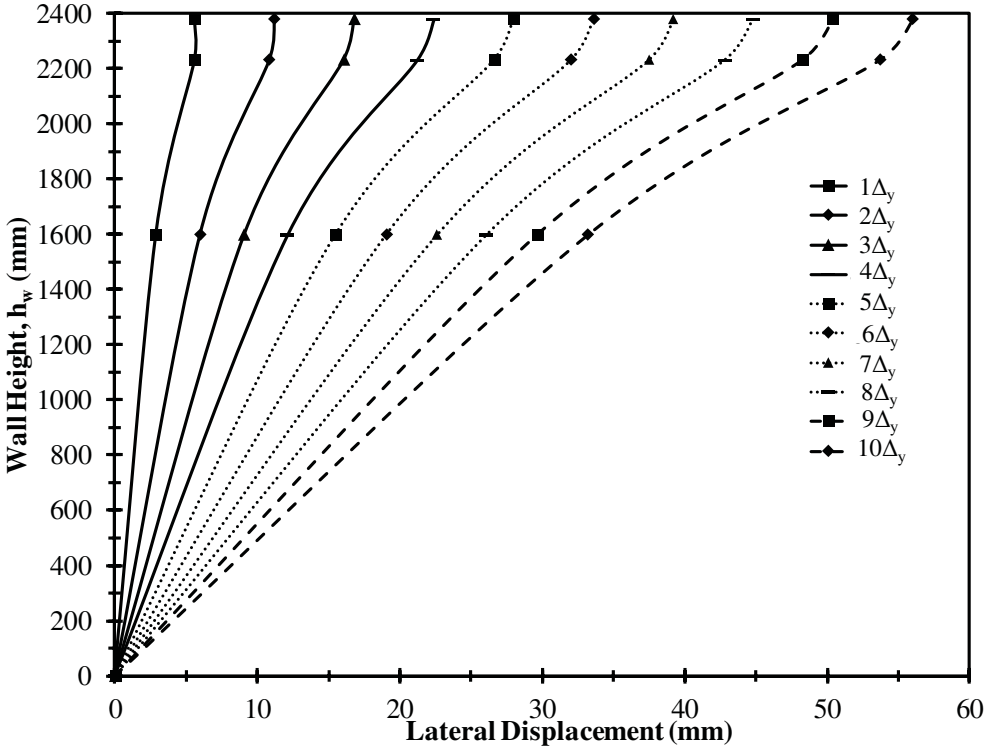

Figure A.14 Lateral displacement profiles along the height of wall W7

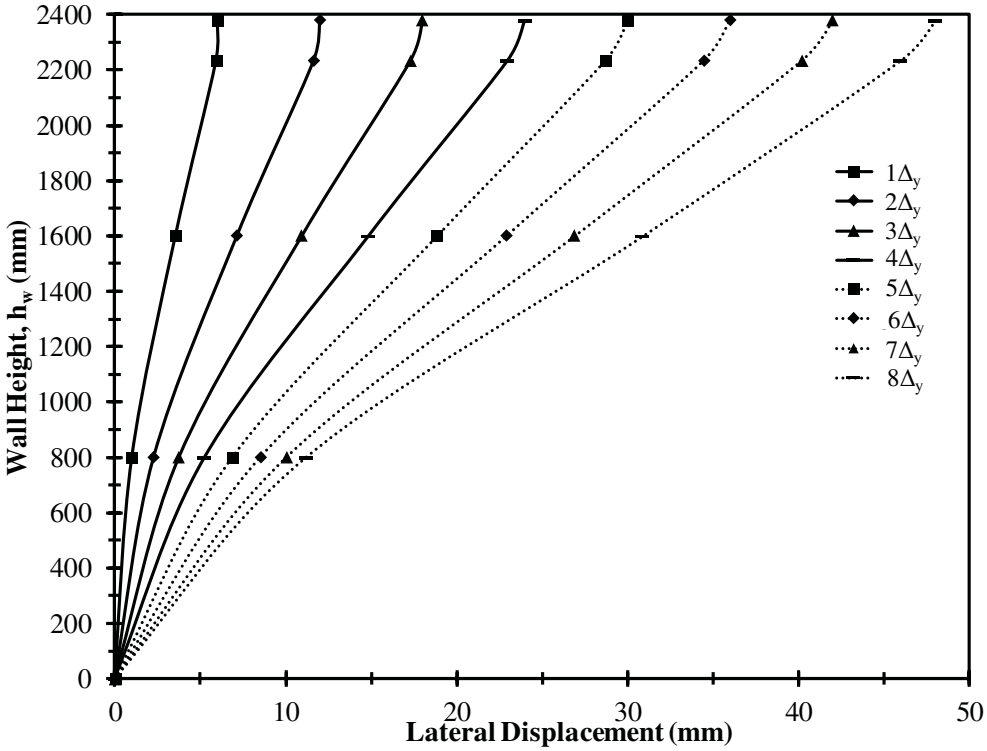

Figure A.15 Lateral displacement profiles along the height of wall W10

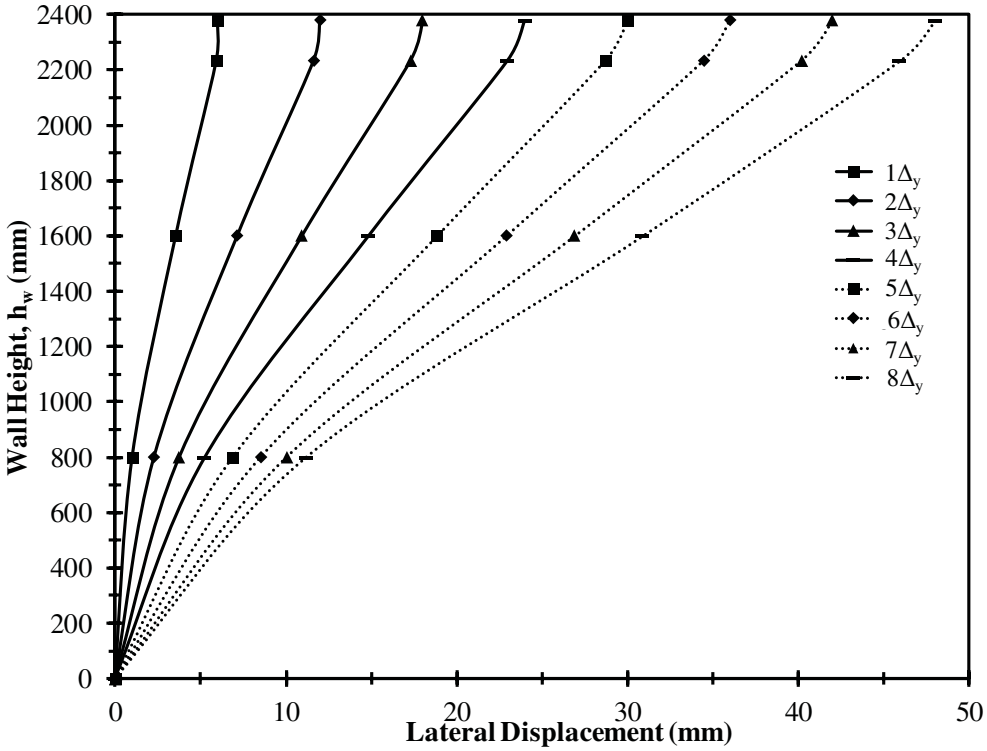

Figure A.16 Lateral displacement profiles along the height of wall W11

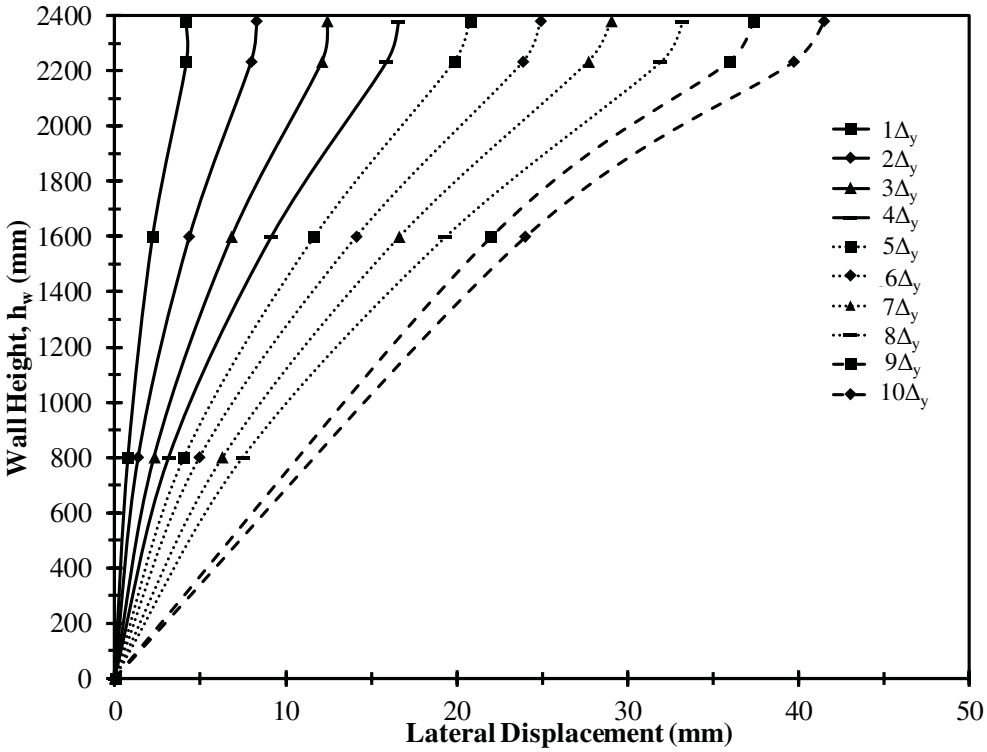

Figure A.17 Lateral displacement profiles along the height of wall W12

A.3 Construction of Concrete Masonry Prisms

(a) (b)

Figure A.18 Construction of four-courses concrete masonry prisms: (a) web (stretcher blocks) and boundary element (C-shaped blocks) prisms; and (b) boundary element (stretcher blocks) prisms

A.4 Testing of the Wall's Constituent Materials

Figure A.19 Sampling of Type S mortar cubes

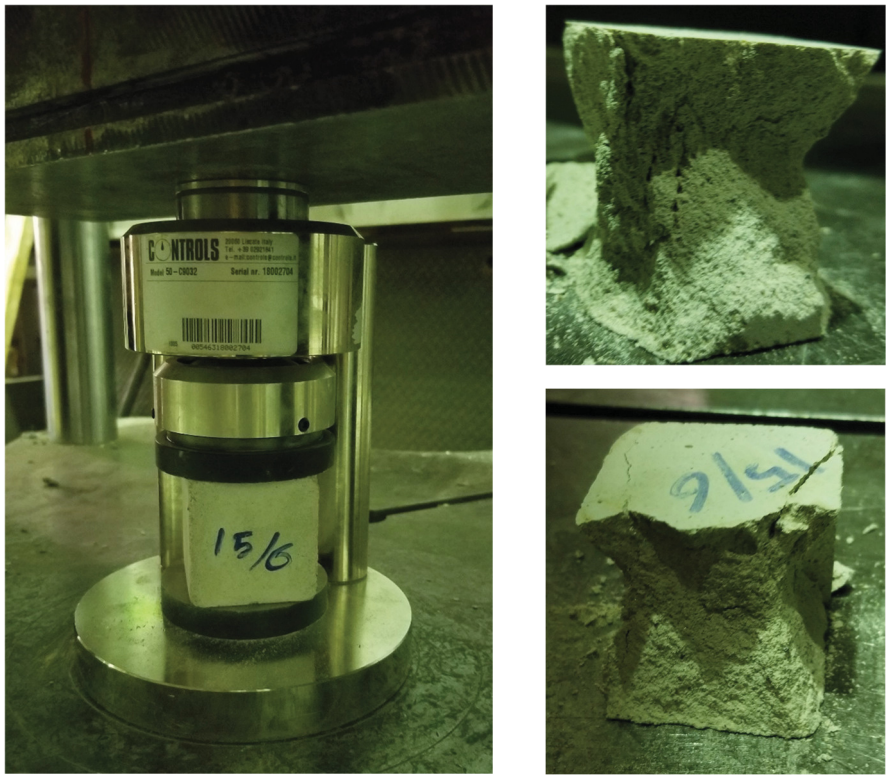

Figure A.20 Testing of Type S mortar cubes

Figure A.21 Testing of the grout cylinders

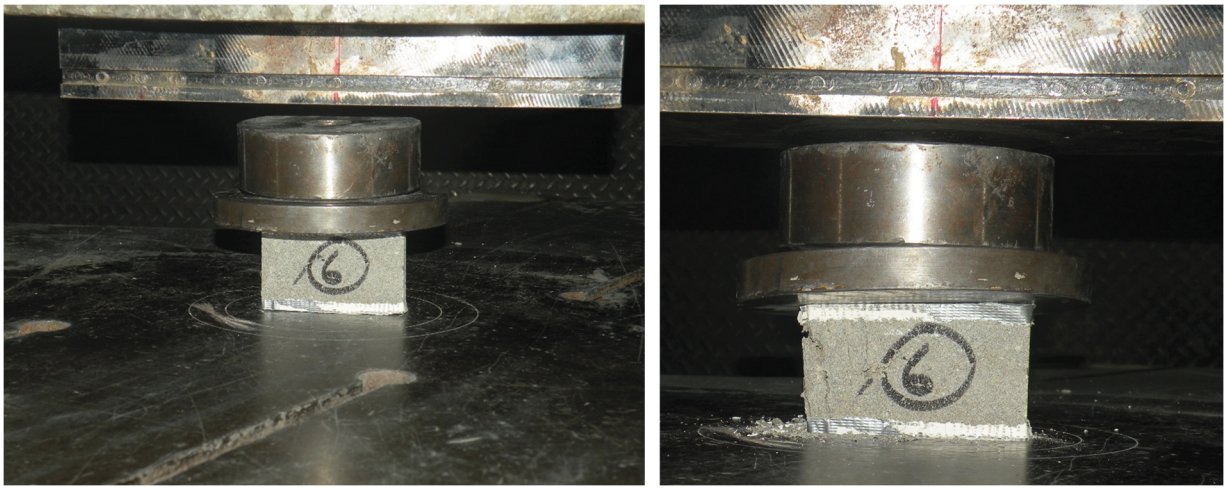

Figure A.22 Testing of half-scale C-shaped blocks' coupons

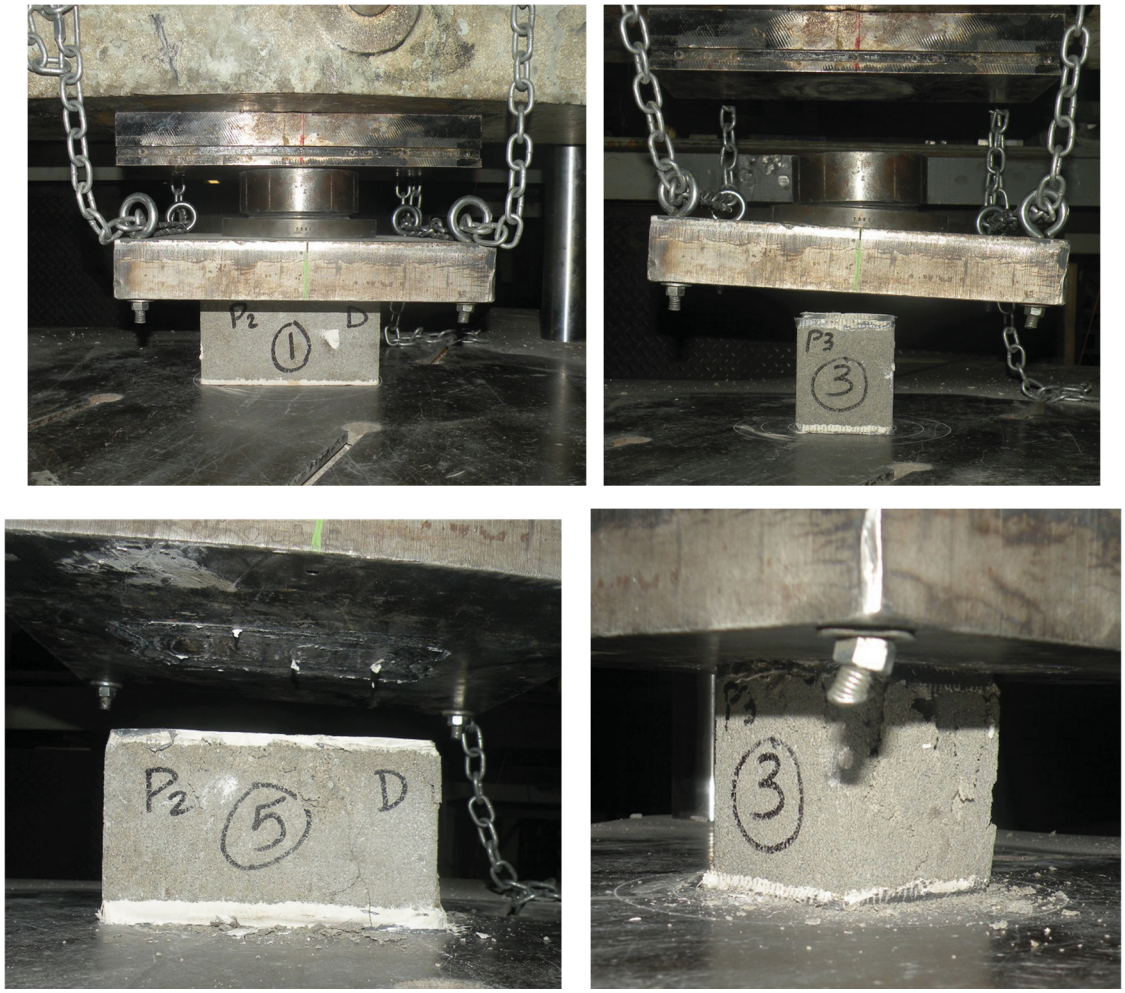

Figure A.23 Testing of half-scale stretcher blocks

Figure A.24 Testing of the bottom and top footings' concrete

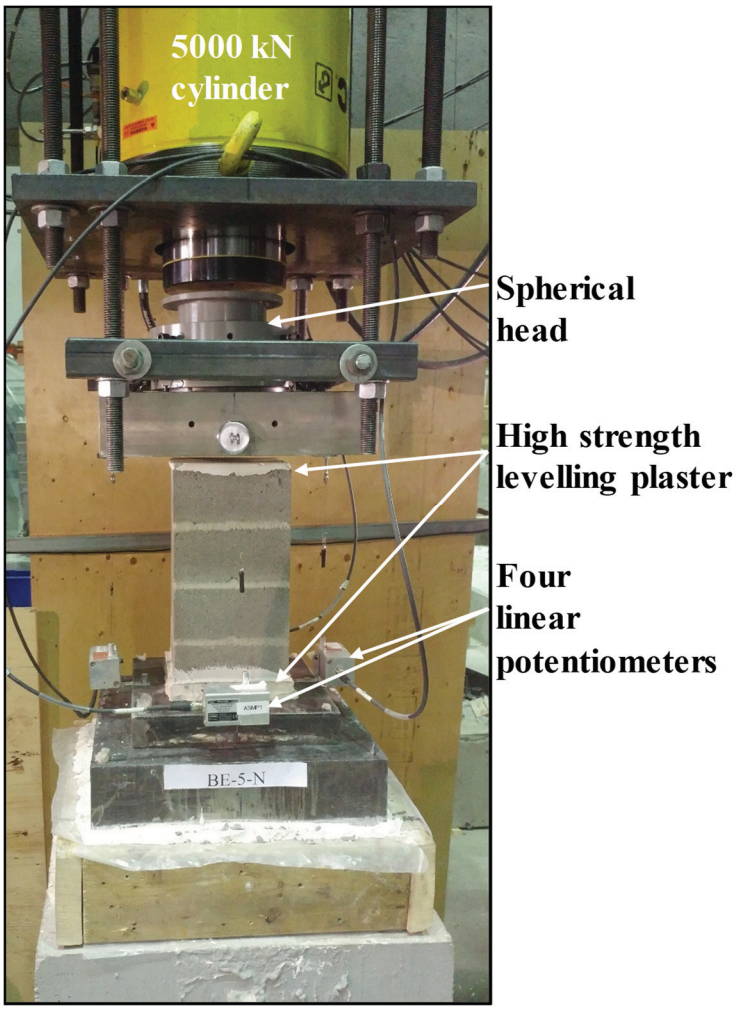

Figure A.25 Testing setup for masonry prisms

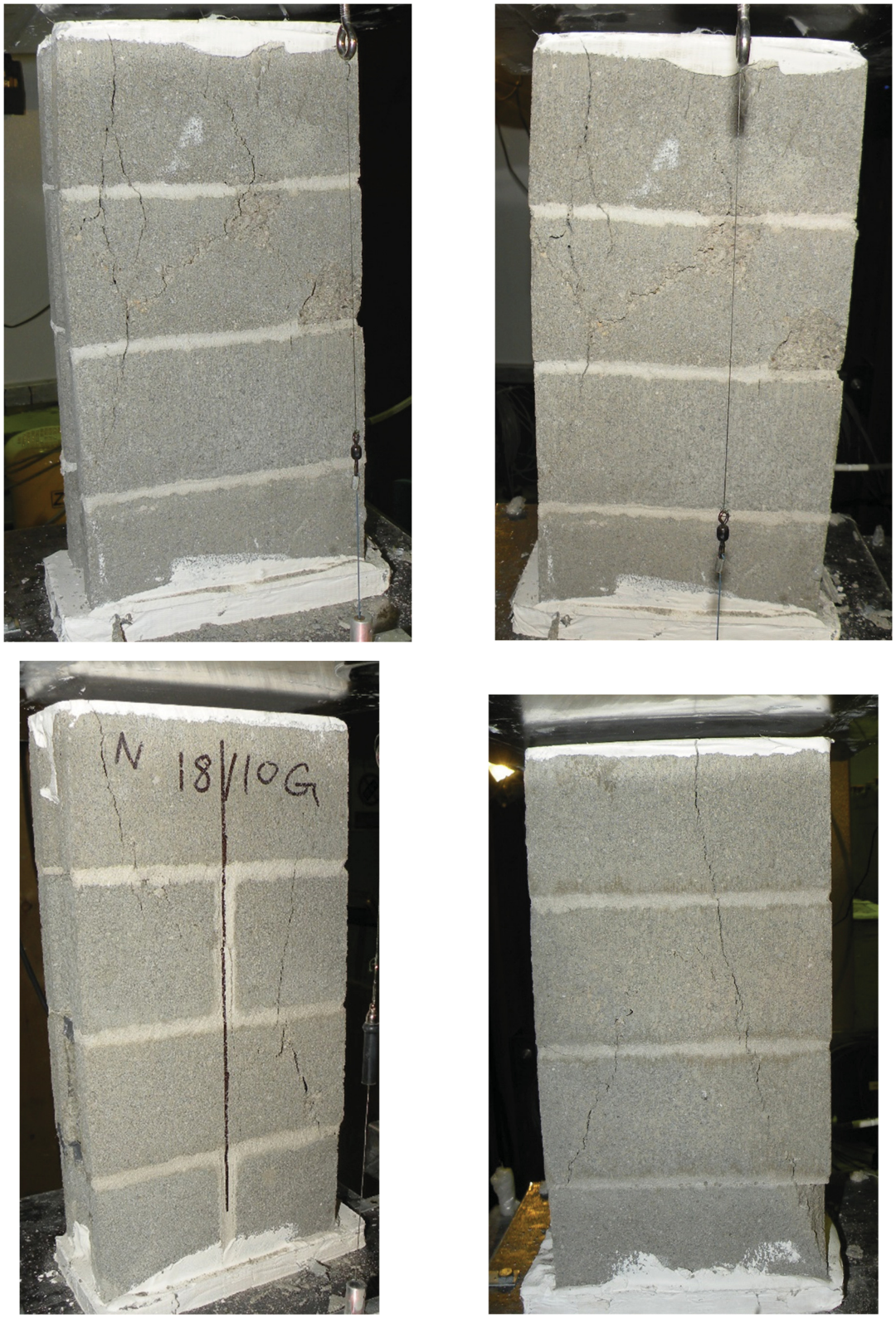

Figure A.26 Typical final damage states of tested web (stretcher blocks) prisms

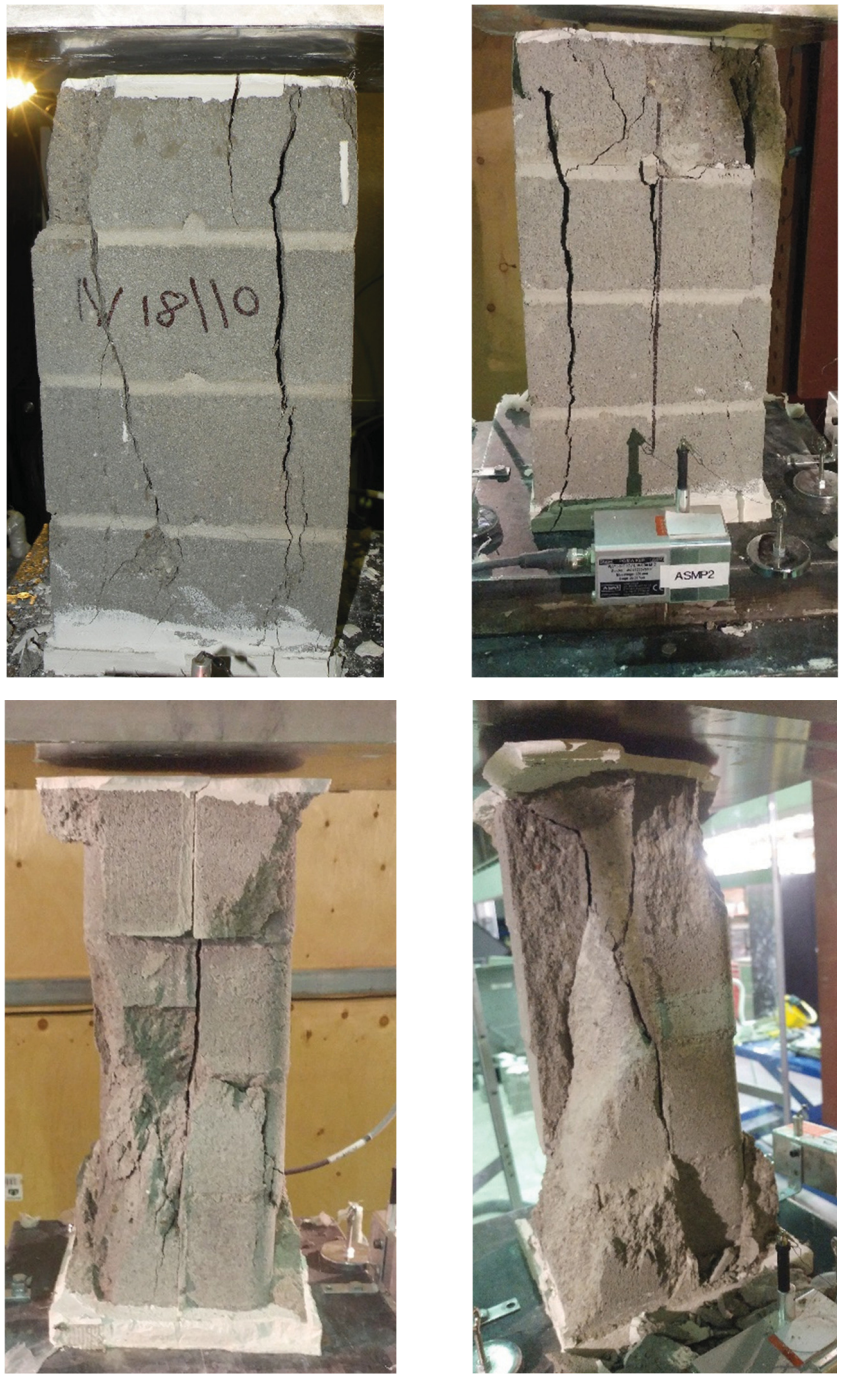

Figure A.27 Typical final damage states of tested boundary element (C-shaped blocks) prisms

Figure A.28 Typical final damage states of tested boundary element (stretcher blocks) prisms

Figure A.29 Testing of #3 reinforcing bars

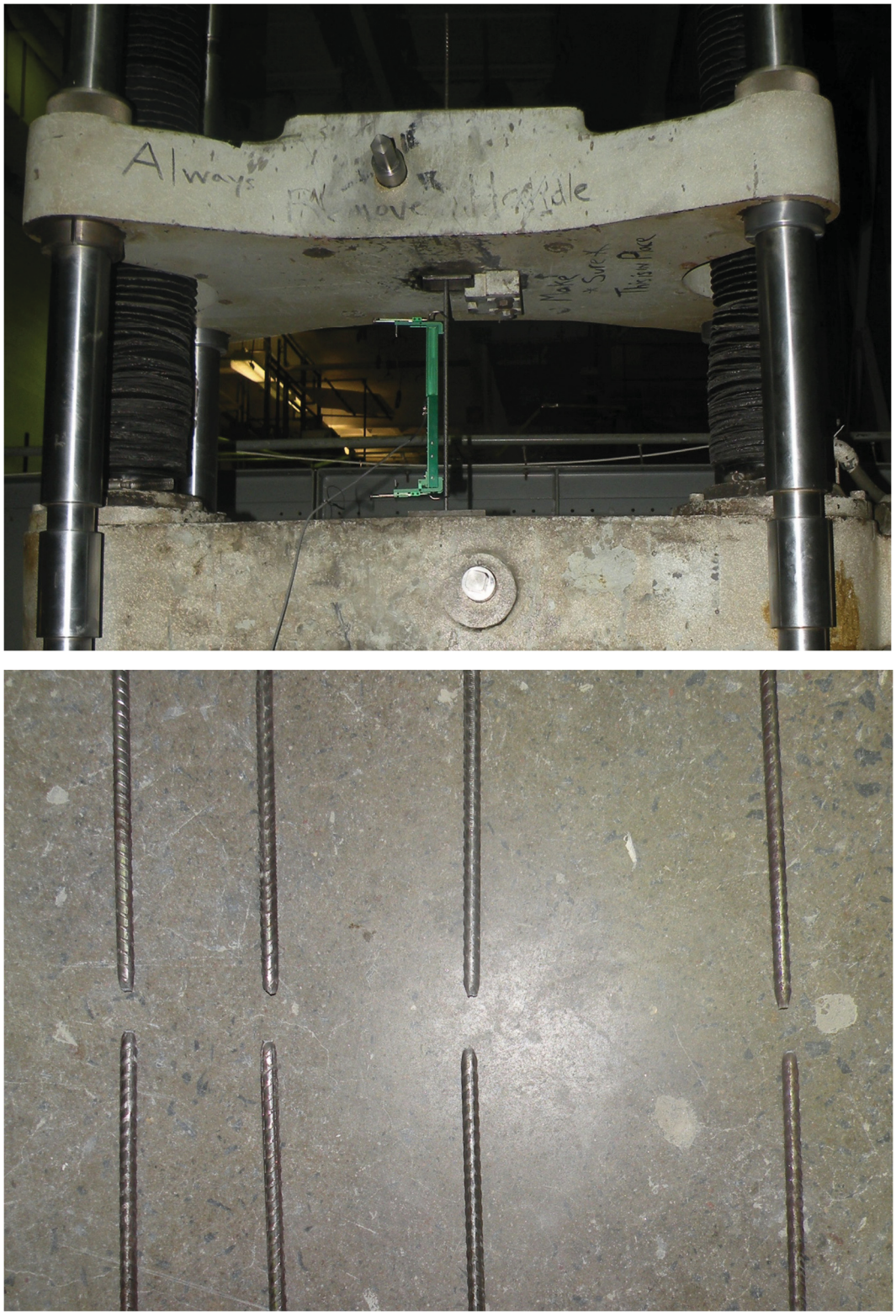

Figure A.30 Testing of D4 and D8 deformed wires

A.5 Additional Results for the Materials' Testing

Table A.4 Sample of boundary element prisms (C-shaped) testing results (W7, W8 and W9)

Specimen	f_{max} (MPa)	$^{*}\varepsilon_0$	$^{**}\varepsilon_{85\%}$	$^{***}\varepsilon_{80\%}$
BE-1	26.51	0.00339	0.00453	0.00490
BE-2	24.83	0.00388	0.00486	0.00514
BE-3	26.20	0.00346	0.00404	0.00424
Average	25.85	0.00358	0.00448	0.00476
c.o.v	3%	7%	9%	10%

* strain at peak stress
** strain at 15% strength degradation
*** strain at 20% strength degradation

Table A.5 Sample of web prisms testing results (W7, W8 and W9)

Specimen	f_{max} (MPa)	ε_0	$\varepsilon_{85\%}$	$\varepsilon_{80\%}$
Web-1	10.45	0.00234	0.00271	0.00278
Web-2	9.35	0.00186	0.00259	0.00264
Web-3	10.96	0.00189	0.00241	0.00244
Average	10.25	0.00203	0.00257	0.00262
c.o.v	8%	13%	6%	7%

Table A.6 Sample of boundary element prisms (C-shaped) testing results (W10, W11 and W12)

Specimen	f_{max} (MPa)	ε_0	$\varepsilon_{85\%}$	$\varepsilon_{80\%}$
BE-1	29.12	0.00362	0.00445	0.00472
BE-2	22.37	0.00365	0.00436	0.00457
BE-3	30.13	0.00317	0.00513	0.00588
Average	27.21	0.00348	0.00465	0.00505
c.o.v	16%	8%	9%	14%

Table A.7 Sample of boundary element prisms (stretcher) testing results (W10, W11 and W12)

Specimen	f_{max} (MPa)	ε_0	$\varepsilon_{85\%}$	$\varepsilon_{80\%}$
BE-1	14.79	0.00277	0.00352	0.00356
BE-2	13.30	0.00303	0.00348	0.00371
BE-3	15.07	0.00253	0.00308	0.00314
Average	14.39	0.00278	0.00336	0.00347
c.o.v	7%	9%	7%	9%

Table A.8 Sample of web prisms testing results (W10, W11 and W12)

Specimen	f_{max} (MPa)	ε_0	$\varepsilon_{85\%}$	$\varepsilon_{80\%}$
Web-1	14.96	0.00211	0.00256	0.00256
Web-2	15.46	0.00188	0.00228	0.00241
Web-3	15.96	0.00206	0.00251	0.00265
Average	15.46	0.00202	0.00245	0.00254
c.o.v	3%	6%	6%	5%

A.6 Variation in Response due to Materials' Variability

As can be seen, the response of reinforced concrete masonry involves the interaction between several constituent materials (i.e. concrete masonry blocks, grout, mortar, and steel reinforcement). Each material exhibits some degree of variability in response due to the natural variation in materials' properties. This is also reflected in the c.o.v. seen in the testing of the constituent materials, which ranged from 3% to 15%. This variability is expected to influence the response of reinforced masonry at the component and system levels. Thus, the findings and observations from the tested walls could be partially affected by the variation in materials' properties. The variability in response due to variation in the properties of the constituent materials is highest in unreinforced masonry, becomes lesser with partial grouting, and is minimized in fully grouted and well reinforced masonry. Hamid and Chandrakeerthy (1992) demonstrated that reducing the horizontal spacing between the grouted masonry cells increased the compression load capacity and reduced the variability of the material. In addition, Bolhassani et al. (2016) noted that the performance consistency and predictability is higher in fully grouted reinforced masonry walls when compared with the partially grouted counterparts.

It is noteworthy to highlight that the variability in the response of the tested walls was minimized by ensuring that the walls were constructed from similar materials by the same professional mason. The walls were also fully grouted, sufficiently reinforced vertically and horizontally, and the end zones were confined with closely spaced hoops. Furthermore, the tested walls were flexure dominated. The flexure behaviour of RCM shear walls is well-defined and exhibits less variation compared to the complex shear response. The flexure behaviour is controlled by the stress-strain of the reinforcing steel, the ultimate compressive strain of the masonry prism, and the buckling of longitudinal rebars, which is controlled by the spacing of stirrups. However, in all cases, the variability in the response of reinforced masonry structural components and system should be acknowledged and accounted for in the design and performance assessment.

Appendix B

Supplemental Information to the Numerical Work (Chapters 5 and 6)

This Appendix presents additional information to the numerical research presented in chapters 5 and 6.

B.1 Additional Validation of the Numerical Model

Tables B.1 and B.2 show a summary of the quantitative verification of the models developed in Seismostruct and *OpenSees*, respectively. Description and details of the element model, section model, and constitutive material models were given in chapters 5 and 6 for Seismostruct and *OpenSees* models, correspondingly. It can be seen that both models were capable of simulating the response of RCM shear walls with reasonable accuracy.

Table B.1 Quantitative validation of the numerical model developed in Seismostruct program

			$\Delta_{y\text{-}Num}/\Delta_{y\text{-}Exp}$		$Q_{y\text{-}Num}/Q_{y\text{-}Exp}$		$Q_{u\text{-}Num}/Q_{u\text{-}Exp}$	
Wall No. in Literature	**Reference**	**Configuration**	**Push (+ve)**	**Pull (-ve)**	**Push (+ve)**	**Pull (-ve)**	**Push (+ve)**	**Pull (-ve)**
W1	(Shedid et al. 2010a)	Rectangular	1.06	0.94	1.11	1.05	1.04	1.00
W2	(Shedid et al. 2010a)	Flanged	0.98	1.02	1.13	1.12	1.05	1.00
W6	(Shedid et al. 2010a)	End confined	0.98	1.03	1.07	1.09	0.98	1.00
W1	(Banting and El-Dakhakhni, 2012)	End confined	0.99	1.00	1.12	1.10	0.96	0.99
W2	(Banting and El-Dakhakhni, 2014)	End confined	0.98	0.98	1.06	1.15	0.98	1.03

Table B.2 Quantitative validation of the numerical model developed in *OpenSees* program

				$\Delta_{y\text{-}Num}/\Delta_{y\text{-}Exp}$		$Q_{y\text{-}Num}/Q_{y\text{-}Exp}$		$Q_{u\text{-}Num}/Q_{u\text{-}Exp}$	
Wall No.	**Wall No. in Literature**	**Reference**	**Configuration**	**Push (+ve)**	**Pull (-ve)**	**Push (+ve)**	**Pull (-ve)**	**Push (+ve)**	**Pull (-ve)**
W1	W1	(Banting and El-Dakhakhni, 2012)	End confined	1.00	1.00	0.89	0.85	1.00	1.05
W2	W2	(Banting and El-Dakhakhni, 2014)	End confined	0.98	0.98	0.91	1.00	1.00	1.02
W3	W6	(Shedid et al. 2010a)	End confined	0.98	1.03	0.81	0.88	1.03	1.03
W4	W1	(Shedid et al. 2010a)	Rectangular	1.06	0.94	0.98	0.89	1.09	1.05
W5	W4	(Shedid et al. 2010a)	Rectangular	0.97	1.03	0.84	0.82	1.09	1.06

The numerical models were also validated against the experimental testing results of walls W7, W8, and W9, which were tested as part of the experimental work of this thesis. These walls varied in the end zone's (boundary element) size and detailing. Figures B.1 and B.2 illustrate the verification of Seismostruct and *OpenSees* models, respectively. Besides, Tables B.3 and B.4 summarize the quantitative validation of the numerical models.

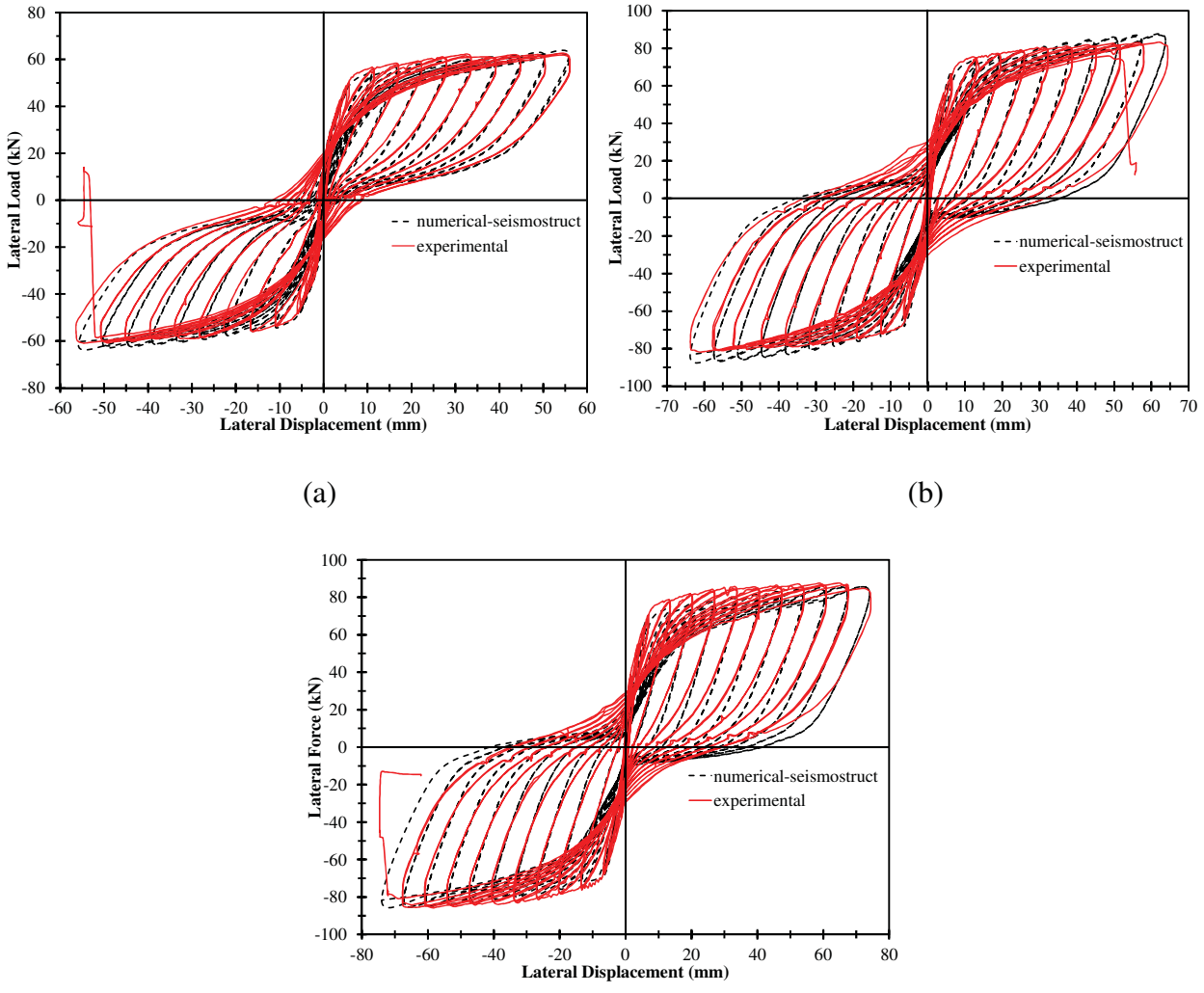

Figure B.1 Experimental and numerical load-displacement response using Seismostruct model: (a) wall W7; (b) wall W8; and (c) wall W9

Table B.3 Quantitative validation of the numerical model developed in Seismostruct program

		$\Delta_{y\text{-}Num}/\Delta_{y\text{-}Exp}$		$Q_{y\text{-}Num}/Q_{y\text{-}Exp}$		$Q_{u\text{-}Num}/Q_{u\text{-}Exp}$	
Wall No.	**Configuration**	**Push (+ve)**	**Pull (-ve)**	**Push (+ve)**	**Pull (-ve)**	**Push (+ve)**	**Pull (-ve)**
W7	End confined	1.07	0.86	0.99	1.00	0.99	1.01
W8	End confined	1.02	1.01	1.02	1.06	1.01	1.03
W9	End confined	0.97	1.05	0.97	1.02	0.93	0.95

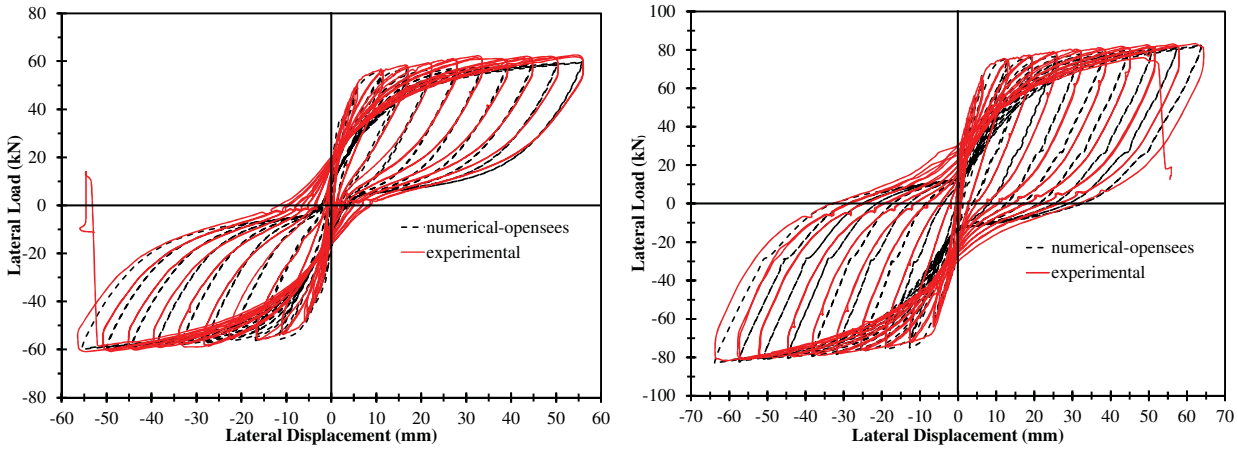

(a) (b)

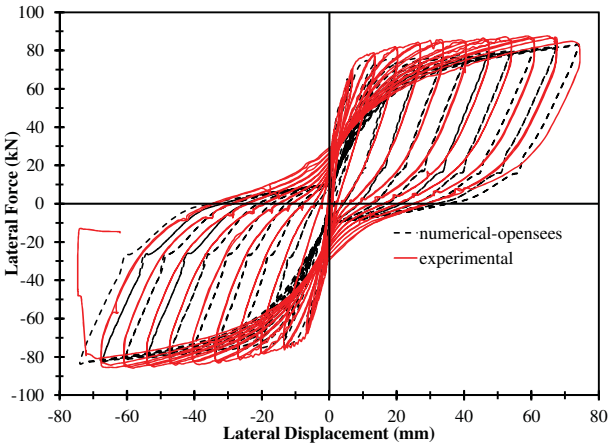

(c)

Figure B.2 Experimental and numerical load-displacement response using *OpenSees* model: (a) wall W7; (b) wall W8; and (c) wall W9

Table B.4 Quantitative validation of the numerical model developed in *OpenSees* program

		$\Delta_{y\text{-}Num}/\Delta_{y\text{-}Exp}$		$Q_{y\text{-}Num}/Q_{y\text{-}Exp}$		$Q_{u\text{-}Num}/Q_{u\text{-}Exp}$	
Wall No.	**Configuration**	**Push (+ve)**	**Pull (-ve)**	**Push (+ve)**	**Pull (-ve)**	**Push (+ve)**	**Pull (-ve)**
W7	End confined	1.12	0.90	0.99	1.00	0.91	0.94
W8	End confined	1.00	1.00	0.94	0.97	0.93	0.96
W9	End confined	0.96	1.04	0.96	0.96	0.88	0.91

B.2 Sensitivity of the Numerical Model

The mesh sensitivity (number of fibers and element's size) of the utilized numerical models in this research was assessed and presented in chapters 5 and 6. The sensitivity of the models were further assessed to the different material and modelling parameters. The model developed in Seismostruct program and utilized in chapter 5 is most suitable for flexure dominated walls. This model is most sensitive to the reinforcement nonlinear modelling parameters, in particular the transition curve initial shape parameter (R), and the transition curve shape calibrating coefficients ($A1$ and $A2$). For the masonry/concrete modelling parameters, the choice of the peak compressive stress (f'_m), the corresponding strain (ε_{mo}), and the elastic modulus (E_m) is also crucial, but less influential. Based on the calibration of the numerical model against the results of the experimentally tested walls (Tables 5.4, 6.3, B.1, and B.2), it was found that using the initial modulus as $1000\,f'_m$ instead of $850f'_m$ increases the accuracy of the simulated response. On the other hand, the model developed in *OpenSees* using the SFI-MVLEM is suitable for flexural dominant walls as well as walls with moderate aspect ratios. This is because that model is capable of capturing the nonlinear shear response and the coupled shear-flexure interaction. As such, this model is sensitive to the shear mechanism modelling parameters (η and α), in addition to the steel and masonry/concrete modelling parameters. However, since all the walls studied in this research were carefully designed to fail in flexure, following the capacity design method, with sufficiently high shear resistance, the modelling parameters of the reinforcing steel were also the most influential on the simulated response.

B.3 Limitations of the Numerical Model

In additions to the limitations mentioned in chapters 5 and 6, this section highlights additional limitations in the utilized numerical models and the performed analyses. These limitations can be addressed in future studies building on the findings of this research. The modelling approaches assumed that only the local failure modes seen in the experimental testing would occur. This is

because the simulated response, using the finite element modelling, was extrapolated from the considered validation parameters (i.e. available specimens' sizes and material properties). More testing is required considering wider ranges of design parameters (e.g. different strengths for the blocks and grout) to enhance the modelling accuracy. The models are incapable of capturing other possible local failure modes, such as the shear failure along the web and boundary element interface. It was assumed that the failure mode remains flexural. Besides, as the modelling was two-dimensional, the effect of the out-of-plane loading on the in-plane failure mode was neglected. The models do not capture the coupling action from the slab and the contribution from the orthogonal walls to the in-plane lateral response. Nevertheless, global failure modes were imposed through post-processing of the analysis results, such as limiting the peak inter-storey drift to the building code's (i.e. NBCC-15) limit.

In the nonlinear time-history analyses, the vertical component of the ground motions was not considered. This was based on the assumption that the vertical acceleration is small and its effects, compared to the gravity loads, can be neglected. This assumption was also needed to optimize the computational time, given the substantial number of analyses performed (due to the number of studied archetype buildings and the used ground motions). However, in case if the vertical component of the ground motions, depending on the studied locations, is significant, it could affect the axial load in the walls. For instance, an upward displacement could increase the axial load in the walls. Conversely, a downward ground motion could result in tensile axial forces, which need to be considered in the flexural design of the walls. As such, it would be useful in future studies to consider the vertical component of ground motions to quantify its effects on the response of the proposed hybrid structural system of ductile and gravity walls.

B.4 Selection of Archetype Buildings

Figure B.3(a) compares the elastic response spectra of the three locations considered in this research. Vancouver and Montréal were used in chapter 5 to investigate the height limits of ductile RCM shear walls with boundary elements. The selection of these locations was mainly to ensure covering the moderate and high seismicity ranges of NBCC-15. In chapter 6, Québec City was selected to represent another region with moderate seismicity in Canada. It is noteworthy that the findings will not significantly change based on the particular selected location, as long as it represents a region with either high or moderate seismic hazard. The structural layout of the

archetype buildings is shown in Figure B.3(b) highlighting the location of the stairs and elevator's shaft. For simplicity, the void of the stairs and elevator's shaft was not shown in the plans presented in chapters 5 and 6. The slab was shown solid to account for the weight of the stairs. It is worth highlighting that considering the weight of the stairs, the structural layout remains symmetric.

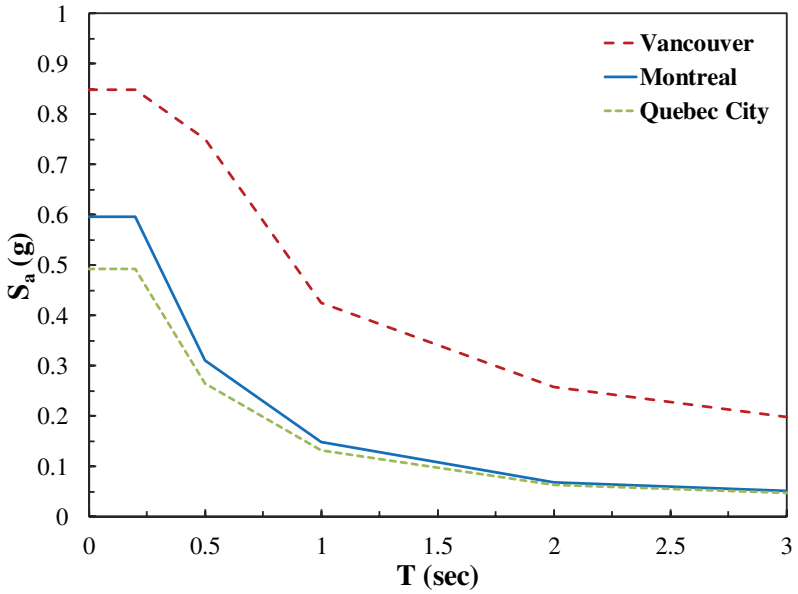

(a)

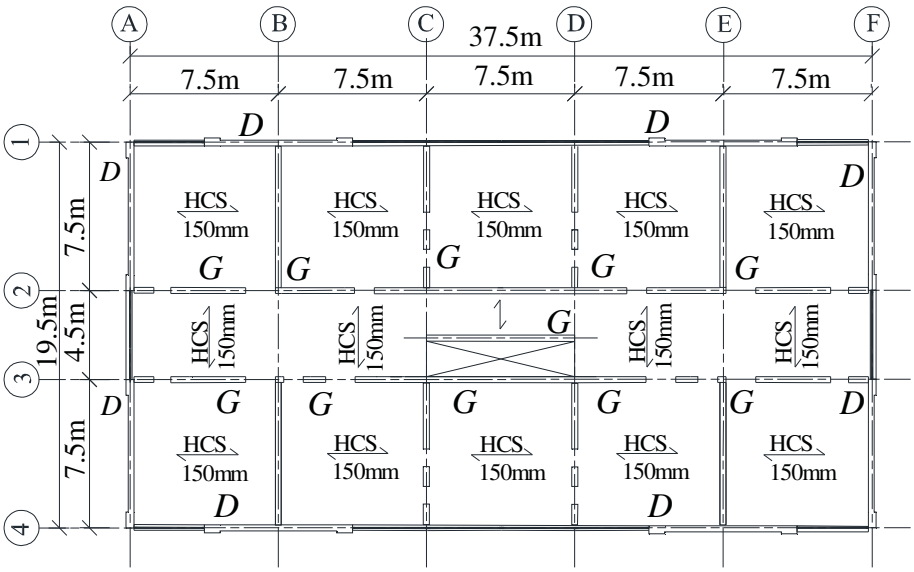

(b)

Figure B.3 (a) Elastic response spectra of selected locations; and (b) Archetype buildings' typical floor plan view